COO-2250-1
MITNE-142

HETEROGENEOUS EFFECTS IN FAST BREEDER REACTORS

by

M. V. Gregory, M. J. Driscoll, D. D. Lanning

January, 1973

Department of Nuclear Engineering
Massachusetts Institute of Technology
Cambridge, Massachusetts 02139

AEC Research and Development Report
UC-34 Physics
Contract AT(11-1)- 2250
U.S. Atomic Energy Commission

MASSACHUSETTS INSTITUTE OF TECHNOLOGY

DEPARTMENT OF NUCLEAR ENGINEERING

Cambridge, Massachusetts

HETEROGENEOUS EFFECTS IN FAST BREEDER REACTORS

by

M. V. Gregory, M.J. Driscoll, D.D. Lanning

January, 1973

COO-2250-1

MITNE - 142

AEC Research and Development Report

UC-34 Physics

Contract AT(11-1) - 2250

U.S. Atomic Energy Commission

DISTRIBUTION LIST

Contract AT(11-1)-2250

U.S. Atomic Energy Commission, Headquarters
Division of Reactor Development and Technology
Reactor Physics Branch (3 copies)

U.S. Atomic Energy Commission
Cambridge Office (2 copies)

Dr. Paul Greebler, Manager
Nuclear Energy Division
Breeder Reactor Department
General Electric Company
310 DeGuigne Drive
Sunnyvale, California 94086 (1 copy)

Dr. Harry Morewitz, Manager
LMFBR Physics and Safety Projects
Atomics International
P.O. Box 309
Canoga Park, California 91305 (1 copy)

Mr. Malcolm Dyos, Manager
Nuclear Development, LMFBR Project
Westinghouse Electric Corporation
Advanced Reactors Division
Waltz Mill Site
P.O. Box 158
Madison, Pennsylvania 15663 (1 copy)

Dr. Robert Avery, Director
Reactor Physics Division
Argonne National Laboratory
9700 South Cass Avenue
Argonne, Illinois 60539 (1 copy)

Dr. Charles A. Preskitt, Jr.
Manager, Atomic and Nuclear Department
Gulf Radiation Technology
P.O. Box 608
San Diego, California 02112 (1 copy)

ABSTRACT

Heterogeneous effects in fast breeder reactors are examined through development of simple but accurate models for the calculation of a posteriori corrections to a volume-averaged homogeneous representation. Three distinct heterogeneous effects are considered: spatial coarse-group flux distribution within the unit cell, anisotropic diffusion, and resonance self-shielding. An escape/transmission probability theory is developed which yields region-averaged fluxes, used to flux-weight cross sections. Fluxes calculated by the model are in substantial agreement with S_8 discrete ordinate calculations. The method of Benoist, as applied to tight lattices, is adopted to generate anisotropic diffusion coefficients in pin geometry. The resulting perturbations from a volume-averaged homogeneous representation are interpreted in terms of reactivities calculated from first order perturbation theory and an equivalent "total differential of k" method. Resonance self-shielding is treated by the f-factor approach, based on correlations developed to give the self-shielding factors as functions of one-group constants.

Various reference designs are analyzed for heterogeneous effects. For a demonstration LMFBR design, the whole-core sodium void reactivity change is calculated to be 90¢ less positive for the heterogeneous core representation compared to a homogeneous core, due primarily to the effects of anisotropic diffusion. Parametric studies show at least a doubling of this negative reactivity contribution is attainable for judicious choices of enrichment, lattice pitch and lattice geometry (particularly the open hexagonal lattice). The fuel dispersal accident is analyzed and a positive reactivity contribution due to heterogeneity is identified.

The results of intra-rod U-238 activation measurements in the Blanket Test Facility are analyzed and compared to calculations. This activation depression is found to be of the order of 10% (surface-to-average) for a typical LMFBR blanket rod and is ascribed to the effect of heterogeneous resonance self-shielding of U-238. Heterogeneous effects on the breeding ratio are studied with the conclusions that accounting for resonance self-shielding reduces the total breeding ratio by over 10%, but heterogeneous effects are not important for breeding ratio calculations.

ACKNOWLEDGMENTS

This report is based on a thesis submitted by Michael V. Gregory to the Department of Nuclear Engineering at the Massachusetts Institute of Technology in partial fulfillment of the requirements for the degree of Doctor of Philosophy.

Financial support from the U.S. Atomic Energy Commission under Contract AT(11-1) - 2250 is gratefully acknowledged.

Typing of the manuscript was very able carried out by Mrs. Mary Bosco.

Computer calculations were performed at the M.I.T. Information Processing Center.

TABLE OF CONTENTS

LIST OF FIGURES

LIST OF TABLES

Table

Table

Chapter 1

INTRODUCTION

1.1 Foreword

The purpose of the research reported herein has been to develop and apply a consistent formalism describing the effects of heterogeneity on fast reactor core and blanket neutronics. Attention is focussed upon the pin geometry characteristic of LMFBR power reactors, and emphasis is placed upon development of simple models which provide clear physical insight into the variety of phenomena involved, but which are sufficiently accurate for reactor physics design calculations.

1.2 Background and Outline

In the course of fast reactor calculations, one commonly makes the approximation that the core may be homogenized in a volume-averaged sense. That is, homogenized cross sections are calculated by:

$$\Sigma = \sum_i V_i \Sigma_i / \sum_i V_i , \qquad (1.1)$$

where the summation is over i regions, each of volume V_i and characterized by macroscopic cross section Σ_i. The justification for this type of simple homogenization is based on the observation that the mean free path is approximately a factor of ten larger than any characteristic dimension over which physical properties change. Thus, the rationale continues, along its mean free path journey through the medium, the average neutron experiences the distinct regions only in an average

sense which may be represented by a simple volume-averaging. The rationale concludes with the claim that this homogenization is valid in an integral sense because the error in the effective multiplication constant, k_{eff}, is small.

However, the classification of effects as "small" requires some caution in the case of fast reactors. This is because the effective delayed neutron fraction is small (roughly 0.0033 for a UO_2-PuO_2 core) and seemingly small errors in k_{eff} assume a larger significance when discussed in terms of reactivity normalized to the delayed neutron fraction. Such significance will be shown to be of great import when the global sodium void reactivity is analyzed in Chapter 6.

In a recent paper, Greebler and Hutchins [1] have estimated the precision of various design parameter calculations for the LMFBR. For the sodium void effect, the current estimate is ± \$1.50; the goal for the demonstration plant is ±\$0.50; while the goal for the target plant of the 1980s is ±\$0.30. This last uncertainty is approximately ± 0.001 in the multiplication constant k; thus the correct representation of heterogeneous effects, which will be shown to have an effect significantly greater than the target precision goal, becomes a design necessity.

The physical assumption underlying the homogenization prescription can be elucidated by looking in detail at the unit cell, extracted from an infinite medium. The unit cell extracted from the homogeneous medium is, of course, itself homogeneous. The flux profile in this cell is flat since the neutron sources and sinks are uniformly distributed. On the other hand, the unit cell in the heterogeneous medium consists of three concentric regions: fuel at the center,

surrounded by clad, which is surrounded by the coolant region. Depending on what energy group one is observing, the flux in the unit cell may be peaked in the fuel region or peaked in the coolant region, due to the localization of different sources in different regions. Thus the simple volume-averaged homogenization is valid only to the degree that the deviation from a flat flux has a negligible effect on the multiplication constant.

A more precise homogenization may be obtained by requiring that average reaction rates be preserved. That is, within an energy group:

$$\Sigma = \frac{\sum_i \int \Sigma_i(\underline{r})\phi_i(\underline{r})\,dV_i}{\sum_i \int \phi_i(\underline{r})\,dV_i} = \frac{\sum_i \bar{\phi}_i V_i \Sigma_i}{\sum_i \bar{\phi}_i V_i}, \tag{1.2}$$

where $\bar{\phi}_i = \int \phi_i(\underline{r})\,dV_i/V_i$ is the average flux in region i.

Various weighting methods have been compared [2], specifically real-flux weighting, as in Eq. (1.2), and bilinear weighting using angularly dependent real and adjoint S_N fluxes. Real-flux weighting is found to yield a more accurate k_{eff} compared to an exact (i.e., not homogenized) Double-S_N calculation extrapolated to S_∞.

Specializing Eq. (1.2) to the three-region unit cell, one has:

$$\Sigma = \frac{\Sigma_1 V_1 + \Sigma_2 V_2(\bar{\phi}_2/\bar{\phi}_1) + \Sigma_3 V_3(\bar{\phi}_3/\bar{\phi}_1)}{V_1 + V_2(\bar{\phi}_2/\bar{\phi}_1) + V_3(\bar{\phi}_3/\bar{\phi}_1)}. \tag{1.3}$$

In the case of a flat flux profile, Eq. (1.3) reduces to Eq. (1.1).

One of the goals of the present work is the development of a simple method to calculate the average flux ratios used in Eq. (1.3) and thereby obtain the detailed heterogeneous cross sections to be compared with

the homogeneous cross sections defined by Eq. (1.1). Chapter 2 is devoted to this topic. Based on elementary perturbation theory in a two-group framework, one may then develop a method of calculating the reactivity contribution due to the non-flat spatial flux distribution (discussed in Chapter 4).

A second major area of consideration deals with the calculation of an appropriate diffusion coefficient. Since the fast reactor is quite frequently modelled by a diffusion theory code, one requires a consistent method to calculate diffusion coefficients. The usual procedure is to adopt the prescription used for homogeneous media with isotropic scattering:

$$D = \frac{1}{3\overline{\Sigma}_{tr}}, \tag{1.4}$$

where $\overline{\Sigma}_{tr}$ is given by the volume-averaging procedure of Eq. (1.1). In Chapter 3, this prescription will be shown to be unsatisfactory and a consistent counter-method will be discussed.

The energy self-shielding effect (not to be confused with the spatial flux distribution effect) is considered in Chapter 5 and found to be a significant effect; calculations neglecting resonance self-shielding are found to give results which differ markedly from those accounting for self-shielding. Self-shielding of the resonances of U-238 is found to greatly reduce the infinite dilution multigroup cross sections characterizing U-238. This energy self-shielding is shown to greatly mitigate the positive sodium voiding reactivity. It also exerts the major effect upon LMFBR blanket calculations.

In Chapter 6, the varied heterogeneous reactivity contributions discussed in earlier chapters are drawn together and applied to the

analysis of several reference fast breeder reactor core designs, while in Chapter 7 the effect of heterogeneity upon the blanket region is analyzed.

Throughout this report, the intent is to treat heterogeneous effects on a phenomenological basis: those physical processes which the homogenization of Eq. (1.1) and the use of infinitely dilute cross-section sets overlook are identified; a quantitative importance (in terms of reactivity) is associated with each identified process. The end goal is the presentation of a consistent method which yields the *a posteriori* correction to a homogeneous calculation.

1.3 Previous Work

The reactivity effects of voiding sodium from a fast reactor core were not fully recognized until 1959 when Nims and Zweifel [3], in analyzing sodium temperature coefficients, pointed out the diverse components of the sodium density coefficient: the competition, upon voiding sodium (or the equivalent in a homogeneous model: reducing the sodium density), between the positive spectral component, the negative leakage component, and the small positive capture component. The impact of the sodium void problem is particularly apparent in a 1964 evaluation of four quite different 1000-MWe fast breeder designs submitted by four vendors [4]. All the design analyses have one common feature: a simple, volume homogenized core is assumed. Each design team relied on their own private prescriptions to account for homogeneous self-shielding, and, even for a fixed geometry, the calculated void coefficients were shown to be markedly sensitive to the cross-section set chosen. Reference 5 provides a good picture of the

anarchy prevailing at the time, with at least four competing cross-section sets (Hansen-Roach, YOM, Hummel, and WAPD-F1) in use.

The largest whole core voiding reactivity was the +2.4% Δk (about +$7.30) calculated for Combustion Engineering's conventional geometry core, while the other designs relied on spoiled geometry (high leakage cores) to accentuate the negative leakage component of the void effect. More recently, GE's analysis of its smaller demonstration plant [6] indicates a whole-core sodium voiding worth of +$1.10. Part of the reduction from the value for the 1000-MWe size is due to the smaller core size (accentuating the negative leakage component) and part due to a better representation of the resonance self-shielding effects using a type of Bondarenko f-factor homogeneous method [7].

Generally, the whole-core sodium voiding effects have not been calculated in a manner which accounts for all three of the heterogeneous effects defined in the preceding section. While there has been considerable study of some of the effects, it has usually been with the emphasis upon one in isolation from the others. Indeed, recognition of the need for consideration of heterogeneous effects in fast vectors is a relatively recent development. As late as 1966 one could read:

> "Heterogeneity of the fuel lattice in typical fast power reactors is not large enough to have an important effect on coolant void reactivity. Also, the spacing of the fuel rods is too close for streaming to significantly improve the leakage component." [8]

The earliest calculation of heterogeneous effects [9] concentrated on the Doppler effect and the error caused by assuming homogeneous self-shielding of the resonances rather than heterogeneous self-shielding, the latter being calculated by an equivalence formalism (an equivalence principle is one which allows the heterogeneous geometry to be

treated as a homogeneous cell to whose "background" non-resonant cross section is added a heterogeneous correction related to the Dancoff factor – all discussed in Chapter 5). The changes in the cross sections resulting from heterogeneous energy self-shielding were found to be negligibly small. Later experiments [10] in plate geometry obtained different reactivity perturbations, varying by more than a factor of two, for various material arrangements all having identical homogenized compositions; from which the conclusion was drawn that calculations assuming homogeneous material distributions are of limited value in highly heterogeneous plate-type critical assemblies.

The methods of perturbation theory have provided one popular tool for the analysis of heterogeneous effects. For changes in the sodium density of up to 5%, first order perturbation theory is generally accurate to ± 10%, though for gross whole-core voiding its results may be in error by a factor of two or more since in that case the change in material constants exceeds the requisite small perturbation [8, 11].

Meneghetti [12, 13, 14] has calculated heterogeneous voiding effects for the plate-type geometry typical of fast critical assemblies, using a hybrid first order perturbation theory analysis: the change in k_{eff} upon gross voiding is obtained by a direct calculation for the homogeneous case, while perturbation theory is used to calculate the heterogeneous corrections. Heterogeneous resonance self-shielding is treated by an equivalence principle. However, for present purposes, the plate geometry is not directly relevant to realistic fast breeder cores. Also, Meneghetti's analysis neglected anisotropic streaming.

Khairallah and Storrer [15, 16, 17, 18] have employed a collision probability concept united with the integral transport equation and

perturbation theory. The heterogeneity is accounted for as a perturbation in the collision probabilities used to describe the medium. First, the finite core is converted to an equivalent infinite core by adding a fictitious leakage cross section to the capture cross section; then the multigroup integral equations are written for the infinite medium in terms of collision probabilities. In the resulting set of equations, homogeneous and heterogeneous media are identically represented with only the collision probabilities taking on different values (their difference being the perturbation) for the two different modellings, homogeneous and heterogeneous.

In Reference 15, the perturbation method is applied, with second order corrections, to a 10% sodium loss with the qualitative conclusion that heterogeneity tends to decrease the positive sodium loss coefficient. Further analysis is presented in Reference 17 with the conclusion that for power reactor cores, heterogeneity causes a 6% to 10% reduction in the sodium loss reactivity, while in critical mock-ups, a 30% to 40% reduction results. These analyses are predicated on the equivalent infinite core defined above, in which for the sodium-out condition both the heterogeneous and homogenous representations result in the same k_{eff}. Such a treatment does not explicitly account for finite core effects which cause the sodium-out, heterogeneous model to predict significant reactivity loss due to anisotropic streaming, as will be discussed in Chapter 4. In Reference 18 the perturbation method is applied to the MASURCA core, but only the normal sodium-in case is analyzed with emphasis upon the effects of heterogeneity upon the critical mass (the sodium voiding effect is not calculated). For 1.27-cm O.D. rods on a 2.65-cm pitch, the heterogeneity effect was found to be 0.027 Δk of

which 0.016 Δk was due to resonance self-shielding and 0.011 Δk due to the "geometry."

Contemporaneously with these latter references, studies were still being carried out which neglected one or more of the heterogeneous effects. For example, Reference 19 presents a detailed design for a variable-core-height reactor (the inner core region being of a lesser height to promote leakage from that zone where the positive spectral component prevails) to decrease the void coefficient; the entire analysis is apparently based on an infinite dilution cross-section set which neglects the very important self-shielding effects of a finite dilution. Jankus and Hummel [20] discuss two-dimensional calculations of void coefficients, still employing the 1964 parameters of Reference 4. Wintzer [21] carries out a calculation using a more sophisticated resonance self-shielding model to replace the usual formalism (which is inapplicable if the unit cell contains resonance material in more than one region); however, he chooses to neglect anisotropic streaming.

The most recent work has been directed toward the analysis of plate-type critical mock-ups [22,23,24,25]. These studies uniformly neglect the effect of anisotropic streaming and are primarily directed toward the plate-type critical assembly cores rather than the cylindrical geometry characteristic of realistic fast power reactor designs. An analysis of a postulated demonstration reactor, discussed in Reference 25, reports a negligible heterogeneity effect (while ignoring anisotropic diffusion); in Reference 26 a similar geometry is analyzed, accounting only for spatial flux distribution effects: perturbations an order of magnitude greater were obtained.

In contrast to much of what has been done to date, the emphasis here will be upon the realistic cylindrical geometry unit cell with all three types of heterogeneous effects taken into consideration. The intent is to develop simple models which allow a rapid calculation of the fundamental physical events uniquely associated with a heterogeneous model and their contribution to the multiplication constant.

Chapter 2

CALCULATION OF FLUX RATIOS IN UNIT CELLS

To perform the detailed homogenization of Eq. (1.3), one requires the average flux ratios. A computer program, such as the ANISN code [27], may be used to obtain flux profiles in the unit cell. However, use of a discrete S_N code or some other equivalent on a production basis simply for the calculation of average flux ratios is extravagant, particularly for parametric studies. Instead, it is worthwhile to develop a simple method solely for the calculation of average flux ratios. The ANISN code can then be reserved as a final check on the results of the simpler theory. This chapter develops the required simpler theory and demonstrates favorable comparison with ANISN S_8 cell calculations.

2.1 Representation of the Unit Cell

Figure 2.1 shows the archetypal three-region unit cell which is the focus of interest. Region 1 is the fuel region, whose outer radius is identical to the outer radius of the fuel pellet. Region 2 is the clad region, whose dimensions are identical to those of the clad. If there is a sodium bond or a gap between the fuel pellet outer radius and the clad inner radius, this additional region may be volume averaged with the clad. Such a subterfuge may seem inconsistent with the spirit of this report (which seeks to correct errors due to volume-weighted homogenization). However, if the gap is very small, then only a small fraction of the unit cell volume is misrepresented by this device, and the error may be assumed negligible. Region 3 is the coolant region

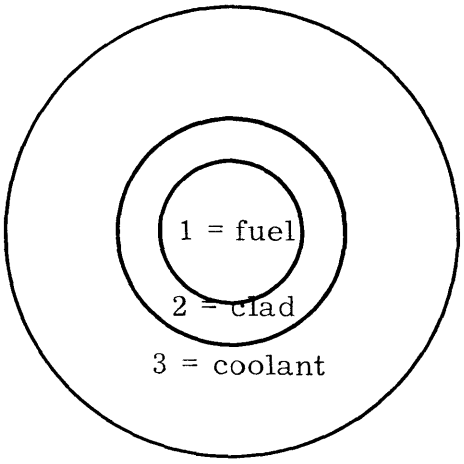

Fig. 2.1 Standard Unit Cell

Fig. 2.2 Mirror Boundary Condition Error

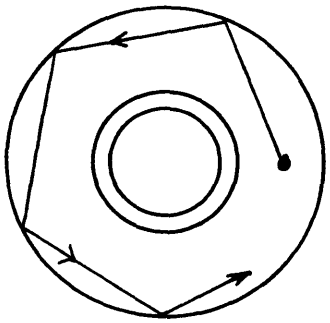

Unit Cell

Neutron never enters fuel region due to specular reflections.

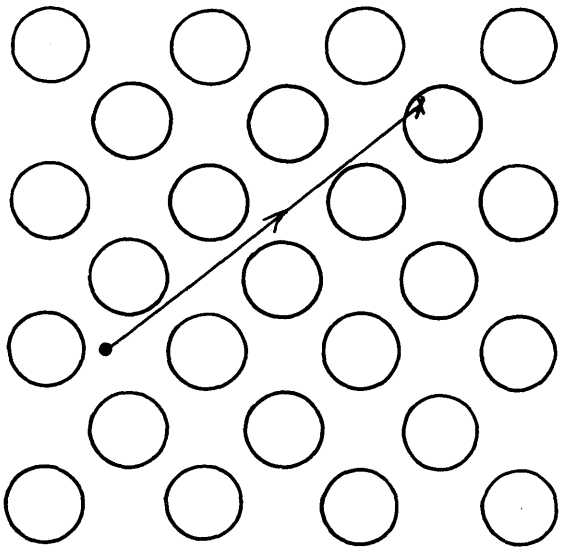

True Lattice

Neutron's initial (or subsequent) path in given direction eventually enters fuel region.

whose outer radius is defined by assigning to each fuel rod its share of the coolant and then assuming the coolant region may be represented by an outer annular region. For a lattice described by an equilateral triangular pitch, P, this cell outer radius is:

$$R = \left(\frac{\sqrt{3}}{2\pi}\right)^{1/2} P . \qquad (2.1)$$

This cylindricalization of the unit cell is identical to the Wigner-Seitz method in thermal reactor physics with one important proviso: the reflection boundary condition at the outer radius needs to be of a particular type, the so-called white boundary condition. Newmarch [28] recognized that though the cylindrical cell approximation with mirror boundary conditions results in little error when applied in a diffusion theory context, serious errors result when the same method is used in conjunction with transport theory.

For tight lattice calculations in thermal reactor physics, it is recognized that, for problems in cylindrical geometry, mirror boundary conditions can produce an over-estimation of the moderator region flux [29]. In a sense, all fast reactor lattices are tight (i.e., the lattice spacing is much smaller than the neutron mean free path); thus a similar problem may prevail in FBR unit cell calculations.

Newmarch [28] pointed out the source of the problem. If the boundary condition assumed is that of perfect (i.e., mirror) reflection, then neutrons emitted at certain angles in the coolant region (see Figure 2.2) can never make their first collision in the fuel region. In the true physical lattice, this same neutron need only traverse several rows of fuel elements before it enters a fueled region. In a good

diffusive medium where the mean free path is much less than the cell diameter, the medium itself acts to distribute the neutron paths through successive collisions so that the events pictured in Figure 2.1 do not occur. For this reason, the mirror boundary condition works well in situations described by diffusion theory (as long as the lattice is not tight). On the other hand, in unit cells typical of fast systems, the physical picture can only be described in terms of transport theory. Indeed, as shown by Fukai [30], the mirror boundary conditions result in significant errors in the calculation of first-flight collision probabilities for the lattice, which in turn affect the calculated flux ratios.

The solution is to employ a white boundary condition, one which returns all neutrons from the boundary with an isotropic distribution. It may be artificially constructed by surrounding the real cell by a region of pure isotropic scattering material at whose outer boundary a mirror boundary condition is imposed [25]. Or one may simply use the white boundary condition option at the real cell outer boundary, as available in ANISN, which mathematically returns neutrons isotropically at the boundary. In this manner one may treat any desired unit cell.

Recent work [31] has shown that the white boundary condition underestimates the flux variation in the cell by forcing the angular flux in the cell to be almost isotropic everywhere. However, the mirror boundary so greatly overestimates the cell flux variation that the white boundary condition is the sole reasonable choice. As an example, in one case the mirror boundary condition tripled the flux peaking in the fuel region (i.e., the mirror boundary condition gives an anomalously high flux in the region where the neutrons are born: in the fuel for fast neutrons,

or in the moderator for thermal neutrons, as found by Newmarch) as compared to the identical calculation with white boundary conditions.

It is noteworthy that the probability method proposed here is independent of these boundary condition ambiguities. As discussed in Section 4.2, the proposed method needs only the correct mean chord length for the geometry of interest; it is only ANISN which requires the white boundary condition.

2.2 Derivation of Unit Cell Boundary Currents

With the object of developing a simple method for calculating the ratio of average fluxes in the various cell regions, the following probabilities are defined:

p_1 = escape probability for neutron born in fuel

p_3 = escape probability for neutron born in coolant

T_{13} = transmission probability from fuel to coolant

T_{31} = transmission probability from coolant to fuel

T_{33} = transmission probability from coolant to coolant via clad without entering fuel

P_1 = escape probability for neutron entering fuel

P_3 = escape probability for neutron entering coolant

Note that p_1 is not the same as P_1 since the two classes of neutrons have different average chord lengths in the fuel (see Appendix A).

In addition, boundary currents are defined (see Figure 2.3):

j^+_S = current entering fuel region

j^-_S = current leaving fuel region

j^+_N = current entering coolant region

j^-_N = current leaving coolant region

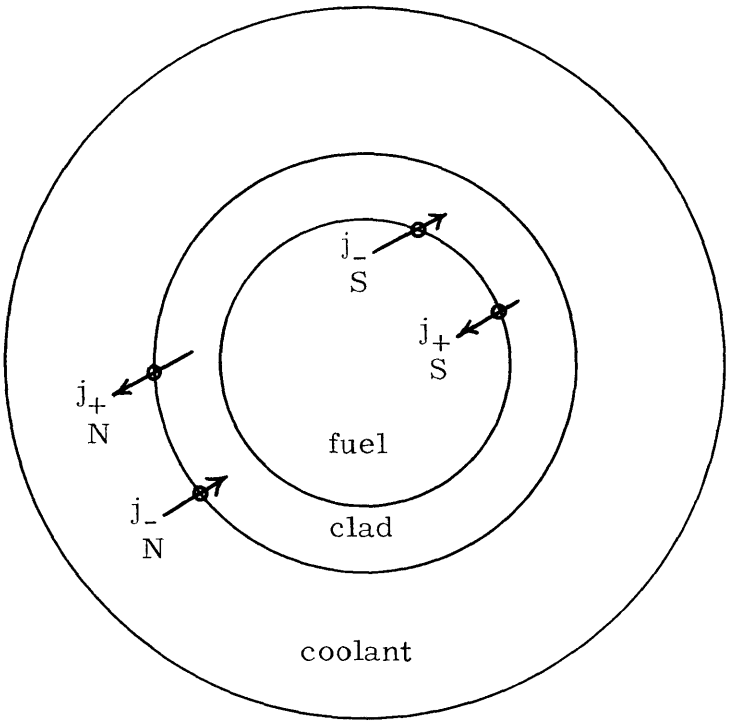

Fig. 2.3 Boundary Current Definitions

Now one proceeds to calculate the current entering the fuel region due to a uniform source of S_1 neutrons/sec cm^3 in the fuel region. To distinguish between the various classes of neutrons according to their prior history, one identifies the n^{th} generation as those neutrons which have made n round trips across the clad (a round trip being fuel-clad-coolant-clad-fuel). Since the unit cell is assumed to be surrounded by an infinite array of identical cells, once a neutron crosses the outer boundary of the coolant region it finds itself in an identical unit cell. All processes are conserved if one makes the statement that all leaving neutrons are reversed in direction at the outer boundary, back toward the interior of the cell. Thus a single cell describes the entire lattice in the cylindrical approximation.

As a matter of notation: a superscript attached to a boundary current (e.g., $j_{+S}^{(n)}$) signifies the contribution of the n^{th} generation of neutrons to that current. With these definitions, one can now proceed with what might accurately be termed a poor man's Monte Carlo calculation of the boundary currents.

On leaving the fuel region, the zeroth generation is attenuated by the product of the three probabilities for a round trip; thus one contribution to $j_{+S}^{(1)}$ is $S_1 p_1 \frac{r_1}{2} T_{13} P_3 T_{31}$, $S_1 p_1 \frac{r_1}{2}$ being the outward bound current of zeroth generation neutrons at the fuel rod surface. This still ignores those neutrons which missed the fuel region on their first attempted return trip and re-entered the coolant. Out of these detoured neutrons, P_3 re-escape the coolant for another attempt to enter the fuel rod. Assuming their next attempt to be successful, this results in another contribution to $j_{+S}^{(1)}$ of $S_1 p_1 \frac{r_1}{2} T_{13} P_3 (T_{33} P_3) T_{31}$. One must still

account for those neutrons making multiple detours and thus add the contribution $S_1 p_1 \frac{r_1}{2} T_{13} P_3 (T_{33} P_3)^m T_{31}$ where m can range from two to infinity.

Adding all such contributions yields:

$$j_{+S}^{(1)} = S_1 p_1 \frac{r_1}{2} \{T_{13}P_3T_{31} + T_{13}P_3(T_{33}P_3)T_{31} + T_{13}P_3(T_{33}P_3)^2 T_{31} + \ldots + T_{13}P_3(T_{33}P_3)^m T_{31} + \ldots\}$$

$$= S_1 p_1 \frac{r_1}{2} \{T_{13}P_3T_{31}(1 + T_{33}P_3 + (T_{33}P_3)^2 + \ldots + (T_{33}P_3)^m + \ldots)\}. \quad (2.2)$$

Recalling that all the quantities in the brackets are probabilities, all less than 1.0 for physically realistic cases, the infinite series may be expressed in a simple closed form giving:

$$j_{+S}^{(1)} = S_1 p_1 \frac{r_1}{2} \left\{ \frac{T_{13}P_3T_{31}}{1 - T_{33}P_3} \right\} . \quad (2.3)$$

This result is only the contribution of the first generation, those having made only one round trip across the clad with any number of detours into the coolant. Of the first generation neutrons, P_1 start out in the second generation. Their attenuation is analogously described by the terms in the brackets of Eqs. (2.2) and (2.3). Thus:

$$j_{+S}^{(2)} = j_{+S}^{(1)} P_1 \left(\frac{T_{13}P_3T_{31}}{1 - T_{33}P_3} \right)$$

$$= S_1 p_1 \frac{r_1}{2} P_1 \left(\frac{T_{13}P_3T_{31}}{1 - T_{33}P_3} \right)^2 . \quad (2.4)$$

Making the obvious extension, the n^{th} generation contribution is:

$$j_{+S}^{(n)} = S_1 p_1 \frac{r_1}{2} \left(\frac{T_{13} P_3 T_{31}}{1 - T_{33} P_3} \right) \left(\frac{P_1 T_{13} P_3 T_{31}}{1 - T_{33} P_3} \right)^{n-1} . \tag{2.5}$$

The desired boundary current due to all generations is the infinite summation:

$$j_{+S} = S_1 p_1 \frac{r_1}{2} \left(\frac{T_{13} P_3 T_{31}}{1 - T_{33} P_3} \right) \sum_{m=0}^{\infty} \left(\frac{P_1 T_{13} P_3 T_{31}}{1 - T_{33} P_3} \right)^{m} . \tag{2.6}$$

In physically realistic cases pertinent to fast reactor unit cells, the clad is thin which results in T_{33} being much less than 1.0, while the other probabilities are all slightly less than 1.0 due to the small average cross sections in a fast spectrum. Thus every term in the infinite series of Eq. (2.6) beyond the first is less than 1.0 and the series may be written in closed form, resulting in:

$$j_{+S} = S_1 p_1 \frac{r_1}{2} \left[\frac{T_{13} P_3 T_{31}}{1 - T_{33} P_3 - P_1 T_{13} P_3 T_{31}} \right] . \tag{2.7}$$

The other boundary currents are calculated in an identical manner; further, the entire process is repeated for a uniform source S_3 in the coolant region. One need only form the correct products of transmission and escape probabilities, and repeatedly write the resulting infinite series in closed form.

The only added feature worthy of note is a pitfall in the calculation of j_{+N} for a coolant region source. Two infinite series appear in the derivation beyond the zeroth generation (see Appendix B, Eq. (B.23)). One series accounts for the subsequent history of the zeroth generation neutrons which contributed to j_{+N} by merely crossing the clad; while the second series accounts for those neutrons which did not contribute to j_{+N} until they had made one round trip across the clad. This

complication is due to the clad/coolant interface being a re-entrant surface and to the manner in which the generation concept has been defined here. The dual infinite series do not appear in the derivation of $j_{\underset{N}{-}}$ for a coolant region source since in that case every neutron in the first generation was in the zeroth generation. In the calculation of $j_{\underset{N}{+}}$, neutrons appear in the first generation without appearing earlier in the zeroth generation. Appendix B details the derivation of the equations for the remaining boundary currents.

The boundary currents resulting from each source in each region may be simply added together since superposition is valid for directional currents. This results in the following general expressions for the boundary currents:

$$j_{\underset{S}{+}} = S_1 p_1 \frac{r_1}{2}\left[\frac{T_{13}P_3T_{31}}{1 - T_{33}P_3 - T_{31}P_1T_{13}P_3}\right] + S_3 p_3 \left(\frac{r_3^2 - r_2^2}{2r_1}\right)\left[\frac{T_{31}}{1 - T_{33}P_3 - T_{31}P_1T_{13}P_3}\right] \tag{2.8}$$

$$j_{\underset{S}{-}} = S_1 p_1 \frac{r_1}{2}\left[\frac{1 - T_{33}P_3}{1 - T_{33}P_3 - T_{31}P_1T_{13}P_3}\right] + S_3 p_3 \left(\frac{r_3^2 - r_2^2}{2r_1}\right)\left[\frac{P_1T_{31}}{1 - T_{33}P_3 - T_{31}P_1T_{13}P_3}\right] \tag{2.9}$$

$$j_{\underset{N}{+}} = S_1 p_1 \frac{r_1^2}{2r_2}\left[\frac{T_{13}}{1 - T_{33}P_3 - T_{31}P_1T_{13}P_3}\right] + S_3 p_3 \left(\frac{r_3^3 - r_2^2}{2r_2}\right)\left[\frac{T_{33} + T_{31}P_1T_{13}}{1 - T_{33}P_3 - T_{31}P_1T_{13}P_3}\right] \tag{2.10}$$

$$j_{\overline{N}} = S_1 p_1 \frac{r_1^2}{2r_2}\left[\frac{P_3 T_{13}}{1 - T_{33}P_3 - T_{31}P_1 T_{13}P_3}\right] + S_3 p_3 \left(\frac{r_3^2 - r_2^2}{2r_2}\right)\left[\frac{1}{1 - T_{33}P_3 - T_{31}P_1 T_{13}P_3}\right] . \qquad (2.11)$$

2.3 Calculation of Regionwise Average Fluxes

By use of the statement of neutron balance, one can calculate the regionwise average fluxes from the boundary currents and the sources. Taking the fuel rod region:

$\Sigma_{a1}\bar{\phi}_1 \pi r_1^2$ = loss rate/unit length by absorption

$2\pi r_1 \left(j_{\overline{S}}^{+} - j_{\overline{S}}^{-}\right)$ = gain rate/unit length by net in-leakage

$\pi r_1^2 S_1$ = gain rate/unit length from internal sources.

Then the statement of neutron balance in the fuel rod is:

$$\Sigma_{a1}\bar{\phi}_1 \pi r_1^2 = 2\pi r_1 \left(j_{\overline{S}}^{+} - j_{\overline{S}}^{-}\right) + \pi r_1^2 S_1 , \qquad (2.12)$$

or

$$\bar{\phi}_1 = \frac{2\left(j_{\overline{S}}^{+} - j_{\overline{S}}^{-}\right) + S_1 r_1}{\Sigma_{a1} r_1} . \qquad (2.13)$$

For the other two regions, one similarly obtains:

$$\Sigma_{a2}\bar{\phi}_2 \pi \left(r_2^2 - r_1^2\right) = 2\pi r_1 \left(j_{\overline{S}}^{-} - j_{\overline{S}}^{+}\right) + 2\pi r_2 \left(j_{\overline{N}}^{-} - j_{\overline{N}}^{+}\right) , \qquad (2.14)$$

or

$$\bar{\phi}_2 = \frac{2r_1\left(j_{\overline{S}}^{-} - j_{\overline{S}}^{+}\right) + 2r_2\left(j_{\overline{N}}^{-} - j_{\overline{N}}^{+}\right)}{\Sigma_{a2}\left(r_2^2 - r_1^2\right)} ; \qquad (2.15)$$

and

$$\Sigma_{a3}\bar{\phi}_3 \pi \left(r_3^2 - r_2^2\right) = 2\pi r_2 \left(j_{\overline{N}}^{+} - j_{\overline{N}}^{-}\right) + \pi\left(r_3^2 - r_2^2\right) S_3 , \qquad (2.16)$$

$$\text{or} \qquad \bar{\phi}_3 = \frac{2r_2\left(j_{+N} - j_{-N}\right) + \left(r_3^2 - r_2^2\right) S_3}{\Sigma_{a3}\left(r_3^2 - r_2^2\right)} . \tag{2.17}$$

It should be noted that for the voided coolant case $\Sigma_{a3} = 0$ and Eq. (2.17) has no meaning; also, clad sources have thus far been ignored. These points will be dealt with in Sections 2.6 and 2.7.

2.4 First Order Escape and Transmission Probabilities

Up to this point, a simple method has been presented which yields the average cell fluxes as a function of source densities and boundary fluxes (which are formulated in terms of various probabilities). Its utility is determined to a large extent by the difficulty or ease with which the required probabilities are calculated.

Because the discussion here is limited to the special case of fast reactor unit cells, useful approximations to the probabilities may be found. In Appendix A, average chord lengths are derived for the escape of neutrons born in a transparent cylinder of radius r_1, and for the escape of neutrons entering this cylinder from the exterior. In the former case, for a spatially uniform source, one finds $\bar{\ell} = \frac{4}{3} r_1$. In the latter case, for an isotropic surface source, one finds $\bar{L} = 2r_1$ (Appendix A.2 proves an even more general relation). From these one deduces a first order approximation for the probabilities p_1 and P_1 for a fuel rod characterized by Σ_{a1}:

$$p_1 = \exp(-\Sigma_{a1}\bar{\ell}) \sim 1 - \Sigma_{a1}\bar{\ell} = 1 - \frac{4}{3}\Sigma_{a1}r_1 , \tag{2.18}$$

$$P_1 = \exp(-\Sigma_{a1}\bar{L}) \sim 1 - \Sigma_{a1}\bar{L} = 1 - 2\Sigma_{a1}r_1 . \tag{2.19}$$

For a more general body, the transmission mean chord length $\bar{L}$ is given by the usual Dirac chord method result [32]: $\bar{L} = 4V/S$ which is $2r_1$ for the cylinder. Postulating the same type of relationship for the escape mean chord length, one obtains: $\bar{\ell} = \frac{8}{3}V/S$ or $\bar{\ell} = \frac{4}{3}r_1$ for the cylinder. These two relations permit one to calculate the probabilities for the annular coolant region which has only one surface of escape, the interior one, due to the reflection boundary condition. In this case, $\bar{L} = 2(r_3^2-r_2^2)/r_2$ and $\bar{\ell} = \frac{4}{3}(r_3^2-r_2^2)/r_2$, which lead to the two coolant region probabilities:

$$p_3 = 1 - \frac{4}{3}\Sigma_{a3}\left(\frac{r_3^2 - r_2^2}{r_2}\right), \tag{2.20}$$

$$P_3 = 1 - 2\Sigma_{a3}\left(\frac{r_3^2 - r_2^2}{r_2}\right). \tag{2.21}$$

The clad transmission probabilities remain to be determined. For the clad, the escape surface is the sum of the inner and outer surface areas. Thus, $\bar{L} = 4V/S = 2(r_2^2-r_1^2)/(r_2+r_1) = 2(r_2-r_1)$, which leads to the transmission probability:

$$T_{13} = 1 - 2\Sigma_{a2}(r_2-r_1), \tag{2.22}$$

$$\text{while} \quad T_{31} = \left(\frac{r_1}{r_2}\right)T_{13}. \tag{2.23}$$

As a simple approximation, it is here suggested that:

$$T_{33} = T_{13} - T_{31}, \tag{2.24}$$

that is, the probability for crossing the clad on an outward bound path is equal to the probability of crossing the clad on an inward bound path

plus the probability of missing the fuel rod on an inward bound path (i.e., $T_{13} = T_{31} + T_{33}$).

Exact expressions for these clad transmission probabilities are known [33]:

$$T_{13} = \frac{4}{\pi} \int_0^{\cos^{-1}\alpha} \frac{(1 - \alpha\cos\theta)(\cos\theta - \alpha)}{(1+\alpha^2+2\alpha\cos\theta)^{3/2}} \mathrm{Ki}_3\left[\sqrt{1+\alpha^2-2\alpha\cos\theta}\ \Sigma_{a2} r_2\right] d\theta \tag{2.25}$$

$$T_{31} = \alpha T_{13} \tag{2.26}$$

$$T_{33} = \frac{4}{\pi} \int_{\frac{\pi}{2} - \cos^{-1}\alpha}^{\pi/2} \mathrm{Ki}_3[2\Sigma_{a2} r_2 \cos\theta] \cos\theta\, d\theta\,. \tag{2.27}$$

where $\alpha = r_1/r_2$ and Ki_3 is a Bickley-Nayler function [34]:

$$\mathrm{Ki}_3(x) = \int_0^{\infty} \frac{e^{-x}\cosh u}{\cosh^3 u}\, du\,. \tag{2.27a}$$

Reference 33 presents a table of evaluated transmission coefficients based on a machine integration of Eqs. (2.25) through (2.27). Table 2.1 compares those results to the transmission probabilities obtained from the simple forms of Eqs. (2.22) through (2.24). A Σr_2 value of 0.1 is displayed in Table 2.1 because that is the smallest Σr_2 value tabulated in Reference 33. For the two-group representation of a fast reactor unit cell discussed later, Σr_2 for group 1 is of the order of 0.02 while for group 2 it is of the order of 0.001; thus the comparison of Table 2.1 is for a regime considerably outside the one in which the theory is claimed to work best. As Σr_2 becomes smaller than 0.1, the agreement between values predicted using the simple theory and those based on the exact equations becomes even better than demonstrated in Table 2.1.

TABLE 2.1

Comparison of Transmission Coefficients with Exact Values

	T_{13}		T_{31}		T_{33}	
α	Eq. (2.22)	Ref. 33	Eq. (2.23)	Ref. 33	Eq. (2.24)	Re
0.8	0.9600	0.9692	0.7680	0.7754	0.1920	0.
0.9	0.9800	0.9837	0.8820	0.8853	0.0980	0.
0.95	0.9900	0.9915	0.9405	0.9419	0.0495	0.

In the above discussion the probabilities of Reference 33 are calculated assuming a cosine angular distribution at the clad surfaces (the basis of Eqs. (2.25) through (2.27)). As a third check on the simple transmission probability formulae, several ANISN unit cell runs were performed. First, the coolant region was assumed to have an infinite absorption cross section while a uniformly distributed isotropic source occupied the fuel region. From the resulting boundary currents calculated by the code, T_{13} was obtained: $T_{13} = (r_2/r_1)/(j_{+}/j_{-})_{N\ S}$. Then the fuel region was assumed to have an infinite absorption cross section while a uniform isotropic source was distributed in the coolant region. Using the boundary currents in the code output: $T_{31} = (r_1/r_2)/(j_{+}/j_{-})_{S\ N}$; while $T_{33} = (j_{+}/j_{-})_{N\ N}$. Table 2.2 compares these ANISN results with those of the simple theory.

TABLE 2.2

Comparison of Transmission Coefficients with ANISN Calculated Values

	T_{13}	T_{31}	T_{33}
ANISN	0.9962	0.8648	0.1311
Simple theory	0.9958	0.8762	0.1195

By their very nature, the ANISN test cases were not constrained to a cosine angular distribution at the clad surface. Instead, the surface angular distribution was that due to an isotropic source distribution in the source region. Nevertheless, the discrepancy between the simple theory and reality as defined by the ANISN results is still

small. One may conclude that the simple clad transmission probability formulae are safe to use for the case of a cosine angular distribution of entering neutrons and for the case where the entering neutrons were born isotropically in the regions external to the clad annulus. Thus the formulae may be generally applied to the analysis of fast reactor unit cells, a claim which will be justified below by comparison with many ANISN unit cell calculations.

2.5 Use of ANISN Test Cell Calculations

The final justification of the simple theory is made by comparing the average flux ratios it predicts with those calculated in a series of ANISN S_8 unit cell problems. Before this comparison was made, a brief sensitivity study of the ANISN flux ratios was performed. First, the effect of mesh spacing was examined: the use of twenty mesh intervals per unit cell region was contrasted to the use of ten mesh intervals per region. The change in the flux ratios on going from the finer to the coarser mesh was of the order of 0.001%, a negligible amount. Thus all subsequent ANISN calculations were made with ten mesh intervals per unit cell region.

Second, the effect of a non-flat source was investigated. In one case, a flat coolant region source distribution was assumed. In the counter-case, a tilted source distribution rising from $1.0/cm^3$ (normalized source strength) in the inner mesh interval to $1.5/cm^3$ in the outer mesh interval was considered. The maximum change in the flux ratios was of the order of 0.04%. From this one concludes that the flux ratios are relatively independent of the assumed intra-region source distribution; thus, for simplicity, one may assume all source

distributions are regionwise flat.

Third, the effect of scattering was investigated. This comparison has a strong bearing on the validity of the simple model developed earlier in which only absorption events were considered in the calculation of the various probabilities. Two ANISN calculations were compared: one in which each region was characterized by its one-group absorption and scattering cross sections; another in which zero scattering cross sections were assumed (in reality, a non-zero $\Sigma_s = 10^{-5}$ cm^{-1} had to be input since ANISN does not converge if the scattering cross section is identically zero). Between the cases with scattering and without scattering, the flux ratios changed by 0.02%, a negligible amount.

Thus the assumption that escape and transmission probabilities in a fast reactor unit cell depend only on absorption events is a valid one. This may also be shown analytically. Appendix A shows that for a parabolic source distribution ($S(r) = 1 + \alpha^2 r^2$), the mean chord length for escape is:

$$\bar{\ell} = \frac{4}{3} r_1 \left[1 - \frac{\alpha^2 r_1^2}{66} + \ldots \right]. \tag{2.28}$$

Using the definition of flux as track lengths per unit volume per unit time, the first flight flux due to a uniform source is (from Appendix A):

$$\phi_{FF}(r) = \frac{\pi}{2} r_1^2 \left[1 - \frac{1}{4}\left(\frac{r}{r_1}\right)^2 + \ldots \right]. \tag{2.29}$$

The distribution of scattering sources is $\Sigma_s \phi_{FF}(r)$, which is a parabolic source with $\alpha^2 = -1/4r_1^2$. Substituting this α^2 in Eq. (2.28) results in the escape mean chord length:

$$\bar{\ell} = \frac{4}{3} r_1 \left[1 + \frac{1}{264}\right] . \qquad (2.29a)$$

Thus the escape mean chord lengths of scattered and nonscattered neutrons differ by less than 0.4%. And since $p \sim 1 - \Sigma_a \bar{\ell}$, with $\Sigma_a \bar{\ell}$ much less than 1.0, the effect on the escape probability is smaller still, as confirmed by the ANISN test cases.

The effect of scattering on the transmission probability is of a different order. For one neutron entering the fuel rod:

$(1 - 2\Sigma_t r_1)$ = escape without interaction

$2\Sigma_s r_1\left(1 - \frac{4}{3}\Sigma_t r_1\right)$ = scatter once and then escape

$\left(2\Sigma_s r_1\right)\left(\frac{4}{3}\Sigma_s r_1\right)\left(1 - \frac{4}{3}\Sigma_t r_1\right)$ = scatter twice and escape

and so on. Summing up all the escapes, one obtains for the transmission probability:

$$P_1 = \left(1 - 2\Sigma_t r_1\right) + 2\Sigma_s r_1\left(1 - \frac{4}{3}\Sigma_t r_1\right)\left\{1 + \frac{4}{3}\Sigma_s r_1 + \left(\frac{4}{3}\Sigma_s r_1\right)^2 + \ldots\right\}$$

$$= 1 - 2\Sigma_t r_1 + 2\Sigma_s r_1 - \frac{8}{3}(\Sigma_s r_1)(\Sigma_a r_1)$$

$$= 1 - 2\Sigma_a r_1\left(1 + \frac{4}{3}\Sigma_s r_1\right) . \qquad (2.30)$$

This is to be compared to the zero scattering result: $P_1 = 1 - 2\Sigma_a r_1$. The same result has been obtained by Stuart [35] by a more elegant analysis employing a variational principle. There will be a sizeable scattering correction whenever $\frac{4}{3}\Sigma_s r_1$ is of the order of 1.0. However, for a typical fast reactor unit cell, $\frac{4}{3}\Sigma_s r_1$ is of the order of 0.05, while $\Sigma_a r_1$ is much less than 1.0, so that the final scattering effect on the transmission coefficient is very small. However, it is emphasized that this is the case only for fast reactor unit cells. In thermal systems, $\frac{8}{3}(\Sigma_a r_1)(\Sigma_s r_1)$ will not be a negligible correction.

As a final test of the sensitivity of the flux ratios to non-zero scatter, a series of ANISN calculations were performed in which only the clad scattering cross section was varied from $\Sigma_s = .01\ cm^{-1}$ to $\Sigma_s = 1.0\ cm^{-1}$. The maximum change in any flux ratio was 0.5%.

From the above sensitivity studies it was concluded that for the purpose of calculating ratios of average fluxes in a fast reactor unit cell:

1. scattering could be ignored
2. all distributed sources could be assumed regionwise flat
3. ten mesh intervals per unit cell region were sufficient.

2.6 Group Sources in the Unit Cell

The stage is now set for testing the simple theory against ANISN results. The initial expectation was that a major effect on the unit cell flux shape would be the peaking of uncollided neutrons in the fuel rod where the fission source was concentrated. Thus a two-group energy description was chosen: the first group (called the first-flight group) extended from 1.4 MeV on up, encompassing the top four groups of the so-called Russian cross-section set [7]. In these four groups, U-238 has a non-negligible fission cross section. The second group (called the multiply-collided group) extended from 1.4 MeV on down. By judicious definition of the regionwise sources, the two groups can be treated in isolation from one another, as will be shown.

For the first-flight group a flat source is assumed in the fuel region, and everywhere else the source is zero. The absorption cross section used in the probabilities in Eqs. (2.18) through (2.24) must include removal from group 1 to 2 as well as true absorption in group 1.

With this proviso, the calculations proceed using Eqs. (2.8) through (2.11) with $S_3 = 0$ to yield the boundary currents, from which the fluxes are calculated.

The sources in the multiply-collided group require a more detailed description since slowing down into group 2 occurs in all three cell regions and to a differing degree in each. It is not correct to take the same flat multiply-collided source throughout the cell. If we let superscripts refer to regions (1 = fuel, 2 = clad, 3 = coolant) and subscripts refer to groups (Σ_{12} = removal from group 1 to 2), then the sources in each region are:

$$S^{(1)} = \Sigma_{12}^{(1)} \phi_1 + \left[\chi_2 \ \nu\Sigma_{f1}^{(1)} \phi_1 + \nu\Sigma_{f2}^{(1)} \phi_2 \right]$$

$$S^{(2)} = \Sigma_{12}^{(2)} \phi_1$$

$$S^{(3)} = \Sigma_{12}^{(3)} \phi_1 .$$

Note that for the purpose of calculating the multiply-collided group sources, the cell fluxes are assumed flat. Since the source normalization is arbitrary, one can divide through by ϕ_1 to give:

$$S^{(1)} = \Sigma_{12}^{(1)} + \chi_2 \left[\nu \Sigma_{f1}^{(1)} + \nu \Sigma_{f2}^{(1)} \frac{\phi_2}{\phi_1} \right] \tag{2.31}$$

$$S^{(2)} = \Sigma_{12}^{(2)} \tag{2.32}$$

$$S^{(3)} = \Sigma_{12}^{(3)} . \tag{2.33}$$

The cross sections are all known; by definition of the group structure, $\chi_2 = 0.43$. However, ϕ_2/ϕ_1 requires an auxiliary calculation, for which one can choose one of the two-group diffusion equations, say the one for group 1 for the entire homogenized core:

$$(\chi_1 \nu \Sigma_{f1} - \Sigma_{12} - \Sigma_{a1} - D_1 B^2)\phi_1 + (\chi_1 \nu \Sigma_{f2})\phi_2 = 0$$

which yields:

$$\frac{\phi_2}{\phi_1} = \frac{\Sigma_{12} + \Sigma_{a1} + D_1 B^2 - \chi_1 \nu \Sigma_{f1}}{\chi_1 \nu \Sigma_{f2}} , \qquad (2.34)$$

where all the constants are homogeneous ones.

The result of Eq. (2.34) is employed in Eq. (2.31) to calculate the multiply-collided source in the fuel region. The justification for using the homogeneous constants and flat cell fluxes to calculate these sources is that their heterogeneous values differ only slightly from the homogeneous ones. Thus the sources given by Eqs. (2.31) through (2.33) are nearly correct, and any small error is expected to have only a weak effect on the average flux ratios.

To confirm the above, two-group ANISN calculations were compared to dual one-group ANISN calculations in which each group was treated in isolation except for the coupled sources given by Eqs. (2.31) through (2.33). The two-group ANISN test was a k_{eff} calculation in which the code solved for the proper distributed sources internally (i.e., the only input required was the geometry and the two-group cross-section set); thus this was a strict test of the simple source equations. The largest deviation in the average flux ratios calculated by the two methods was 0.04%, implying that the isolated group, source-coupled calculation is a good approximation to the full two-group calculation.

Referring back to the boundary current equations, (2.8) through (2.11), one notes that they imply the absence of clad region sources (i.e., $S_2 = 0$), which contradicts the above discussion, especially Eq. (2.32). Thus the simple theory offered here must be incomplete

until some account of those neutrons born into the multiply-collided group in the clad has been made.

If one wishes to account for the clad source in the manner of Appendix B, some formalism must be developed which yields the percentage of zeroth generation neutrons entering the coolant, and the percentage entering the fuel. Thereafter, each group may be traced independently through its generations. It is reasonable to assume the multiply-collided neutrons are born in the clad with isotropically distributed directions. Then for a transparent clad, the average percentage of zeroth generation neutrons entering the fuel (called ξ) is equal to the average angle formed by tangents to the fuel rod which intersect along the locus of points formed by extending a radius of the fuel rod through the clad, divided by 2π. Of course, the percentage of zeroth generation neutrons entering the fuel rod from non-transparent clads is equal to ξ multiplied by a clad escape probability.

Various definitions of the clad escape probability were analyzed. In no case were reasonable flux ratios calculated since the equations derived were very sensitive to small changes in the parameters (e.g., a small change in ξ or the clad escape probability would change an unreasonable positive flux ratio into an even more unreasonable negative flux ratio). For this reason, an entirely different approach was adopted to unite multiply-collided clad sources with the simple escape and transmission probability theory; namely, an extended reciprocity relation was postulated. The conventional reciprocity theorem states: "the one-velocity flux at $\underline{r}'$ due to a unit source at $\underline{r}$ is the same as the one-velocity flux observed at $\underline{r}$ when the source is moved to $\underline{r}'$ " [36]. Strictly speaking, the case here is that of a two-group problem (the

reciprocity theorem holds only for the one-group case where the diffusion equation operator is self-adjoint), in which there is a distributed source (the reciprocity theorem speaks of a unit point source), and the quantity of interest is a regionwise average flux (not simply the flux at a point of the reciprocity theorem). Thus it is apparent that some caution is required in applying a reciprocity relation to the present case.

The extended reciprocity relation postulated here is: the total flux in region A due to a uniformly distributed source in region B is the same as the total flux in region B when the uniformly distributed source has been moved to region A. If this statement is valid, then clad region sources may be simply treated by artificially moving them to the fuel rod region (or alternatively the coolant region).

The extended reciprocity relation was tested by a series of computer experiments. First, ANISN three-region slab cells were examined, the problem being described in Figure 2.4. The results for the total fluxes with a unit source being alternately placed in each region are presented in Table 2.3. Those total fluxes joined by a line are the ones that the extended reciprocity relation predicts to be equal. The maximum deviation from the required equality is 0.06%; thus the reciprocity relation appears validated, at least in slab geometry.

In fact, for a special case, the extended reciprocity relation can be derived analytically; namely, the case in which neutrons move only parallel to the x-axis. For this case the kernel (i.e., the flux at x due to a unit source/unit volume at ξ) is: $K(x,\xi) = Ce^{-\lambda|\xi-x|}$. Figure 2.5 illustrates the nomenclature.

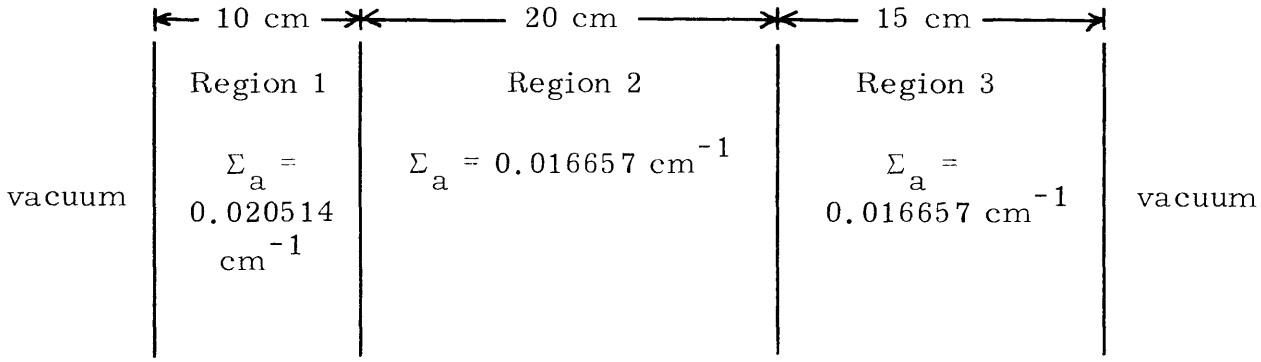

Fig. 2.4 Slab ANISN Cell for Reciprocity Test

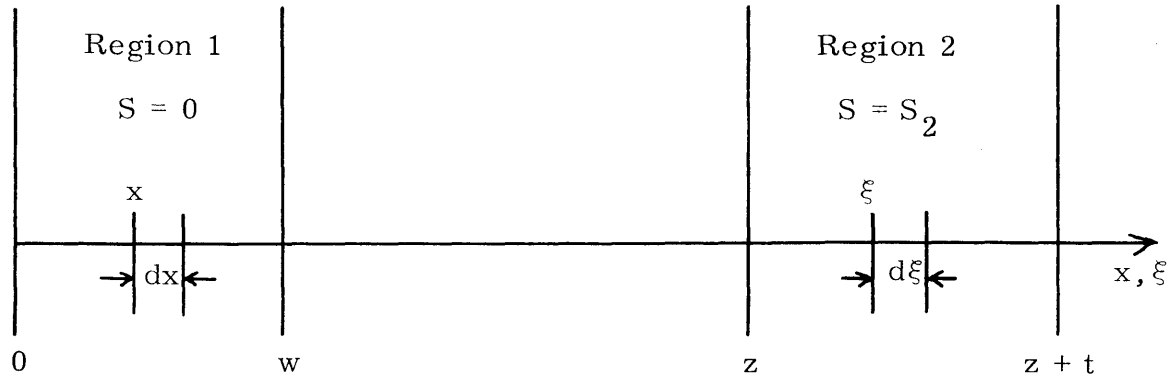

Fig. 2.5 Geometry for Reciprocity Proof (Eq. 2.35)

TABLE 2.3

ANISN Slab Cell Total Fluxes

	S_2=1.0, S_1=S_3=0	S_1=1.0, S_2=S_3=0	S_3=1.0, S_1=S_2=0	S_2=1.0, S_3=S_1=0
ϕ_{T1}	102.510	159.612	6.93964	102.510
ϕ_{T2}	700.897	102.528	160.470	700.897
ϕ_{T3}	160.507	6.93577	406.774	160.507

For the flux distribution in region 1, one has:

$$\phi_1(x) = \int_z^{z+t} S(\xi)K(x,\xi)\,d\xi = \frac{CS_2\, e^{\lambda x}}{\lambda}\,[e^{-\lambda z} - e^{-\lambda(z+t)}]. \qquad (2.35)$$

Which leads to the total flux:

$$\phi_{T1} = \phi_{12} = \int_0^w \phi_1(x)\,dx = \frac{CS_2}{\lambda^2}\,[e^{\lambda w}-1][e^{-\lambda z} - e^{-\lambda(z+t)}]. \qquad (2.36)$$

Now letting the source occupy region 1 leads to the region 2 fluxes:

$$\phi_2(x) = \int_0^w S(\xi)K(x,\xi)\,d\xi = CS_1\, e^{-\lambda x}[e^{\lambda w}-1] \qquad (2.37)$$

$$\phi_{T2} = \phi_{21} = \int_z^{z+t} \phi_2(x)\,dx = \frac{CS_1}{\lambda^2}\,[e^{\lambda w}-1][e^{-\lambda z} - e^{-\lambda(z+t)}]. \qquad (2.38)$$

Or for $S_1 = S_2$, $\phi_{21} = \phi_{12}$, thus the reciprocity holds exactly for those regions which contain the same source per unit volume, for this special geometry.

On the other hand, the unit cell of interest is the cylindrical one for which the above guarantees do not necessarily hold. Thus more ANISN computer experiments were performed, in the realistic geometry of Figure 2.6. Table 2.4 sums up the results in a manner analogous to Table 2.3. The maximum deviation from the prescribed equality is 0.17% (for clad-coolant reciprocity). For clad-fuel reciprocity, the deviation is 0.02%. In either case, the deviations from a strict equality are small, and thus the ANISN computer experiments have substantiated the extended reciprocity relation postulated here.

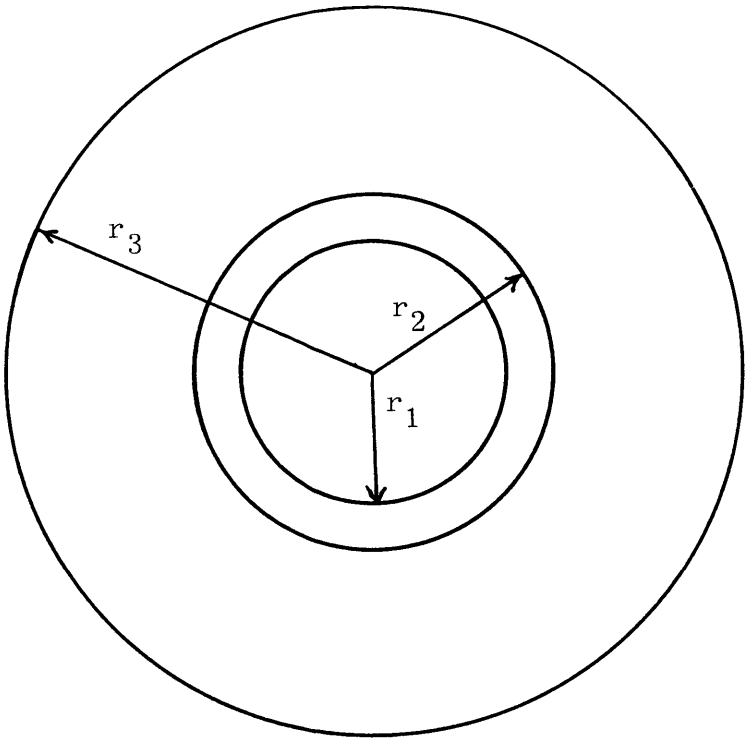

Region parameters:

$r_1 = 0.27$ cm, $\Sigma_{a1} = 0.2$ cm^{-1}

$r_2 = 0.3675$ cm, $\Sigma_{a2} = 0.01$ cm^{-1}, $\Sigma_{s2} = 0.1$ cm^{-1}

$r_3 = 0.6$ cm, $\Sigma_{a3} = 0.005$ cm^{-1}

Fig. 2.6 Cylindrical ANISN Reciprocity Test

TABLE 2.4

ANISN Cylindrical Cell Total Fluxes

	S_2=1.0, S_3=S_1=0	S_1=1.0, S_2=S_3=0	S_3=1.0, S_1=S_2=0	S_2=1.0, S_3=S_1=0
ϕ_{T1}	**0.727015**	1.29643	**3.14582**	0.727015
ϕ_{T2}	0.426476	**0.726903**	**1.82684**	0.426476
ϕ_{T3}	1.82991	**3.14662**	8.08063	**1.82991**

Clad region sources for the multiply-collided group may now be incorporated into the simple theory. First, the calculation of the boundary currents is performed using Eqs. (2.8) through (2.11) in which clad sources are ignored. This yields initial values for the average fluxes in the fuel and coolant regions in the absence of clad sources.

Second, the calculation is repeated with an artificial fuel region source equal to the coolant region source given by Eq. (2.32), the sources in the other two regions being set identically equal to zero. By use of the extended reciprocity relation, the resulting total flux in region 2 can be interpreted as the true total flux in region 1 due to the true source in region 2. Dividing this quantity by the volume of region 1 yields the average flux in region 1 due to sources in region 2. When this result is added to the initial value of $\bar{\phi}_1$ in the absence of clad region sources, the result obtained is the average flux in the fuel due to all sources in the unit cell. The clad-coolant reciprocity treatment is exactly analogous. The result is a model which handles clad region sources in a reasonable manner.

2.7 Final Modifications to the Model

One final change is required in the simple theory. It is possible to derive an analytic expression for the mean chord length for transmission through the annular clad [37]:

$$\bar{L} = \frac{r_1}{\pi}\left[2\sin^{-1}\left(\frac{r_1}{r_2}\right) - \pi\left(\frac{r_1}{r_2}\right)^2 + 2\left(\frac{r_1}{r_2}\right)\sqrt{1-\left(\frac{r_1}{r_2}\right)^2}\right], \qquad (2.39)$$

which is more sophisticated than the $\bar{L} = 2(r_2 - r_1)$ used in Eq. (2.22).

Table 2.5 lists the resulting clad probabilities for the two formulations for one particular cell. The simple expression of Eq. (2.22) results in a good approximation to the more detailed result in the regime of interest.

TABLE 2.5

Transmission Probabilities for Two Definitions of $\bar{L}$

	Eq. (2.22)	Eq. (2.39)
T_{13}	0.9965	0.9975
T_{31}	0.9209	0.9218
T_{33}	0.0756	0.0757

However, when the two sets of transmission probabilities are used in Eq. (2.15) to calculate $\bar{\phi}_2$ for a test cell, the Eq. (2.22)-based probabilities give a value of 1.0000 (normalized) while the Eq. (2.39)-based probabilities result in a value of 1.3526 (normalized). It appears that Eq. (2.15) is extremely sensitive to small changes in the values of the clad transmission probabilities. The reason for this sensitivity is that Eq. (2.15) has a numerator which is the difference between two almost identical large quantities, while the denominator is a small quantity; thus any small changes in the numerator are magnified greatly.

The solution is to assume the average flux in the clad is the simple average of the inner and outer clad surface fluxes (i.e., a simple linear interpolation). Several ANISN test cells showed this to be valid to within 0.04%. The surface fluxes themselves are calculated from the

boundary currents by the rule:

$$\phi_s = 2(j_+ + j_-)\,, \tag{2.40}$$

which may be derived under the same conditions as Fick's law, with the added condition of negligible absorption. In a wide range of ANISN test cells, Eq. (2.40) was found to deviate from the actual ANISN calculated flux by a maximum of 2%, thus the rule appears to have a wider applicability than the limited conditions of its derivation would imply. On this basis, Eq. (2.40) was incorporated into the theory as a replacement for Eq. (2.15) in the calculation of average clad region fluxes.

In the case of the multiply-collided fluxes, the reciprocity treatment of the clad sources leads to problems. Since the reciprocity theorem is not applied to boundary currents, an equation of the type of Eq. (2.40) has no applicability. Instead, another linear approximation is made:

$$\bar{\phi}_2 = \frac{1}{2}(\bar{\phi}_1 + \bar{\phi}_3)\,. \tag{2.41}$$

Thus, for the first-flight group, the average clad region flux is calculated via Eq. (2.40); while for the multiply-collided group, the average clad region flux is obtained from Eq. (2.41) after the reciprocity corrected values of $\bar{\phi}_1$ and $\bar{\phi}_3$ are already known. Because the flux shape in the clad is well behaved and the clad itself is a relatively thin region, such simple relationships work well in determining $\bar{\phi}_2$.

The case of voided sodium is of great interest; thus Eq. (2.17) needs a replacement whenever $\Sigma_{a3} = 0$. By inspecting the results of ANISN calculations for voided coolant regions, it was noted that the average flux in the voided coolant region was approximately equal to

the flux at the outer surface of the clad. Thus, for this case, $\bar{\phi}_3$ is arbitrarily set equal to the clad outer surface flux which is calculated from Eq. (2.40).

To summarize the model developed here to calculate regionwise average fluxes:

1. $\bar{\phi}_1$ and $\bar{\phi}_3$ are calculated knowing the regionwise flat sources and resulting boundary currents as functions of escape and transmission probabilities.

2. Escape and transmission probabilities are expressed in simple first order forms.

3. The regionwise sources are calculated assuming flat cell fluxes and group fluxes based on homogeneous core constants.

4. Clad region sources are dealt with by artificially transforming them into fuel and coolant region sources and then applying an extended reciprocity relation.

5. Due to sensitivity problems, $\bar{\phi}_2$ is calculated only as a simple average of the surrounding region average fluxes for the multiply-collided group, and as a simple average of the clad surface fluxes for the first-flight group.

2.8 Comparison of Model Results with ANISN S_8 Calculations

Tables 2.6 and 2.7 compare the fully developed simple model with a series of ANISN unit cell calculations. The 28 cases cover a wide spectrum of cell specifications; a number of them represent stricter tests of the theory than required for fast reactor unit cells (in particular, cases 2, 13, and 25).

TABLE 2.6

Comparison of Theory and ANISN Results

Case	$\bar{\phi}_1/\bar{\phi}_3$	ANISN	Δ	$\bar{\phi}_1/\bar{\phi}_2$	ANISN	Δ
1	0.97791	0.96640	-0.01151	0.96303	0.96444	0.00141
2	0.96939	0.96841	-0.00098	0.98446	0.95890	0.02555
3	0.95113	0.95253	0.00140	0.97495	0.96679	-0.00816
4	0.99146	0.99108	-0.00038	0.99571	0.98683	-0.00888
5	0.96392	0.96499	0.00107	0.98163	0.97567	-0.00596
6	1.00129	0.99637	-0.00492	1.00065	0.99792	-0.00272
7	0.99304	0.99930	0.00626	0.99651	0.99950	0.00299
8	1.00074	1.00084	0.00010	1.00037	1.00036	-0.00001
9	0.99070	0.99069	-0.00001	0.99570	0.99649	0.00079
10	0.99762	0.99802	0.00040	0.99881	0.99876	0.00005
11	1.00649	1.00699	0.00050	1.00426	1.00592	0.00166
12	1.00724	1.00702	-0.00022	1.00504	1.00513	0.00009
13	1.13524	1.11145	-0.02379	1.05477	1.06206	0.00729
14	1.00454	1.00474	0.00020	1.00246	1.00274	0.00028
15	1.00481	1.00510	0.00029	1.00273	1.00324	0.00051
16	0.98417	0.98395	-0.00022	0.99213	0.99256	0.00043
17	0.95232	0.95436	0.00204	0.97255	0.97464	0.00209
18	0.97961	0.98378	0.00417	0.99214	0.99268	0.00054
19	0.98585	0.98545	-0.00040	0.99229	0.99154	-0.00075
20	0.98559	0.98522	-0.00037	0.99227	0.99170	-0.00057
21	0.94529	0.94733	0.00204	0.96657	0.96642	-0.00015
22	0.94700	0.94893	0.00192	0.96799	0.96863	0.00064
23	1.00411	1.00419	0.00008	1.00283	1.00323	0.00040
24	1.00428	1.00427	-0.00001	1.00285	1.00322	0.00037
25	1.07465	1.06608	-0.00857	1.03976	1.03986	0.00010
26	1.00443	1.00455	0.00011	1.00312	1.00364	0.00052
27	0.94499	0.94695	0.00196	0.96652	0.96641	-0.00011
28	1.00859	1.00907	0.00048	1.00523	1.00641	0.00118

Note: see Table 2.7 for key to cases.

TABLE 2.7

Case Descriptions for Table 2.6

Cell A: $r_1 = 0.3$ cm, $r_2 = 0.375$ cm, $r_3 = 0.6$ cm

$\Sigma_{a1} = 0.2\ cm^{-1}$, $\Sigma_{a2} = 0.01\ cm^{-1}$, $\Sigma_{s2} = 0.1\ cm^{-1}$, $\Sigma_{a3} = 0.005\ cm^{-1}$

Cell B: (Carbide cell) $r_1 = 0.34036$ cm, $r_2 = 0.3683$ cm, $r_3 = 0.70309$ cm

$\Sigma_{a1} = 0.01666\ cm^{-1}$, $\Sigma_{s1} = 0.30957\ cm^{-1}$, $\Sigma_{a2} = 5.63E-4\ cm^{-1}$,

$\Sigma_{s2} = 0.289374\ cm^{-1}$, $\Sigma_{a3} = 1.61E-5\ cm^{-1}$, $\Sigma_{s3} = 0.0868729$

Cell C: (Oxide cell) $r_1 = 0.2794$ cm, $r_2 = 0.3175$ cm, $r_3 = 0.535386\ cm^{-1}$

$\Sigma_{a1} = 0.0652\ cm^{-1}$, $\Sigma_{a2} = 0.05583\ cm^{-1}$, $\Sigma_{s2} = 1.E-5\ cm^{-1}$,

$\Sigma_{a3} = 8.68E-3\ cm^{-1}$

Cell D: (Carbide cell - first flight) same geometry as Cell B

$\Sigma_{a1} = 0.08836\ cm^{-1}$, $\Sigma_{s1} = 0.09522\ cm^{-1}$, $\Sigma_{a2} = 0.05583\ cm^{-1}$,

$\Sigma_{s2} = 0.150161\ cm^{-1}$, $\Sigma_{a3} = 8.68E-3\ cm^{-1}$, $\Sigma_{s3} = 0.036297\ cm^{-1}$

Cell E: $r_1 = 0.3$ cm, $r_2 = 0.4$ cm, $r_3 = 0.6$ cm

$\Sigma_{a1} = 0.2\ cm^{-1}$, $\Sigma_{a2} = 7.5E-3\ cm^{-1}$, $\Sigma_{s2} = 0.075\ cm^{-1}$, $\Sigma_{a3} = 5.E-3\ cm^{-1}$

Cell F: Same geometry as Cell E

$\Sigma_{a1} = 0.2\ cm^{-1}$, $\Sigma_{a2} = 0.01\ cm^{-1}$, $\Sigma_{s2} = 0.1\ cm^{-1}$, $\Sigma_{a3} = 5.E-3\ cm^{-1}$

Case	Description	Case	Description
1	Cell A, $S_1 = S_3 = 1.0$, $S_2 = 0$	6	Cell B, $S_1 = S_2 = S_3 = 1.0$
2	Cell A, $S_2 = 1.0$, $S_3 = S_1 = 0$	7	Cell B, $S_1 = 0.17103$, $S_2 = 0.0565$, $S_3 = 0.008176$
3	Cell A, $S_2 = S_3 = 1.0$, $S_1 = 0$		
4	Cell A, $S_1 = S_2 = 1.0$, $S_3 = 0$	8	Cell B, $S_1 = 0.202289$, $S_2 = 0.0565$, $S_3 = 0.008176$
5	Cell A, $S_1 = S_2 = S_3 = 1.0$		

(Continued)

Table 2.7 continued

Case	Description	Case	Description
9	Cell C, $S_1=S_3=1.0$, $S_2=0$	19	Case 14 except $S_3=1.0$, $S_1=S_2=0$
10	Cell C, $S_1=S_2=S_3=1.0$	20	Case 15 except $S_3=1.0$, $S_1=S_2=0$
11	Cell C, $S_1=1.0$, $S_2=S_3=0$	21	Cell E, $S_3=1.0$, $S_1=S_2=0$
12	Case 11 except $\Sigma_{a1}=0.2\ cm^{-1}$	22	Cell A, $S_3=1.0$, $S_1=S_2=0$
13	Case 11 except $\Sigma_{a3}=0.2\ cm^{-1}$	23	Cell E, $S_1=1.0$, $S_2=S_3=0$
14	Case 11 except $\Sigma_{a2}=\Sigma_{s2}=0$	24	Cell A, $S_1=1.0$, $S_2=S_3=0$
15	Case 11 except $\Sigma_{a2}=$ 8.68E-3 cm^{-1}	25	Case 24 except $\Sigma_{a3}=0.1\ cm^{-1}$
16	Cell C, $S_3=1.0$, $S_1=S_2=0$	26	Cell F, $S_1=1.0$, $S_2=S_3=0$
17	Case 12 except $S_3=1.0$, $S_1=S_2=0$	27	Cell F, $S_3=1.0$, $S_2=S_1=0$
18	Case 13 except $S_3=1.0$, $S_1=S_2=0$	28	Cell D, $S_1=1.0$, $S_2=S_3=0$

In general, the agreement between the simpler theory and the S_8 ANISN calculations inspires confidence in the model (in particular, cases 8, 11, and 28 which represent realistic fast reactor unit cells show the simple theory agreeing very well with the more sophisticated ANISN calculations). On this basis, the simple model is adopted as the standard source of average flux ratios for unit cells, and ANISN is retired from this role for the remainder of the discussion except where the effects of new embellishments to the theory require substantiation.

2.9 Conclusions

A method has been developed which allows an accurate calculation of average flux ratios for the three regions of the unit cell. The use of a discrete ordinate code to calculate these quantities in a fast reactor unit cell is thereby rendered unnecessary, with the method developed here yielding results comparable to an S_8 ANISN calculation. The method developed is simple enough to allow rapid desk calculator based solutions or may be automated by coding a simple program.

Chapter 3

ANISOTROPIC DIFFUSION

One basic analytic tool used in studying the physics of the fast reactor is the diffusion theory code, an example of which is 2DB [38]. Use of such a code requires one to deal with the diffusion coefficient, for which the customary prescription is:

$$D = \frac{1}{3\bar{\Sigma}_{tr}} , \qquad (3.1)$$

where $\bar{\Sigma}_{tr}$ is the volume-averaged macroscopic transport cross section. Strictly speaking, Eq. (3.1) is valid only for homogeneous media characterized by isotropic scattering. The requirement of isotropic scattering is not a limiting one for fast reactors. In Reference 2, two sets of 12-group cross-section sets, one having isotropic scatter and the other P_1-anisotropy, were used in plate heterogeneity studies. The difference between the $\Delta k/k$ heterogeneity factors in the two calculations was less than 5%. Thus scattering anisotropy is not a significant factor for the fast reactor cell and one can justifiably use P_0 cross sections only. In thermal systems containing hydrogen, such a statement would not be valid.

The second requirement for the validity of Eq. (3.1), a homogeneous medium, is not so easily disposed of. This chapter will describe a procedure for obtaining diffusion coefficients which specifically account for the heterogeneous cell geometry, thus making superfluous the prescription of Eq. (3.1); while in the following chapter the use of Eq. (3.1) will be shown to cause an error of the order of $1 in reactivity.

3.1 The Phenomenon of Anisotropic Diffusion

In a truly homogeneous medium there is no ambiguity in the definition of a diffusion coefficient since the physical properties of the medium are constant along any path the neutron may choose. Such is not the case in the heterogeneous cell. Using an illustration due to Michelini [39]: consider a very thin slab surrounded by a large region. The net current in the k direction is:

$$J_k = -D_k \frac{\partial \phi}{\partial k} \qquad (k = x,y,z). \tag{3.2}$$

Since the slab is very thin, the current (which is a quantity obtained by integrating over the volume) does not feel the presence of the slab. In contrast, the derivative of the flux, which is a point-sensitive quantity, may undergo strong fluctuations. If k is parallel to an interface between the two different materials, the neutrons in their net motion parallel to the interface do not cross any discontinuities in physical properties, and thus the flux shape does not undergo any significant changes. On the other hand, if k is normal to the interface, all neutrons moving in that direction cross the material discontinuity so the flux derivative suffers a discontinuity due to the discontinuity in D. Thus the D_k of Eq. (3.1) cannot both be the same. Michelini shows that in the limit of a vanishingly thin slab, the parallel D in the slab tends to the classical diffusion coefficient of the surrounding region, while the perpendicular D in the slab tends to the classical diffusion coefficient of the slab itself.

The result, then, is that the diffusion coefficient for this thin slab is not the same in all directions; moreover, the value of the anisotropic

diffusion coefficients describing the slab are dependent on the properties of the surrounding medium as well as the geometry (i.e., the slab thickness). At the next level of complexity is the question of how one arrives at a single set of diffusion coefficients which describe the entire cell (i.e., in the above example: both the slab and the surrounding medium for a significantly thick slab). The following artifice sheds some light on the problem.

An analogy is available which, though not strictly valid for fast reactor cells, serves a useful pedagogical purpose [40]. In the diffusion approximation, the neutron current $j = -D \nabla \phi$ is analogous to the current in Ohm's law; in which case, the diffusion coefficient corresponds to the electric conductance (the reciprocal of the resistance). Equivalent diffusion coefficients may then be obtained by referring to the analogous case in circuit theory. Thus, for a current parallel to the region interfaces, D is given by conductances in series:

$$D_{\parallel} = \sum_i v_i D_i , \tag{3.3}$$

where v_i is the volume fraction of the i^{th} material in the cell. For a current normal to the region interfaces, D is given by conductances in parallel:

$$\frac{1}{D_{\perp}} = \sum_i \frac{v_i}{D_i} . \tag{3.4}$$

On an even simpler level, the two different diffusion coefficients may be discovered as a result of a basic ambiguity in the definition of an average diffusion coefficient. Namely, if one has a two-component system described by D_1 and D_2, how does one obtain an average D for

the two materials? One possibility is to volume-average the D_i themselves. A second possibility is to volume-average the Σ_{tr_i} for each region and to calculate an average D from the average Σ_{tr}, a process which is identical to volume-averaging $1/D_i$. The prescription of Eq. (3.1), which is equivalent to this latter averaging procedure, is just another form of Eq. (3.4); thus the diffusion coefficient in the perpendicular direction is the same as the single classical diffusion coefficient. On the other hand, the parallel diffusion coefficient is the volume-average of the D_i. Hence, the resolution of the ambiguity is that both averaging procedures are admissible, with one procedure (averaging D_i) valid for the parallel diffusion coefficient and the other procedure (averaging $1/D_i$) valid for the perpendicular diffusion coefficient.

Selengut [41] presents general forms for the diffusion coefficient (the above discussion held only for slab geometry) which are derived assuming a linear flux shape and requiring that the equivalent cell and the actual cell be indistinguishable with respect to leakage and absorption characteristics. Those results are very similar to the forms based on the above electrical analogy, being identical for slab geometry. However, such procedures are not applicable to fast reactor cells since their common primary assumption is that the cell diameter is large compared to the neutron's mean free path, the antithesis of the situation in a fast reactor cell. Thus the electrical analogy gives one an inkling as to why the radial and axial diffusion coefficients differ but not a procedure for calculating them at the unit cell level. However, the conductance model may be applicable in a FBR on a larger scale: for example, the insertion of subassemblies of a differing composition

(with the proviso that the regions involved be several mean free paths in extent) into a core could be treated using the analogy.

3.2 Available Methods of Calculation

The original treatments of anisotropic diffusion were motivated by the desire to account for the effect of holes in thermal reactor cores. The earliest treatment, by Behrens [42], presented a method of correcting the mean square distance that the neutron travels in a given number of collisions, accounting for the presence of voids. The migration area was assumed to vary with the neutron mean square path in particular directions. A subsequent study by Laletin [43] indicated that the identification of the square of the neutron diffusion length with one-sixth of the mean square distance to the point of absorption was valid only for diffusion parallel to cylinders and not for perpendicular diffusion, thus contradicting one of Behrens' assumptions. Carter [44] modified the Behrens treatment so that perpendicular diffusion was properly treated.

Work by Leslie [45] generalized the treatment beyond an emphasis on dealing with holes in media to consider adjacent media of varying composition. His treatment evolved from the definition of a "new" flux, based on a tilted source (i.e., $xq(x)$ where $q(x)$ is the true source distribution and x the space variable), as well as the ordinary flux resulting from a source distribution $q(x)$. Then the axial (or parallel) diffusion coefficient was obtained by weighting with the normal flux, while the radial (or perpendicular) diffusion coefficient was obtained by weighting with the "new" flux. The drawback of Leslie's procedure is the requirement of a transport theory calculation for the "new"

tilted-source flux. Leslie presents an approximate solution in which diffusion theory rather than transport theory is used to calculate the "new" flux. When this approximate result is used for weighting purposes, it results in precisely the forms of the diffusion coefficients derived by Selengut [41]. The latest variation on this theme has been contributed by Williams [46,47] in which the P_N equations are used to derive normal and tilted cell fluxes which are in turn related to axial and radial diffusion coefficients.

The above theories may be labelled the "English school" of approach to anisotropic diffusion since their methods are in a sense all lineal descendants of Behrens' original theory. A different viewpoint is provided by the "Franco-Italian school," one in which the diffusion coefficients are based on collision probability methods. In this "school" the original role equivalent to Behrens' is played by Benoist. In recent years, Benoist's formalism has been the one dominating the representation of anisotropic diffusion.

The procedures of the "English school" have several drawbacks for present purposes. The earlier work dealing primarily with corrections for holes is not easily generalized to non-void heterogeneous cells. Leslie's treatment is hobbled by the requirement of a transport theory calculation for his "new" flux. When diffusion theory is used as an approximation in Leslie's theory, the result is not applicable to fast reactor unit cells since those results, like Selengut's, are based on the assumption of a cell diameter much larger than one mean free path. Williams' treatment is sufficiently general; however, its complexity renders it unattractive. Thus it is the theory of Benoist, which offers sufficient generality to treat both voided and unvoided cells and has

useful asymptotic simplifications for the fast reactor regime, that is the method of choice here. The following sections will concentrate on that theory.

3.3 Benoist's Treatment of Anisotropic Diffusion

3.3.1 Basic Derivation

Benoist [48,49,50] has obtained the anisotropic diffusion coefficients based on a leakage formalism. An outline of his derivation is sketched here, leaving the algebraic complexities to the references.

Since the reason for calculating diffusion coefficients is the need to know the leakage from a zone of the reactor, the primary step is to relate the net leakage $\mathcal{F}$, and hence the diffusion coefficient, to the current $\underline{J}$ and the flux Φ:

$$\mathcal{F} = \sum_k D_k B_k^2 = \frac{\int_{v_1}^{v_2} dv \int_{V\,\text{cell}} \nabla \underline{J}(\underline{r},v)\, dV}{\int_{v_1}^{v_2} dv \int_{V\,\text{cell}} \Phi(\underline{r},v)\, dV}, \qquad (3.5)$$

where B_k^2 is the k-directed buckling, v the speed variable, and V the volume variable. The intent is to write the integrals of $\nabla \underline{J}$ and ϕ in some manageable form and relate the D_k to the result.

Two hypotheses are made: first, that the source density distribution $Q(\underline{r},\underline{\Omega},v)$ can be written as the product of a "macroscopic function" $\psi(\underline{r})$ and a known function $q(\underline{r},\underline{\Omega},v)$ which represents the source distribution in an infinite system, with $\underline{\Omega}$ being the direction vector. The macroscopic function is taken to be the known solution of the Helmholtz equation for the homogeneous medium:

$$\left(\nabla_k^2 + B_k^2\right)\psi_k = 0 . \tag{3.6}$$

The validity of this first hypothesis is discussed in Section 3.4.1.

The physics of the situation is described by the Boltzmann integral equation which is cast into the form of Peierls' integral operator H:

$$Hf = \int_0^\infty dv' \int_V dV' \frac{e^{-\widetilde{\Sigma R}}}{4\pi R^2} \Sigma_s(\underline{r}, \underline{\Omega}\cdot\underline{\Omega}', v' \rightarrow v)\, f(\underline{r}', \underline{\Omega}', v') , \tag{3.7}$$

where Σ_s is the scattering kernel and $\widetilde{\Sigma R}$ the optical thickness, leading to the Boltzmann equation:

$$N = H(Q + N) , \tag{3.8}$$

where N is the collision density. The H operator is defined by an integral over the volume of the cell, and the second hypothesis is that the functions $\psi(\underline{r})$ and $q(\underline{r}, \underline{\Omega}, v)$ may be analytically continued so that the operator's domain of integration extends to infinity. This is the classical image reactor hypothesis which is valid when the dimensions of the medium are large (i.e., many mean free paths in length), as they are in a power reactor.

A second integral operator K is defined:

$$Kf = \int_\infty dV' \frac{e^{-\widetilde{\Sigma R}}}{R^2} f(\underline{r}', \underline{\Omega}', v') . \tag{3.9}$$

After a series of manipulations, the flux and current may be written as:

$$\Phi = \psi\phi - \frac{K}{1 - H}(v\nu\underline{\Omega}\cdot\underline{\nabla}\psi) \tag{3.10}$$

$$\underline{J} = \psi\underline{j} - \frac{K\underline{\Omega}}{1 - H}(v\nu\underline{\Omega}\cdot\underline{\nabla}\psi) , \tag{3.11}$$

where ϕ is the infinite medium flux, $\underline{j}$ the infinite medium current, and

ν the infinite medium directional flux.

At this point, two more hypotheses are introduced: that the curvature of the macroscopic function $\psi(\underline{r})$ in any direction, due to the periodicity of the system in that direction, is small; that the curvature of $\psi(\underline{r})$ in any direction, due to the rate of decrease of $e^{-\widetilde{\Sigma R}}$ in that direction, is small. Both these hypotheses hold true in fast reactor unit cells where the cell fluxes are near-flat spatially. With these hypotheses, one may commute the H and $\underline{\nabla}\psi$ operators in Eqs. (3.10) and (3.11), since in that case $\underline{\nabla}\psi(\underline{r}')$ may be replaced by its one term Taylor series expansion, $\underline{\nabla}\psi(\underline{r})$. This yields:

$$\Phi = \psi\,\phi - \underline{\phi}_1 \cdot \underline{\nabla}\psi \tag{3.12}$$

$$J_k = j_k\psi - \sum_{k'} j_{1k'k}\nabla_{k'}\psi\ , \tag{3.13}$$

where $\underline{\phi}_1 = \frac{K}{1-H}(v\nu\,\underline{\Omega})$ and $j_{1k'k} = \frac{K\Omega_k}{1-H}(v\nu\,\Omega_{k'})$.

As a result, in Eqs. (3.12) and (3.13) the finite medium flux and current have been written in terms of the infinite medium flux and current minus a correction.

These expressions for the current and flux are substituted into the original leakage expression of Eq. (3.5). The vector $\underline{j}_{1k}$ whose components are the $j_{1kk'}$ is introduced, and ρ_k is defined to be the k-component of the vector joining the center of the cell to the point at $\underline{r}$. One may then write:

$$D_k(v) = \frac{\int_V j_{1kk}\,dV + \int_V \rho_k\,\nabla\underline{j}_{1k}\,dV}{\int_V \phi\,dV}\ , \tag{3.14}$$

which is the general expression for the anisotropic diffusion coefficient. Benoist claims the second term in the numerator of Eq. (3.14) is a small correction (more discussion on this point is presented in Section 3.4.2) and ignorable, leading finally to the approximate form of the anisotropic diffusion coefficient:

$$D_k(v) = \frac{1}{3} \frac{\sum_i \sum_j V_i \phi_i \lambda_j P^*_{ij,k}}{\sum_i V_i \phi_i} , \tag{3.15}$$

where

$$P^*_{ij,k}(v) = \frac{3}{V_i \phi_i \lambda_j} \int \frac{K\Omega_k}{1-H} (v \delta_i \Omega_k \nu) \, dV, \tag{3.16}$$

and where $\delta_i = 1$ in volume V_i and zero everywhere else. Thus the calculation of the anisotropic diffusion coefficients reduces to the calculation of the $P^*_{ij,k}$ functions, Benoist's so-called transport probabilities. The following section will discuss particular forms suitable for fast reactor cores which greatly simplify the calculation of anisotropic diffusion coefficients.

A different derivation of just the axial diffusion coefficient D_z has been presented by Bonalumi [51]. Bonalumi's direct derivation confirms that for D_z (unlike for D_r), the absorption correction of Eq. (3.14) is absent. In addition, if the transport probabilities are written in series form (see ahead, Eq. 3.17) where the n^{th} term represents the n^{th} collision probability weighted along the k-direction, the direct derivation confirms that only the first term remains for D_z with the higher order angular correlation terms vanishing.

A brief notation of some of the literature associated with Benoist's theory is appropriate at this point. Reference 52 applies the theory to fuel rods with a central void region. The relevant probabilities are tabulated in graphical, parametric form; however, the range of the variables is that characteristic of thermal systems which makes the tabulations useless for fast systems. Michelini [53] derives simple relations for anisotropic diffusion coefficients describing thin regions and applies them to BWR fuel elements. In Reference 39, a more rigorous treatment is presented. General space-dependent anisotropic diffusion coefficients are derived with the important conceptual conclusion that the classical diffusion coefficient is inaccurate because it is a material constant and is hence discontinuous across material boundaries, while $D_{||}$ is found to be continuous across boundaries. The theory as formulated is limited to slab geometry. A final amplification of Michelini's theory is presented in Reference 54, where it is generalized to rectangular regions in XY geometry. Applications of the above are consistently directed toward thermal systems, with a typical effect of anisotropic diffusion on k_{eff} of 0.005 $\Delta k/k$.

A more detailed discussion of the calculation of the required collision probabilities for use in Benoist's theory may be found in References 55, 56, and 57. For present purposes, the asymptotic forms presented in the following section will suffice.

3.3.2 Useful Asymptotic Forms for Fast Reactor Cells

To calculate the anisotropic diffusion coefficients, one must calculate the transport probabilities of Eq. (3.16). Benoist expands the

transport probabilities in a series of terms corresponding to different collisions:

$$P^{*}_{ij,k} = \frac{\Sigma_j}{\Sigma_{tj}} \sum_{\ell=0}^{\infty} P^{(\ell)}_{ij,k}, \tag{3.17}$$

where Σ_t is the total cross section and Σ the transport cross section (this convention of using t to indicate total values and no subscript to indicate transport values is adopted for Σ and λ throughout this discussion). The first term $P^{(0)}_{ij,k}$ is the oriented first collision probability, defined as the probability that a neutron born in region i will have its first collision in region j, weighted along the k direction:

$$P^{(0)}_{ij,k} = \frac{3}{V\lambda_{tj}} \int_{V_j} dV_j \int_{V_i} dV_i \, \Omega_k \, \frac{e^{-\widetilde{\Sigma R}}}{4\pi R^2}. \tag{3.18}$$

The series of Eq. (3.17) converges more quickly when the dimensions over which physical properties change (the "channels") become small compared to the neutron mean free path, and at the limit of infinitely small channels, only the first term remains. One would expect that for a fast reactor cell, very few terms in the series are required; indeed in Reference 50, from a parametric study presented by Benoist, one concludes that only the first term $P^{(0)}_{ij,k}$ is required (it gives D_r correctly to within 0.04% compared to a higher order truncation). Thus only the oriented first collision probabilities are required to calculate the anisotropic diffusion coefficients.

In Appendix VIII of Reference 48, Benoist presents formulae applicable to tight lattices in light water systems, a tight lattice being one in which the lattice pitch is much less than the neutron mean free

path. Since such a condition is generally true in the fast reactor (i.e., all fast reactors have a tight lattice structure), Benoist's results may be applied directly to the cases of interest here. Thus the anisotropic diffusion coefficients are:

$$D_k = \frac{1}{3}\lambda_m \left\{ 1 + \frac{V_u}{V_t} \cdot \frac{\phi_m}{\phi_t} \left(1 - \frac{\lambda_m}{\lambda_u} \right) \left[1 + \frac{\lambda_u}{\lambda_m} \left(\frac{\phi_u}{\phi_m} - \frac{\lambda_m}{\lambda_u} \right) P_{uu,k} \right] \right\}, \qquad (3.19)$$

where

$$P_{uu,k} = P^0_{uu,k} + (1 - P_{uu,k}) \frac{(1-\Gamma_{m,k})\Gamma_{u,k}}{1 - (1-\Gamma_{m,k})(1-\Gamma_{u,k})} \quad . \qquad (3.20)$$

In the above equations, u = fuel, m = moderator, t = total, and ϕ is the region average flux. $P_{uu,k}$ is the first collision probability in the fuel, the zero superscript being omitted. The form of D_k is based on the assumption that all neutrons are born in the fuel. Two-group source calculations indicate that the ratio between fuel and coolant region sources for the multiply-collided group discussed in the prior chapter is 16 to 1; thus, such an assumption holds fairly well.

The various terms of Eq. (3.20) have physical significance: $P^0_{uu,k}$ is that part of the first collision probability due to capture in the fuel of those neutrons which never entered the moderator, while the second term represents the part due to capture of neutrons which have made multiple traversals of both fuel and moderator. Γ_m and Γ_u are, respectively, the probabilities that a neutron incident on the moderator and fuel regions experience a collision there. Thus the ratio in the second term of Eq. (3.20) is analogous to the familiar infinite series of products of collision probabilities expressed in closed form which were detailed in the previous chapter. Since Benoist's results are for

a two-region cell, the clad has been homogenized into the fuel.

Clearly, the Γ will depend on the geometry and the entering neutron distribution. For cylindrical geometry and a cosine entering distribution, Benoist calculates:

$$\Gamma_{u,k} = \frac{2\eta}{\xi_k}(1-P^0_{uu,k}) \tag{3.21}$$

$$\Gamma_{m,k} = \frac{2\eta_m}{\xi_k}(1-P^0_{mm,k}), \tag{3.22}$$

where $\xi_r = \frac{9}{8}$, $\xi_z = \frac{3}{4}$ and $\eta = \frac{2V_u}{S\lambda_u}$, $\eta_m = \frac{2V_m}{S\lambda_m}$, S being the interface surface area.

Benoist tabulates the $P^0_{ii,k}$ probabilities in terms of two functions, T_r and T_z, which have η as arguments. For η equal to zero, T_r and T_z take on the values of 1. and 2., respectively. Again, fast reactor systems lend themselves to an asymptotic treatment since in that case the values of η are near zero (η less than 0.1), so that approximate forms of the T_i developed by Bonalumi [57] for cylindrical geometry are applicable:

$$T_r = \frac{1 + 2\eta}{1 + 2\eta(C+\eta)} \tag{3.23}$$

$$T_z = \frac{2T_r}{1 + \frac{\eta}{0.51 + \eta}}, \tag{3.24}$$

where

$$C = 1 + \frac{1}{3 + \frac{11}{3}\eta}. \tag{3.25}$$

Thus the procedure for calculating the anisotropic diffusion coefficients is to first calculate the T_i functions from Eqs. (3.23) and

(3.24), set the $P^0_{ii,k} = \eta_i T_k(\eta_{ti})$, and calculate the Γ functions from Eqs. (3.21) and (3.22). This yields the required information for calculating the first collision probabilities from Eq. (3.20) which in turn are used to calculate the anisotropic diffusion coefficients from Eq. (3.19).

For the sodium voided case, Eq. (3.19) is not valid since it yields an infinite diffusion coefficient. Instead, the following form of the diffusion coefficient is used [58]:

$$D_k = \frac{1}{3}\lambda_u \left[1 + \frac{V_m}{V_t}\left(1 + \eta_m \frac{\lambda_m}{\lambda_u} Q^*_{mk}\right)\right], \tag{3.26}$$

where $$Q^*_{mk} = Q_k - \frac{2}{\xi_k} + \frac{1}{\eta_u\left(1 - P^0_{uu,k}\right)}, \tag{3.27}$$

and $Q_z = 2.$, $Q_r = 1.$

It is instructive at this point to choose one sample cell and calculate diffusion coefficients using the three models: homogeneous, heterogeneous-Selengut, and heterogeneous-Benoist. Table 3.1 presents the parameters describing the chosen cell, while Table 3.2 lists the resulting diffusion coefficients for each model.

TABLE 3.1

Sample Cell for D_k Calculation

Region	Outer Radius (cm)	D (cm) Group 1	Group 2
Fuel (UO_2)	0.2797	2.0469	0.95464
Clad (Fe)	0.3175	1.6220	0.78860
Coolant (Na)	0.4508	7.5507	3.0810

For the homogeneous case, the diffusion coefficients are calculated from Eq. (3.1), while for the heterogeneous-Benoist case, Eq. (3.19) is employed. For the heterogeneous-Selengut model, the pedagogical example invoked in Section 3.1, D_z is calculated from Eq. (3.3) while D_r is obtained from the cylindrical geometry form equivalent to Eq. (3.4):

$$D_r = \left[\frac{(1+v)D_0 + (1-v)D_1}{(1-v)D_0 + (1+v)D_1} \right] D_1 , \qquad (3.27a)$$

where the averaging process is applied twice to two regions at a time, "0" being the inner region of volume fraction v, and "1" being the outer region. That is, Eq. (3.27a) is first applied to the (fuel) + (clad) region pair, and then to the (fuel + clad) + (coolant) region pair.

TABLE 3.2

Diffusion Coefficients for Sample Cell

Model		D (cm) Group 1	D (cm) Group 2	D_{het}/D_{hom} Group 1	D_{het}/D_{hom} Group 2
Homogeneous	D_z	3.0917	1.4126		
	D_r	3.0917	1.4126		
Benoist	D_z	3.1150	1.4310	1.0075	1.0130
	D_r	3.0963	1.4169	1.0014	1.0030
Selengut	D_r	4.1276	1.7746	1.3351	1.2563
	D_z	4.7730	2.0076	1.5438	1.4212

The Selengut model clearly predicts much augmented diffusion coefficients; however, that model is invalid for fast reactor cells since its primary assumption is that the cell diameter is much larger than a neutron mean free path, and it is of interest here only because it was referred to in an analogy used earlier.

On the other hand, the Benoist theory predicts more reasonably moderate increases in the diffusion coefficients (of the order of 1%) due to anisotropic leakage. The above calculation is for a case with coolant present. For the sodium voided case, the anisotropy increases, as will be discussed later, to several percent. The effects will be translated into terms of reactivity in the next chapter.

3.3.3 Comparison with Experiments

Benoist [48,49] has made a detailed comparison of his theory with experimental measurements, analyzing seven different types of experiments ranging from the variation of critical assembly buckling to the measurement of decay constants as a function of B_k^2 by pulsed neutron experiments. Typically, the migration areas or diffusion lengths are obtained by measurement of bucklings for various configurations. That is, taking the equation:

$$K_\infty = 1 + M_r^2 B_r^2 + M_z^2 B_z^2 , \qquad (3.28)$$

upon dividing through by M_r^2, the ratio M_z^2/M_r^2 can be taken as the slope for a series of measurements in which B_z^2 is varied. This ratio of the migration areas can be calculated from the Benoist theory and is found to be in general agreement with the measured ratio, comparisons being made for four moderators: BeO, D_2O, H_2O and graphite. Discrepancies can be explained by pointing to finite size effects in those systems

which are small since the Benoist theory is primarily applicable to large systems (viz., the second hypothesis of Section 3.3.1).

The ratio of the radial diffusion coefficient to the moderator diffusion coefficient has been measured for a highly anisotropic lattice (heavy water containing air-fulled tubes) with the experimental result $1.29 \pm .02$ agreeing well with the theoretical value of 1.28 [59]. Axial streaming has been investigated, and Benoist's theory found to give the correct angular correlation corrections [60]; that is, the higher order terms of Eq. (3.17). Behrens' theory, which is equivalent to the zero order Benoist solution detailed in the last section, has been compared with Monte Carlo calculations as well as UO_2 experiments [61], and the conclusion drawn that the axial diffusion coefficient is predicted well, while the radial anisotropy is significantly underpredicted as compared to Monte Carlo calculations. The results of Reference 59, however, contradict this latter conclusion on the basis of experimental results.

In sum total, one has reasonable confidence in applying the theory of Benoist to anisotropic diffusion in thermal systems, based on experimental confirmation. By extension, the theory should be even closer to reality when applied to fast systems since they are considerably less heterogeneous, making the hypotheses upon which the theory is based (*vide* Section 3.3.1) even more valid for fast systems then for thermal systems.

There has been a recent awakening of interest in anisotropic diffusion to explain discrepancies in plate versus pin reactivity effects in fast reactor critical assembly measurements [31]. Though no calculation of the anisotropic diffusion effect is performed in Reference 31,

an *ad hoc* increase of 8% in the effective diffusion constant for the plate geometry is shown to account for all of the discrepancy. One is tempted to suggest that the method of Benoist (or a variation thereof) be applied to analyze the plate geometry, as has been done here for pin geometry. Quite recent work in the Federal Republic of Germany [89] has been directed precisely along such lines, applying the theory of Benoist to plate-type fast critical assemblies.

3.4 Corrections to the Benoist Theory

Various refinements may be added to the Benoist theory developed in the earlier sections, primarily in the form of corrections to the original calculation. Firstly, the discussion of Sections 3.3.1 and 3.3.2 is inherently directed toward a monoenergetic problem, for which Benoist [48,49] has calculated the corrections required to take into account the effect of group coupling. In addition, errors in his conclusions regarding the absorption correction of Eq. (3.14) have been pointed out by various authors [62,63,64]. The following two subsections will discuss these corrections with the useful conclusion that for fast reactor systems, these corrections are negligible.

3.4.1 Group Coupling Corrections

We return to the first hypothesis of the Benoist theory: that the source distribution is factorable into a macroscopic function and a lattice-periodic function. Such a treatment neglects the coupling between various groups; namely, the spatial variation of the slowing-down sources into different groups.

The absorption term of Eq. (3.14), which was assumed to be negligible, is:

$$\delta_a D_r = \frac{\int_V \rho_r \nabla j_{1r} \, dV}{\int_V \phi \, dV} , \tag{3.29}$$

where the notation is taken from Section 3.3.1 with k = r. In the context of a two-group theory and by use of various manipulations based on the assumption of an isotropic directional flux, Benoist concludes that the absorption correction for the fast group is:

$$\frac{\delta_a D_r^{(1)}}{\frac{1}{3}\lambda_m^{(1)}} = -\frac{1}{8\pi} K_m^2 \frac{V_m^2}{V_t} \left(\frac{D_r^{(1)}}{\frac{1}{3}\lambda_m^{(1)}} - \frac{\phi_m^{(1)}}{\phi_t^{(1)}} \right) , \tag{3.30}$$

where $K_m^2 = \Sigma_{am}/D_m$ and m = moderator. Then assuming an equilibrium between the fast absorption and slow source corrections, Benoist finds the thermal group scattering correction is:

$$\delta_s D_r^{(2)} = -\frac{\phi_t^{(1)}}{\phi_t^{(2)}} \delta_a D_r^{(1)} , \tag{3.31}$$

where the flux ratio is the average lattice fast flux divided by the average lattice slow flux. Benoist finds $\delta_a D_r^{(2)}$ much less than $\delta_a D_r^{(1)}$, and $\delta_s D_r^{(1)}$ much less than $\delta_s D_r^{(2)}$, thus only the quantities in Eqs. (3.30) and (3.31) are of significance.

These coupling corrections may be applied to a two-group calculation for a typical fast reactor cell, where the two groups are the first-flight and multiply-collided groups identified earlier. A typical cell has the following parameters:

$$r_{fuel} = 0.36 \text{ cm}, \quad r_{outer} = 0.57 \text{ cm}$$

$$\text{uncorrected } D_r^{(1)} = 3.3 \text{ cm}$$

$$\frac{1}{3}\lambda_m^{(1)} = 7.6 \text{ cm}$$

$$\Sigma_{am}^{(1)} = 0.01 \text{ cm}^{-1}$$

$$\Sigma_{tr_m}^{(1)} = 0.044 \text{ cm}^{-1}$$

$$\frac{V_m^2}{8\pi V_t} = 0.015 \text{ cm}^3$$

To use Eq. (3.30), assume $\phi_m^{(1)}/\phi_t^{(1)} = 0$ in lieu of calculating the actual ratio; this assumption will predict an overly large correction. With these quantities:

$$\delta_a D_r^{(1)} = -(7.6)(.015)(.0013)(3.3/7.6) = -6 \times 10^{-5} \text{ cm}$$

$$\delta_s D_r^{(2)} = -(\phi^{(1)}/\phi^{(2)})(-6 \times 10^{-5} \text{ cm}).$$

It is apparent that $\delta_a D_r^{(1)}$ is an entirely negligible correction to the monoenergetic diffusion coefficient. Since $\phi^{(1)}/\phi^{(2)}$ is of the order of 10^{-1}, $\delta_s D_r^{(2)}$ is an even smaller correction. One concludes that for a fast reactor unit cell, group coupling corrections are unnecessary.

3.4.2 Blackburn's Anisotropy Correction

Blackburn originally pointed out an error in Benoist's calculation of the absorption correction due to his assumption of an isotropic directional flux. Bridge and Howarth [64] have performed an analysis on the CAGR lattice in which the absorption correction was found to consist of two parts, one of which Benoist neglected due to his flux assumption. For the case of a graphite lattice, where relatively large

cross-channel gradients occur, Bridge and Howarth found the original Benoist calculation to be in error by as much as 13%.

However, the case of interest here is the fast reactor cell. Bonalumi [63] has developed a method to calculate these corrections in a simple manner. The corrected diffusion coefficient may be written as:

$$D_r = D_0 + D_{an} + D_s - D_a , \tag{3.32}$$

where D_0 is the principal part of the Benoist diffusion coefficient, D_a is the absorption correction (in absolute value) and D_s the source correction, both discussed in the prior subsection. The new correction is D_{an}, Blackburn's anisotropy correction:

$$D_{an} = \frac{\int_V x j_0 \, dV}{\phi_0 V_t} . \tag{3.33}$$

Because Benoist assumed an isotropic directional flux, the current $j_0 \equiv 0$ and D_{an} vanished. On the other hand, by taking advantage of the fact that $j_0 = 0$ on the cell surface, using Green's theorem to transform to a surface integral, and making a simple statement of neutron balance, it is possible to write:

$$D_{an} = - \frac{(q_m - \Sigma_{am}\bar{\phi}_m)V_m}{8\pi\phi(b)} , \tag{3.34}$$

where V_m is the moderator volume per unit cell length, $\phi(b)$ is the cell edge flux, $\bar{\phi}_m$ the average moderator region flux, and $q_m = \Sigma_{rm}\phi^{(1)}$ the slowing-down source. To obtain Eq. (3.34), the simplifying assumption that $(q - \Sigma_a\phi)$ is regionwise flat has been made.

Again performing the calculation for the typical fast reactor cell where the additional assumption of a flat cell flux is made (i.e., $\phi(b) = \bar{\phi}_m$), one finds for the first-flight group where $q_m = 0$:

$$D_{an}^{(1)} = \left(\frac{V_m}{8\pi}\right)\Sigma_{am}^{(1)} = (.03)(.01) = 0.0003 \text{ cm.}$$

For the multiply-collided group where $q_m = \Sigma_{rm}\phi_m^{(1)}$:

$$D_{an}^{(2)} = -\left(\frac{V_m}{8\pi}\right)\left[\Sigma_{rm}\frac{\phi_m^{(1)}}{\phi_m^{(2)}} - \Sigma_{am}^{(2)}\right]$$

$$= -(.03)[(.01)(0.1) - (.00004)] = -0.00003 \text{ cm.}$$

To serve as a basis of comparison in deciding how important these anisotropy corrections are, one notes that the quantity of interest is the difference between the homogeneous and the anisotropic Benoist diffusion coefficients, which typically is about 0.01 cm. In that context, the larger of the two flux anisotropy corrections (the first-flight group value) is negligible, being of the order of 3% of the principal Benoist anisotropy. From another viewpoint, the Benoist calculation results in a 1% anisotropy; the Blackburn anisotropy correction adds to that an additional 0.03%. In either case, the correction to the principal term of the Benoist anisotropic diffusion coefficient is negligible for the specific case of fast reactor cells, and the asymptotic forms of Section 3.3.2 may be employed without recourse to source corrections, absorption corrections, or flux anisotropy corrections.

3.5 Leakage Treatment in Finite Cores

At this point, it is appropriate to return to the topic of Chapter 2, flux ratios in unit cells, and account for the presence of these unit

cells in a core of finite size. The earlier discussion was solely concerned with cells enclosed by the white boundary condition; thus no accounting was made for leakage from the unit cell and its effect upon the flux ratios. A method of coupling the average flux ratios with the anisotropic diffusion coefficients is required.

The first question of interest involves the manner in which the flux ratios vary from cell to cell in a finite reactor. Since the available calculational tool for the present work is limited to the one-dimensional ANISN code, the desired investigation can only be carried out in slab geometry. Figure 3.1 describes the "Gedanken" problem postulated. The results of an ANISN S_8 calculation are presented in the form of the ratio of average fuel flux to average coolant flux in Table 3.4.

TABLE 3.3
Cell Constants (cm^{-1})

		Group 1	Group 2
Fuel:			
	Σ_a	0.020504	0.016657
	$\nu\Sigma_f$	0.053880	0.020419
	Σ_{gg}	0.091667	0.030580
	$\Sigma_{g,g+1}$	0.068804	—
Coolant:			
	Σ_a	4.178E-5	1.613E-5
	Σ_{gg}	0.034939	0.085275
	$\Sigma_{g,g+1}$	0.008176	—

TABLE 3.4
Cell-Dependent Flux Ratios (ϕ_{fuel}/ϕ_{cool})

Cell Number	Group 1	Group 2
1	1.00856	1.00148
2	1.00855	1.00148
3	1.00853	1.00150
4	1.00849	1.00151
5	1.00842	1.00154
6	1.00829	1.00160
7	1.00810	1.00175
8	1.00822	1.00247
9	1.01259	1.01460

Fig. 3.1 Multi-Cell Slab Core

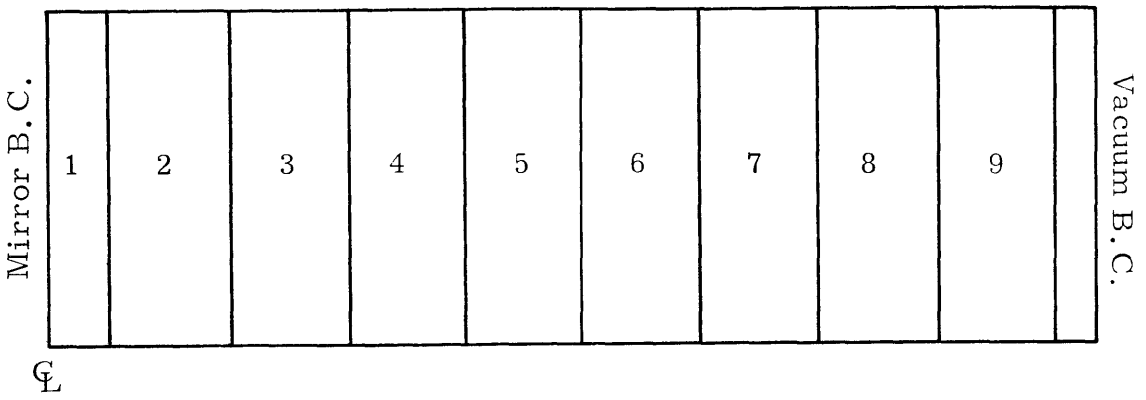

Detail of single cell:

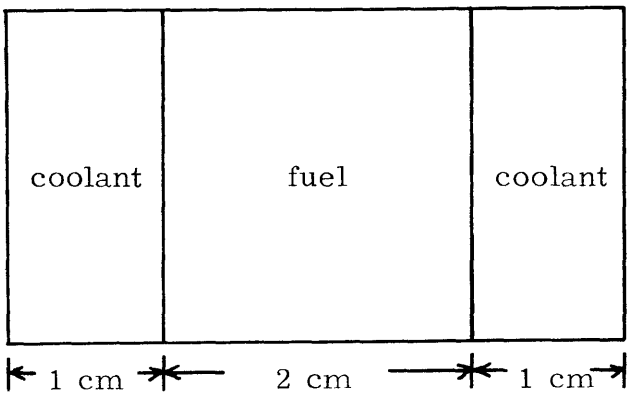

Since the slab was decreed to be infinitely long axially in order to isolate the effect of one-dimensional leakage, axial leakage has been ignored. It is apparent that the flux ratios remain very nearly constant from cell to cell, regardless of position, until the boundary is reached. However, in the boundary cell the flux in both groups is reduced by more than a factor of four compared to the central cell, with the heterogeneous effects occurring there having a lesser impact on the reactivity. Thus the assumption that the flux fine structure is identical in each cell is a reasonable approximation when the basic quantity of interest is an integral parameter such as a multiplication constant.

The final link in the chain requires that the flux ratio calculations for a single isolated cell with reflective boundary conditions yield the same values as for the cell in a finite core. This is achieved by adding the familiar DB^2 correction to the macroscopic absorption cross section.

For the validation of this procedure, an ANISN calculation was performed for the isolated unit cell of Figure 3.1. The buckling is equated to $-\nabla^2\phi/\phi$, which is calculated by applying a central difference formula to various pointwise flux values given by the 9 cell slab ANISN results:

$$\frac{1}{\phi_k}\nabla^2\phi_k = \phi_{k+1} - 2\phi_k + \phi_{k-1} - \frac{1}{12}\left[\phi_{k+2} - 4\phi_{k+1} + 6\phi_k - 4\phi_{k+1} + \phi_{k-2}\right] + \frac{1}{90}\left[\phi_{k+3} - 6\phi_{k+2} + 15\phi_{k+1} - 20\phi_{k-1} - 6\phi_{k-2} + \phi_{k-3}\right]. \quad (3.35)$$

Table 3.5 lists the group buckling values calculated at three locations. The DB^2 correction was then calculated using the central core values for the bucklings, with the radial diffusion coefficient calculated from Eq. (3.4).

TABLE 3.5
Group Buckling Values (cm^{-2})

Location	B_1^2	B_2^2
Center of core	0.0013986	0.0013829
Center of cell 2	0.0013588	0.0013835
Center of cell 4	0.0013330	0.0014019

When the isolated, reflected cell calculation is performed with the DB^2 correction, one finds $(\phi_f/\phi_c)_1 = 1.00916$ and $(\phi_f/\phi_c)_2 = 1.00146$, reasonably close to the central cell values in the finite core given in Table 3.4. In addition, the isolated cell calculation yields $k = 1.1037$ while the slab core calculation yields $k = 1.1083$. We conclude that the effects of radial leakage from a cell in a finite lattice upon the flux ratios in that cell are reasonably accounted for by adding a $D_r B_r^2$ correction to the absorption cross section in an isolated, reflected cell. Thus the methods of Chapter 2, developed for a unit cell in an infinite lattice, may be retained for the cell in a finite lattice with the one proviso that all macroscopic absorption cross sections be augmented by the term $(D_r B_r^2 + D_z B_z^2)$.

One should take cognizance of the coupling between the flux ratios and the anisotropic diffusion coefficients. Namely, from Eq. (3.19), it is apparent that the anisotropic diffusion coefficients depend on ratios of the fluxes, while the flux ratios themselves depend on the diffusion coefficients through the DB^2 correction. Thus an iterative procedure suggests itself: to calculate the diffusion coefficients assuming flat cell fluxes, to calculate the flux ratios using these initial diffusion

coefficients, and then to calculate first iterate diffusion coefficients. The cell flux ratios in fast reactor cells are generally so nearly unity that even the first iteration yields a negligible change in the anisotropic diffusion coefficients (i.e., the change is in the fifth significant figure which, based on the method discussed in the next chapter, results in a change in the reactivity effect of the order of 0.1¢). Thus only when the flux ratios depart significantly (e.g., more than 10%) from unity does the coupling between the flux ratios and the diffusion coefficients require an iterative solution; such a condition does not occur in a typical fast reactor unit cell.

3.6 Conclusions

The method of Benoist for calculating anisotropic diffusion coefficients has been investigated. Its basic hypotheses have been shown to be valid for fast reactor unit cells and useful asymptotic forms applicable to these cells have been collected. The corrections to the Benoist theory important for thermal lattices have been discussed with the conclusion that they are negligible for fast reactor unit cells; thus the first order form of the Benoist theory is valid for these cells. The methods of calculating flux ratios in infinite lattices can be extended to cells in finite lattices by a DB^2-type correction to the macroscopic absorption cross sections.

Chapter 4

REACTIVITY EFFECTS OF HETEROGENEITY

The preceding two chapters contain a discussion of the methods which allow the calculation of cross sections characterizing the heterogeneous nature of the FBR unit cell. Since the differences between these heterogeneous constants and those describing a volume-averaged, homogeneous medium are sufficiently small, the methods of first order perturbation theory may be employed to calculate the reactivity difference between neutron balances computed using these two models.

A two-group model is adopted as the minimum useful approach. The groups are chosen to allow a separation of the peaking of first-flight neutrons in the fuel rod from the absorptive depression of lower energy neutrons in the fuel rod. This objective can be accommodated by choosing a group one cut-off at 1.4 MeV. This chapter presents a two-group perturbation theory model and points out the significant reactivity contributions, with the exception of energy self-shielding effects which have been reserved for the entirety of Chapter 5. In addition, a simpler direct calculation of the reactivity contributions, equivalent to perturbation theory for an equivalent bare core, is presented.

4.1 A Useful Approximation to First Order Perturbation Theory

As is well known, the reactivity due to small changes in system properties may be expressed in terms of perturbation integrals [16,65]

$$\frac{\Delta k}{k} = \frac{\int_V [\phi^*]^T[\delta P][\phi]dV}{\int_V [\phi^*]^T[P_0][\phi]dV} - \frac{\int_V [\nabla\phi^*]^T[\delta D][\nabla\phi]dV}{\int_V [\phi^*]^T[P_0][\phi]dV}, \qquad (4.1)$$

where the ϕ^* are the adjoint group fluxes and ϕ the group fluxes, all characteristic of the unperturbed case in the first order perturbation theory approximation; P_0 is the fission production matrix, δP the perturbation matrix exclusive of changes in the diffusion constant, while δD is the perturbation in the latter quantity. Thus, with knowledge of the homogeneous-medium fluxes, and by defining the difference between the homogeneous and heterogeneous constants as the perturbations, one may employ Eq. (4.1) to calculate the reactivity equivalent of the heterogeneities. Various simplifications will be assumed which make the perturbation integrals tractable.

A more direct calculation of the reactivity effect may be performed by considering the multiplication constant to be a multi-variable function. That is, in the two-group model one has the multiplication constant:

$$k(\Sigma_{a1}, \Sigma_{a2}, \Sigma_{12}, \nu\Sigma_{f1}, \nu\Sigma_{f2}, D_{1r}B_r^2, D_{2r}B_r^2, D_{1z}B_z^2, D_{2z}B_z^2) =$$

$$\frac{\chi_1\nu\Sigma_{f1}}{\Sigma_{12} + \Sigma_{a1} + D_{1r}B_r^2 + D_{2r}B_r^2} + \frac{\chi_2\nu\Sigma_{f2}}{\Sigma_{a2} + D_{2r}B_r^2 + D_{2z}B_z^2}$$

$$+ \frac{\chi_1\nu\Sigma_{f2}\Sigma_{12}}{(\Sigma_{12}+\Sigma_{a1}+D_{1r}B_r^2+D_{1z}B_z^2)(\Sigma_{a2}+D_{2r}B_r^2+D_{2z}B_z^2)}, \qquad (4.2)$$

from which the total differential, Δk, can be formed:

$$\Delta k = \frac{\partial k}{\partial \Sigma_{a1}} \Delta\Sigma_{a1} + \frac{\partial k}{\partial \Sigma_{a2}} \Delta\Sigma_{a2} + \frac{\partial k}{\partial \Sigma_{r}} \Delta\Sigma_{r} + \frac{\partial k}{\partial (\nu\Sigma_{f1})} \Delta(\nu\Sigma_{f1})$$

$$+ \frac{\partial k}{\partial (\nu\Sigma_{f2})} \Delta(\nu\Sigma_{f2}) + \frac{\partial k}{\partial (D_{1r}B_r^2)} \Delta(D_{1r}B_r^2) + \frac{\partial k}{\partial (D_{2r}B_r^2)} \Delta(D_{2r}B_r^2)$$

$$+ \frac{\partial k}{\partial (D_{1z}B_z^2)} \Delta(D_{1z}B_z^2) + \frac{\partial k}{\partial (D_{2z}B_z^2)} \Delta(D_{2z}B_z^2) , \qquad (4.3)$$

To calculate the reactivity $\Delta k/k$, the differentials in Eq. (4.3) are taken to be the differences between the homogeneous and the heterogeneous constants. This procedure will be termed the "direct" method.

It is also of interest to investigate the validity of the "direct" calculation of the reactivity effect by reducing the integrals in the perturbation theory approach and comparing the result to the "direct" method. First, it should be emphasized that the expression for the two-group k given by Eq. (4.2) is for the specific case of a one region medium; thus the blanket and reflector regions are implicitly treated through a reflector savings correction. In that case, the two-group equations can be rearranged to yield ratios of the fluxes:

$$\frac{\phi_1}{\phi_2} = \frac{\chi_1 \nu\Sigma_{f2}/k}{\Sigma_{a1} + \Sigma_{12} + D_1 B^2 - \chi_1 \nu\Sigma_{f1}/k} \qquad (4.4a)$$

$$\frac{\phi_1^*}{\phi_2^*} = \frac{\Sigma_{12} + \chi_2 \nu\Sigma_{f1}/k}{\Sigma_{a1} + \Sigma_{12} + D_1 B^2 - \chi_1 \nu\Sigma_{f1}/k} . \qquad (4.4b)$$

These ratios may be used to simplify the integrals of Eq. (4.1) since the flux ratios and the material constants are all space-independent.

One additional property, useful in simplifying the perturbation integrals, arises due to the limitation of the calculation to equivalent

bare cores (i.e., bare cores with a reflector savings correction): the diffusion constant perturbation may be treated without necessitating the calculation of flux gradients. We assume that the unperturbed group fluxes may be written as:

$$\phi_i(r,z) = A_i J_0(B_r r) \cos(B_z z) . \tag{4.5}$$

Concentrating on the second term of Eq. (4.1), one finds that the following identity holds:

$$\int_{V\ \text{core}} (\nabla\phi)^2\, \delta D\, dV = \int_{V\ \text{core}} B^2\phi^2 \delta D\, dV , \tag{4.6}$$

where $B^2 = B_r^2 + B_z^2$. It should be emphasized that the above identity is valid only for the case of a bare equivalent core in which there occurs a uniform diffusion constant perturbation everywhere, and the integration is to be carried out over the entire core volume. In that case, the cross-terms obtained upon squaring the gradient vanish due to orthogonality while other nonmatching terms are zero on the boundary; the integral identity of Eq. (4.6) holds due to these fortuitous conditions.

Using the above identity, the diffusion constant perturbation can be treated in the same manner as the other perturbations in Eq. (4.1). Under the above conditions, the following expression for the perturbation theory form of the reactivity is found:

$$\frac{\Delta k}{k} = \left\{ \left[\chi_1 \delta(\nu\Sigma_{f1}) - \delta\Sigma_{12} - \delta\Sigma_{a1} - B_r^2 \delta D_{r1} - B_z^2 \delta D_{z1} \right] \left[\frac{\phi_1^*}{\phi_2^*} \right] \left[\frac{\phi_1}{\phi_2} \right] \right.$$

$$+ \left[\chi_1 \delta(\nu\Sigma_{f2}) \right] \left[\frac{\phi_1^*}{\phi_2^*} \right] + \left[\chi_2 \delta(\nu\Sigma_{f1}) + \delta\Sigma_{12} \right] \left[\frac{\phi_1}{\phi_2} \right]$$

$$\left. + \left[\chi_2 \delta(\nu\Sigma_{f2}) - \delta\Sigma_{a2} - B_r^2 \delta D_{r2} - B_z^2 \delta D_{z2} \right] \right\} \left\{ \chi_1 \nu\Sigma_{f1} \left(\frac{\phi_1}{\phi_2} \right) \left(\frac{\phi_1^*}{\phi_2^*} \right) \right.$$

$$\left. + \chi_1 \nu\Sigma_{f2} \left(\frac{\phi_1^*}{\phi_2^*} \right) + \chi_2 \nu\Sigma_{f1} \left(\frac{\phi_1}{\phi_2} \right) + \chi_2 \nu\Sigma_{f2} \right\}^{-1} , \qquad (4.7)$$

where the flux ratios are given by Eqs. (4.4a) and (4.4b). This is the simplified result which is to be compared with the "direct" method of Eq. (4.3).

When the equivalent bare core, first order perturbation theory is used to calculate the reactivity effect of the various heterogeneities, it yields a value essentially identical to that calculated using the total differential of k from Eq. (4.3): in all FBR cases investigated, the two results differ only in the sixth significant figure. Thus the total differential method for calculating heterogeneous reactivity effects (i.e., the "direct" method) is equivalent to a two-group perturbation theory calculation for an equivalent bare core.

The validity of the "direct" model for calculating the heterogeneity corrections due solely to the non-flat flux component (i.e., all effects exclusive of anisotropic diffusion) was confirmed with ANISN S_8 calculations into which first the homogeneous constants were input, after which the calculation was repeated with the heterogeneous constants. The change in k_{eff} given by the ANISN results agreed with that calculated

by the total differential of k method in all cases to within ±1¢ in reactivity (assuming $\beta = 0.0033$). To put this result into proper perspective: the non-flat flux component is of the order of 15¢ or less, thus while the uncertainty of ±1¢ is relatively large (>6%), the importance of this quantity, as will be shown in the next section, is relatively small, being considerably outweighed by the effect of anisotropic diffusion.

Similarly, one can now quantify the effect of the errors in the methods developed in Chapter 2 for the calculation of region-averaged cell flux ratios. Performing two calculations of the heterogeneous reactivity effect, the first using the flux ratios given by an ANISN S_8 cell calculation and the second using the escape/transmission probability theory results developed here, one finds that in the example of Case 11 in Table 2.6, the net discrepancy due to the differing flux ratios is 0.5¢ in reactivity, a negligible quantity. Thus the escape/transmission probability formalism of Chapter 2 is entirely adequate for use in calculating the heterogeneous reactivity effects of non-flat cell fluxes.

The "direct" model's predictions for the reactivity effect of the anisotropic diffusion perturbations are not as easily verified. The common diffusion theory codes, such as 2DB, are unable to account correctly for anisotropic diffusion coefficients because only one diffusion coefficient is defined per region. The usual manner in which leakage is treated [38] is to convert the volume integral $\int D\nabla^2\phi \, dV$ into the surface integral in the form of a finite difference representation for the leakage at mesh point "0":

$$\int_{\text{cell}} D\underline{\nabla}\phi \cdot d\underline{A} = \sum_{i=1}^{4} \bar{D}_k \frac{A_k}{\ell_k} (\phi_k - \phi_0) , \tag{4.8}$$

where $$\bar{D}_k = \frac{D_0 D_k (h_0 + h_k)}{D_0 h_k + D_k h_0} , \tag{4.9}$$

with the labelling conventions defined in Figure 4.1. For the case of anisotropic diffusion, the leakage at point "0" is more properly described by:

$$\sum_{k=1}^{4} \bar{D}_k \frac{A_k}{\ell_k} (\phi_k - \phi_0) = \sum_{k=1}^{2} \bar{D}_k^{(r)} \frac{A_k}{\ell_k} (\phi_k - \phi_0) + \sum_{k=3}^{4} \bar{D}_k^{(z)} \frac{A_k}{\ell_k} (\phi_k - \phi_0) , \tag{4.10}$$

where explicit recognition has been made of the fact that the radial and axial diffusion coefficients differ.

Nevertheless, in the case of the equivalent bare core, an equivalent diffusion coefficient may be defined:

$$\langle D \rangle = \frac{D_r B_r^2 + D_z B_z^2}{B_r^2 + B_z^2} . \tag{4.11}$$

Assuming a uniform mesh structure and recognizing that the equivalent core is homogeneous, one finds from Eq. (4.9) that $\bar{D}_k = \langle D \rangle$ everywhere. Under these conditions, the homogeneous leakage algorithm becomes:

$$\mathcal{L}_{\text{hom}} = \langle D \rangle \frac{A_0}{\ell_0} \sum_{k=1}^{4} (\phi_k - \phi_0) , \tag{4.12}$$

while the anisotropic leakage algorithm becomes:

$$\mathcal{L}_{\text{ani}} = D_0^{(r)} \frac{A_0}{\ell_0} \sum_{k=1}^{2} (\phi_k - \phi_0) + D_0^{(z)} \frac{A_0}{\ell_0} \sum_{k=3}^{4} (\phi_k - \phi_0) . \tag{4.13}$$

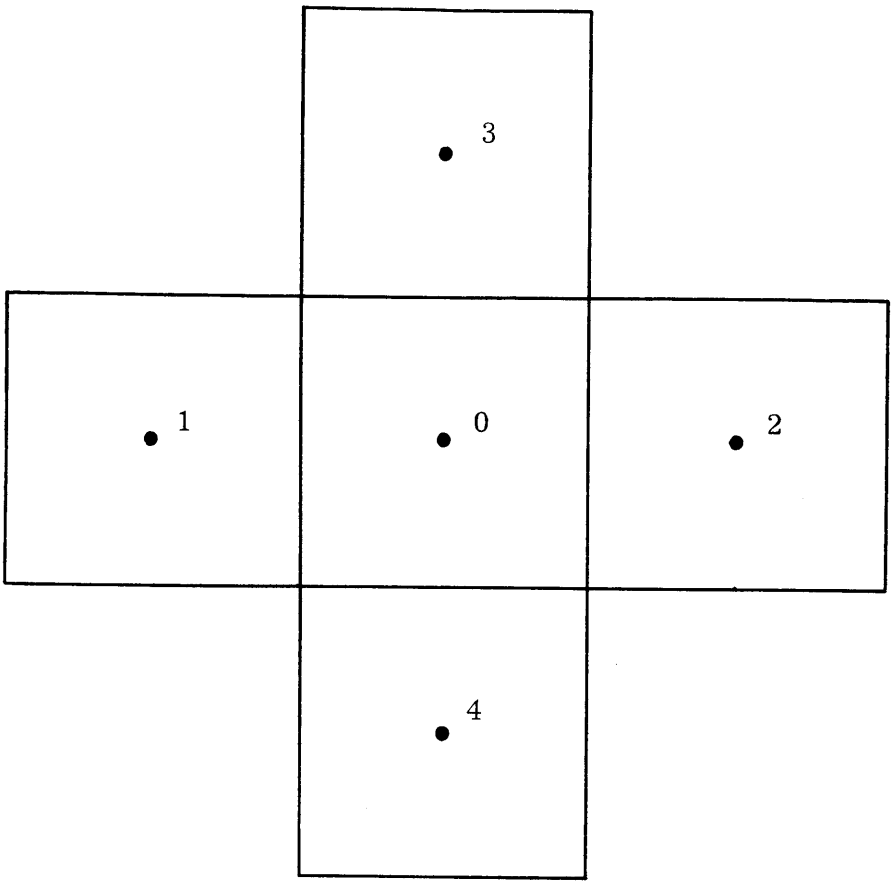

A_k = area of boundary between mesh point k and mesh point 0

$\bar{D}_k$ = effective diffusion constant between mesh point k and mesh point 0

ℓ_k = distance between mesh point k and mesh point 0

D_k = diffusion constant of region k

h_k = radial width of region k

Fig. 4.1 Mesh Structure in 2DB Finite Difference Representation

Thus, for the prescribed equivalent diffusion coefficient to be valid as defined by Eq. (4.11), one requires $\mathcal{L}_{hom} = \mathcal{L}_{ani}$, which is equivalent to the two requirements:

$$\frac{B_r^2}{B_z^2 + B_r^2} = \frac{\sum_{k=1}^{2} (\phi_k - \phi_0)}{\sum_{k=1}^{4} \phi_k - 4\phi_0} , \tag{4.14}$$

and

$$\frac{B_z^2}{B_z^2 + B_r^2} = \frac{\sum_{k=3}^{4} (\phi_k - \phi_0)}{\sum_{k=1}^{4} \phi_k - 4\phi_0} . \tag{4.15}$$

One final manipulation reduces these last two equalities to a single equality which must be satisfied for the equivalent diffusion constant to be valid:

$$B_z^2[(\phi_1 - \phi_0) + (\phi_2 - \phi_0)] = B_r^2[(\phi_3 - \phi_0) + (\phi_4 - \phi_0)] . \tag{4.16}$$

Dividing both sides of Eq. (4.16) by the uniform mesh interval and allowing that interval to become infinitesimal results in the condition:

$$B_z^2\left[\left(\frac{\partial\phi}{\partial r}\right)_1 - \left(\frac{\partial\phi}{\partial r}\right)_2\right] = B_r^2\left[\left(\frac{\partial\phi}{\partial z}\right)_3 - \left(\frac{\partial\phi}{\partial z}\right)_4\right] . \tag{4.17}$$

Carrying out the same manipulation again results in:

$$B_z^2\left[\frac{\partial^2\phi}{\partial r^2}\right] = B_r^2\left[\frac{\partial^2\phi}{\partial z^2}\right] , \tag{4.18}$$

or finally $B_z^2[-B_r^2\phi] = B_r^2[-B_z^2\phi]$ which is indeed an equality.* Thus for a uniform medium, and in the limit of infinitesimal mesh spacing, the equivalent diffusion coefficient given by Eq. (4.11) results in the same calculated leakage as a proper anisotropic leakage representation.

With the above discussion in mind, the mean diffusion coefficient described by Eq. (4.11) may now be used as the single diffusion coefficient in 2DB calculations for a uniform cylindrical core in rz geometry. An identical set of constants was used in the diffusion coefficient perturbation calculation described in the last section and in a 2DB calculation. The latter was repeated with transport cross sections decreased by a factor of 0.996446 in group 1 and 0.993633 in group 2, these factors being the ratios of the homogeneous diffusion coefficients to the equivalent diffusion coefficients obtained by using the Benoist theory and Eq. (4.11). The 2DB calculations predicted a -46.7¢ effect due to anisotropic diffusion while the perturbation theory value was -53.9¢. This discrepancy of 13% between the two values is acceptable. In particular, the mesh intervals in the 2DB calculation (3.370 cm radially and 3.049 cm axially) were significantly non-infinitesimal, with the definition of the equivalent diffusion coefficient being non-exact in this event. One would consequently place more faith in the perturbation theory value than in the one calculated using 2DB.

---

*The observant reader will note that $\nabla_r^2 = \frac{\partial^2}{\partial r^2} + \frac{1}{r}\frac{\partial}{\partial r}$, the second term of which is missing from Eq. (4.18) for the required next step: $\nabla_r^2\phi = -B_r^2\phi$. That is because the above discussion implicitly assumes the transformation from the cylindrical rz space to a rectangular rz space (viz., Fig. 4.1). Upon transformation back to the cylindrical space, the required $\frac{1}{r}\frac{\partial}{\partial r}$ term reappears in Eq. (4.18).

The same analysis for the sodium-out case is of greater interest since the degree of anisotropy is greater: for the test cell, the factors decreasing Σ_{tr} in groups 1 and 2 were 0.991798 and 0.982402, respectively. The perturbation theory calculation indicated a contribution of -\$1.69 due to anisotropic diffusion, while the 2DB value was -\$1.45. In this case the discrepancy was slightly larger than the 13% observed for the sodium-in case.

Earlier it was shown that the mean diffusion coefficient defined by Eq. (4.11) gives the correct anisotropic leakage for a uniform system in the limit of infinitesimal mesh spacing. In order to verify this, the sodium-out 2DB calculations were repeated after halving of the mesh intervals (now 1.685 cm radially and 1.5245 cm axially). For the finer mesh structure, 2DB yielded a -\$1.58 (i.e., 7% low) reactivity contribution due to anisotropic diffusion, to be compared to -\$1.45 (i.e., 14% low) for the coarser mesh and -\$1.69 (the reference value) for the perturbation theory result. Thus it appears that the mesh spacing is important in diffusion theory calculations that incorporate the mean diffusion coefficient method. In addition, the perturbation theory result appears to be confirmed since the 2DB diffusion code result tends to approach the perturbation theory value in the limit of fine mesh spacing. Roughly speaking, halving the mesh spacing, halves the error implicit in making the mean diffusion coefficient approximation to the anisotropic diffusion coefficients. In order to reduce the error to less than 1%, the mesh spacing needs to be of the order of 0.2 cm, which would result in a prohibitive running time for the calculation. Thus the perturbation theory calculation is far more attractive for finding the reactivity contribution of the anisotropic leakage than a direct diffusion code calculation.

4.2 Identification of the Individual Reactivity Contributions

The total differential Δk provides a direct measure of the importance to be placed upon each heterogeneous perturbation: the $\left(\frac{\partial k}{\partial \Sigma_x}\right)$ multiplier is the weight to be given to the perturbation $\Delta\Sigma_x$. Table 4.1 lists the nine perturbation multipliers and their values for a representative FBR unit cell.

TABLE 4.1
Perturbation Multipliers

$$\frac{\partial k}{\partial \Sigma_{a1}} = -\left[\frac{\chi_1 \nu\Sigma_{f1}}{\left(\Sigma_{12}+\Sigma_{a1}+\overline{D_1 B^2}\right)^2} + \frac{\chi_1 \nu\Sigma_{f2}\Sigma_{12}}{\left(\Sigma_{12}+\Sigma_{a1}+\overline{D_1 B^2}\right)}\right] = -20.02$$

$$\frac{\partial k}{\partial \Sigma_{a2}} = -\left[\frac{\chi_2 \nu\Sigma_{f2}}{\left(\Sigma_{a2}+\overline{D_2 B^2}\right)^2} + \frac{\chi_1 \nu\Sigma_{f2}\Sigma_{12}}{\left(\Sigma_{12}+\Sigma_{a1}+\overline{D_1 B^2}\right)\left(\Sigma_{a2}+\overline{D_2 B^2}\right)}\right] = -163.48$$

$$\frac{\partial k}{\partial \nu\Sigma_{f1}} = \left[\frac{\chi_1}{\Sigma_{12}+\Sigma_{a1}+\overline{D_1 B^2}}\right] = 18.87$$

$$\frac{\partial k}{\partial \nu\Sigma_{f2}} = \left[\frac{\chi_2}{\Sigma_{a2}+\overline{D_2 B^2}} + \frac{\chi_1 \Sigma_{12}}{\left(\Sigma_{12}+\Sigma_{a1}+\overline{D_1 B^2}\right)\left(\Sigma_{a2}+\overline{D_2 B^2}\right)}\right] = 177.94$$

$$\frac{\partial k}{\partial D_{1i} B_i^2} = -\left[\frac{\chi_1 \nu\Sigma_{f1}}{\left(\Sigma_{12}+\Sigma_{a1}+\overline{D_1 B^2}\right)^2} + \frac{\chi_1 \nu\Sigma_{f2}\Sigma_{12}}{\left(\Sigma_{12}+\Sigma_{a1}+\overline{D_1 B^2}\right)^2}\right] = -19.21$$

$$\frac{\partial k}{\partial D_{2i} B_i^2} = -\left[\frac{\chi_2 \nu\Sigma_{f2}}{\left(\Sigma_{a2}+\overline{D_2 B^2}\right)^2} + \frac{\chi_1 \nu\Sigma_{f2}\Sigma_{12}}{\left(\Sigma_{12}+\Sigma_{a1}+\overline{D_1 B^2}\right)\left(\Sigma_{a2}+\overline{D_2 B^2}\right)^2}\right] = -156.81$$

where $\overline{D_j B^2} \equiv D_{jr} B_r^2 + D_{jz} B_z^2$; $j = 1, 2$; $i = r, z$

It is apparent that the perturbations in the multiply-collided group have a consistently larger weighting; however, the values of the perturbations themselves are smaller than for the first-flight group; thus the products remain of the same order of magnitude.

Tables 4.2 and 4.3 present the results for a typical FBR cell. At this juncture, only the relative magnitudes of quantities are of interest and more detailed discussion of the effects for specific cells will be presented in Chapters 6 and 7. Using the perturbations given in Table 4.2, the reactivity effect of each is calculated with the results presented in Table 4.3. Throughout, the column labelled "perturbation" refers to "heterogeneous" minus "homogeneous," while the direction of the perturbation yielding the reactivity contribution is the change from homogeneous constants to heterogeneous constants.

TABLE 4.2

Heterogeneous Cross-Section Perturbations (Na In)(cm^{-1})

Cross Section	Homogeneous	Heterogeneous	Perturbation
Σ_{a1}	0.00594414	0.00596404	0.00001990
Σ_{a2}	0.00597820	0.00597701	-0.00000119
$\nu\Sigma_{f1}$	0.0150227	0.0150737	0.0000510
$\nu\Sigma_{f2}$	0.00677904	0.00677765	-0.00000139
Σ_{12}	0.0335229	0.0335829	0.0000600
$D_{1z}B_z^2$	0.00220976	0.00222643	0.00001667
$D_{1r}B_r^2$	0.00104778	0.00104934	0.00000156
$D_{2z}B_z^2$	0.00100303	0.00101660	0.00001357
$D_{2r}B_r^2$	0.000475596	0.000477098	0.000001502

TABLE 4.3

Heterogeneous Reactivity Contributions (Na In)

Effect	Contribution
Group 1 fission	20.7¢
Group 1 absorption	-8.6
Group 1 removal	-3.8
Group 1 radial leakage	-0.7
Group 1 axial leakage	-7.2
Group 2 fission	-5.0
Group 2 absorption	3.9
Group 2 radial leakage	-4.9
Group 2 axial leakage	-44.1
Total	-49.6¢

Throughout, the conversion to ¢ and $ of reactivity is based on $\beta_{eff} = 0.0033$. The contributions from fission, absorption, and removal events are due to non-flat cell fluxes, while the leakage contributions are due to anisotropic diffusion. From these results, one concludes that the purely homogeneous calculation, for the sodium-in condition, overpredicts the reactivity by half a dollar. Note that the two-group model developed here is not expected to accurately calculate the absolute value of the reactivity; rather, it is used to calculate the reactivity difference between a homogeneous and a heterogeneous representation, that is, an a posteriori correction to a homogeneous calculation which may be of any degree of sophistication required.

Tables 4.4 and 4.5 report analogous results for the sodium-out condition in the same cell.

TABLE 4.4

Heterogeneous Cross-Section Perturbations (Na Out) (cm^{-1})

Cross Section	Homogeneous	Heterogeneous	Perturbation
Σ_{a1}	0.00593931	0.00595056	0.00001125
Σ_{a2}	0.00522278	0.00522330	0.00000052
$\nu\Sigma_{f1}$	0.0150827	0.0151115	0.0000288
$\nu\Sigma_{f2}$	0.00624499	0.00624562	0.00000063
Σ_{12}	0.0288451	0.0288826	0.0000375
$D_{1z}B_z^2$	0.00221218	0.00225130	0.00003912
$D_{1r}B_r^2$	0.00118822	0.00119218	0.00000396
$D_{2z}B_z^2$	0.00106308	0.00110109	0.00003801
$D_{2r}B_r^2$	0.000571009	0.000575298	0.000004289

TABLE 4.5

Heterogeneous Reactivity Contributions (Na Out)

Effect	Contribution
Group 1 fission	12.9¢
Group 1 absorption	-5.5
Group 1 removal	-2.9
Group 1 radial leakage	-1.9
Group 1 axial leakage	-19.0
Group 2 fission	2.4
Group 2 absorption	-1.8
Group 2 radial leakage	-14.7
Group 2 axial leakage	-130.5
Total	-161.0¢

With the sodium voided, the cell fluxes are more nearly flat, reducing that component of the heterogeneity effect. However, the major heterogeneous contribution is the -$1.50 due to preferential streaming of neutrons in the voided coolant regions, an effect which the homogeneous model completely overlooks. Adding up all contributions, one finds that the homogeneous calculation overpredicts the reactivity by $1.61.

The ultimate quantity of interest is the effect of the heterogeneities on the sodium void reactivity. For the example under consideration here, the homogeneous calculation overpredicts the sodium-out reactivity by $1.61 and the sodium-in reactivity by $0.50. Thus the homogeneous calculation yields a whole core sodium voiding worth which is $1.11 too positive in reactivity (neglecting resonance self-shielding effects described in Chapter 5).

To generalize as to which effects are important and which are not: from the results presented in Tables 4.3 and 4.5, one notes that the net effect due to non-flat cell fluxes is +7.2¢ for the sodium-in case and +5.1¢ for the sodium-out case, leading to a difference of only 2.1¢ in the sodium void calculation. On the other hand, the net effects due to anisotropic diffusion are -56.9¢ and -166.1¢ for the sodium-in and sodium-out cases, respectively. Due to partial cancellation of the components (i.e., augmented fission in the fuel is accompanied by augmented parasitic capture in the fuel), the non-flat cell flux contributes very little to the heterogeneous reactivity effect. The major contribution is that due to anisotropic diffusion, particularly when the core is voided.

4.3 The DELKHET Code

The procedures of Chapter 2 for calculating average flux ratios in the cell, the method of Benoist for calculating anisotropic diffusion coefficients discussed in Chapter 3, and the calculation of reactivity equivalents for the heterogeneous perturbations of the homogeneous cell constants discussed earlier in this chapter have been united in the form of the DELKHET code (see detailed description in Appendix E), an elementary programming of the relevant equations discussed in the present text. The calculation of the anisotropic diffusion coefficients is carried through one iteration in order to account for the effect of non-flat cell fluxes on the resulting diffusion coefficients. As input, one enters a two-group cross-section table, number densities, cell geometry, a value for β_{eff}, and the two-group fission spectrum. The output yields the region-averaged cell flux ratios, the heterogeneous cell constants, and a breakdown of the nine individual components of the heterogeneous reactivity effect. Execution time for the object deck on the IBM 370/165 is less than 0.02 minutes per case.

Since a one-group model will be under discussion in the next chapter, a one-group version of DELKHET has been created. A test problem was analyzed using a consistent set of cross sections (i.e., two-group and one-group cross sections collapsed from 26 groups over an identical spectrum using ANISN). Table 4.6 summarizes the results.

TABLE 4.6

Sensitivity of the Heterogeneous Reactivity Effect to the Group Model

		One Group	Two Groups
Na In	Δk/k	-50.0¢	-59.0¢
Na Out	Δk/k	-150.0¢	-167.6¢
	Net void effect	-$1.00	-$1.09

The effect of the group model chosen is not great, with the one-group model underestimating the effects by less than 20%. For the net sodium void effect, calculated by subtraction, the one-group model is accurate to within 10%. Thus the retention of a two-group model is not imperative; however, it does provide additional useful physical insight into the problem.

4.4 Conclusions

The heterogeneous cell constants calculated using the methods of the prior two chapters have been translated into terms of their reactivity effect, using a two-group equivalent bare core model. An approximation (called the "direct" method) to first order perturbation theory is developed and shown to yield identical results for the equivalent bare core model. The heterogeneous effects calculated using either the perturbation theory or the equivalent "direct" method were found to compare favorably with calculations using the ANISN and 2DB codes. In the absence of resonance self-shielding effects (to be discussed in the following chapter), the primary effect was found to be that due to anisotropic diffusion. The use of anisotropic diffusion

coefficients in place of a single homogeneous diffusion coefficient was found to reduce the reactivity contribution of whole-core sodium voiding by about one dollar. In contrast, the effects of non-flat cell fluxes were only about 2% of the anisotropic diffusion effect.

Chapter 5

SELF-SHIELDING OF RESONANCES

Prior to this point, resonance self-shielding effects have been omitted: namely, all calculations have been performed using cross-section sets for infinitely diluted constituent materials. In reality, the constituent materials in the unit cell are at a finite density; and, further, the most important resonant material, U-238, is restricted to the fuel rod, causing increased self-shielding of the resonances. This chapter is a study of the effects of finite dilution and lumping of resonant material upon the multiplication constant and sodium voiding reactivity. Correlation techniques are presented which yield self-shielding factors for U-238 based on defined spectral indices.

5.1 Energy Self-Shielding Defined

Some confusion may arise from the various usages of the term "self-shielding." Spatial flux-weighting effects were discussed in Chapter 2, where the term referred to the spatial variation of the flux in a coarse group (i.e., group width much greater than resonance width) multi-group sense, due to the localization of sources and sinks within the unit cell -- for the sake of clarity, this may be termed the flux distribution effect. Typically, these two components of the flux are separated by the multi-group assumption that the flux within a particular group is separable in space and energy:

$$\phi_i(r,E) = \varphi_i(r)\ \theta_i(E)\,. \qquad (5.0)$$

Hence, the procedures of Chapter 2 dealt only with the component $\varphi_i(r)$ in a two-group framework, in the absence of resonance self-shielding.

If resonance self-shielding is accounted for, there is a negligible change in the $\varphi_i(r)$: Tables 5.1 and 5.2 present results for the unit cell of Table 4.3 which indicate use of a heterogeneous resonance self-shielded two-group set in place of an infinite dilution two-group set affects the average flux ratios by an amount equivalent to about 3¢ in reactivity.

TABLE 5.1

Self-Shielding Effects on Heterogeneous Contributions

Effect	Na In		Na Out	
	Infinite Dilute	Self-Shielding	Infinite Dilute	Self-Shielding
Group 1 fission	+20.7¢	+19.4¢	+12.9¢	+12.1¢
Group 1 absorption	-8.6	-8.5	-5.5	-5.3
Group 1 removal	-3.8	-3.3	-2.9	-2.6
Group 1 radial leakage	-0.7	-0.7	-1.9	-1.9
Group 1 axial leakage	-7.2	-6.8	-19.0	-18.0
Group 2 fission	-5.0	-0.4	+2.4	-0.1
Group 2 absorption	+3.9	+0.3	-1.8	+0.1
Group 2 radial leakage	-4.9	-4.8	-14.7	-14.8
Group 2 axial leakage	-44.1	-42.5	-130.5	-127.6

TABLE 5.2

Resonance Self-Shielding Effects on Heterogeneous Correction to Voiding Worth

	Infinite Dilution	Self-Shielded
Na In $\Delta k/k$	-49.6¢	-47.3¢
Na Out $\Delta k/k$	-161.0¢	-158.0¢
Net voiding effect	-$1.11	-$1.11

Resonance self-shielding alters primarily the contributions from group 2 fission and group 2 absorption, which are effects opposite in sign. As shown in Table 5.1, the result is a cancellation of effects with the overall result remaining unchanged. Thus, on a practical level, one may consider the resonance self-shielding effects in isolation from anisotropic diffusion and spatial flux distribution effects. On the other hand, $\theta_i(E)$ changes markedly when self-shielding is accounted for: in a 26-group calculation, the flux in the lower energy groups ($E < 1$ keV) is observed to increase by orders of magnitude. Fast reactor blanket results are of a different class and will be discussed in Chapter 7.

Two different types of self-shielding will be considered: homogeneous and heterogeneous. The former takes cognizance of the fact that the cell constituents are at some finite number density (in contrast to the infinite dilution model), while the latter accounts in addition for the fact that the fuel is lumped at the center of the cell. Strictly speaking, the heterogeneous resonance self-shielding effect is the difference between these two types of self-shielding. Since the effect of adding self-shielding to an infinite dilution model is also of interest here, the discussion in this chapter will go beyond the heterogeneous effects to consider self-shielding in general.

Table 5.3 summarizes the various models which are of interest. The relationship between these models can be more clearly defined by means of the f-factor formalism [73,82]. The macroscopic cross section for a homogenized cell may be written as:

TABLE 5.3
Summary of Physical Models

Model	Details
1. Infinitely dilute model	The cross sections used are for all elements at infinite dilution in a homogeneous medium; no resonance self-shielding.
2. Spatial flux distribution model	The cross sections used are weighted to account for coarse group flux variation in the unit cell; resonance energy self-shielding not accounted for since infinite dilution cross sections are used in the weighting.
3. Homogeneous resonance self-shielding model	The cross sections used account for resonance self-shielding for elements in a homogeneous medium (finite dilution).
4. Heterogeneous resonance self-shielding model	The cross sections used account for resonance self-shielding for elements in specified heterogeneous geometry. Spatial component of energy self-shielding accounted for: equivalent to an ultra-fine group approach (group width less than resonance width).

N.B. The term "self-shielding" in this chapter always refers to self-shielding of U-238 absorption and scattering resonances.

$$\Sigma_x^g = \frac{\sum_j \sum_i N_{ij} f_{x,i}^g \langle \sigma_{x,i} \rangle_g \phi_j^g V_j}{\sum_j \phi_j^g V_j} \qquad (5.1)$$

where:

f = self-shielding factor (≤ 1)

g = group number

x = process (e.g., absorption)

j = region (e.g., fuel region)

i = material (e.g., U-238)

$\langle \sigma_{x,i} \rangle_g$ = average microscopic group g cross section for process x, element i, in the absence of self-shielding (i.e., infinite dilution)

N = number density

ϕ = average flux

V = volume

Thus we see that in Table 5.3, the infinitely dilute model corresponds to $f \equiv 1$, ϕ_j the same for all j; the spatial flux distribution model corresponds to ϕ_j not the same in all regions; the homogeneous self-shielding model corresponds to $f < 1$ with f calculated for a homogeneous medium; and the heterogeneous resonance self-shielding model corresponds to $f < 1$ with some account being made of the heterogeneous geometry of the unit cell in the calculation of f. Generally, heterogeneous self-shielding decreases the value of f compared to homogeneous self-shielding (i.e., lumping the absorber increases the resonance self-shielding).

The comparisons of Tables 5.1 and 5.2 involved the processing of cross sections two ways: the "infinite dilution" results were obtained

by using Eq. (5.1) with f = 1 (i.e., the procedures of Chapter 2), while the "self-shielded" results were based on calculations with the heterogeneous value of f < 1 for U-238. This chapter investigates the effect of employing various simplifications in the calculation of the f-factor and presents a correlation which yields f for a standard, heterogeneous FBR cell.

One should keep in mind that heterogeneous resonance self-shielding has associated with it a spatial flux dip which should not be confused with the spatial flux distribution effect under discussion here. The calculation of the spatial component of heterogeneous resonance self-shielding is discussed in Sections 7.3.1 and 7.3.2, where it is pointed out that coarse group calculations do not give the proper result. Instead, calculation of the heterogeneous self-shielding effect's spatial component requires an ultra-fine group calculation where the group width is much less than the resonance width. Throughout this chapter, heterogeneous self-shielding effects will be treated by the appropriate f-factor (*vide* Eq. 5.1), and information on the spatial flux dip that such self-shielding causes is implicitly carried in the value of the f-factor. Section 7.3.2 presents a method for extracting that implicit spatial flux dip from the heterogeneous self-shielding factor.

5.2 The MIDI Code

Self-shielded U-238 cross sections for the present study were obtained through the use of the MIDI code [66], a modified version of the IDIOT code [67]. MIDI was used to calculate self-shielded cross sections for U-238 in groups 11 through 21 (21.5 keV through 4.65 eV) of the ABBN 26-group set. The energy group structure is described in Table 5.4.

TABLE 5.4

Energy Group Structure of 26-Group Set

Group	E_n	Δu_n
1	6.5 - 10.5 MeV	0.48
2	4.0 - 6.5 MeV	0.48
3	2.5 - 4.0 MeV	0.48
4	1.4 - 2.5 MeV	0.57
5	0.8 - 1.4 MeV	0.57
6	0.4 - 0.8 MeV	0.69
7	0.2 - 0.4 MeV	0.69
8	0.1 - 0.2 MeV	0.69
9	46.5 - 100 KeV	0.77
10	21.5 - 46.5 MeV	0.77
11	10.0 - 21.5 KeV	0.77
12	4.65 - 10.0 KeV	0.77
13	2.15 - 4.65 KeV	0.77
14	1.0 - 2.15 KeV	0.77
15	465 - 1000 eV	0.77
16	215 - 465 eV	0.77
17	100 - 215 eV	0.77
18	46.5 - 100 eV	0.77
19	21.5 - 46.5 eV	0.77
20	10.0 - 21.5 eV	0.77
21	4.65 - 10.0 eV	0.77
22	2.15 - 4.65 eV	0.77
23	1.0 - 2.15 eV	0.77
24	0.465 - 1.0 eV	0.77
25	0.215 - 0.464 eV	0.77
26	0.252 eV	0.77

Based on the narrow resonance approximation (used for the resolved resonance region), the code calculates the flux in resonance k:

$$\phi_k(E) = \frac{\sigma_n}{\sigma_n + \sigma_{sr}(E) + \sigma_{ar}(E)} , \tag{5.2}$$

where σ_n is the total nonresonant scattering cross section per resonant absorber atom, constant within the resonance; where $\sigma_{sr}(E)$ is the microscopic resonant scattering cross section and $\sigma_{ar}(E)$ is the microscopic resonant absorption cross section. The resonant cross sections are calculated from a library of resonance parameters using the single-level, Doppler-broadened Breit-Wigner model.

The self-shielded cross section is then found from:

$$\sigma_x = \frac{\sum_{k=1}^{N} \int_{\Delta E} \sigma_{xk}(E)\, \phi_k(E)\, dE}{\int_{\Delta E} \phi(E)\, dE} , \tag{5.3}$$

where the x subscript refers to the cross section of interest, N is the number of resonances within the group, and $\phi(E)$ is the total flux. For the unresolved resonances, the sum over the N resonances is replaced by an average for the group. For isolated resonances, chi-squared distributions are used to generated the required averages; where applicable, overlap corrections are made.

Heterogeneous effects are dealt with by an equivalence relation [9,66] which modifies the total nonresonant scattering cross section:

$$\sigma_n = \frac{\Sigma_p + \Sigma_m + \Sigma_h}{N_r} , \tag{5.4}$$

where Σ_p and Σ_m are the nonresonant scattering cross sections due to light and heavy elements, respectively, in the fuel lump; Σ_h is the heterogeneous contribution, the effective nonresonant cross section due to neutron leakage from the lump; N_r is the number density of the resonant element in the lump. The equivalence principle yields:

$$\Sigma_h = \frac{1 - C}{\bar{\ell}} \frac{K}{1 + (K-1)C} , \tag{5.5}$$

where $\bar{\ell}$ is the mean chord length (4V/S), C the Dancoff factor, and K a factor which corrects the rational approximation for its known underestimate of the escape probability P:

$$P = \frac{1}{1 + \Sigma_t \bar{\ell}/K} . \tag{5.6}$$

The Dancoff factor for cylindrical cells is calculated using Sauer's method [68]:

$$C = \frac{\exp(-\tau \Sigma_m \bar{\ell}_m)}{1 - (1-\tau)\Sigma_m \bar{\ell}_m} , \tag{5.7}$$

where "m" refers to the coolant, and τ is a geometrical index given for a hexagonal lattice as:

$$\tau = \frac{\sqrt{\frac{\pi}{2\sqrt{3}}} \cdot \sqrt{1 + VR} - 1}{VR} - 0.12 , \tag{5.8}$$

with VR the coolant-to-fuel volume ratio. The factor K is calculated by the extended equivalence relation of Kelber [69] for the resolved narrow resonances, while for the unresolved resonances one assumes the customary value of 1.3 [66].

The treatment of the heterogeneous effect using Eqs. (5.5) through (5.8) has one interesting result for the case of constant volume ratio: the heterogeneous correction is virtually independent of the fuel rod radius. Table 5.5 presents results for two different rod radii, but with a constant fuel-to-coolant ratio.

TABLE 5.5
Effect of Pin Size on Self-Shielding

	σ_s^{28} (barns)		σ_a^{28} (barns)	
Group	$\bar{\ell}$ = .8 cm	$\bar{\ell}$ = .0005 cm	$\bar{\ell}$ = .8 cm	$\bar{\ell}$ = .0005 cm
11	11.09	11.13	0.4913	0.4936
12	11.85	11.94	0.7844	0.7929
13	12.04	12.31	0.6178	0.6300
14	10.54	10.60	0.7073	0.7268
15	10.91	11.00	0.9568	0.9941
16	9.756	9.798	0.9198	0.9605
17	12.60	12.77	1.489	1.558
18	13.60	13.78	4.450	4.640
19	12.37	12.48	3.709	3.837
20	11.13	11.20	9.695	10.01
21	9.565	9.585	9.794	10.13

It is remarkable that the amount of self-shielding increases so little with an increase of three orders of magnitude in fuel pin diameter. On close inspection of Eq. (5.5), one finds that the change in the mean chord length is compensated for by the change in the Dancoff factor, so that Σ_h remains roughly constant. The physical implication is that a

FBR lattice of small radius fuel rods on a narrow pitch exhibits approximately the same degree of self-shielding as a FBR lattice of large radius fuel rods on a wide pitch, provided the fuel-to-coolant volume ratio is the same in both cases. In effect, the neutron in either case has traversed the same amount of U-238 in reaching any identical relative point (e.g., half-way into either radius fuel rod): in fact, the mean free path for absorption within the resonance ranges from approximately 280 cm in group 11 to 14 cm in group 21. This leads one to conclude that the effect of heterogeneity on self-shielding in the FBR is small, as will be demonstrated directly in the following section.

5.3 The Effect of Self-Shielding on Reactivity

5.3.1 Calculations in Spherical Geometry

To gain some preliminary understanding of how the various cross-section sets affect reactivity, one-dimensional spherical ANISN S_8 calculations in 26 groups were performed. The reactor geometry was such that its volume was equal to a typical 1000-MWe core and blanket; each region was individually described in the calculation. The oxide core was composed of two enrichment zones of equal volume, 12% Pu-239 in the inner and 17% Pu-239 in the outer. For the voided case, sodium was removed only from the central zone. Thus the formulation of the problem highly emphasized the positive spectral component of the sodium voiding effect with the result of underscoring changes due to the self-shielding representation. Table 5.6 summarizes the results. The reactivities resulting from voiding the central zone using the various self-shielding prescriptions are presented in Table 5.7 (where $\Delta k/k = (k_{out} - k_{in})/k_{out}$).

TABLE 5.6

Self-Shielding Effects in Spherical Geometry

Case	k
Infinite dilute, Na In:	0.99743
Na Out:	1.03889
Heterogeneous self-shielded, Na In:	1.09426
Na Out:	1.10253
Na Out (with Na In self-shielding):	1.10328
Homogeneous self-shielded, Na In:	1.08926
Na Out:	1.09732
Na Out (only σ_a self-shielded):	1.09097
Na Out (only σ_a self-shielded + Na In self-shielding):	1.09855

TABLE 5.7

Central Zone Sodium Voiding Reactivities

Case	Δk/k
Infinitely dilute:	+$12.56
Heterogeneous self-shielded:	+$ 2.51
Heterogeneous self-shielded (Na In self-shielding):	+$ 2.73
Homogeneous self-shielded:	+$ 2.44
Homogeneous self-shielded (Na In σ_a self-shielding):	+$ 2.30

N.B. $\beta \equiv 0.0033$

One should recognize that the comparisons in this chapter between infinite dilution results and various self-shielded results are all predicated on the assumption of a negligible contribution due to the spatial flux distribution effect. That is, the input for the ANISN and 2DB code calculations consists of tables of microscopic cross sections: either infinite dilution values, or the latter times the appropriate f-factor. Such a procedure is equivalent to Eq. (5.1) with all the region fluxes (ϕ_j) identical. When the spatial component of self-shielding (i.e., heterogeneous self-shielding) is factored into the calculation, it is done so by altering the value of the f-factor in Eq. (5.1). Thus, only energy self-shielding is the effect of interest in this chapter.

Several observations can be made based on the results of Table 5.7. First, infinite dilution cross sections underpredict the multiplication constant by up to 9%, and overpredict the central zone sodium voiding effect by \$10 compared to the self-shielded calculations. Second, the sophistication of the self-shielding model chosen has a relatively small effect upon the results of interest here. The crudest possible self-shielding model, homogeneous self-shielding of the absorption resonances only with no accounting made of the change in self-shielding upon voiding sodium, underpredicts the central zone sodium voiding effect by 20¢ and underpredicts the multiplication constant by less than 0.4% compared to the reference calculation (heterogeneous self-shielding with changes in self-shielding upon voiding). A detailed, homogeneously self-shielded calculation underpredicts the central zone sodium voiding effect by 7¢ and underpredicts the multiplication constant by less than 0.6%. Using the heterogeneously self-shielded constants from only the sodium-in case results in overpredictions of the central

zone sodium voiding effect by 22¢, and of the multiplication constant by less than 0.1%.

Although the theoretical justification for use of self-shielding corrections is clear, it is worthwhile to cite some pertinent experimental data which confirm that such corrections produce results in quantitative agreement with measurements in an LMFBR environment. Leung et al. [70] have demonstrated that a significant improvement in predicted activation traverses is obtained using self-shielded U-238 cross sections. A typical result of that work is presented in Figure 5.1.

Thus the following observation may be made: for the calculation of integral quantities, a nonrigorous variety of self-shielding models yield results reasonably close to those given by a detailed and realistic modelling, and all examined here were significant improvements upon the infinite dilution model.

The spherical geometry calculations were used to investigate one additional effect: the result of core size scale-up. That is, an extremely large core would require a relatively low enrichment with an attendant softer spectrum. In that case, the question arises as to how the increase in the weight of self-shielding effects due to the softer spectrum (i.e., more neutrons in the resonant groups) changes the sodium void reactivity. To investigate this point, ANISN calculations were performed for a 1000-cm radius bare core of a single enrichment zone of 9% Pu-239 in UO_2, with the inner half-volume being the voided region. Using infinite dilution cross sections, ANISN predicted a central region void reactivity of +$28.39 while the self-shielded set indicated +$9.65. Thus the positive sodium void effect does increase with core size, irrespective of the increase in self-shielding effects

Fig. 5.1 Effect of U-238 Self-Shielding on U(n, γ) Reaction Rate Calculations

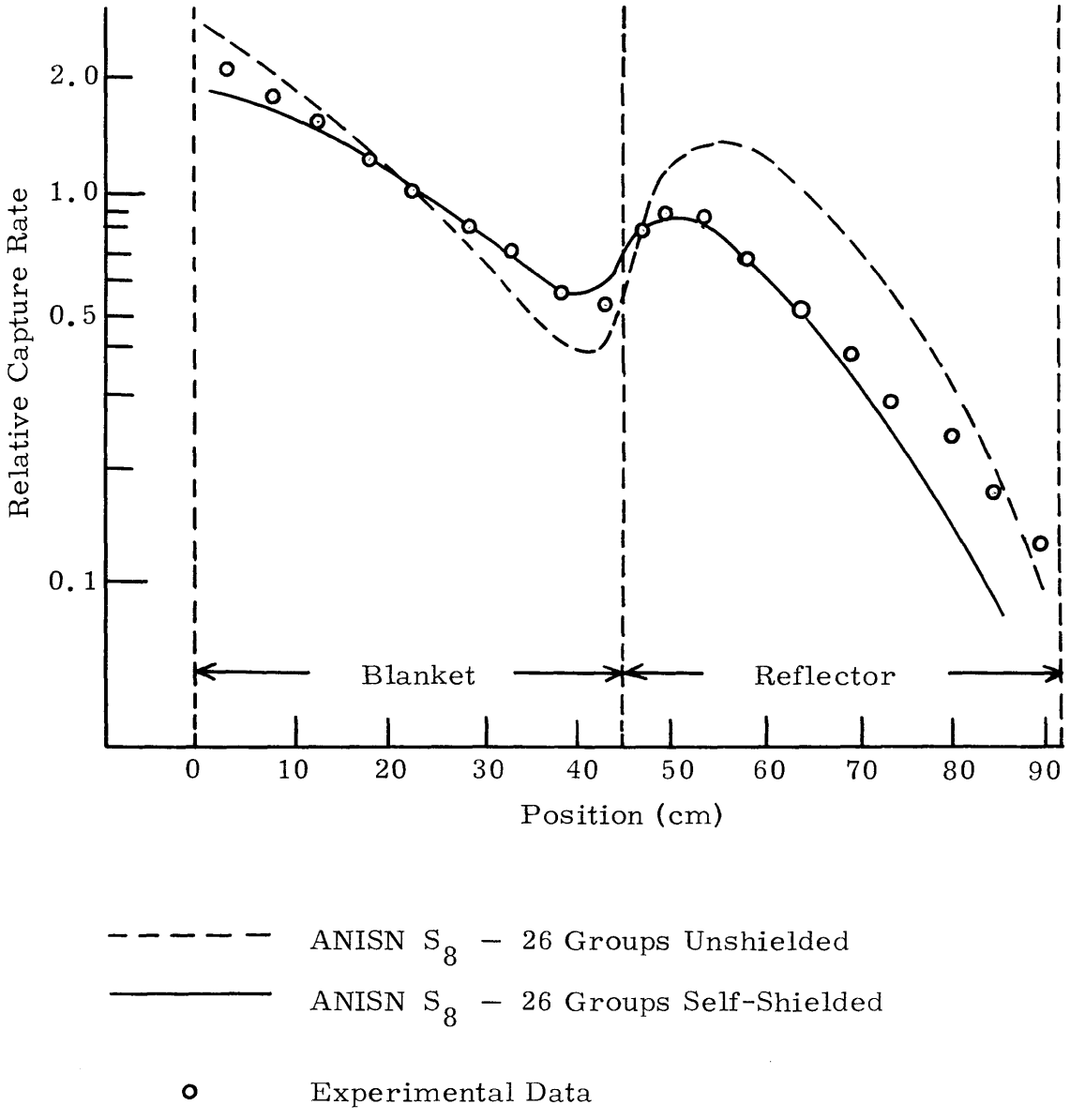

due to the softer spectrum. However, the infinite dilution calculations demonstrate a much greater positive effect than the self-shielded calculations, indicating that the increased self-shielding does indeed mitigate the positive void effect, but not to the point where any particular advantage of extremely large size is evidenced. It is useful to reiterate at this point that while the necessity for resonance self-shielding might appear self-evident, the early studies which caused such preoccupation with the sodium void effect [e.g., Reference 3], as well as some relatively recent ones [e.g., Reference 19], did not account for this important phenomenon.

In summarizing the spherical geometry calculations, one can make the following six observations:

1. Accounting for U-238 self-shielding reduces the inner-core voiding reactivity by \$10 compared to infinite dilution calculations.

2. Homogeneous self-shielding underestimates the inner-core voiding reactivity by 7¢ and the multiplication constant by 0.6% compared to heterogeneous self-shielding.

3. Using Na In self-shielding for the Na Out condition overestimates the inner-core voiding reactivity by 22¢.

4. Accounting only for U-238 σ_a self-shielding and ignoring self-shielding of elastic scattering resonances underestimates the inner-core voiding reactivity by 36¢.

5. Infinite dilution cross sections underestimate k_{eff} by up to 9%.

6. Increases in self-shielding in large, lower enrichment cores

are not sufficient to overcome increases in the positive sodium void effect due to the greater predominance of the positive spectral component.

5.3.2 Calculations in Cylindrical Geometry

One-dimensional calculations, discussed in the previous subsection, are a good guide for physical insight; however, they do not include the leakage from a core of realistic geometry in a rigorous manner. For this reason, 26-group 2DB calculations were performed in a realistic rz-geometry. The core examined was described by the parameters listed in Table 5.8.

TABLE 5.8
Reactor Description – 2DB Calculations

Core height:	76.2 cm
Core radius:	110.0 cm
Core central zone radius:	55.0 cm
Radial blanket thickness:	42.4 cm
Axial blanket thickness:	45.7 cm
Mesh points per core radius:	10
Mesh points per radial blanket thickness:	10
Mesh points per core half-height:	10
Mesh points per axial blanket thickness:	10
Unit cell radii (fuel pellet, clad, coolant boundary)	
Core:	0.2794 cm, 0.3175 cm, 0.45075 cm
Radial blanket:	0.6350 cm, 0.6858 cm, 0.75335 cm
Axial blanket:	0.2794 cm, 0.3175 cm, 0.45075 cm
Regionwise number densities ($10^{24}/cm^3$)	
U-238 (UO_2):	0.0218
Na (800° F):	0.0224
Fe:	0.0848

Two sets of enrichments were used: a two-zone core with 12%/16% Pu-239 for the infinite dilution calculations and a reduced enrichment core with 10.5%/14% Pu-239 for the self-shielded calculations, the latter being required because the first core was overenriched using the self-shielded set. Table 5.9 tabulates the multiplication constants for the cases considered.

Table 5.9
2DB Cylindrical Geometry Results

Case	k
12%/16% loadings	
Infinite dilute, Na In:	0.98632
Na Out:	1.00895
Central Na Out:	1.00042
Heterogeneous self-shielded, Na In:	1.07090
Na Out:	1.06125
10.5%/14% loadings	
Heterogeneous self-shielded, Na In:	1.00343
Na Out:	0.99180
Central Na Out:	1.00389
Homogeneous self-shielded, Na In:	1.00305
Na Out:	0.99214
Central Na Out:	1.00381

N.B. Na Out = sodium voided from whole core.
Central Na Out = sodium voided only from inner enrichment zone.

The self-shielded calculations utilized the self-shielded U-238 cross sections given by the results of MIDI in the homogeneous and heterogeneous options for the specific enrichments and sodium-in or

sodium-out condition; radial and axial blanket cells were treated in individual MIDI calculations since the respective blanket unit cells are dimensionally different. As found in the spherical geometry calculations, the infinite dilution calculations underestimate k_{eff} by about 8% or less; the homogeneously self-shielded results are reasonably close to the heterogeneously self-shielded multiplication constants which they underestimate by less than 0.04%. Thus the observations formulated in the last subsection are substantiated.

Table 5.10 presents the calculated sodium voiding reactivities for the 2DB rz-geometry study.

TABLE 5.10
Sodium Void Effects in Cylindrical Geometry

Case	$\Delta k/k$
12%/16% loadings:	
Infinite dilute, whole core	+$6.79
Infinite dilute, central zone	+$4.27
Heterogeneous self-shielded, whole core	-$2.75
10.5%/14% loadings:	
Heterogeneous self-shielded, whole core	-$3.55
Heterogeneous self-shielded, central zone	+$0.14
Homogeneous self-shielded, whole core	-$3.33
Homogeneous self-shielded, central zone	+$0.23

N.B. $\beta \equiv .0033$

Paralleling the spherical geometry calculations, the 2DB results in Table 5.10 indicate that self-shielding of U-238 absorption and scattering resonances decreases the whole-core sodium voiding

reactivity by approximately $10 compared to infinite dilution based calculations. The self-shielded calculations indicate a slight positive reactivity contribution in voiding the central zone (due to the predominance of the positive spectral component) which becomes significantly negative as the entire core is voided, in contrast to the infinite dilution calculation which predicts a large positive reactivity effect in voiding the whole core. The homogeneous representation of self-shielding is found to underestimate the whole-core reactivity change by 22¢ compared to the heterogeneous calculation (i.e., the difference due to using the heterogeneous or homogeneous options in MIDI). In general, the conclusions applicable to the spherical geometry calculations in the prior subsection remain valid for the cylindrical geometry results.

In conclusion, one notes that the heterogeneous model for self-shielding contributes relatively little to the sodium voiding reactivity: specifically, -22¢ in the above example. As such, it is somewhat larger than the heterogeneous effect of the spatial flux distribution. However, both effects would be outweighed by the effect of anisotropic diffusion discussed in earlier chapters (of the order of -$1. in reactivity). Most important, all three effects serve to decrease the positive reactivity contribution due to voiding sodium.

The calculations of sodium voiding effects have been necessarily approximate here, with some sacrifice of the spatial mesh representation (20 × 20) being made to perform the calculation in 26 groups. Additionally, it is well known that the void effect calculated is very sensitive to the cross-section set chosen and the core representation, which was greatly simplified here as consisting of only five elements (U-238, Pu-239, O, Fe, and Na) in a repeating unit cell structure.

Thus the results of Table 5.10 are not intended to be definitive calculations for the case at hand. The results are useful in the sense that conclusions may be made as to the relative importance of the self-shielding model chosen -- none, homogeneous, or heterogeneous. In summary, one may make three observations:

1. Infinite dilution calculations of multiplication constants, and particularly changes caused by voiding sodium, are to be treated with scepticism.

2. Homogeneously self-shielded calculations are sufficient for the calculation of multiplication constants to within about 0.04% and whole- or half-core sodium voiding to within approximately 25¢ of reactivity.

3. The importance of heterogeneous energy self-shielding effects in terms of the reactivity perturbation ranks in the middle of our trinity of effects: higher than the effects of spatial flux distributions and lower than the effects of anisotropic diffusion.

5.4 U-238 Self-Shielding Correlations

Prior work by Sheaffer et al. [71,72] has indicated that FBR spectra may be correlated against certain one-group spectral indices. Two spectrum characterization parameters are introduced:

$$S = \frac{\nu \Sigma_f}{\nu \Sigma_f + \xi \Sigma_{tr}} \tag{5.9}$$

$$R = \frac{\nu \Sigma_f}{\Sigma_r} , \tag{5.10}$$

where the constants are one-group values (Σ_r being the cross section

for removal of neutrons from above 1.4 MeV). These indices are used to correlate one-group microscopic cross sections in the form:

$$\sigma_j = \sigma_{0j} \chi^{g_j} , \tag{5.11}$$

where χ is the appropriate spectral index (R for the fission cross section of fertile material and S for all other cross sections). The correlation parameters σ_{0j} and g_j are tabulated by Sheaffer et al. for microscopic fission, absorption, and transport (the j variable) cross sections for most elements of interest. An iterative procedure is used to calculate the spectral indices: an initial guess is used to obtain the correlated one-group constants; the resulting constants are used in Eqs. (5.9) and (5.10) to calculate new spectral indices, which in turn are used to calculate new one-group constants. The iterative process has been shown to converge rapidly.

One should note that this is a homogeneous correlation in that all media of the same homogeneous composition have identical spectral indices. In addition, the Sheaffer correlations were obtained based on infinite dilution constants. The next two subsections develop both an extension of the one-group method which yields correlations for U-238 self-shielding factors and a modification of the one-group method to account for self-shielding effects. The results of the previous section which indicate that heterogeneous self-shielding effects change negligibly with geometry are invoked: the self-shielding correlations established here are all based on the standard core unit cell described in Table 5.8. The standard heterogeneous cell calculations yield correlations generally applicable to realistic FBR unit cells, being far closer to reality than a homogeneous treatment. The correlations

are offered with the caveat that they are applicable only to cylindrical geometry unit cells typical of an FBR -- in particular, they are not intended for slab geometry cells typical of critical assemblies where heterogeneous self-shielding effects are considerably larger [73].

5.4.1 Multi-Group Correlations

A correlation which yields group-by-group self-shielding factors represents a somewhat easier goal than a single group correlation since the self-shielding within a group can be expected to be a relatively slowly varying function of the correlation one has chosen. That is, when the core's composition is altered, the shape of the flux within a particular group changes relatively little although the overall spectrum may change greatly. On the other hand, a one-group correlation has to deal implicitly with changes in the full spectrum over which the collapsing is carried out. It is worthwhile to develop a group-by-group self-shielding correlation first to suggest what form the ultimate one-group self-shielding correlation might take.

One should note that the self-shielding correlations developed here are solely for U-238. A more detailed model would concern itself with self-shielding for the other constituent elements in the core as well as for control material. A more sophisticated analysis [25] for the significantly more heterogeneous slab lattice geometry indicates that self-shielding effects on the capture and fission cross sections of Pu-239 are large but of virtually equal and opposite sign with a negligible net effect; whereas sodium plus stainless steel self-shielding effects are counterbalanced by self-shielding effects of opposite sign in carbon, Pu-240, and other miscellaneous constituents. The overall effect in

terms of reactivity is found to be 96% of the effect calculated for U-238 self-shielding only. Thus the limitation here of applying self-shielding corrections to U-238 alone is a reasonably accurate one in the context of developing simple models.

The correlations presented here are essentially empirical in that their specific forms were established on a trial-and-error basis. Some suggestion of the appropriate form for the correlation function is provided by Reference 74, where the effective resonance integral is correlated against the ratio $N\sigma_0 \Gamma_a/\Gamma \Sigma_s$, where N is the number density of the resonant material and Γ_a the partial width for absorption. Sheaffer's work [71,72] also provided some inspiration. Various combinations of one-group constants were investigated to establish which grouping yielded a generally linear correlation of the group-by-group self-shielding factor. Figures 5.2 through 5.23 present the "best" (i.e., most smoothly fitted curve) correlation found: f_i versus $\Sigma_{ai}^{28}\left[\frac{1}{\Sigma_a} + \frac{1}{\xi\Sigma_{tr}}\right]$ where the constants within the brackets are the infinite dilution, one-group values for the core, while Σ_{ai}^{28} is the macroscopic absorption cross section for group i, for U-238. By definition, f_i is the self-shielding factor, the ratio of the self-shielded cross section to the infinite dilution cross section for group i. Σ_{ai}^{28} is the absorption cross section of U-238 alone, in group i, at infinite dilution; while the other constants are characteristic of the homogenized medium. All other combinations of one-group constants tested yielded widely scattered distributions of points.

Each point of Figures 5.2 through 5.23 represents one MIDI code calculation. The cases studied varied from 9% to 25% in enrichment (Pu-239 in UO_2), with variation in coolant-to-fuel volume ratios from

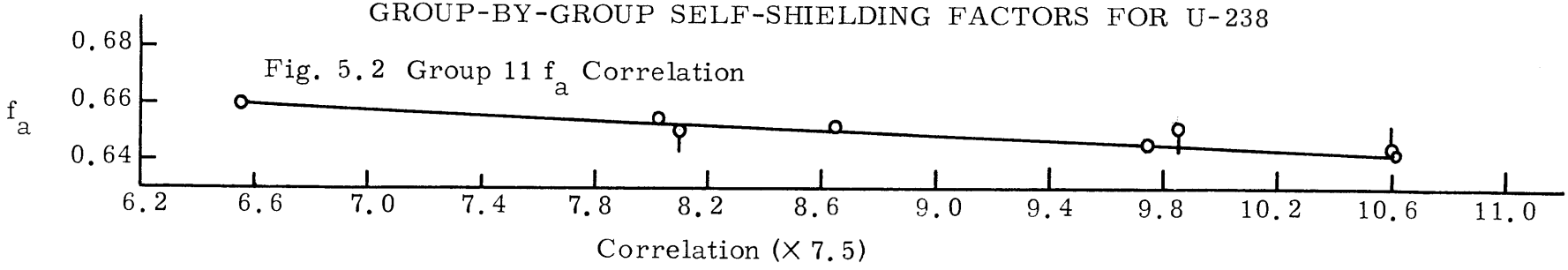

Fig. 5.2 Group 11 f_a Correlation

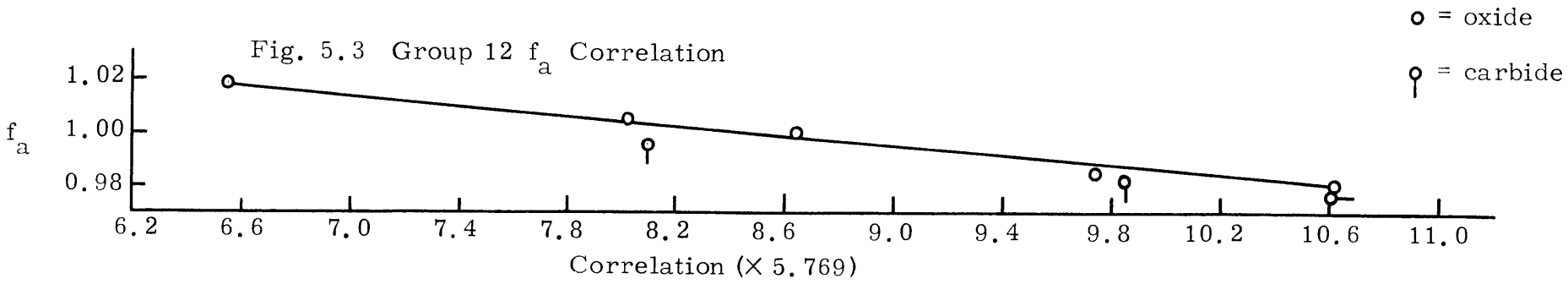

Fig. 5.3 Group 12 f_a Correlation

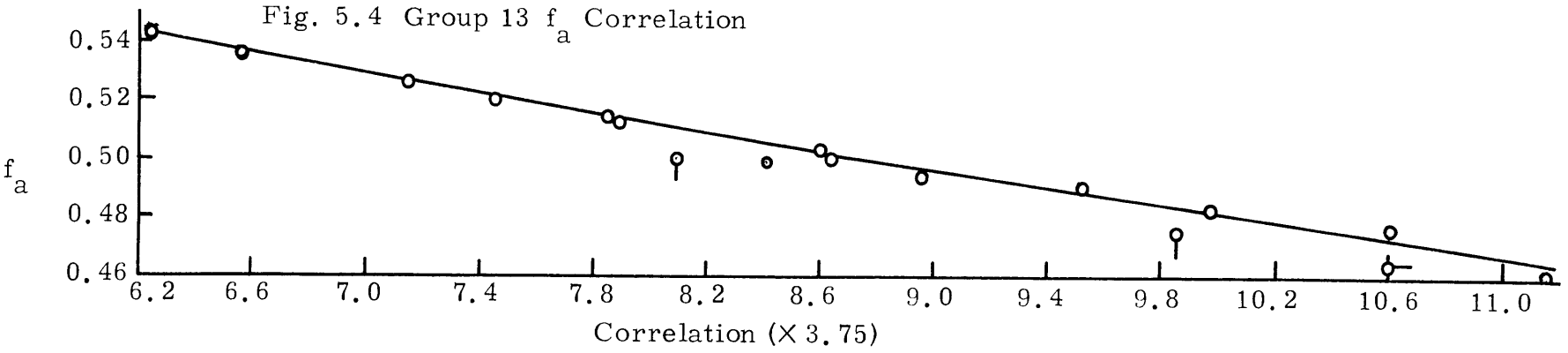

Fig. 5.4 Group 13 f_a Correlation

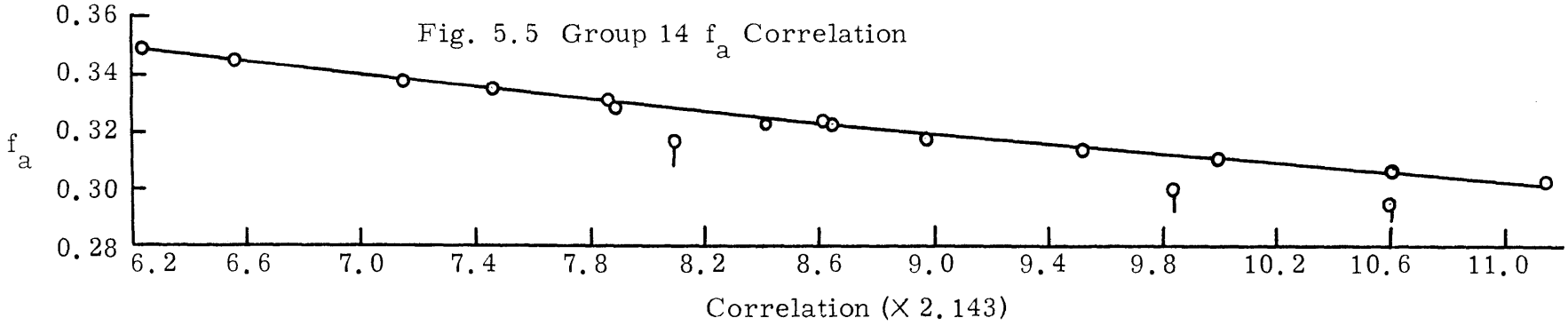

Fig. 5.5 Group 14 f_a Correlation

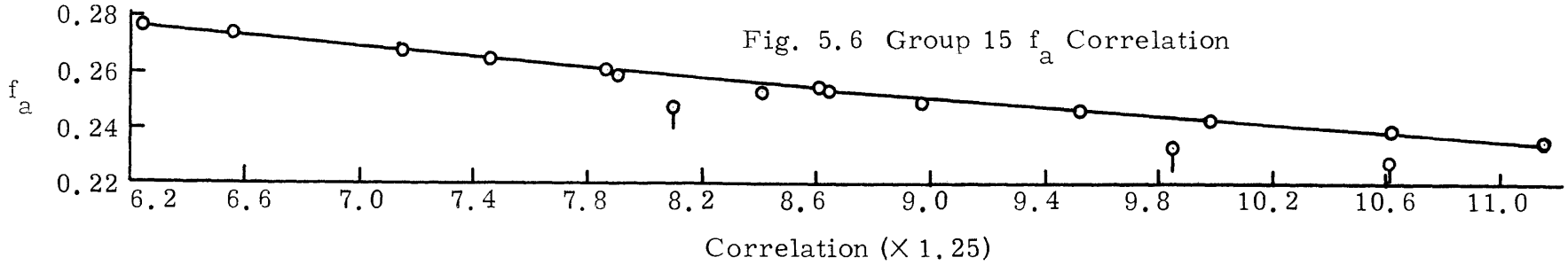

Fig. 5.6 Group 15 f_a Correlation

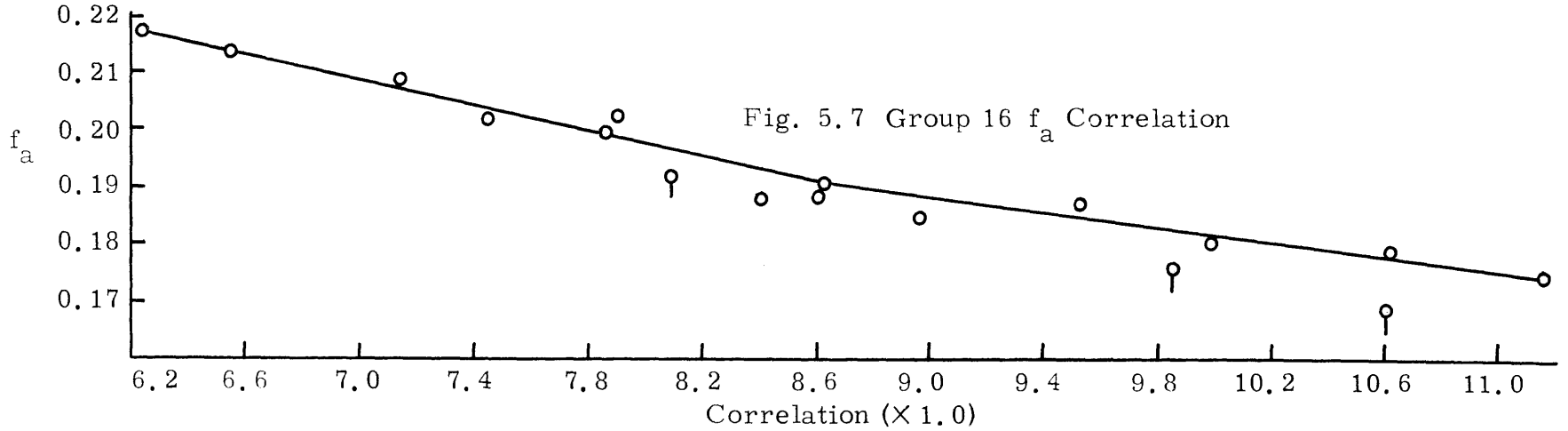

Fig. 5.7 Group 16 f_a Correlation

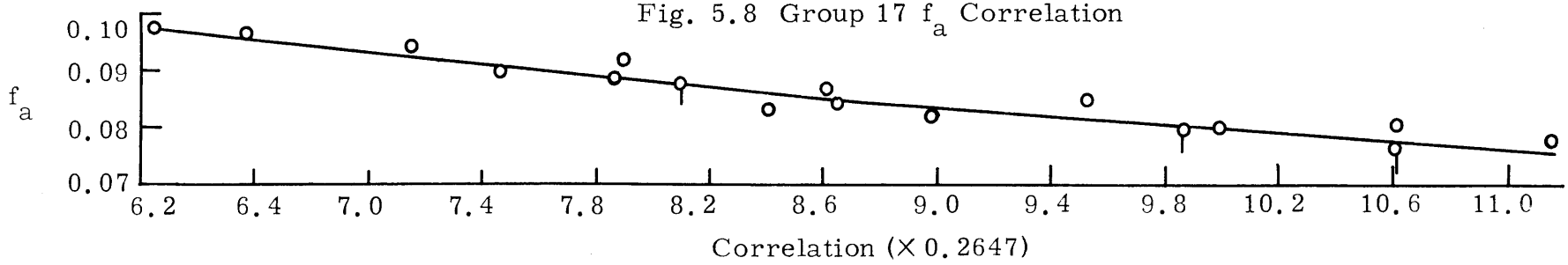

Fig. 5.8 Group 17 f_a Correlation

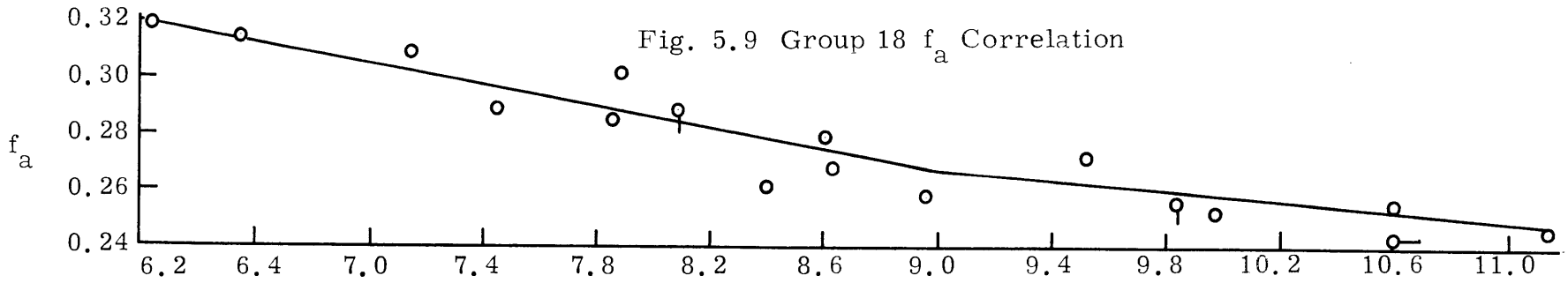

Fig. 5.9 Group 18 f_a Correlation

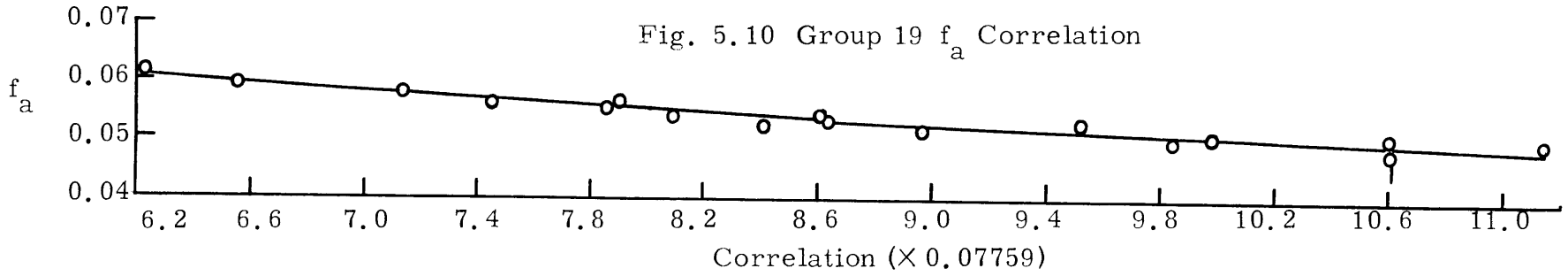

Fig. 5.10 Group 19 f_a Correlation

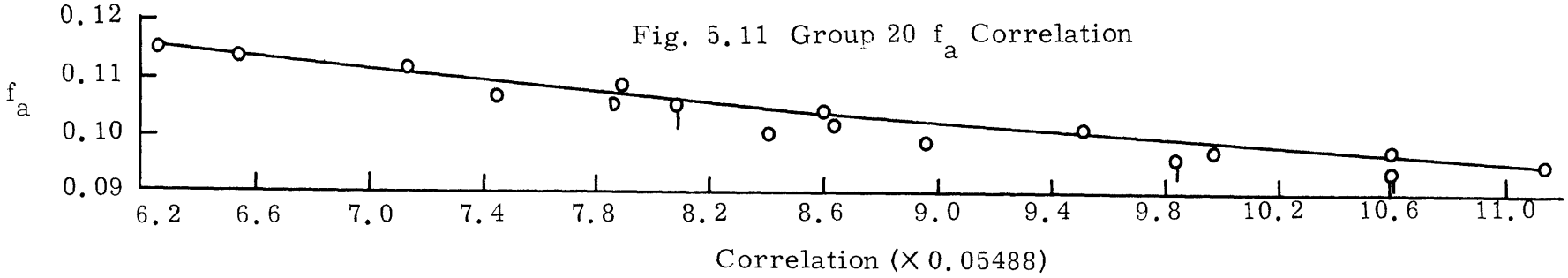

Fig. 5.11 Group 20 f_a Correlation

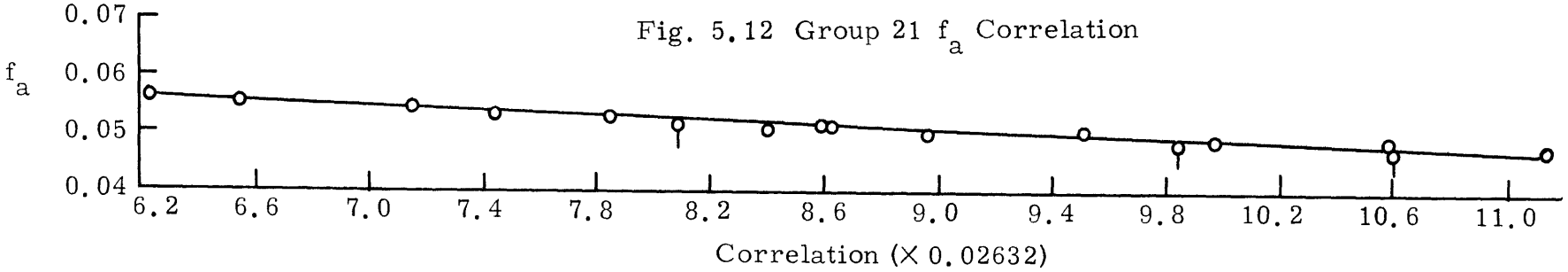

Fig. 5.12 Group 21 f_a Correlation

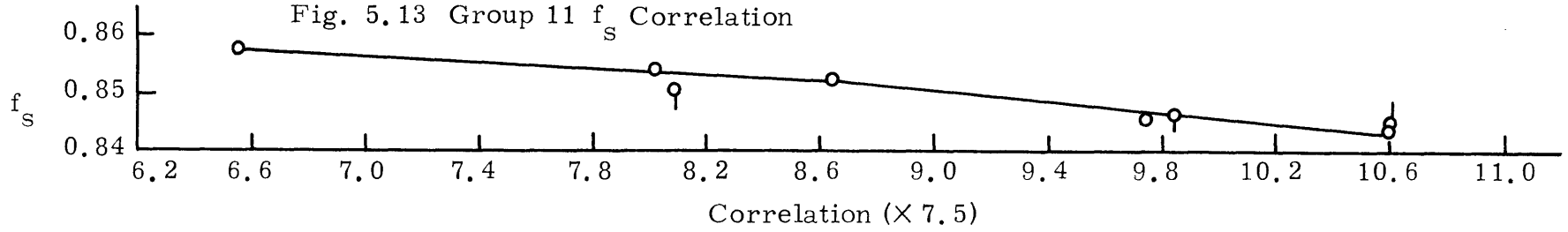

Fig. 5.13 Group 11 f_s Correlation

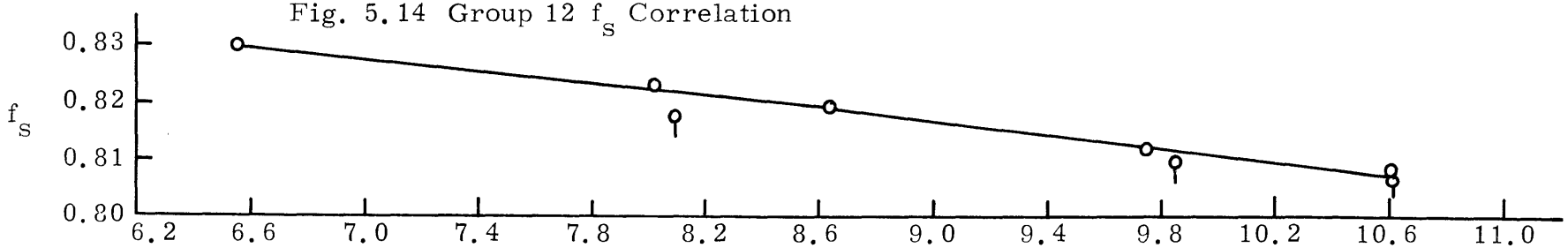

Fig. 5.14 Group 12 f_s Correlation

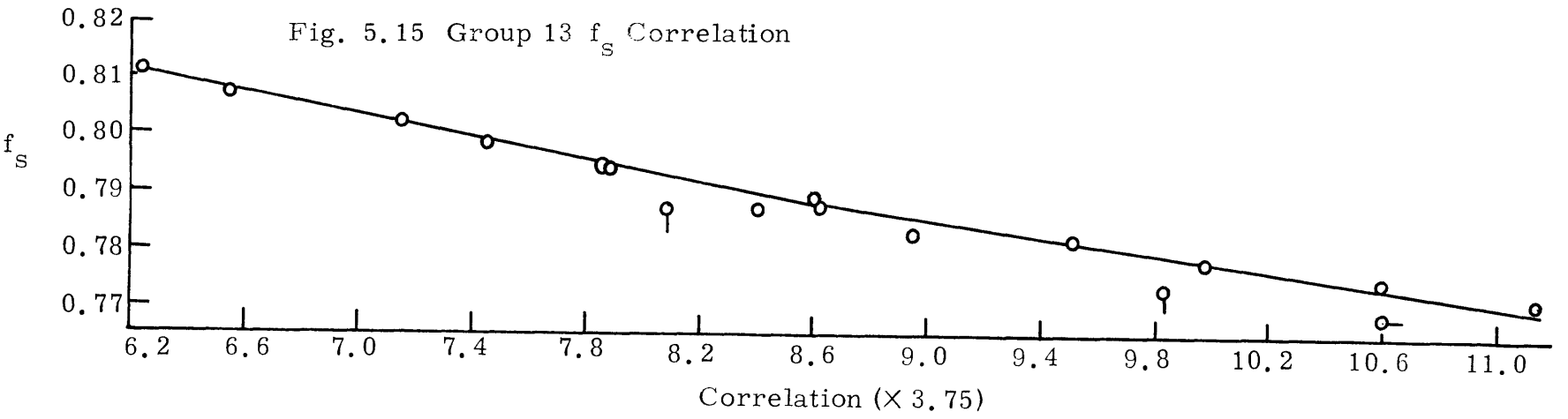

Fig. 5.15 Group 13 f_s Correlation

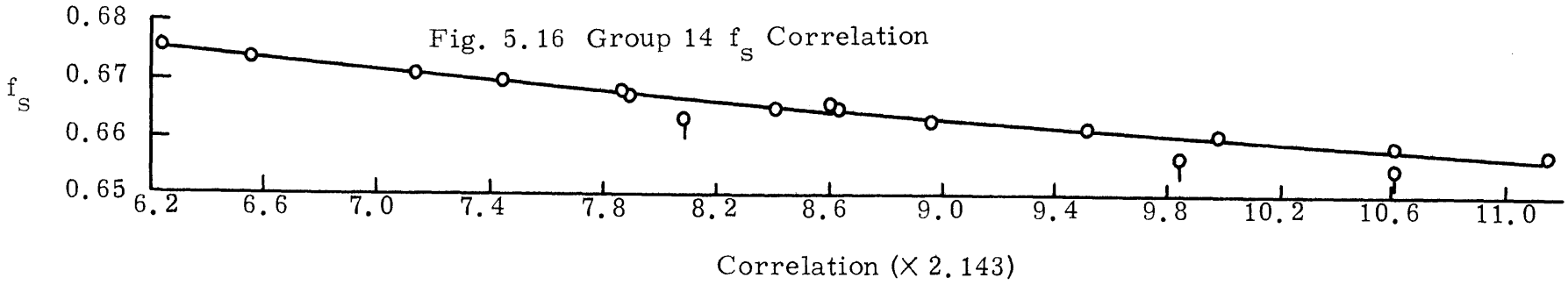

Fig. 5.16 Group 14 f_s Correlation

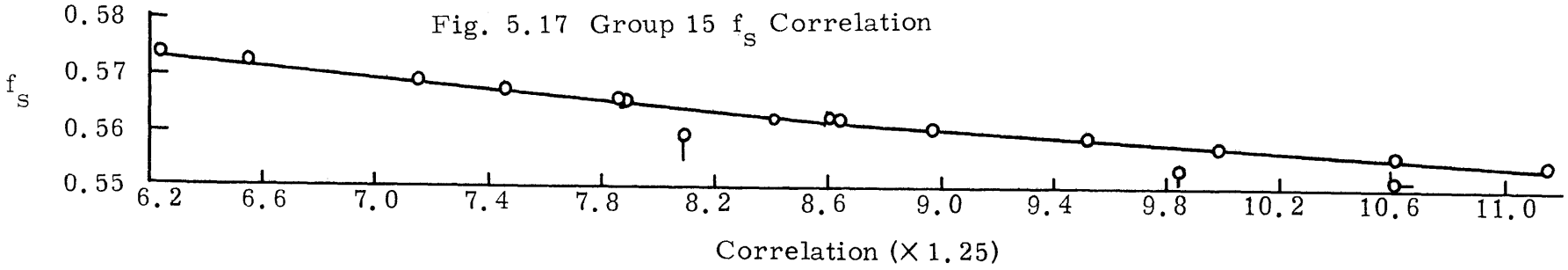

Fig. 5.17 Group 15 f_s Correlation

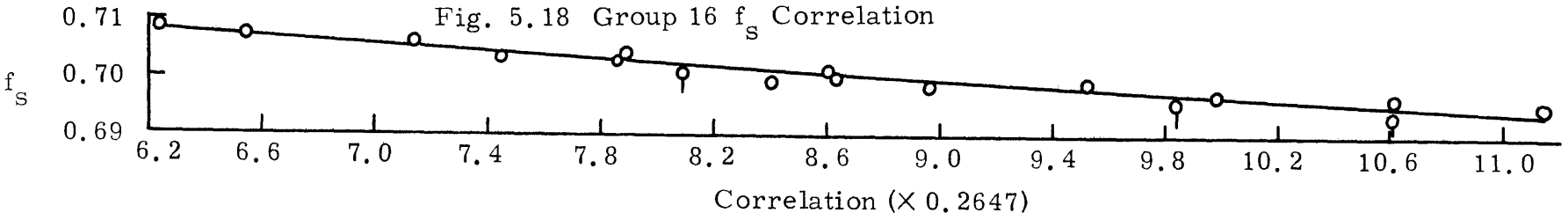

Fig. 5.18 Group 16 f_s Correlation

Fig. 5.19 Group 17 f_s Correlation

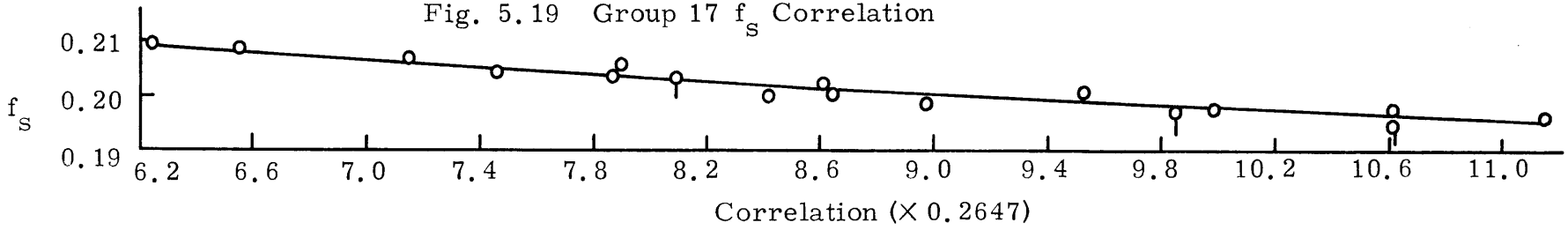

Fig. 5.20 Group 18 f_s Correlation

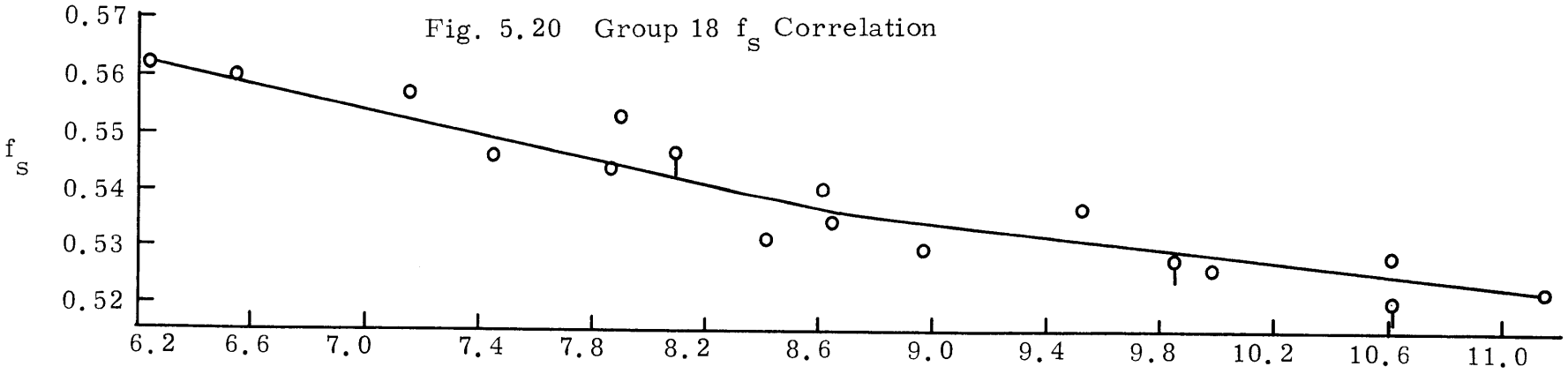

Fig. 5.21 Group 19 f_s Correlation

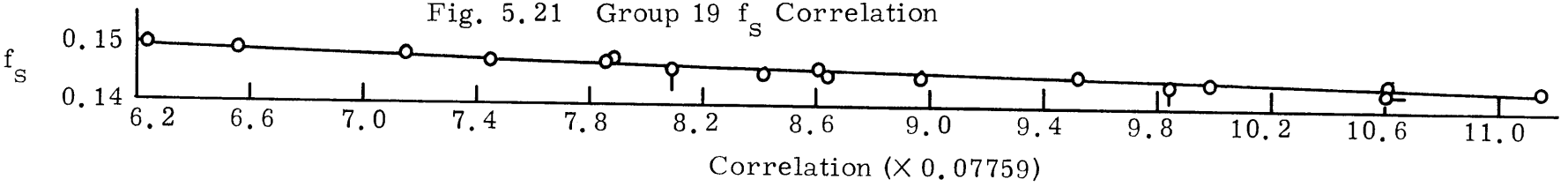

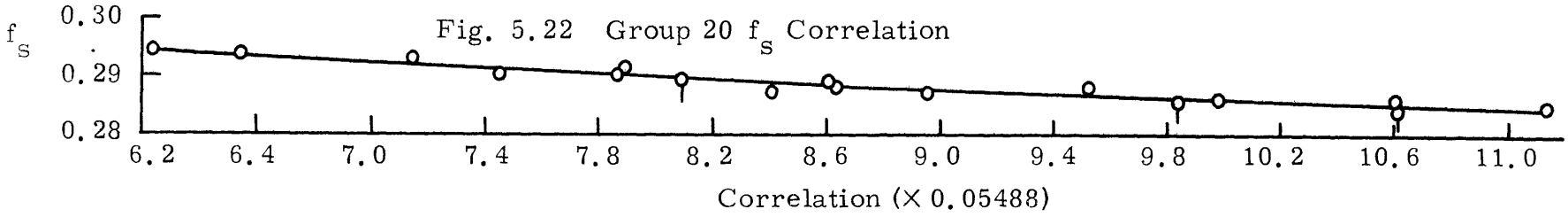

Fig. 5.22 Group 20 f_s Correlation

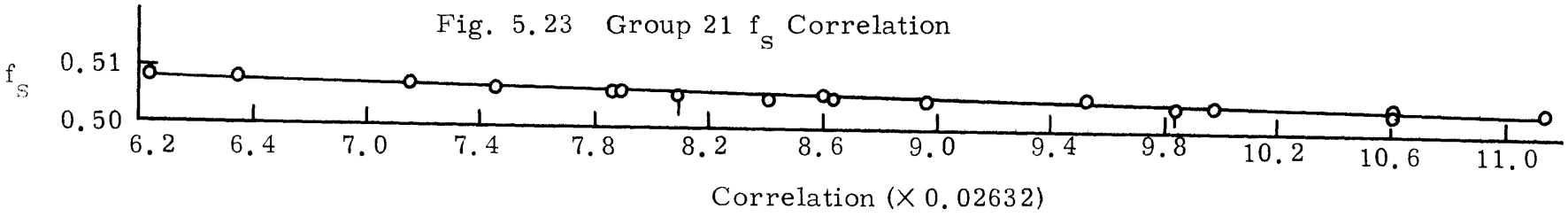

Fig. 5.23 Group 21 f_s Correlation

1.0 to 2.0. In addition to the oxide-fueled cases, three carbide-fueled cells were investigated, whose results indicate correlated curves parallel to but displaced slightly from the oxide curves.

The carbide cell datum points are identified in Figures 5.2 through 5.25 by a bar through the point. The difference between the carbide and oxide cells is ascribed to the small differences between the oxygen and carbon scattering cross sections (carbon being generally larger while lacking a resonance in group 5) as well as the density difference between the two fuel types (the U-238 in the carbide being more dense than in the oxide by a factor of 1.35). Similar comments apply to the one-group correlation presented in the next subsection. The correlation can be used for both cases without significant error.

The correlations presented here permit one to look up the group-by-group self-shielding factors for the 26-group ABBN set in a direct manner. One need only calculate the spectral indices characteristic of the medium to calculate the correlation's abscissa value which immediately yields the value of the self-shielding factor.

5.4.2 One-Group Correlations

One-group correlations were investigated by collapsing 26-group ABBN sets (incorporating U-238 self-shielding corrections from MIDI) down to one-group using the ANISN code for a critical spherical geometry. As before, a trial-and-error procedure was employed to establish the best (i.e., smoothest linear curve) correlation. Starting from the correlation established for the group-by-group self-shielding factor, one finds that an additional parameter is required for the correlation, as well as a slightly different function for the scattering cross section

f-factor. The two self-shielding correlations established were:

$$f_a \text{ vs. } \Sigma_a^{28}\left[\frac{1}{\Sigma_a} + \frac{a}{\xi\Sigma_{tr}}\right]$$

and

$$f_s \text{ vs. } \Sigma_a^{28}\left[\frac{1}{\nu\Sigma_f} + \frac{b}{\xi\Sigma_{tr}}\right],$$

where a = -1.40 and b = -1.00. The linearity of the resulting fit is quite sensitive to the values of a and b: for example, a = -1.42 and b = -0.95 cause significant departures from a straight line fit (i.e., kinks appear in the correlation curves). As for the group-by-group case, the correlations are entirely empirical. Figures 5.24 and 5.25 present the one-group correlations established here. Table 5.11 presents the best linear fits representing the correlation.

The one-group correlations which appear here are semi-heterogeneous in the sense that the self-shielded cross sections were obtained by MIDI calculations for a standard heterogeneous cell: fuel pellet diameter = 0.5588 cm, pitch = 0.8585 cm. As shown previously, the differences in the calculated k_{eff} and sodium void reactivity between using homogeneously and heterogeneously self-shielded cross sections are fairly small (0.04% and 25¢, respectively). Thus the result using the standard heterogeneous correlations should be virtually identical to a detailed heterogeneous calculation for any reasonable cell geometry.

5.4.3 A Self-Shielded One-Group Method

With the above correlations available, the one-group model of Sheaffer et al. [71] may be modified to take the heterogeneous self-shielding of U-238 into account. One first calculates the S and R

TABLE 5.11

One-Group U-238 Self-Shielding Correlations

Self-shielding factor	Correlation χ
f_a = absorption self-shielding	$\Sigma_a^{28}\left[\frac{1}{\Sigma_a} - \frac{1.40}{\xi\Sigma_{re}}\right]$
f_s = scattering self-shielding	$\Sigma_a^{28}\left[\frac{1}{\nu\Sigma_f} - \frac{1.00}{\xi\Sigma_{tr}}\right]$

Correlation constants: $f = m\chi + b$

	χ	m	b
f_a:			
	$\chi \leq 0.1406$	-0.6456	0.9399
	$\chi > 0.1406$	-0.5232	0.9227
f_s:			
	$\chi \leq 0.06063$	-0.1490	0.9743
	$0.06063 < \chi \leq 0.07445$	-0.1158	0.9723
	$\chi > 0.07445$	-0.1269	0.9732

N.B. The above fits are for oxide cores. For carbide cores, the following corrections are applied:

-0.030 for f_a and -0.004 for f_s.

spectral indices for the infinite dilution representation, from which the abscissa values of Figures 5.24 and 5.25 may be calculated. This yields directly the f_a and f_s self-shielding factors for U-238.

For the remainder of the calculation, the cross sections of U-238 remain fixed at their infinite dilution values multiplied by the

Fig. 5.24 One-Group Correlation – Absorption

U-238 f_a vs. $\Sigma_a^{28}\left[\frac{1}{\Sigma_a} - \frac{1.40}{\xi\Sigma_{tr}}\right]$

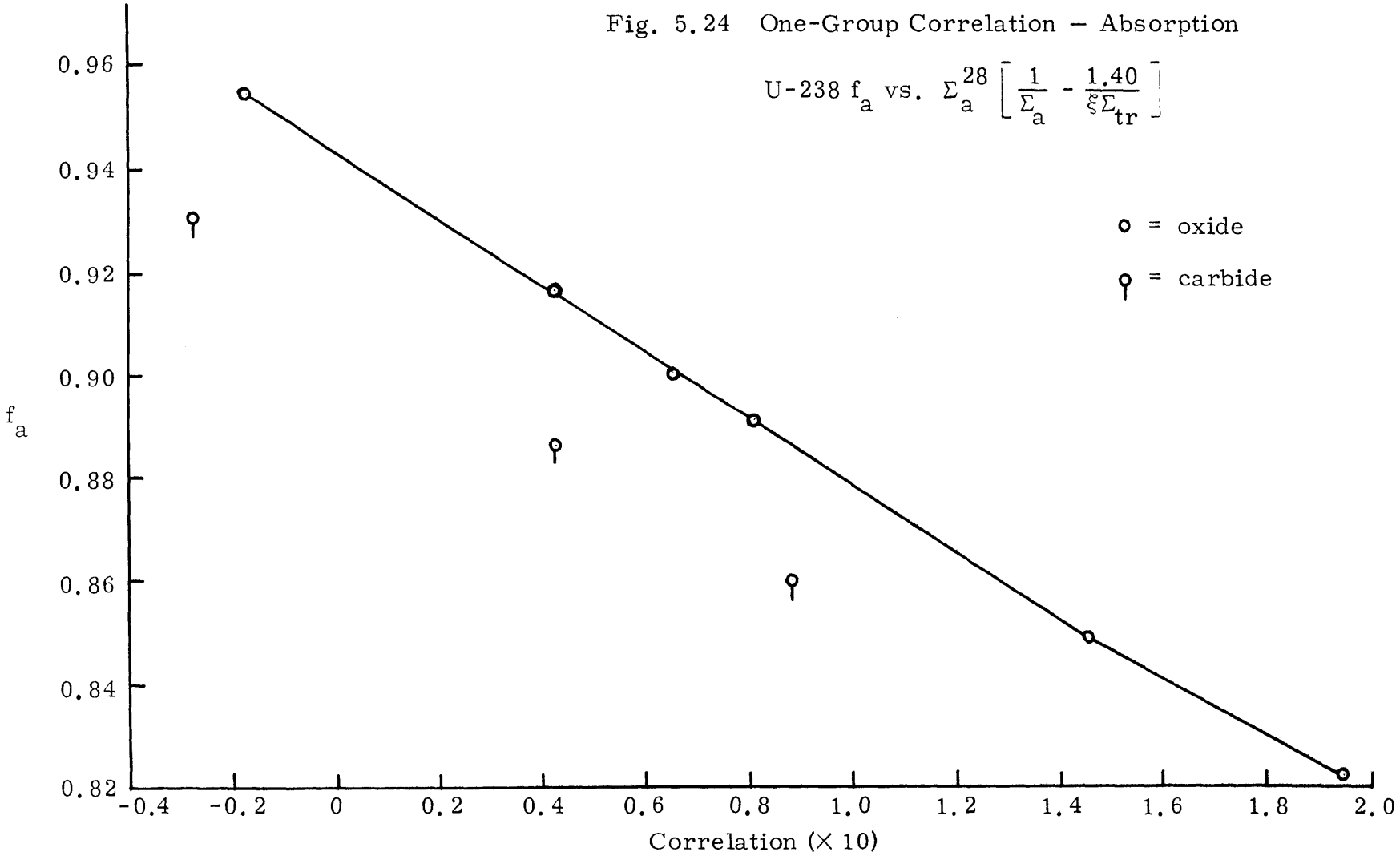

Fig. 5.25 One-Group Correlation – Scattering

U-238 f_s vs. $\Sigma_a^{28}\left[\frac{1}{\nu\Sigma_f} - \frac{1.0}{\xi\Sigma_{tr}}\right]$

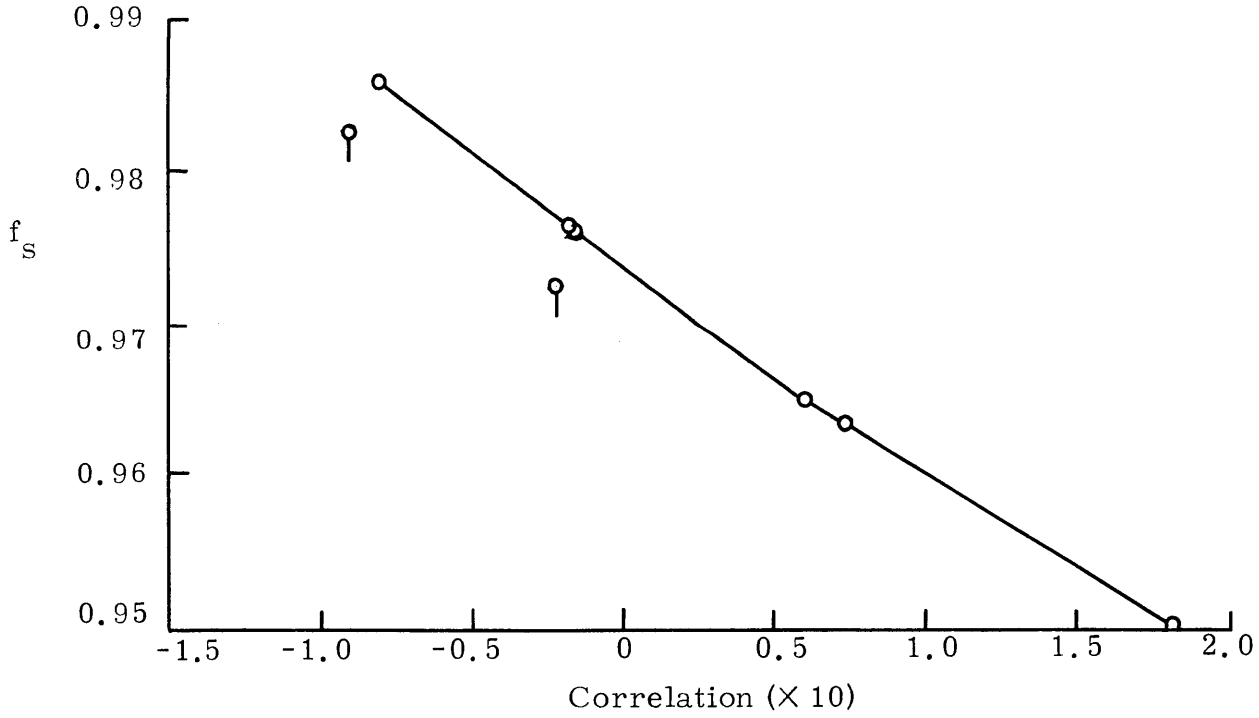

appropriate f-factors. The self-shielded U-238 constants are then employed in the calculation of new spectral indices; the same iterative procedure is used to calculate the new indices, except that only the non-U-238 cross sections are affected by the varying indices during the iterations. Upon convergence, one has new values for S and R which reflect the altered values of all other cross sections due to the changed spectrum as well as the correlated, self-shielded cross sections of U-238. Figure 5.26 summarizes the procedure in block diagram form. The procedure has been coded into a minor program (see Appendix E.3).

The above self-shielding correlations were obtained for 300° K conditions. Sheaffer et al. have correlated the temperature change in σ_a for U-238 against the spectral index S. The following quadratic relations were established:

$$\text{for } T = 300°\,K \rightarrow T = 900°\,K: \quad \Delta\sigma_a = .0351 - .0888S + .0580S^2 \quad (5.12)$$

$$\text{for } T = 900°\,K \rightarrow T = 2100°\,K: \quad \Delta\sigma_a = .0238 - .0556S + .0335S^2 \quad (5.13)$$

The temperature correlation was checked here by performing MIDI calculations for 300° K, 900° K, and 2100° K, and using ANISN to collapse the temperature-corrected, self-shielded cross sections to a single group. The self-shielded, one-group method yielded the spectral index S = 0.3468 for the 12% Pu-239 enriched oxide core. Table 5.12 compares the changes in the cross sections predicted by the correlation to those obtained by MIDI and ANISN. The agreement is quite good. It implies that the methods used in the MIDI code are consistent with the ABBN f-factor technique which formed the basis of the correlation.

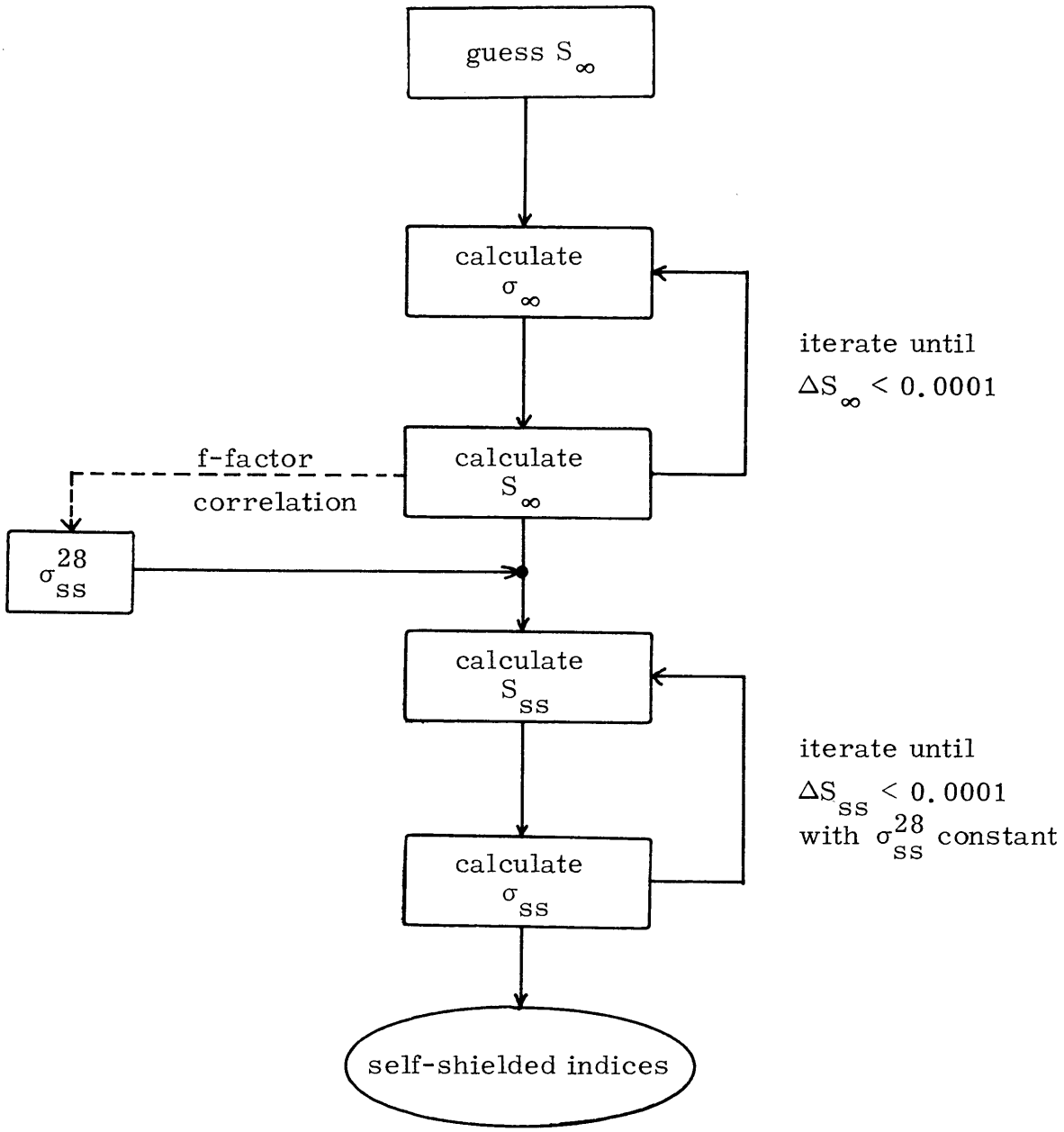

N.B. ∞ = infinite dilution values

ss = self-shielded values

Fig. 5.26 Calculation of Self-Shielded Spectral Indices

TABLE 5.12
Temperature Corrections

ΔT	$\Delta\sigma_a$ (barns)	
	Correlation	MIDI + ANISN
300° K - 900° K	0.0113	0.0112
900° K - 2100° K	0.0085	0.0092

The one-group scattering cross section changes with temperature as well. No correlation for its behavior is available; however, the following prescriptions were established:

$$\Delta\sigma_s \cong 9.6 * \Delta\sigma_a \quad (300° K - 900° K)$$

$$\Delta\sigma_s \cong 5.4 * \Delta\sigma_a \quad (900° K - 2100° K)$$

As shown by Tables 5.6 and 5.7, completely neglecting the self-shielding of the scattering cross section leads to errors in k_{eff} of 0.6% and in the half-core sodium voiding effect of 36¢. This suggests that accounting for self-shielding at 300° K and correcting for temperature changes by the above prescriptions should result in a negligible error.

As a final check upon the validity of the one-group method as modified to account for self-shielding, several parallel ANISN-collapsed calculations were performed. Some results of that comparison are given in Table 5.13. The self-shielded model predicts k_∞ approximately as well as, or better than, the original correlation predicts the infinite dilution k_∞. Considering the self-shielded ANISN calculation as the reference standard, the infinite dilution one-group model consistently underpredicts k_∞; while the self-shielded one-group model generally overpredicts k_∞, but with a much smaller absolute error.

TABLE 5.13

One-Group Models vs. ANISN

	Infinite Dilution		Self-Shielded	
	Correlation	ANISN	Correlation	ANISN
12% Core (Na In)				
Σ_a (cm^{-1})	0.005343	0.005266	0.004844	0.004881
$\nu\Sigma_f$ (cm^{-1})	0.006670	0.006271	0.006651	0.006700
k_∞	1.248	1.191	1.373	1.373
25% Core (Na In)				
Σ_a	0.006452	0.006229	0.006270	0.006119
$\nu\Sigma_f$	0.01257	0.01197	0.01256	0.01210
k_∞	1.948	1.922	2.003	1.977
16% Core (Na In)				
Σ_a	0.005594	0.005466	0.005246	0.005311
$\nu\Sigma_f$	0.008541	0.008054	0.008528	0.008340
k_∞	1.527	1.473	1.626	1.570
16% Core (Na Out)				
Σ_a	0.005114	0.004839	0.004940	0.004730
$\nu\Sigma_f$	0.008451	0.007930	0.008440	0.008005
k_∞	1.653	1.639	1.709	1.692

Thus one can conclude that the self-shielding modification does permit the one-group method to deal with physically more realistic systems.

5.5 Conclusions

Comparative multi-group calculations using infinite dilution and self-shielded U-238 cross sections have demonstrated that major errors in k_{eff} and sodium void reactivity result if resonance self-shielding is neglected. Homogeneous resonance self-shielding has been shown to be the major effect, with heterogeneous resonance self-shielding a lesser added correction. The heterogeneous resonance self-shielding of a standard FBR cell geometry is well described by a correlation of one-group f-factors against specific functions of one-group cross sections at infinite dilution. A technique has been presented whereby a one-group method may be modified to account for heterogeneous resonance self-shielding of U-238.

Chapter 6

HETEROGENEOUS EFFECTS IN REFERENCE FBR DESIGNS

In the first five chapters, the formalism required for the calculation of heterogeneous effects has been developed. In this chapter, various reference fast breeder designs will be examined for the occurrence of significant heterogeneous reactivity effects. Parametric studies varying rod pitch, enrichment, and clad thickness are discussed. Heterogeneous effects in blankets are discussed in the following chapter.

6.1 1000-MWe LMFBR Designs

Table 6.1 presents the core parameters of interest for four 1000-MWe LMFBR designs [75], while Table 6.2 summarizes the unit cell descriptions used in the DELKHET code calculations for the four reference designs.

TABLE 6.1
1000-MWe LMFBR Core Parameters [75]

	AI	B & W	GE	CE
Core height (in.)	42.8	34.7	30.0	24.0
L/D	0.42	0.29	0.308	0.225
Fuel material	PuO_2-UO_2	PuO_2-UO_2	PuO_2-UO_2	PuC-UC
Enrichment (at. %)	10.5/13.1	10.4/11.2/13.0	10.73/13.45	9.78/11.79
Fuel density (%TD)	85	85	85	–
Fuel pin OD (in.)	0.30	0.28	0.25	0.40
Pitch (in.)	0.363	0.337	0.300	0.451
Clad thickness (in.)	0.0175	0.010	0.010	0.011
Na Void Reactivity (whole core)	$8.07	$7.50	–	$3.82

TABLE 6.2

DELKHET Description of Reference Cores

	AI	B & W	GE	CE
Core height (cm)	108.7	88.1	76.2	61.0
Core radius (cm)	129.4	152.0	123.7	135.5
Unit cell radii (cm):				
r_1	0.3366	0.3302	0.2921	0.4801
r_2	0.3810	0.3556	0.3175	0.5080
r_3	0.4841	0.4494	0.4001	0.6015
Average enrichment (at. %)	11.8	11.5	12.1	10.8
Regionwise number densities:				
Pu-239	0.002435	0.002373	0.002497	0.002976
U-238	0.018199	0.018260	0.018138	0.024576
O(C)	0.041267	0.041265	0.041269	(0.027551)
Na	0.0224	0.0224	0.0224	0.0224
Fe	0.0848	0.0848	0.0848	0.0848

The cell description is approximate in that the clad is represented as pure iron, while the fuel has only two heavy element constituents, U-238 and Pu-239. Multi-enrichment zones are represented by a single average enrichment. In addition, the core is represented as a collection of unit cells only; thus structural material, such as subassembly duct walls, is unaccounted for in the DELKHET treatment.

The equivalent bare core model requires the calculation of a reflector savings for the blanket regions [76]. An initial guess for the blanket savings is calculated from:

$$\delta = \frac{D_c}{D_r}\sqrt{\frac{D_r}{\Sigma'_{ar}}}\ , \qquad (6.1)$$

where "r" refers to the blanket constants and "c" to the core, and $\Sigma'_{ar} \equiv \Sigma_{ar} - \nu\Sigma_{fr}$. Table 6.3 presents the standard blanket constants assumed for all four designs. Note that the constants are sensitive to the absence or presence of sodium in the core, as well as being different for axial or radial blankets due to the greater volume fraction of U-238 in the radial blanket. Thus Eq. (6.1) yields four values of blanket savings: radial and axial, for the sodium-in and sodium-out conditions.

TABLE 6.3
Blanket Constants for Analyses

		Radial Blanket	Axial Blanket
Na In Core			
	D_r (cm)	1.0877	1.4740
	Σ_{ar} (cm^{-1})	0.0068660	0.0042081
Na Out Core			
	D_r (cm)	1.1058	1.4580
	Σ_{ar} (cm^{-1})	0.0065542	0.0039745

To arrive at a consistent blanket savings (i.e., one which gives a critical core geometry identical to the design parameters), the following iterative procedure was adopted. The savings ratio ξ is defined:

$$\xi = \frac{\delta_r}{\delta_z} , \tag{6.2}$$

which is the ratio of radial to axial savings calculated from Eq. (6.1) using constants from Table 6.3. Then the consistent axial savings δ'_z is calculated from:

$$B^2 = \left(\frac{2.4048}{R + \xi\delta'_z}\right)^2 + \left(\frac{3.1416}{H + 2\delta'_z}\right)^2 , \tag{6.3}$$

where B^2 is the known total critical buckling, R and H are the core dimensions given in Table 6.2. Once the unknown consistent axial savings δ'_z has been found, the consistent radial savings is $\delta'_r = \xi\delta'_z$. For example, the initial blanket savings for the G.E. core (sodium-in) were calculated to be $\delta_r = 16.0$ cm and $\delta_z = 17.6$ cm, while the consistent blanket savings were found to be $\delta'_r = 11.1$ cm and $\delta'_z = 12.2$ cm. The sodium-out savings are calculated from the voided savings ratio η:

$$\eta = \frac{(\delta_r)_{\text{Na Out}}}{(\delta_r)_{\text{Na In}}} , \tag{6.4}$$

which is calculated using Eq. (6.1) and Table 6.3. Next, the consistent sodium-out savings are calculated from $(\delta'_r)_{\text{Na Out}} = \eta(\delta'_r)_{\text{Na In}}$ and $(\delta'_z)_{\text{Na Out}} = (\eta/\xi)(\delta'_r)_{\text{Na Out}}$. The end result for the sodium-in case is a total buckling identical to the critical buckling, which is divided axially and radially in a consistent manner; as well as buckling values for the sodium-out state which correctly account for the increase in blanket savings for a voided core. In a sense, the reflector savings obtained by these procedures are artificial quantities: they are the required reflector savings for $k = 1.0$ with the given core geometry and the given two-group cross-section set. (In fact, the initial blanket savings guess for the carbide core utilized oxide reflector constants). However, the procedures established ensure that the ratio of the axial leakage decrement (due to axial blanket savings) to the radial leakage decrement (due to radial blanket savings) is correctly preserved.

Table 6.4 summarizes the DELKHET code results for the four reference cores.

TABLE 6.4
Heterogeneous Effects in 1000-MWe Designs
(cents* of reactivity – exclusive of self-shielding)

	AI	B & W	GE	CE
Na In				
Spatial	5.8	3.6	3.5	3.1
Ani. Diff.	-31.9	-33.1	-31.5	-33.5
Net	-26.1	-29.5	-28.0	-30.5
Na Out				
Spatial	3.6	1.2	1.2	2.0
Ani. Diff.	-95.7	-98.0	-88.7	-84.1
Net	-92.1	-96.8	-87.5	-82.2
Net Void Effect	-66.0	-67.3	-59.5	-51.7

*β = 0.0033 for oxide cores (AI, B & W, GE)
β = 0.0040 for carbide core (CE)

The results in Table 6.4 have been divided into two classes: those contributions due to anisotropic diffusion, and those due to spatial flux variation in the unit cell. Anisotropic diffusion is clearly the dominating heterogeneous effect. The heterogeneous contribution of resonance self-shielding was not calculated for each reference design since, as shown in Chapter 5, a typical heterogeneous geometry (as given in Table 5.9) characterizes the range of FBR designs quite well as far as heterogeneous effects on the multiplication constant are concerned. The results of Chapter 5 demonstrate that for a typical FBR configuration,

the heterogeneous resonance self-shielding contribution is +11.5¢ for the sodium-in condition and +2.4¢ for the sodium-out condition, with a net sodium void effect of -9.1¢, which may be added to the results of Table 6.4 to assess the totality of effects considered in this work. The original homogeneous results for the whole-core voiding reactivity are given in Table 6.1.

Thus all three heterogeneous effects, resonance self-shielding, flux shape, and anisotropic diffusion, reduce the magnitude of the whole-core sodium void reactivity. Anisotropic diffusion does so by creating a negative heterogeneous contribution to the sodium-in case and a still larger negative contribution to the sodium-out case, while the other two effects create a positive heterogeneous contribution for the sodium-in case and a lesser positive contribution for the sodium-out case; the net effect is a reduced voided reactivity. Figure 6.1 illustrates the trends at work.

In Chapter 4, sample calculations were presented, ranking the importance of various heterogeneous contributions: those results suggest an anisotropic diffusion contribution somewhat larger than the ones calculated for the four reference designs. In part, this difference is due to the larger lattice pitch in the illustrative case of Chapter 4 (this effect is discussed further in Section 5.3). However, part of the difference is due to the treatment of blanket savings. In Chapter 4, identical blanket savings were assumed for the sodium-in and sodium-out cases, while the calculations for the reference designs discussed in this chapter include the blanket savings more systematically. It is of interest to perform the calculation for the G.E. design (a 15% enrichment case) using both options: accounting for the increase

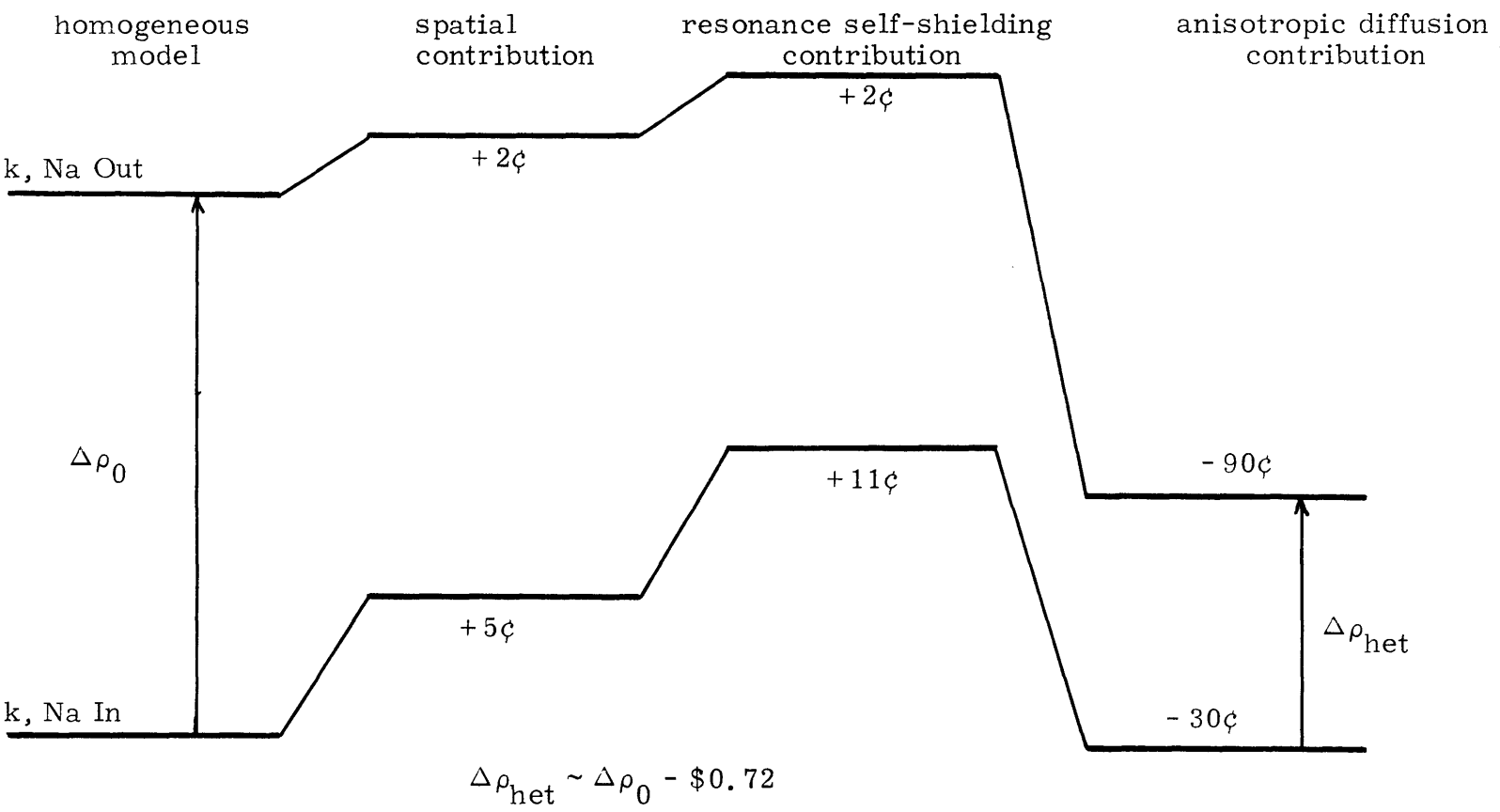

Fig. 6.1 Heterogeneous Effects on Sodium-Void Reactivity

in blanket savings for the voided case (different savings) as opposed to using the same sodium-in blanket savings in both cases (same savings). Table 6.5 presents a comparison of results using both techniques.

TABLE 6.5
Effect of Blanket Savings Representation

	Different Savings*	Same Savings*
2-group k_{eff}, Na Out	1.0285	0.99067
$(\Delta k)_{het}$ for Na Out	-111.7¢	-127.7¢
$(\Delta k/k)_{het}$ for Na Out	-114.7¢	-126.5¢
2-group k_{eff}, Na In	1.0000	1.0000
Net heterogeneous void effect	-75.5¢	-87.3¢

*See text

Not accounting for the increased blanket savings results in a significant underprediction of k_{eff} and an overprediction of the heterogeneous effect upon whole-core voiding by approximately 16%.

In summary of this subsection: the single most important observation is the relatively large magnitude of the heterogeneous contribution of anisotropic diffusion. Most earlier analyses of FBRs [e.g., Reference 25] have concerned themselves with the heterogeneous contributions due to resonance self-shielding and spatial flux distribution effects; the effect of anisotropic diffusion has been almost uniformly neglected, although it has been shown here to play the dominant role. To gain proper perspective, one should recall that the target goal for accuracy in calculating the sodium void effect for the commercial FBR plant of the 1980s is ±$0.30 [1]. To meet this goal,

a proper accounting of the heterogeneous effects due to anisotropic diffusion is imperative. Conversely, the combined other effects, except for resonance self-shielding, are well within this criterion.

6.2 Demonstration Plant Design

The effect of heterogeneity on a representative demonstration LMFBR plant core design is considered separately in this subsection because a demo core differs in size and enrichment from the 1000-MWe designs, and also because it is closer to a construction date. Table 6.6 summarizes the physical parameters for the Westinghouse 300-MWe design [77], while Table 6.7 lists the unit cell descriptions used in the DELKHET code.

TABLE 6.6
Demonstration Plant Design Core Parameters

Core height (in.)	36
L/D	0.436
Fuel material	PuO_2-UO_2
Enrichment (at. %)	18.91/26.47
Fuel density (% TD)	84
Fuel pellet OD (in.)	0.194
Pitch (in.)	0.285
Clad thickness (in.)	0.015

TABLE 6.7
DELKHET Description of Demonstration Core

Core height (cm)	91.44
Core radius (cm)	94.07
Unit cell radii (cm):	
r_1	0.2464
r_2	0.2845
r_3	0.3801
Enrichment (at. %)	22.2
Regionwise number densities:	
Pu-239	0.0045354
U-238	0.015894
O	0.040859
Fe	0.0848
Na	0.0224

The notable differences between the demonstration plant design and the 1000-MWe design are the smaller fuel pin diameter, the higher enrichment, and the smaller core radius. The first has the effect of reducing the heterogeneous resonance self-shielding, the second the effect of increasing the fast flux peaking in the fuel rod, which increases the contribution of the spatial heterogeneity component, while the last increases the core leakage and hence the contribution of anisotropic diffusion. Although the resonance self-shielding effect was not calculated separately for the demonstration core, the other two expectations are confirmed by the DELKHET results presented in Table 6.8.

TABLE 6.8
Heterogeneous Effects in Demonstration Core
(cents* of reactivity – exclusive of self-shielding)

Na In	¢
Spatial	13.3
Ani. Diff.	-43.6
Net	-30.3
Na Out	
Spatial	12.4
Ani. Diff.	-131.7
Net	-119.3
Net Void Effect	-89.0

*β = 0.0033

From these results, one concludes that the heterogeneous effect on the whole-core sodium void worth in the demonstration plant core is approximately 50% larger than in the 1000-MWe core. The increased

positive contribution due to spatial flux distribution effects is more than compensated for by the even larger increase in the negative anisotropic diffusion component. As a point of reference: the target accuracy for calculating the sodium void reactivity in the demonstration core is ±$0.50 [1], thus anisotropic diffusion effects must be taken into account. Moreover, the whole-core sodium voiding effect for a demonstration-size plant is of the order of +$1.10 [6], calculated with no consideration of anisotropic diffusion. If anisotropic diffusion effects are included, the results above lead one to a whole-core sodium voiding effect of only +22¢ of reactivity. The heterogeneous reactivity effect of anisotropic diffusion thus offers a significant mechanism to mitigate the whole-core sodium voiding accident in the demonstration FBR plant.

6.3 Effect of Design Choices on Heterogeneity

In this section, the G.E. 1000-MWe design is used as a basis for some parametric studies. The effects of varying enrichment, fuel pin pitch, and clad thickness upon the various heterogeneous contributions are investigated.

6.3.1 Enrichment

The G.E. core design was the subject of DELKHET calculations for two average enrichment values: 12.1% as in the reference design, and a 15% enrichment variant. For both cases (as in subsequent parameter calculations), the reference L/D value was assumed fixed. The radial and axial blanket savings were calculated from Eq. (6.1) where the term consisting of blanket constants,

$\frac{1}{D_r}\sqrt{\frac{D_r}{\Sigma'_{ar}}}$, was defined to be that constant which gave the consistent blanket savings for the reference core when multiplied by D_c. On that basis, the core radius R is calculated as the only unknown in the equation:

$$B^2 = \left(\frac{2.4048}{R+\delta_r}\right)^2 + \left(\frac{3.1416}{2(L/D)R+2\delta_z}\right)^2 , \qquad (6.5)$$

where B^2 is the critical buckling of the off-design core. Table 6.9 compares the results for the two enrichments.

TABLE 6.9

Effect of Enrichment on Heterogeneity
(cents of reactivity – exclusive of self-shielding)

	$\epsilon = 12.1\%$	$\epsilon = 15\%$
Na In		
Spatial	3.5	5.2
Ani. Diff.	-31.5	-44.5
Net	-28.0	-39.3
Na Out		
Spatial	1.2	4.1
Ani. Diff.	-88.7	-118.8
Net	-87.5	-114.7
Net Void Effect	-59.5	-75.4
Critical Core Dimensions:		
Height (cm)	76.2	53.5
Radius (cm)	123.7	86.9

As was observed for the demonstration reactor core, the higher enrichment increases the spatial flux component, while the resulting smaller core size increases the negative contribution due to

anisotropic diffusion. The major contribution to the spatial flux component is due to the augmented group 1 fission in the fuel rod (increasing from +11.2¢ to +13.1¢, sodium-in; from +6.9¢ to +8.7¢, sodium-out) for the higher enrichment.

6.3.2 Clad Thickness

The effect of doubling the clad thickness while keeping the other volumes fixed was also investigated. As for the other parametric studies, the critical geometry was calculated from Eq. (6.5) employing the same consistent calculation of the blanket savings. Table 6.10 reports the results.

TABLE 6.10

Effects of Clad Thickness, t, on Heterogeneity
(cents of reactivity – exclusive of self-shielding)

	t = 0.01 in.	t = 0.02 in.
Na In		
Spatial	3.5	6.7
Ani. Diff.	-31.5	-25.7
Net	-28.0	-19.0
Na Out		
Spatial	1.2	3.8
Ani. Diff.	-88.7	-70.0
Net	-87.5	-66.2
Net Void Effect	-59.5	-47.2
Critical Core Dimensions:		
Height (cm)	76.2	88.9
Radius (cm)	123.7	144.3

As expected, the effect of increasing the clad thickness while keeping the fuel and coolant volumes fixed is to decrease the effective enrichment homogenized over the unit cell; thus a larger critical core size is required with attendant decreases in core leakage and in the contribution of anisotropic diffusion. The increase in the spatial flux distribution effect is due to the relative decrease in the average clad and coolant region fluxes as compared to the average fuel region flux, resulting from the addition of more clad volume. The net effect is to decrease the heterogeneous reactivity effect.

6.3.3 Lattice Pitch

The final parameter varied in this investigation was the lattice pitch. Clearly, as the spacing is increased, the coolant occupies a larger and larger fraction of the unit cell volume; hence the negative anisotropic diffusion component can be expected to increase. Table 6.11 summarizes the DELKHET code calculations for this parametric variation.

Several conclusions can be drawn from the results in Table 6.11. First, it is apparent that for the sodium-in condition, the negative reactivity contribution of anisotropic diffusion reaches a maximum and thereafter decreases with increasing pitch. This is due to reduced leakage from the large-pitch, large critical size cores: beyond P = 1.05 cm, the product $(\delta D)_{het} B^2$ decreases. On the other hand, no such limit is reached for the sodium-out case: the increase in the void volume with increasing pitch provides a sufficient heterogeneous perturbation of D to overcome the decreasing B^2; thus $(\delta D)_{het} B^2$ increases.

TABLE 6.11

Effects of Lattice Pitch on Heterogeneity
(cents of reactivity – exclusive of self-shielding)

	P=0.7620 cm v/o* = 0.3703	P=0.90 cm v/o=0.5485	P=1.05 cm v/o=0.6683	P=1.25 cm v/o=0.7660
Na In				
Spatial	3.5	8.2	11.5	16.4
Ani. Diff.	-31.5	-55.5	-65.1	-62.0
Net	-28.0	-47.3	-53.6	-45.6
Na Out				
Spatial	1.2	3.6	4.4	5.6
Ani. Diff.	-88.7	-197.9	-299.4	-401.4
Net	-87.5	-194.3	-295.0	-395.8
Net Void Effect	-59.5	-147.0	-241.4	-350.2
Critical Core Geometry:				
Height (cm)	76.2	104.5	139.8	194.3
Radius (cm)	123.7	169.7	227.0	315.4

*v/o = volume percent of coolant in cell

The positive spatial contribution increases with increasing pitch for precisely the same reason as when the clad thickness was doubled: the average flux in the coolant region is depressed relative to that in the fuel region by the addition of more coolant volume in the unit cell. It is notable that a significantly smaller increase in the spatial contribution occurs for the voided cell; the effect is geometrical, namely changes in mean chord lengths rather than in the value of $\Sigma_a \bar{\ell}$ as for the sodium-in case.

We conclude that varying the lattice pitch has the most significant effect upon the heterogeneous reactivity contributions. By increasing the lattice pitch from 0.7620 cm in the original design to 0.90 cm, the negative heterogeneous contribution to the whole core sodium-voiding reactivity is magnified by a factor of 2.5. However, it should be kept in mind that the larger core will also have a larger whole-core homogeneous voiding worth, thus part of the more favorable negative heterogeneity effect is outweighed by a more positive homogeneous void worth.

A conjunction of both desirable trends is achieved if the increased fuel rod pitch is also accompanied by an increased enrichment. Table 6.12 compares the heterogeneous contributions for various pitch values at an enrichment of 15% against the reference design.

TABLE 6.12

Effects of Pitch and Enrichment on Heterogeneity
(cents of reactivity – exclusive of self-shielding)

	ϵ = 12.1%	ϵ = 15%		
Na In	P=0.7620 cm	P=0.90 cm	P=1.05 cm	P=1.25 cm
Spatial	3.5	11.8	16.2	23.0
Ani. Diff.	-31.5	-80.8	-97.7	-98.2
Net	-28.0	-69.0	-81.5	-75.2
Na Out				
Spatial	1.2	6.2	10.3	13.6
Ani. Diff.	-88.7	-266.1	-404.5	-548.5
Net	-87.5	-259.9	-394.2	-534.9
Net Void Effect	-59.5	-190.9	-312.7	-459.7
Critical Core Dimensions:				
Height (cm)	76.2	72.7	96.1	130.7
Radius (cm)	123.7	118.1	156.0	212.2

The conclusion to be drawn from the above parametric studies is that the beneficial aspects of the heterogeneous reactivity contribution, as far as the whole core sodium-voiding accident is concerned, are maximized when the core enrichment and fuel rod spacing are as large as possible, while the clad thickness is kept to a minimum. It is the thermal-hydraulic and mechanical design constraints which generally determine the latter two of these parameters; thus they are outside the province of this work. However, the above results make clear in which direction these design variables are to be changed in order to take maximum advantage of heterogeneous effects in mitigating the consequences of a sodium-voiding accident.

6.3.4 Lattice Geometry

Work by Newton [78] has suggested that lattice geometry has a significant effect on leakage in a FBR. That is, keeping all volume fractions constant, Newton showed that an open hexagonal lattice doubles the leakage increment due to anisotropic diffusion effects as compared to a triangular lattice; Behrens' theory [42] formed the basis of that calculation.

Since the theory of Benoist provides a more sophisticated formalism to analyze the lattice geometry effect, it is of interest to examine the G.E. 1000-MWe reference design in two forms: the original triangular pitch, and an open hexagonal modification (see Figure 6.2). The fuel rods are identical in both lattices; to maintain the same coolant-to-fuel volume ratio, the hexagonal pitch is related to the triangular pitch by: $p_h = \sqrt{\frac{2}{3}}\, p_t$.

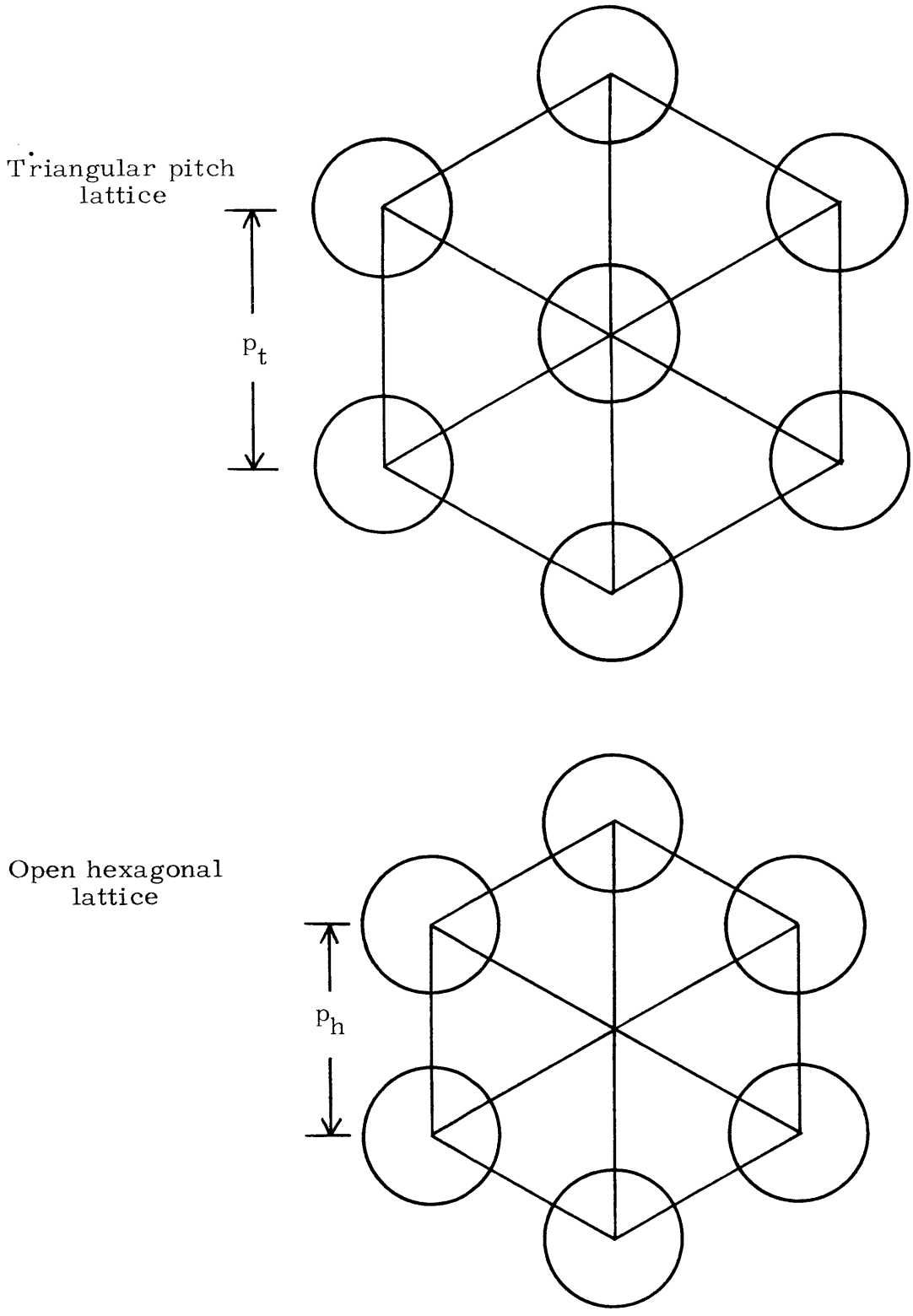

Fig. 6.2 Lattice Geometry

The triangular pitch lattice may be viewed as a hexagonal lattice with a fuel pin occupying the center of each hexagon. If the open hexagonal lattice is represented by the typical cylindricalized unit cell, the unit cell is found to be identical to the triangular lattice (as it must, since the volume fractions are identical). However, a more natural unit cell for the hexagonal lattice is the "inside-out" unit cell: the central region of the unit cell represents a cylindricalization of the coolant volume within the hexagon, while the outer annulus represents a cylindricalization of the two fuel rods per hexagon (i.e., each fuel rod is shared by three adjacent hexagons; hence 6/3 of the six fuel rods are included in eachhexagon). Clad and fuel are homogenized. Since mean chord lengths can be determined for any given cell geometry, it is not required, but merely convenient, that the cell be cylindricalized for the computation of anisotropic diffusion effects.

The Benoist theory was applied to the "inside-out" unit cell representing the open hexagonal lattice, and the results are compared to the original triangular pitch calculations. In Table 6.13, the anisotropic diffusion coefficients calculated in the two cases are reported in terms of the ratio of the diffusion coefficient perturbation for the open hexagonal pitch to the perturbation for the triangular pitch (in the two-group notation of DELKHET). The prediction by Behrens' theory that R=2 is seen, in general, to overestimate the lattice effect; the anisotropicity ratio for radial leakage does equal approximately 2 (unlike the Benoist theory, Behrens' formalism does not yield distinct radial and axial diffusion coefficients).

TABLE 6.13

Anisotropicity Ratios for Lattices

$$R = \frac{(D_{ani} - D_{hom})_{hex}}{(D_{ani} - D_{hom})_{tri}}$$

Na In		R
	Group 1 radial	1.9095
	Group 1 axial	1.7688
	Group 2 radial	2.0787
	Group 2 axial	1.7471
Na Out		
	Group 1 radial	2.0155
	Group 1 axial	1.7954
	Group 2 radial	2.0534
	Group 2 axial	1.8056

Recalling that the reactivity effect is obtained by taking the product of the perturbation multiplier (see Table 4.1) and the perturbation itself, and noting that both lattices are of identical homogenized composition (and thus have identical perturbation multipliers), one may obtain the reactivity effects for the hexagonal lattice by multiplying the triangular lattice values by the anisotropicity ratios. These reactivity effects due to anisotropic leakage are presented in Table 6.14. One concludes that the hexagonal lattice increases the desired negative effect due to anisotropic leakage upon the whole-core sodium-voiding effect by a factor of 1.8 (the factor of 2 predicted by the Behrens theory is thus reasonably close to the result of the more sophisticated Benoist theory). Thus lattice geometry provides yet another means to augment the desired effects of heterogeneity.

TABLE 6.14
Leakage Reactivity in Hexagonal and Triangular Lattices
(cents of reactivity)

Na In		Hex	Tri
	Group 1 radial	-0.6	-0.3
	Group 1 axial	-7.6	-4.3
	Group 2 radial	-3.7	-1.8
	Group 2 axial	-43.9	-25.1
	Total	-55.8	-31.5
Na Out			
	Group 1 radial	-1.4	-0.7
	Group 1 axial	-18.1	-10.1
	Group 2 radial	-11.1	-5.4
	Group 2 axial	-130.9	-72.5
	Total	-161.5	-88.7
Net Void Effect		-105.7	-57.2

The important result confirmed here is that if one constructs an open hexagonal lattice consisting of fuel rods identical to those in a triangular lattice, with both lattices having an identical coolant-to-fuel volume ratio, the open hexagonal lattice will provide a far larger negative reactivity contribution during the sodium-voiding accident, due to augmented anisotropic leakage.

6.4 Sodium Temperature Coefficient

The sodium temperature coefficient is of interest because of its relation to reactivity feedback, stability, and control system design. For the large core size typical of the 1000-MWe designs, the coefficient is positive and of the order of $1.5 \times 10^{-5}/^{\circ}C$ (for smaller core

sizes it is a negative quantity; e.g., for the 300-MWe demo size, a typical value is $-9 \times 10^{-7}/°C$ [92]). Thus it is worthwhile to calculate the effect of the anisotropic diffusion correction upon this quantity.

For consistency, the G.E. core design was again the focus of attention. DELKHET calculations were carried out for 100%, 99%, 98%, and 97% sodium densities. The temperature coefficient is calculated from:

$$\frac{\partial \rho}{\partial T} = \left(\frac{\Delta \rho}{\Delta V/V}\right) \alpha \tag{6.6}$$

where α is the volumetric expansion coefficient of sodium, $3 \times 10^{-4}/°C$ (the value near 700°C). In Table 6.15, the results of DELKHET calculations for the reference design and a parametric variation (enrichment of 15%, pitch of 1.25 cm) are reported.

TABLE 6.15
Anisotropic Diffusion and Sodium Density

Density	Reference Design		Variation	
	$(\Delta k)_{ani}$	$\Delta \rho^*$	$(\Delta k)_{ani}$	$\Delta \rho^*$
100%	-0.0010395	—	-0.0032406	—
99%	-0.0010529	-1.34×10^{-5}	-0.0032940	-5.34×10^{-5}
98%	-0.0010663	-1.34×10^{-5}	-0.0033538	-5.98×10^{-5}
97%	-0.0010759	-9.6×10^{-6}	-0.0034069	-5.31×10^{-5}

*The difference between successive values of $(\Delta k)_{ani}$

From Eq. (6.6), one finds that the anisotropic diffusion component of the sodium temperature coefficient is of the order of $-4 \times 10^{-7}/°C$ for the reference design. This is a negligible correction which is not

sufficiently negative to mitigate the positive temperature coefficient. If the calculation is performed for the rather extreme parametric variation case, the anisotropic diffusion contribution is found to be of the order of $-1.6 \times 10^{-6}/°C$, a factor of four larger than for the reference design, but still negligible in terms of the effect upon the total sodium temperature coefficient. Thus, for this particular parameter, accounting for anisotropic diffusion leads to a negligible correction to the homogeneous calculation.

6.5 The Gas-Cooled Fast Reactor

The GCFR is an interesting case for heterogeneity calculations since it is neutronically equivalent to a voided LMFBR. Although there is no void reactivity effect to which heterogeneous corrections must be applied, heterogeneity is expected to reduce the multiplication factor compared to a homogeneous modelling of the core, which cannot correctly account for neutron streaming in the gas-coolant channels.

Table 6.16 presents the core parameters of interest for the Gulf General Atomic designs for a 300-MWe demonstration GCFR and for a 1000-MWe plant [79,80], while Table 6.17 reports the unit cell description input to DELKHET. The results of the DELKHET code calculations are presented in Table 6.18.

One observes that heterogeneity (exclusive of heterogeneous resonance self-shielding effects) reduces the multiplication constant calculated by a simple homogeneous modelling of the GCFR core by 0.00849 for the 300-MWe demonstration design. As expected, the major part of the effect is due to anisotropic diffusion. The 1000-MWe design is characterized by a larger void fraction; however, the larger core has

TABLE 6.16

GCFR Core Parameters

	300 MWe	1000 MWe
Core height (cm)	100	135
L/D	0.5	0.5
Fuel material	PuO_2-UO_2	PuO_2-UO_2
Enrichment (at. %)	18.5	15.9
Smear fuel density (% TD)	80	84.1
Fuel pin OD (cm)	0.723	0.603
Clad OD/ID	1.15	1.10
Pitch (cm)	0.9804	–*

*Calculated from given void fraction = 0.547

TABLE 6.17

GCFR Unit Cell Descriptions

	300 MWe	1000 MWe
Unit cell radii (cm):		
r_1	0.3143	0.2741
r_2	0.3615	0.3015
r_3	0.5147	0.4480
Regionwise number densities:		
Pu-239	0.003597	0.003248
U-238	0.015847	0.017182
O	0.038888	0.040860
Fe	0.0848	0.0848

TABLE 6.18

Heterogeneous Effects in GCFRs
(cents* of reactivity – exclusive of self-shielding)

	300 MWe	1000 MWe
Spatial	13.4	8.6
Ani. Diff.	-270.6	-249.3
Net	-257.2	-240.7

*β = 0.0033

a smaller buckling, thus the overall anisotropic diffusion contribution is smaller. For the 1000-MWe GCFR, Δk due to anisotropic streaming is -0.00823.

After the analysis in this work was completed, a reference was discovered which confirmed the calculations performed here. Pellaud [81] has calculated the effect of anisotropic streaming on the 300-MWe demonstration GCFR. Using a slightly modified Benoist analysis, Pellaud performed calculations in one and ten energy groups; the former using a one-group perturbation theory method, and the latter using a two-dimensional diffusion theory code modified to accept directional diffusion coefficients. Table 6.19 compares Pellaud's results to those obtained here.

TABLE 6.19
Effect of Anisotropic Streaming on 300-MWe GCFR

	Pellaud - 1 Group	Pellaud - 10 Groups	DELKHET - 2 Groups
Δk	-0.011	-0.008	-0.00893

The DELKHET two-group calculation gives a result between Pellaud's one-group and ten-group calculations; the closeness of the DELKHET result to the ten-group value indicates that the two-group calculation is sufficient. Though this comparison does not provide an absolute check on the calculations since the Benoist analysis is common to both values, the agreement does validate the techniques employed in the DELKHET code.

6.6 The Fuel Dispersal Accident

As an indication that the effect of heterogeneity is not always beneficial in a safety sense, the fuel dispersal accident is considered in this section. The fuel dispersal accident postulates the physical homogenization of the core (the issue of possible mechanisms for such an event is not considered here) in such a manner that the reactivity "tied-up" with heterogeneity suddenly becomes available. For the designs under study in this chapter, Table 6.20 lists the reactivity insertions which would result from a homogenization of the core.

TABLE 6.20
Fuel Dispersal Accident
(dollars of reactivity – exclusive of self-shielding)

		Na In	Na Out
1000 MWe			
	AI	$0.26	$0.92
	B & W	$0.30	$0.97
	GE	$0.28	$0.88
	CE	$0.30	$0.82
	GGA	–	$2.41*
300 MWe			
	W	$0.30	$1.19
	GGA	–	$2.57*

*Gas-cooled

The positive reactivity gain on homogenizing the core is due primarily to the loss of anisotropic streaming effects; the spatial flux distribution and resonance self-shielding effects yield small negative contributions which are overcome by the positive loss-of-leakage

contribution. The fuel dispersal causes a relatively small positive contribution for the sodium-in case; however, if sodium has been voided from the core prior to the core homogenization, the reactivity insertion approaches one dollar for the LMFBRs. The largest fuel dispersal reactivity contribution, in excess of two dollars, is demonstrated by the gas-cooled cores. However, it is difficult to envision a realistic mechanism for such an accident in a GCFR.

One should recall that the effects of energy self-shielding (which are ignored in the results of Table 6.20) as calculated for the typical FBR geometry of Chapter 5 contribute of the order of -10¢ for the sodium-in case and -2¢ for the sodium-out case toward the fuel dispersal accident. Hence, in Table 6.20 the positive sodium-in reactivities are slightly high, while the sodium-out values are essentially correct.

If one postulates a sodium-voiding accident which leads to an explosive homogenization of the core, the heterogeneous effects act differently during different phases of the accident: during the initial voiding of the core, heterogeneity reduces the reactivity insertion; however, once core-homogenization occurs, the reactivity associated with heterogeneity materializes as a positive reactivity insertion. Thus careful modelling of this genre of postulated accidents requires consideration of anisotropic diffusion effects (and to a lesser degree, heterogeneous spatial flux distribution effects and resonance self-shielding effects) for a realistic physical description of the underlying processes.

6.7 Conclusions

Specific core designs have been investigated for the effects of heterogeneity on multiplication constants and sodium-void reactivities. For the 1000-MWe LMFBR designs, heterogeneity is found to reduce the positive sodium-void effect (whole core) by approximately 70 cents in reactivity, due primarily to anisotropic diffusion. For the LMFBR demonstration plant, this reduction approaches 90 cents. The open hexagonal lattice geometry is found to nearly double the negative reactivity contribution due to anisotropic leakage during the sodium-voiding accident as compared to a triangular lattice of identical rods and fuel-to-coolant volume ratio. The GCFR is shown to contain a Δk due to heterogeneity of approximately -0.008. Parametric studies have shown that the heterogeneous reactivity effects may be considerably increased by a slight increase in enrichment coupled with an increase in fuel rod pitch. Heterogeneity is demonstrated to cause a positive reactivity insertion for the fuel dispersal accident. Heterogeneous effects upon the Doppler coefficient were not considered here; however, Reference 9 indicates such effects are negligible.

Chapter 7

HETEROGENEOUS EFFECTS IN FBR BLANKETS

In this chapter, the focus of attention is upon heterogeneous effects in fast breeder reactor blankets. Experimental results obtained from the Blanket Test Facility (BTF) [83] of the MIT LMFBR Blanket Physics Project are reported as well as analytical studies of blanket heterogeneity.

7.1 Self-Shielding Characterization of the BTF

In the BTF, a typical LMFBR blanket is mocked-up by the unit cell configuration pictured in Figure 7.1. On a homogenized basis, the BTF unit cell and a typical blanket cell are essentially identical [70]. This does not necessarily insure that the identity holds on the level of heterogeneous effects, particularly for heterogeneous resonance self-shielding effects: the BTF consists of uranium metal rods with the oxygen, normally associated with the LMFBR's UO_2 fuel, in the sodium chromate external to the rod.

A comparison of resonance self-shielding effects using the MIDI code was undertaken. The results are reported in Table 7.1 in terms of the MIDI-generated, heterogeneously self-shielded U-238 cross sections for the BTF unit cell, while the analogous values for typical LMFBR axial and radial blanket unit cells are reported as fractions of the BTF unit cell value. The typical radial blanket rod is assumed to have an outside diameter of 0.5 inch on a pitch of 0.565 inch, while for the typical axial blanket rod, the respective values are 0.25 inch

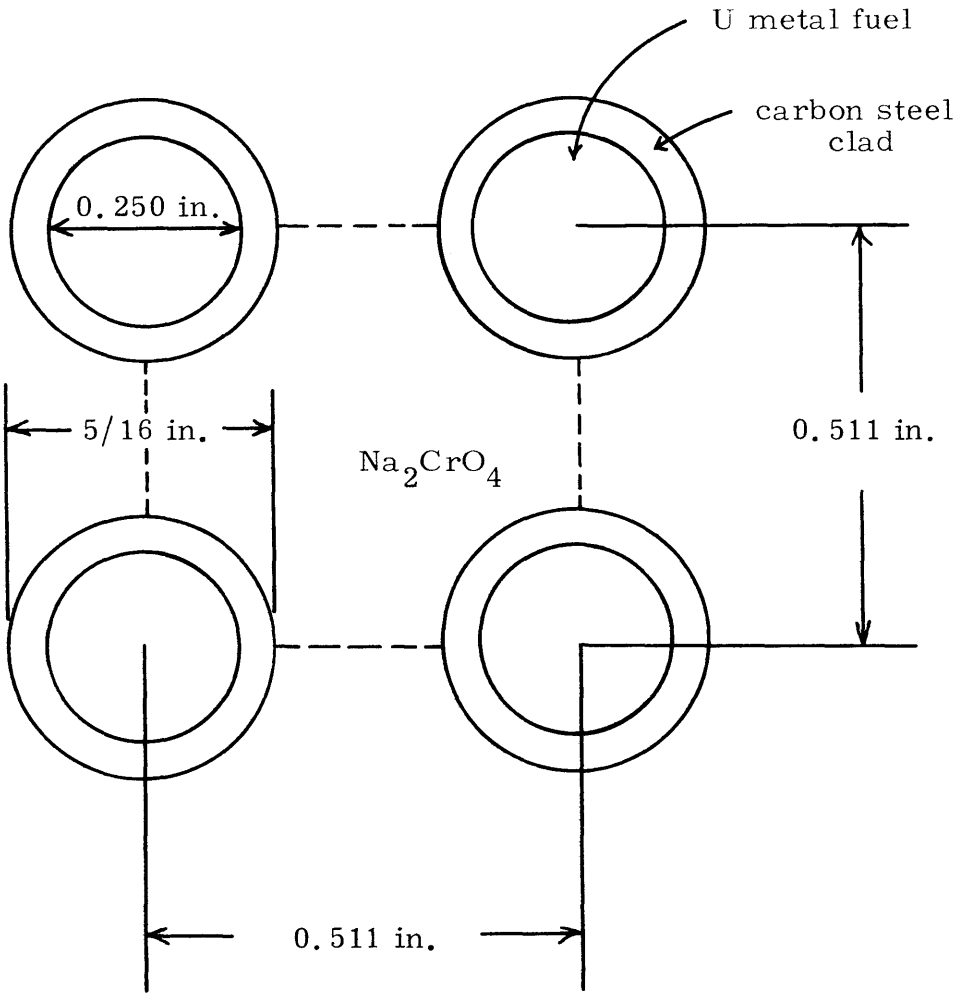

Fig. 7.1 Unit Cell Geometry for Standard Chromate Subassemblies of Blanket No. 2

TABLE 7.1

BTF Resonance Self-Shielding Comparison

	BTF (barns)		(Typical Blanket σ) ÷ (BTF σ)			
			Axial		Radial	
Group	σ_a	σ_s	abs	scat	abs	scat
11	0.4843	10.99	1.0010	1.0009	0.9738	0.9864
12	0.7641	11.65	1.0059	1.0034	0.9627	0.9777
13	0.5480	11.56	1.0361	1.0112	0.9407	0.9818
14	0.6142	10.27	1.0451	1.0078	0.9324	0.9883
15	0.8075	10.55	1.0578	1.0104	0.9226	0.9858
16	0.7276	9.574	1.0686	1.0049	0.9089	0.9939
17	1.200	11.91	1.0642	1.0160	0.9208	0.9815
18	3.281	12.53	1.0585	1.0144	0.9137	0.9785
19	2.676	11.47	1.0486	1.0096	0.9152	0.9826
20	7.265	10.60	1.0406	1.0066	0.9310	0.9896
21	7.730	9.446	1.0445	1.0021	0.9352	0.9969

and 0.338 inch. From the comparison of Table 7.1, it is evident that as far as heterogeneous resonance self-shielding effects are concerned, the BTF is intermediate between a typical radial and a typical axial blanket, being somewhat closer to the latter.

7.2 Experimental Intra-Rod Activation Profile Measurements in the BTF

7.2.1 Six-Piece Foil Measurements

Measurements of the activation profile within a UO_2 rod using a foil made up of six concentric annuli have been performed [84]. These measurements were performed using the BTF special sodium subassembly which, unlike the standard chromate subassembly, consisted of 0.5-inch outside diameter UO_2 fuel rods on a 0.61-inch triangular pitch immersed in solid sodium. The six-piece foil measurements confirmed that, to within a ± 2% error in the calculated activation, the intra-rod activation profile could be represented by a universal shape function:

$$A(r) = C_0 + C_1 \mathcal{E}\left[\left(\frac{r}{a}\right)^2\right], \tag{7.1}$$

where C_0 and C_1 are constants, a is the rod radius, and $\mathcal{E}$ is the complete elliptic integral of the second kind.

The results obtained by curve-fitting the universal shape function to various activation measurements (i.e., the calculated values of C_0 and C_1) may be interpreted in terms of a useful ratio, F, which is an index of heterogeneous self-shielding:

$$F = \frac{\bar{A}_f}{A_s} = \frac{\int_0^a A(r)\, dV}{A(a) \int_0^a dV}, \tag{7.2}$$

that is, the ratio of the average activation within the rod to the activation at the surface. Substituting Eq. (7.1) into Eq. (7.2) and performing the integration, one obtains:

$$F = \frac{C_0 + \frac{4}{3} C_1}{C_0 + C_1}. \tag{7.3}$$

Thus the C_0 and C_1 coefficients lead directly to the F-factor, and Table 7.2 presents the ratios calculated from the data of Reference 84.

TABLE 7.2
Six-Piece Foil F-Factors for UO_2 Rods*

Measurement	F
Fission product activity	1.1221
Fission product activity	1.0447
Fission product activity	1.0609
Np-239 activity	0.89703
Np-239 activity	0.85478
Np-239 activity	0.90501

*Middle blanket row

The fission product measurements reveal flux peaking within the rod due to fission enhancement by the first-flight group, while the Np-239 activity measurements reveal flux depression within the rod due to U-238 capture self-shielding.

7.2.2 Two-Piece Foil Measurements

Two-piece foil measurements of the activation profile within rods in the chromate subassembly and the special sodium subassembly have been performed as well: as can be seen from Eq. (7.1), only two parameters are needed to determine the activation shape within the validity of the model confirmed by six-piece foil irradiations. A derivation is required which relates these measurements to the activation ratio F. To do so, we let A_i be the activity of the i^{th} foil region ($i = 1$ for the central disk of radius R_1, $i = 2$ for the outer annulus of outer radius a), so that:

$$\frac{A_1}{A_1 + A_2} = \frac{\int_0^{R_1} A(r)\, dV}{\int_0^{a} A(r)\, dV} = \frac{y^2 + zI}{1 + \frac{4}{3} z}, \tag{7.4}$$

where A(r) is given by Eq. (7.1), $I \equiv \frac{2}{a^2} \int_0^{R_1} \mathcal{E}\left[\left(\frac{r}{a}\right)^2\right] r\, dr$; $y \equiv R_1/a$, and $z \equiv C_1/C_0$. Now, from the definition of Eq. (7.3), $F = \left(1 + \frac{4}{3} z\right)/(1+z)$. Thus we may solve Eq. (7.4) for z and then calculate F, giving:

$$F = \frac{\frac{4}{3} - \left(\frac{a}{R_1}\right)^2 I}{\frac{1}{3}\left(\frac{A_1}{A_1 + A_2}\right)\left(\frac{a}{R_1}\right)^2 - \left(\frac{a}{R_1}\right)^2 I + 1}. \tag{7.5}$$

The observables are the foil weights w_i and the activities of the foils A_i; from which, $C_1 = A_1/w_1$ and $C_2 = A_2/w_2$, which lead to the identity:

$$\left(\frac{A_1}{A_1 + A_2}\right)\left(\frac{a}{R_1}\right)^2 = \frac{C_1(w_1 + w_2)}{C_1 w_1 + C_2 w_2}. \tag{7.6}$$

We may finally write the F-factor as:

$$F = \frac{\left(\frac{w_1 + w_2}{w_1}\right) \int_0^{\left(\frac{w_1}{w_1 + w_2}\right)} \mathcal{E}(x)\, dx - \frac{4}{3}}{\left(\frac{w_1 + w_2}{w_1}\right) \int_0^{\left(\frac{w_1}{w_1 + w_2}\right)} \mathcal{E}(x)\, dx - \frac{1}{3}\left[\frac{C_1(w_1 + w_2)}{C_1 w_1 + C_2 w_2}\right] - 1}. \tag{7.7}$$

The results presented in this section are all based on calculating F from Eq. (7.7), where C_1 and C_2 are the specific activities calculated from the measured activities A_1 and A_2 and w_i the foil weights. Experimental details are discussed in Reference 85.

The F-factors calculated from two-piece foil measurements for both the 0.43-inch OD UO_2 rods in the special sodium subassembly [86] in Blanket No. 2 and the 0.25-inch OD uranium metal rods in the standard chromate subassembly [86,87] of Blankets No. 2 and No. 3 are reported in Tables 7.3 and 7.4.

TABLE 7.3
Two-Piece Foil F-Factors for UO_2 Rods*

Case	Description	Fission Product Activity	Np-239 Activity
1	Sodium absent	0.9605	0.9359
2	Sodium present	1.056	0.9005
3	Sodium present	1.078	0.9132

*Middle blanket row (Blanket No. 2)

TABLE 7.4
Two-Piece Foil F-Factors for Metal Rods

Blanket Position	Fission Product Activity	Np-239 Activity
Ref. 86 – Blanket No. 2		
Front row	1.005	0.9063
Middle row	0.9796	0.8954
Outer row	–	0.8683
Ref. 87 – Blanket No. 3		
Front row	1.0003	0.9140
Outer row	1.0374	0.8423

Several observations may be made. First, cases 2 and 3 in Table 7.3 (which represent two foils within the same rod, albeit

at slightly different positions) indicate the effect of experimental uncertainty upon the calculated F-factor, since both results reflect the measurement of the same quantity. The results of Tables 7.2 and 7.3 are directly comparable since only the foil details differ (i.e., six-piece versus two-piece). These results suggest F of the order of 1.05 for the fission product activity measurements and F of the order of 0.90 for the Np-239 activity measurements. Second, the effect of position within the blanket upon the Np-239 measurements is clearly demonstrated by the results in Table 7.4: the deeper into the blanket, the larger the flux depression measured. This phenomenon may be ascribed to the softening of the spectrum with blanket depth, which places more neutrons in the lower energy groups, which in turn have larger absorption resonances. In addition, case 1 in Table 7.3 suggests that in the absence of sodium, the self-shielding decreases slightly. Comparing middle row results for both UO_2 rods and metal rods half their diameter (but with 2.2 times the U-238 density) suggests the self-shielding effects are comparable in both types of rods (confirming the conclusions of Section 7.1). Fifth, the fission product activity measurements for the metal rods are inconclusive due to the magnitude of the experimental uncertainty. Results calculated from the measurements of References 86 and 87 give opposing results for the fission product activations: both indicate an F of about 1.0 in the front blanket row, but then predict opposite trends with increasing blanket depth. One should note that in one case the blanket is reflected by steel (Blanket No. 2, Reference 86); while in the other case, a graphite reflector is employed (Blanket No. 3, Reference 87). Lastly, the uncertainty in the F-factors due to the uncertainty in the activation

measurements [87] are of the order of 5% for the fission product activity measurement and of the order of 0.5% for the Np-239 activity measurement. Thus the experimental uncertainty obscures any conclusion one may make about the first-flight flux shape beyond the observation that it is essentially flat. On the other hand, the ratio of the average activation in the rod to the surface activation is unmistakably of the order of 0.9 with a definite increase in the U-238 capture dip with blanket depth.

7.3 Theoretical Analysis of BTF Measurements

In this section, the attempt to predict analytically the results of the intra-rod activation measurements is discussed, with an emphasis on heterogeneous resonance self-shielding effects.

7.3.1 The Failure of Coarse-Group Multi-Group Calculations

If one attempts to calculate the intra-rod activation shape using, say, the ANISN code in 26 groups, the flux dip predicted by the Np-239 activation measurements is simply not seen.* For a unit cell representation with a shell source characteristic of a typical blanket spectrum in the outer coolant region, the total flux at the rod center is 0.9943 times that at the rod surface, a negligible flux dip compared to the measured average-to-surface activation ratio of 0.9. Looking at the flux group-by-group, only below 130 eV does the flux within a group given by ANISN show a dip approaching the measured 10% value for the activation profile. Clearly, the typical multi-group calculation is incapable of duplicating the measured activation dip. On the other hand, the MIDI calculation performed to yield the proper resonance self-shielded cross sections is capable of treating the problem because

*Even using unshielded (infinite dilution) cross sections.

it assumes a continuous flux representation within each resonance (*vide* Eq. 5.2), which is equivalent to an infinite-number-of-groups representation. Thus one must look beyond multi-group calculations for a method of calculating the measured activation dip in the BTF rods.

7.3.2 Relationships Among Various Self-Shielding Factors

It is possible to derive a relationship between the self-shielding factor F used earlier in analyzing the experimental results and the heterogeneous self-shielding factor for cross sections f^*, defined as:

$$f^* = \sigma^*_{af}/\sigma_{af} \,, \tag{7.8}$$

where σ_{af} is the absorption cross section of fuel, and σ^*_{af} is the absorption cross section of fuel when it is homogenized over the cell. Recall earlier that the definition of the overall self-shielding factor f in terms of the MIDI-generated cross sections was $f = (\sigma_{ss})_{het}/\sigma_{\infty\ dil}$ so that:

$$f = \frac{(\sigma_{ss})_{het}}{(\sigma_{ss})_{hom}} \times \frac{(\sigma_{ss})_{hom}}{\sigma_{\infty\ dil}} \tag{7.9}$$

or $f = (f^*)(g)$. Note that σ^*_{af} is the cross section given by MIDI in the heterogeneous option, $(\sigma_{ss})_{het}$; while σ_{af} is the cross section given by the homogeneous option, $(\sigma_{ss})_{hom}$. For clarity, Table 7.5 summarizes the various self-shielding factors used in this work.

Equating fine-group reaction rates in the homogeneous cell and in the fuel rod yields (since blanket rods are the subject, only absorptions in U-238 are considered):

TABLE 7.5

Summary of Self-Shielding Factors Used

Factor	Description
$F = \bar{A}_f / A_s$	Ratio of average activation in rod to surface activation, calculated from activation profile measurements.
$f = (\sigma_{ss})_{het} / \sigma_{\infty\ dil}$	Ratio of heterogeneously self-shielded cross section to infinite dilution cross section.
$f^* = (\sigma_{ss})_{het} / (\sigma_{ss})_{hom}$	Ratio of heterogeneously self-shielded cross section to homogeneously self-shielded cross section.
$g = (\sigma_{ss})_{hom} / \sigma_{\infty\ dil}$	Ratio of homogeneously self-shielded cross section to infinite dilution cross section.

$$\Sigma^*_{afi} \bar{\psi}_{ci} V_c = \Sigma_{afi} \bar{\psi}_{fi} V_f \ , \qquad (7.10)$$

where: Σ^*_{afi} = absorption cross section in fine-group i of fuel homogenized over total cell volume, V_c

Σ_{afi} = absorption cross section in fine-group i of fuel in rod of volume V_f

$\bar{\psi}_{ci}$ = cell-averaged flux in fine-group i

$\bar{\psi}_f$ = average flux in fuel rod in fine-group i.

Now,

$$f^*_i = \frac{\Sigma^*_{afi} V_c}{\Sigma_{afi} V_f} \ , \qquad (7.11)$$

and comparing Eqs. (7.11) and (7.10) leads to the result:

$$f_i^* = \overline{\psi}_{fi}/\overline{\psi}_{ci} . \tag{7.12}$$

From the two-region escape/transmission probability cell model for parabolic flux distributions (see Appendix C):

$$\overline{\psi}_{mi} - \psi_{si} = \psi_{si} - \overline{\psi}_{fi} , \tag{7.13}$$

where $\overline{\psi}_{mi}$ is the average flux in the coolant region and ψ_{si} the flux at the fuel rod surface for fine-group i. Equation (7.13) may be re-written as:

$$\frac{\overline{\psi}_{mi}}{\overline{\psi}_{fi}} = 2\frac{\psi_{si}}{\overline{\psi}_{fi}} - 1 = \frac{2}{F_i} - 1 . \tag{7.14}$$

In Eq. (7.14), the equality $F_i \equiv \overline{A}_{fi}/A_{si} = \overline{\psi}_{fi}/\psi_{si}$ has been employed; it is valid within a <u>fine</u> group since U-238 is the primary absorber in the blanket so that the constant of proportionality between flux and activation within the fine group is the group absorption cross section. By definition, the cell-averaged fine-group flux is:

$$\overline{\psi}_{ci} = \left(\frac{V_m}{V_c}\right)\overline{\psi}_{mi} + \left(\frac{V_f}{V_c}\right)\overline{\psi}_{fi} , \tag{7.15}$$

from which:

$$\frac{\overline{\psi}_{ci}}{\overline{\psi}_{fi}} = \left(\frac{V_m}{V_c}\right)\left(\frac{\overline{\psi}_{mi}}{\overline{\psi}_{fi}}\right) + \frac{V_f}{V_c} \equiv \frac{1}{f_i^*} . \tag{7.16}$$

Substituting Eq. (7.14) into Eq. (7.16) leads to the desired final result:

$$F_i = \left\{1 + \frac{1 - f_i^*}{2f_i^*(1-v)}\right\}^{-1} , \tag{7.17}$$

where v is the volume fraction of fuel, V_f/V_c.

The assumption is made that Eq. (7.17) holds not only on a fine-group level but also on a many-group basis (i.e., the i-subscript is suppressed), so that F may be identified with the activation ratio calculated from the data of the activation measurements (*vide* Np-239 activity in Tables 7.2 through 7.4). Note that for homogeneous self-shielding only, $f^* = 1$ and $F = 1$ (though still $g < 1$).

Strictly speaking, F should be calculated from the F_i of Eq. (7.17) in the following manner:

$$F = \frac{\sum_i \bar{A}_{fi}}{\sum_i A_{si}} = \frac{\sum_i F_i A_{si}}{\sum_i A_{si}} = \frac{\sum_i F_i w_i f_i^* g_i(\sigma_{\infty\ dil})_i}{\sum_i w_i f_i^* g_i(\sigma_{\infty\ dil})_i}, \qquad (7.18)$$

where w_i is the group i weight (i.e., normalized flux for group i, with representative values listed in Table 7.6). That is, the F_i are weighted to arrive at the F-factor. Instead, the simplifying assumption is made that Eq. (7.17) holds with the "i" suppressed, and f_i^* is then the quantity to be weighted (as shown below) to arrive at the f^*-factor. Comparative calculations show that this simplifying assumption leads to a negligible error of 0.1% in the F-factor. The BTF measurements have shown that F is about 0.9. For the metal rod case where $v = 0.75$, this requires $f^* = 0.95$; while for the UO_2 rods, $v = 0.82$, thus requiring $f^* = 0.96$.

To utilize Eq. (7.17), one must calculate the overall f^*-factor. That quantity may be obtained by appropriately averaging the group-by-group self-shielding factors. The group-averaged homogeneously and heterogeneously self-shielded cross sections may be obtained from:

$$(\sigma_{ss})_{hom} = \frac{\sum_i w_i g_i (\sigma_{\infty\ dil})_i}{\sum_i w_i}, \tag{7.19}$$

$$(\sigma_{ss})_{het} = \frac{\sum_i w_i f_i^* g_i (\sigma_{\infty\ dil})_i}{\sum_i w_i}. \tag{7.20}$$

From the above, one calculates the f^*-factor:

$$f^* = \frac{\sum_i w_i f_i^* g_i (\sigma_{\infty\ dil})_i}{\sum_i w_i g_i (\sigma_{\infty\ dil})_i}, \tag{7.21}$$

where f_i^* and g_i are different from unity only in the self-shielded groups 11 through 21, while the summations are over all 26 groups.

Table 7.7 presents the group-by-group f_i^*-factors and the g_i-factors for the BTF UO_2 rods, obtained by performing two MIDI calculations: one for a homogeneous cell description which yields the g_i and a second for a heterogeneous cell description which yields the f_i (see definitions in Table 7.5). Then the quotient f_i/g_i yields the f_i^*-factors. The group weights given in Table 7.6 for the BTF are taken from Reference 70 for a position 24.4 cm into the blanket. Using these quantities together with the infinite dilution cross sections of the ABBN set, Eq. (7.21) yields $f^* = 0.9841$, which is to be compared to $f^* = 0.96$ calculated from the experimental determination of F. This leads to a prediction of the average-to-surface activation ratio, F, of 0.9570 (recall experimentally F = 0.9) which, though a considerable

TABLE 7.6

Group Weights for Blanket and Core Spectra
(Arbitrary Normalization*)

Group	BTF	Core	Group	BTF	Core
1	0.1432	0.5155	14	16.08	8.722
2	0.7948	3.229	15	12.63	4.989
3	1.534	6.716	16	9.006	2.123
4	3.671	14.30	17	5.494	0.6410
5	5.738	17.74	18	2.446	0.1225
6	16.96	36.83	19	1.054	0.02640
7	27.50	45.62	20	0.3086	0.00281
8	32.61	45.84	21	0.08392	0.00039
9	35.22	39.74	22	0.08384	0.00022
10	27.22	28.20	23	0.06608	0.00009
11	31.03	24.96	24	0.04161	0.00001
12	17.64	13.40	25	0.01762	0
13	4.384	21.87	26	0.00418	0

*Normalization different for BTF and core

TABLE 7.7

f^*- and g-Factors for UO_2 Rods

Group	f^*	g	ad hoc f^*
11	0.9814	0.6225	0.95
12	0.9607	0.9264	0.93
13	0.9903	0.4338	0.96
14	0.9848	0.2769	0.95
15	0.9792	0.2113	0.95
16	0.9722	0.1512	0.94
17	0.9736	0.06676	0.94
18	0.9736	0.2053	0.94
19	0.9753	0.04329	0.94
20	0.9802	0.08416	0.95
21	0.9801	0.04313	0.95

improvement over the multi-group ANISN prediction of virtually no dip, still represents a significant underprediction of the measured activation dip.

It is of interest to impose an ad hoc decrease in the f_i^*-factors of approximately 3%, the choices for the ad hoc f_i^* being given in Table 7.7 under the appropriate column. With this set of f_i^*, one calculates $f^* = 0.9632$ and $F = 0.9041$, very nearly those values obtained from the BTF measurements. To provide an appreciation of the significance of this ad hoc change in the f_i^*, Table 7.8 presents both the MIDI-generated, heterogeneously self-shielded cross sections and those implied by the ad hoc change. One observes that only a very slight decrease in the theoretical group-by-group self-shielded cross sections is required (approximately 3%) to give the measured activation dip correctly. Or from a different perspective, the calculated activation dip is exceedingly sensitive to the calculated self-shielded cross sections, with high precision being required for the latter. Thus experiments of this type provide a very strict test of the method for calculating heterogeneous self-shielding: the implication of the results presented here is that the equivalence formulae utilized in the MIDI code underpredict heterogeneous self-shielding effects by several percent in the resulting group cross sections.

At first glance, it may be unexpected that such a small change in the group cross sections could be paralleled by a sizeable change in the activation dip. However, on closer examination, one notes that many narrow resonances occur in a typical coarse-group (e.g., group 13A of the MIDI library is populated by 49 resonances from 3003 eV to 3858 eV, all less than 1 eV in width and separated from one another

TABLE 7.8
U-238 Self-Shielded σ_a
(barns)

Group	MIDI (hom)	MIDI (het)	ad hoc (het)
11	0.467	0.458	0.444
12	0.722	0.694	0.672
13	0.521	0.516	0.500
14	0.582	0.573	0.552
15	0.761	0.745	0.723
16	0.680	0.661	0.640
17	1.132	1.105	1.067
18	3.079	2.998	2.895
19	2.511	2.449	2.360
20	6.901	6.764	6.556
21	7.375	7.228	7.006

by the order of 12 eV to 30 eV). Thus a slight change in the coarse-group-average cross section (roughly proportional to the area under the resonances plus the area under the non-resonant background cross section) could be associated with a large change in the amplitude of the individual resonances. It is this "amplification effect" which can cause a small change in the coarse-group cross section to be associated with a large change in the activation dip. One should also note from Table 7.8 that the smallest coarse-group cross sections correspond to the largest activation dip. Indeed, the larger the degree of self-shielding (i.e., the larger the activation dip), the smaller the broad-group cross sections calculated by MIDI. This is exactly opposite to the result given by a multi-group calculation and points out the defect of coarse-group multi-group theory in predicting intra-rod flux shapes.

One other possible source for the discrepancy may be the incorrect calculation of the blanket spectrum over which the weighting in Eq. (7.21) is carried out. For the moment, assume the blanket spectrum is softer than calculated, resulting in a relatively larger neutron population in the resonance groups, hence a larger depression. To ascertain the effect of such a discrepancy, the BTF flux values given in Table 7.6 for groups 11 through 26 were arbitrarily doubled. The resulting f^* value was then found to be 0.9808, a slight decrease from the value of 0.9841 calculated for the theoretical spectrum, but still significantly larger than the required value of 0.96. Thus even a factor of two uncertainty in the lower energy flux does not account for the underprediction in the resonance flux dip (in contrast to the ad hoc decrease in the heterogeneously self-shielded cross sections given in Table 7.8 which does account for the discrepancy).

Lastly, errors in the resonance parameters themselves (e.g., resonance widths, spacing) are a possible source of the discrepancy.

The variation of the measured activation dip with increasing blanket depth is also calculable utilizing Eq. (7.21), since the softer spectrum can be represented by an increase in the relative magnitude of the group weights w_i in the resonance groups, leading to an increased f^*. Interestingly enough, generating the f_i^* and g_i factors for a typical core unit cell (12% enrichment) and using the mid-core spectrum given in Table 7.6 (the result of a 2DB calculation), one obtains f^* and F factors substantially the same as calculated for the BTF case. Thus if intra-rod activation profile measurements are performed on a fuel rod in a FBR core, the measured dip is predicted to be comparable to that measured in the BTF. Conversely, measurements

in the BTF are applicable to both core and blanket fuel.

It is important to note that the activation dip measurements analyzed in this section deal with the effects of heterogeneous resonance self-shielding (i.e., the spatial component of an energy self-shielding effect). This (ultra fine group) "spatial" effect is to be kept distinct from the so-called (coarse group) spatial flux distribution effect discussed in earlier sections. Though somewhat arbitrary, this dichotomy is based on the usual assumption of separability of the flux in energy and space (*vide* Eq. (5.1), which is repeated here:

$$\Sigma_x^g = \frac{\sum_j \sum_i N_{ij} f_{x,i}^g \langle \sigma_{x,k} \rangle_g \phi_j^g V_j}{\sum_j \phi_j^g V_j} \quad).$$

The spatial flux distribution effect enters into the calculation of an appropriately homogenized cross section through the ϕ_j^g weights. On the other hand, the effect of resonance self-shielding on the cross-section processing is concentrated in the f-factors. Thus, for U-238 absorption and scattering in the resonant groups, the resonance flux dip does not appear in the ϕ^g flux weights; instead, the homogenization of Eq. (5.1) is accomplished by utilizing multiplicative f-factors less than unity. Whereas, for non-resonant materials, the ϕ^g flux weights are applied to the non-resonant microscopic cross sections and the f-factors are unity. This distinction between the energy and space components of the flux leads to the U-238 resonance flux dip being treated implicitly through the f-factors, while the spatial cross section averaging for non-resonant materials is explicitly treated by weighting with calculated group-flux values (the ϕ^g).

7.3.3 Peaking in the First-Flight Group Flux

The fission product activation measurements of the flux peaking in the first-flight group at the center of the rod lend themselves to a considerably more straightforward analysis since one need not deal with resonance self-shielding effects. In fact, the escape/transmission probability formalism of Chapter 2 provides the necessary analytic tools. For example, a DELKHET calculation for the BTF metal rod predicts $\bar{\phi}_f/\phi_s = 1.017$, whereas the measured F-factor, the fission product activation ratio, for various blanket positions [86,87] has been: 1.005, 0.9796, 1.0003, 1.0373 with a ± 5% error band. In this case, the theory is more believable than the measurements, due to the experimental uncertainty.

7.4 Heterogeneous Effects and the Breeding Ratio

A quantity of interest in the FBR is, naturally enough, the breeding ratio (used here to denote the total breeding ratio of core and blankets). This section examines the effect of heterogeneity upon the calculated breeding ratio: in particular, the effects of anisotropic diffusion and resonance self-shielding.

7.4.1 Anisotropic Diffusion and the Breeding Ratio

Anisotropic diffusion increases the leakage of neutrons from the core to the blanket, thus one expects its effect to be an increase in the breeding ratio. The effect was investigated by performing several one-dimensional 2DB calculations, allowing only axial leakage in one case, and only radial leakage in the other case. Each case was calculated using both the homogeneous prescription for the diffusion coefficient and the Benoist theory result for the appropriate directional diffusion

coefficient. To dramatize the effect, these calculations were performed for a voided core which maximizes the leakage. The radial calculation predicted a 0.1% increase (i.e., BR_1-BR_2/BR_1) in the breeding ratio and the axial calculation predicted a 0.4% increase (roughly speaking, a net increase of 0.5% in the breeding ratio due to anisotropic diffusion). An analogous two-dimensional calculation has been performed for a GCFR [81] which predicted a 0.6% increase, which is consistent with the above results. For the normal LMFBR operating condition with sodium in the core, the effect is predicted to be approximately a factor of three less (the approximate ratio of the sodium-in to sodium-out heterogeneous diffusion coefficient perturbation). Thus the increase in the breeding ratio due to anisotropic diffusion is negligible, especially for the LMFBR. In passing, one recalls that the reactivity effect associated with the spatial flux distribution effect is an order of magnitude less than that associated with anisotropic diffusion; by extension, the former's effect upon the breeding ratio will also be negligible.

7.4.2 Resonance Self-Shielding and the Breeding Ratio

For the core analyzed in Section 5.3.2 (see Tables 5.8, 5.9, and 5.10), breeding ratios were calculated for each type of cross section set. The results are presented in Table 7.9.

TABLE 7.9
Effect of Self-Shielding on Breeding Ratio

Case	k	BR
Infinite dilution (12%/16%)	1.000	1.4977
Het. self-shielded (12%/16%)	1.071	1.1982
Het. self-shielded (10.5%/14%)	1.003	1.3489
Hom. self-shielded (10.5%/14%)	1.003	1.3508

One notes that the infinite dilution set (i.e., no resonance self-shielding) is considerably over-optimistic in the breeding ratio calculated. If the cross-section set is heterogeneously self-shielded and the calculation repeated, the breeding ratio decreases precipitously (self-shielding decreases absorptions in U-238, hence decreasing production of Pu-239) while k increases, and an over-enriched core results. If the enrichment is then reduced so that k returns to 1.0, the breeding ratio increases to assume a value 11% smaller than the original value for the infinite dilution calculation. The difference between the breeding ratios calculated from a homogeneously self-shielded set and a heterogeneously self-shielded set is quite small: heterogeneous self-shielding is found to reduce the breeding ratio by 0.14%.

The effect of the self-shielding model upon the calculated Pu-239 inventory in the blanket for a single 100-day time-step in 2DB is presented in Table 7.10 in terms of a normalized inventory (1.0 equals 42.51 kg). One observes that the infinite dilution calculation yields the highest value for the blanket inventory; the same calculation using heterogeneously self-shielded cross sections (recall an over-enriched core results) predicts a 23.2 kg smaller (i.e., 14% less) total blanket inventory. Decreasing the core enrichment in order to return the reactor to k = 1.0, and using appropriate heterogeneously self-shielded cross sections, increases the inventory by 9.8 kg (i.e., 7%) compared to the over-enriched core results. The homogeneously self-shielded calculation overpredicts the total blanket inventory by 0.4 kg (i.e., 0.3%) as compared to the heterogeneously self-shielded calculation.

TABLE 7.10

Effect of Self-Shielding on Blanket Pu-239 Inventory (100 Days Burn-Up)

Case	Blanket Region[2] Inventory[1]									
	12	13	14	15	16	17	Radial	Axial	Corner	Total
Infinite dilution (12%/16%)	1.120	0.2439	0.6471	1.380	0.3665	0.07600	1.364	2.027	0.4425	3.834
Het. self-shielded (12%/16%)	0.9428	0.2326	0.5530	1.148	0.3418	0.07903	1.175	1.701	0.4208	3.297
Het. self-shielded (10.5%/14%)	1.000	0.2452	0.6057	1.233	0.3622	0.08335	1.245	1.839	0.4456	3.530
Hom. self-shielded (10.5%/14%)	1.001	0.2455	0.6077	1.236	0.3624	0.08343	1.247	1.844	0.4458	3.537
Region volume (liters)	612.2	719.9	434.4	1303.	734.7	863.9				

Key:

(1) Normalized inventory:
1.0 = (Pu-239 number density of 0.1749E-3 in volume of 612.2 liters) = 42.51 kg of Pu-239

(2) Radial blanket = region 12 + region 13

Axial blanket = region 14 + region 15

Corner blanket = region 16 + region 17

Thus we conclude that significant errors in the amount of Pu-239 bred result if k is not maintained near 1.0, with major differences in the breeding gain (BR - 1). On the other hand, differences in the results using heterogeneous or homogeneous resonance self-shielding models are quite small.

The two significant conclusions in this comparison are that neglecting U-238 self-shielding causes a significant error in the calculated breeding ratio, and that a homogeneous self-shielding model is sufficient to calculate the breeding ratio to within 0.2% for the LMFBR.

7.5 Conclusions

Intra-rod foil activation measurements have been performed for the BTF which indicate a 10% U-238 activation dip (average to surface) occurs within a typical FBR blanket rod. This measured dip can be ascribed to heterogeneous self-shielding effects (i.e., the spatial component of resonance self-shielding) within the rod, and as such the measurement is shown to provide a very sensitive test of the heterogeneous resonance self-shielding model used in self-shielding calculations. Intra-rod measurement of fission product activation suggests a peaking of first-flight neutrons within the rod (i.e., the fast effect), and the result is predictable, based on escape/transmission probability analysis. The breeding ratio is shown to be a quantity which is sensitive to the presence or absence of resonance self-shielding; however, heterogeneity has a negligible effect upon the breeding ratio. Use of the "ad hoc" cross sections of Table 7.8 would change the results of previous chapters negligibly since that set

represents a small change in the heterogeneously resonance self-shielded cross sections; one should recall that integral quantities such as the multiplication constant are negligibly affected by the resonance self-shielding model (*vide* Section 5.3).

Chapter 8

SUMMARY AND RECOMMENDATIONS

8.1 Summary

Heterogeneous effects in fast breeder reactors have been investigated by developing simple but accurate models which account for the various physical phenomena that are overlooked in a volume-averaged homogenization. The focus of attention was upon the pin geometry characteristic of LMFBR power reactors.

Three distinct components of heterogeneity were identified: the effect of spatial flux distributions within the unit cell, the effect of anisotropic diffusion, and the effect of resonance self-shielding.

An escape/transmission probability method to calculate the regionwise average fluxes in the unit cell was formulated in Chapter 2. The currents at the boundaries between the various cell regions were found to be directly expressible in terms of the sources within the regions and the probabilities of occurrence for certain escape and transmission events. The region-averaged fluxes calculated by using the above method were found to compare favorably with ANISN S_8 [27] unit cell calculations. On this basis, the probability method was used to generate the fluxes employed in flux-weighting the regionwise cross sections in a manner which accounted for coarse-group spatial flux distribution within the unit cell.

In Chapter 3, the increased leakage in a heterogeneous lattice as compared to a homogeneous medium (particularly when coolant is voided) was treated by adapting the method of Benoist [48]. Anisotropic

diffusion coefficients were calculated from the Benoist theory for tight lattices. The augmented leakage in the heterogeneous lattice was characterized in terms of directional diffusion coefficients which are larger than the single multi-directional diffusion coefficient calculated for a homogeneous medium.

In Chapter 4, the cross-section perturbations due to the cell flux-weighting and the directional diffusion coefficients (the perturbation being the difference between the volume-homogenized constants and the heterogeneous constants calculated by the methods of Chapters 2 and 3) were interpreted in terms of reactivity effects by use of first order perturbation theory as well as by an analogous "total differential method" which is shown to give identical results for an equivalent bare core.

Resonance self-shielding effects were discussed in Chapters 5 and 7, with blanket effects being the focus of the latter. The effects of various resonance self-shielding models were investigated in Chapter 5 by means of direct, multi-group diffusion theory calculations of the multiplication constant. Significant discrepancies were discovered if calculations were made which ignored resonance self-shielding effects, i.e., major underprediction of the multiplication constant and major overpredictions of the sodium void reactivity and the breeding ratio. On the other hand, heterogeneous resonance self-shielding effects as opposed to homogeneous resonance self-shielding effects were found to be of lesser importance. It was shown that a defined "average" heterogeneous unit cell is quite adequate for calculations involving any realistic FBR geometry. Simple correlations were established which gave directly the U-238 self-shielding factors for a wide range of

compositions. In Chapter 7, analyses of Blanket Test Facility intra-rod measurements provided an index for judging heterogeneous resonance self-shielding models for U-238. A measured 10% depression (average-to-surface) of the resonance flux was found to be significantly underpredicted by the theory.

Reference FBR designs were analyzed in Chapter 6 in terms of heterogeneous effects (exclusive of resonance self-shielding). The major heterogeneous contribution was found to be that due to anisotropic diffusion. A net decrease in the magnitude of the whole-core sodium void reactivity addition was calculated to be of the order of 60¢ (for $\beta = 0.0033$) for the reference 1000-MWe designs. For a demonstration plant design, the heterogeneity was found to decrease whole-core sodium void reactivity by the order of 90¢. Parametric studies showed that by making a judicious choice of core enrichment, lattice pitch, and lattice geometry, the negative heterogeneous effect could be increased by a factor greater than two over the reference design values. The fuel dispersal accident was also investigated with the conclusion that heterogeneity provided a positive reactivity effect for this event, being fairly negligible for the LMFBR (of the order of +20¢) except for the voided core (about +90¢), but fairly large for the GCFR (about +$2.40). However, no realistic whole-core dispersal mechanism for such an accident in the GCFR was suggested. The simple model developed here for calculating the reactivity effect due to anisotropic diffusion, which is the major contributor, was found to give favorable results when compared to a more detailed, multi-group two-dimensional anisotropic diffusion code calculation.

The simple models developed in this work provide an a posteriori heterogeneous correction to a homogeneous calculation for the same medium. The phenomenological treatment adopted has the added advantage of giving concurrent physical insight into the nature of the heterogeneous processes.

In overall summary, several points bear reiteration:

1. It is sufficient to account for only homogeneous resonance self-shielding and anisotropic diffusion to obtain key parameters within their target accuracy (i.e., k ± 1%, BR ± 3%, whole-core Na void reactivity ± 50¢). Specifically, one may neglect coarse-group flux shape effects.

2. All heterogeneous effects serve to decrease the positive sodium void effect; hence most contemporary calculations which neglect one or more of the heterogeneous effects (particularly anisotropic diffusion) are overly conservative, and thus safety design margins are undoubtedly greater than presently established.

3. The ABBN f-factor formalism is adequate to deal with resonance self-shielding.

4. The BTF U-metal blanket is a good simulator of UO_2-Na blanket heterogeneity effects.

8.2 Recommendations for Future Work

The area for future endeavor which suggests itself most strongly is the possibility of performing strict experimental checks of various heterogeneous resonance self-shielding models through intra-rod activation measurements, as alluded to in Section 7.3.2. Such

measurements would provide a validation of the various equivalence formulations extant which account for heterogeneous resonance self-shielding by establishing an equivalent homogeneous cell. In particular, the extended equivalence relation proposed by Kelber [69] for the calculation of the K-correction factor (*vide* Eqs. (5.5) and (5.6)) could be compared against the standard formulation in which K assumes some value between 1.3 and 1.35; in addition, the Dancoff factor formulae suggested by Sauer [68] and the MC^2 code [91] could be tested. The basis of these comparisons would be the precision with which the measured activation depression within a fuel rod was calculable. As shown in Section 7.3.2, such a procedure provides a technique for validating the coarse-group, heterogeneously self-shielded cross sections. Additional work should be directed toward developing a more sophisticated theory to relate heterogeneous self-shielding factors to the measured activation dip.

Another fertile area for further work lies in the precinct of resonance self-shielding correlations. The correlations developed here were somewhat elementary in that only U-238 resonance self-shielding was considered, essentially because the required MIDI resonance parameter libraries for other elements were unavailable to develop broader correlations. Recently, a Pu-239 resonance library for MIDI has been prepared. It would be of interest to perform direct multigroup calculations of the multiplication constant (sodium-in and sodium-out), using the MIDI-generated self-shielded cross sections with Pu-239 resonances represented, to ascertain what effect self-shielding of those resonances has on the conclusions of Section 5.3, which were based solely on U-238 resonance self-shielding. Some

modification of the correlations presented here may be required due to the interaction between overlapping U-238 and Pu-239 resonances. In addition, correlations for Pu-239 self-shielding factors could be developed, probably quite similar in form to those presented in Section 5.4 for U-238. The expanded one-group correlation model of Sheaffer, which now incorporates resonance self-shielding, may find somewhat wider applicability: for example, the analysis of Doppler coefficient measurements performed on SEFOR. For completeness, the effects of heterogeneity on light element resonance scattering (e.g., in sodium) should be investigated; as well as the entirety of Th-232 self-shielding effects since the latter material has been suggested as a major blanket constituent.

More detailed core representation within the context of the simple model is in order. For example, gross heterogeneities such as control rod regions and in-core test loops have been found to cause region-wide flux heterogeneities in FBR cores [6,90], suggesting that a homogeneous, equivalent bare core representation is not a sufficient basis for the first order perturbation theory calculation of heterogeneous reactivity effects. The results obtained here for whole-core voiding are of sufficient interest to suggest an examination of local voiding in light of heterogeneous effects.

Calculations of the whole-core fuel dispersal accident and its attendant insertion of reactivity, quite large in the case of the GCFR, suggest an area for further study; in particular, further analysis should seek to ascertain if any realistic mechanisms can be established for the propagation of such an accident.

The theory of Benoist is well-established. Any further work in this area would best be devoted to the formulation of a fairly detailed experimental verification in a FBR-oriented application. The analytical formalism required to calculate anisotropic diffusion effects in plate-geometry using the theory of Benoist is available in the German KAPER code [89] and was found to adequately analyze a sodium void traverse experiment in which the plate orientation was rotated 90° between two sets of measurements. It would be of some interest to employ the KAPER formalism in analyzing the heterogeneity measurements of Reference 31 in which only an ad hoc assumption was made concerning the effect of anisotropic diffusion. This should provide further confirmation of the validity of the Benoist theory in fast systems.

Lastly, the escape/transmission probability theory does not immediately suggest itself as a candidate for future effort for FBR applications of the type considered herein, especially since the final heterogeneous reactivity contribution due to the coarse-group spatial flux distribution effect is insignificant compared to the other heterogeneities. However, the unit cell theory may find wider applicability (e.g., in thermal lattice analysis) due to its efficiency of use. On a fine-group level, it has the potential of replacing the equivalence principles currently in use by providing a direct calculation of heterogeneous resonance self-shielding effects. In addition, the question of the proper unit cell boundary condition remains. Of the two available choices, mirror or white, the latter boundary condition yields more reasonable results, though recent work [31] has suggested it causes an underprediction in the cell-flux structure. There is no explicit

assumption about the type of reflective boundary condition in the probability theory; however, it is found to give good agreement with ANISN calculations employing the white boundary condition. Thus the implications of the choice of boundary condition may be further investigated.

8.3 Conclusion

The single, overall conclusion which this work reaffirms is that simple models can have a great utility in the analysis of fast reactor neutronics. To a large extent, complex computer-oriented calculations have been considered *de rigueur* in reactor analysis; however, simple methods are capable of providing significant physical insight and quite respectable accuracy for design calculations of particular parameters.

Appendix A

MEAN CHORD LENGTH CALCULATIONS

A.1 Internal Sources

For the calculation of escape probabilities to be used in the formalism of Chapter 2, one requires the mean chord length for neutrons born in the fuel rod. The fundamental assumption of the calculation is that the rod may be treated as a transparent medium.

Figure A.1 pictures the situation for an isotropic source at point S inside the transparent rod, emitting neutrons along the escape chord $\overline{SB}$ described by the azimuthal angle ϕ and the angle of inclination θ. Averaging all possible escape paths originating at point S over all solid angles gives the "local" mean chord length:

$$\ell = \frac{1}{4\pi} \int_{\phi=0}^{2\pi} \int_{\theta=0}^{\pi} \overline{SB} \sin\theta \, d\theta \, d\phi \, . \tag{A.1}$$

Recognizing that $\overline{SB} \sin\theta = \overline{PC}$, allows one integration to be performed, leaving:

$$\ell = \frac{1}{4} \int_{0}^{2\pi} \overline{PC} \, d\phi \, . \tag{A.2}$$

The law of cosines gives:

$$\overline{PC} = -r \cos\phi + R \sqrt{1 - \left(\frac{r}{R}\right)^2 \sin^2\phi} \quad , \tag{A.3}$$

which when substituted into Eq. (A.2) leads to:

$$\ell = R \int_{0}^{\pi/2} \sqrt{1 - \left(\frac{r}{R}\right)^2 \sin^2\phi} \, d\phi \, . \tag{A.4}$$

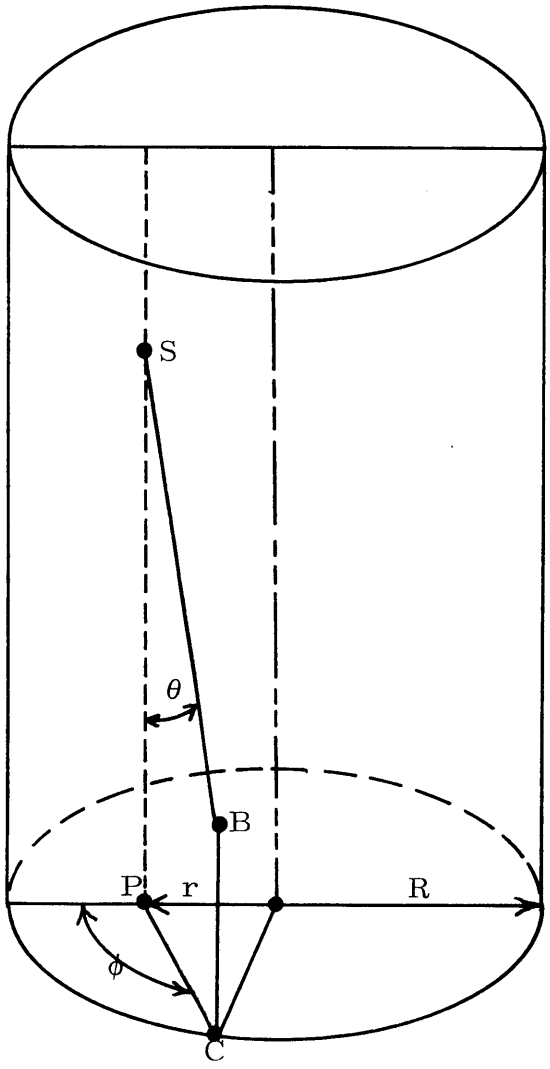

Fig. A.1 Escape Chord Length from Transparent Cylinder

The above integral is recognized as the complete elliptic integral of the second kind $\mathcal{E}\left(\frac{r^2}{R^2}\right)$ with a known series expansion, thus:

$$\ell = R\mathcal{E}\left(\frac{r^2}{R^2}\right) = \frac{\pi R}{2}\left[1 - \frac{1}{4}\left(\frac{r}{R}\right)^2 - \frac{3}{64}\left(\frac{r}{R}\right)^4 + \ldots\right]. \tag{A.5}$$

To calculate the mean chord length, the source distribution function S(r) needs to be specified. The mean chord length is given by:

$$\bar{\ell} = \frac{\int_0^R 2\pi r\ \ell(r)\, S(r)\, dr}{\int_0^R 2\pi r\, S(r)\, dr}, \tag{A.6}$$

where $\ell(r)$ is given by Eq. (A.5). For a general parabolic source distribution:

$$S(r) = 1 + \alpha^2 r^2, \tag{A.7}$$

and the mean chord length is calculated to be:

$$\bar{\ell} = \frac{4}{3} R\left[1 - \frac{\alpha^2 R^2}{66} + \ldots\right]. \tag{A.8}$$

In the case of a uniform source distribution, $\alpha \equiv 0$ and one has $\bar{\ell} = \frac{4}{3}R$, the result used in Section 2.4.

A.2 External Sources

For the calculation of transmission probabilities to be used in the formalism of Chapter 2, one requires the mean chord length within the fuel rod of neutrons entering the region from an outside source. Again, the medium is assumed to be transparent.

Figure A.2 pictures the situation where S is now at the surface of the rod and the transmission chord length is $\overline{SB}$. For the entering distribution $f(\theta)$:

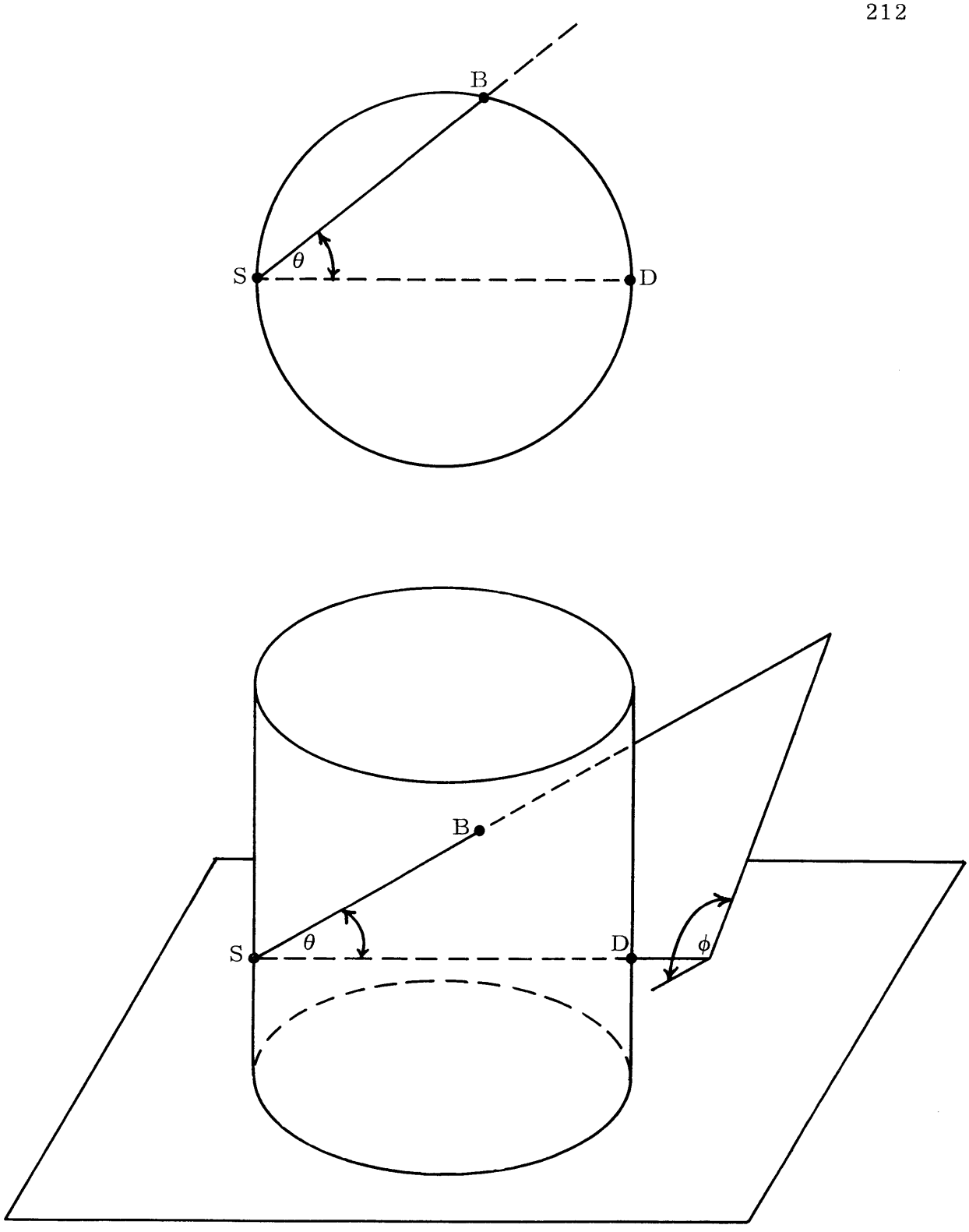

Fig. A.2 Transmission Chord Length Through Transparent Cylinder

$$\bar{\ell} = \frac{2}{\pi} \int_{\psi=0}^{\pi/2} \int_{\theta=0}^{\pi/2} \overline{SB}\, f(\theta)\, d\theta\, d\psi \ . \tag{A.9}$$

The chord $\overline{SB}$ can be identified as:

$$\overline{SB} = \frac{2R \cos\theta}{1 - \sin^2\theta \sin^2\psi} \ , \tag{A.10}$$

which leads to the mean chord length:

$$\bar{\ell} = 2R \int_0^{\pi/2} f(\theta)\, d\theta \ . \tag{A.11}$$

For an isotropic distribution (e.g., $f(\theta) = \cos\theta$), $\bar{\ell} = 2R$, the result used in Section 2.4.

Interestingly enough, if the distribution is normalized so that the integral in Eq. (A.11) is unity, then $\bar{\ell} = 2R$ regardless of the form of the distribution (this normalization of $f(\theta)$ corresponds to one neutron emitted into the right half plane). Thus, to first order, the transmission probability is independent of the incident angular distribution for all distributions which are a function only of the angle between the neutron direction and the normal to the surface.

Appendix B

FURTHER BOUNDARY CURRENT EQUATIONS

In this appendix, the derivations of the remaining boundary current equations for the escape/transmission probability model of the FBR unit cell are given. As such, this section is an amplification and continuation of the derivation presented in Section 2.2.

For fuel region source density S_1

To calculate j_{-S}:

$$j_{-S}^{(0)} = S_1 p_1 \frac{r_1}{2} \tag{B.1}$$

$$j_{-S}^{(1)} = S_1 p_1 \frac{r_1}{2} \{T_{13}P_3T_{31}P_1 + T_{13}P_3(T_{33}P_3)T_{31}P_1 + T_{13}P_3(T_{33}P_3)^2T_{31}P_1 + \ldots\} \tag{B.2}$$

$$j_{-S}^{(2)} = S_1 p_1 \frac{r_1}{2} \left(\frac{T_{13}P_3T_{31}P_1}{1 - T_{33}P_3}\right)\{T_{13}P_3T_{31}P_1 + \ldots + T_{13}P_3(T_{33}P_3)^mT_{31}P_1 + \ldots\} \tag{B.3}$$

$$\therefore\ j_{-S} = S_1 p_1 \frac{r_1}{2}\left[\frac{1 - T_{33}P_3}{1 - T_{33}P_3 - T_{13}P_3T_{31}P_1}\right] \tag{B.4}$$

To calculate j^{+}_{N} :

$$j^{(0)}_{+N} = S_1 p_1 \left(\frac{r_1^2}{2r_2}\right)\{T_{13}+T_{13}(P_3T_{33})+T_{13}(P_3T_{33})^2+\ldots\} \quad (B.5)$$

$$j^{(1)}_{+N} = S_1 p_1 \left(\frac{r_1^2}{2r_2}\right)\left(\frac{T_{13}}{1-T_{33}P_3}\right)\{P_3T_{31}P_1T_{13}+P_3T_{31}P_1T_{13}(P_3T_{33}) + P_3T_{31}P_1T_{13}(P_3T_{33})^2+\ldots\} \quad (B.6)$$

$$j^{(2)}_{+N} = S_1 p_1 \left(\frac{r_1^2}{2r_2}\right)\left(\frac{T_{13}}{1-T_{33}P_3}\right)\left(\frac{P_3T_{31}P_1T_{13}}{1-T_{33}P_3}\right)^2 \quad (B.7)$$

$$\therefore\ j^{+}_{N} = S_1 p_1 \left(\frac{r_1^2}{2r_2}\right)\left[\frac{T_{13}}{1-T_{33}P_3-T_{13}P_3T_{31}P_1}\right] \quad (B.8)$$

To calculate j^{-}_{N} :

$$j^{(0)}_{-N} = P_3\, j^{(0)}_{+N} \quad (B.9)$$

$$j^{(1)}_{-N} = P_3\, j^{(1)}_{+N} \quad (B.10)$$

$$\therefore\ j^{-}_{N} = S_1 p_1 \left(\frac{r_1^2}{2r_2}\right)\left[\frac{P_3T_{13}}{1-T_{33}P_3-T_{13}P_3T_{31}P_1}\right] \quad (B.11)$$

For coolant region source density S_3

To calculate j^{+}_{S} :

$$j^{(0)}_{+S} = S_3 p_3 \left(\frac{r_3^2-r_2^2}{2r_1}\right)\{T_{31}+(T_{33}P_3)T_{31}+(T_{33}P_3)^2T_{31}+\ldots\} \quad (B.12)$$

$$j^{(1)}_{+S} = S_3 p_3 \left(\frac{r_3^2-r_2^2}{2r_1}\right)\left(\frac{T_{31}}{1-T_{33}P_3}\right)\{P_1T_{13}P_3T_{31}+P_1T_{13}P_3(T_{33}P_3)T_{31} + P_1T_{13}P_3(T_{33}P_3)^2T_{31}+\ldots\} \quad (B.13)$$

$$j^{(2)}_{+S} = S_3 p_3 \left(\frac{r_3^2-r_2^2}{2r_1}\right)\left(\frac{T_{31}}{1-T_{33}P_3}\right)\left(\frac{P_1T_{13}P_3T_{31}}{1-T_{33}P_3}\right)^2 \quad (B.14)$$

$$\therefore\ j_{+S} = S_3 p_3 \left(\frac{r_3^2 - r_2^2}{2r_1}\right)\left[\frac{T_{31}}{1 - T_{33}P_3 - T_{31}P_1T_{13}P_3}\right] \tag{B.15}$$

To calculate j_{-S}:

$$j_{-S}^{(0)} = P_1\, j_{+S}^{(0)} \tag{B.16}$$

$$\therefore\ j_{-S} = S_3 p_3 \left(\frac{r_3^2 - r_2^2}{2r_1}\right)\left[\frac{P_1T_{31}}{1 - T_{33}P_3 - T_{31}P_1T_{13}P_3}\right] \tag{B.17}$$

To calculate j_{-N}:

$$j_{-N}^{(0)} = S_3 p_3 \left(\frac{r_3^2 - r_2^2}{2r_2}\right)\{1 + T_{33}P_3 + (T_{33}P_3)^2 + \ldots\} \tag{B.18}$$

$$j_{-N}^{(1)} = S_3 p_3 \left(\frac{r_3^2 - r_2^2}{2r_2}\right)\left(\frac{1}{1 - T_{33}P_3}\right)\{T_{31}P_1T_{13}P_3 + T_{31}P_1T_{13}P_3(T_{33}P_3) + T_{31}P_1T_{13}P_3(T_{33}P_3)^2 + \ldots\} \tag{B.19}$$

$$j_{-N}^{(2)} = S_3 p_3 \left(\frac{r_3^2 - r_2^2}{2r_2}\right)\left(\frac{1}{1 - T_{33}P_3}\right)\left(\frac{T_{31}P_1T_{13}P_3}{1 - T_{33}P_3}\right)^2 \tag{B.20}$$

$$\therefore\ j_{-N} = S_3 p_3 \left(\frac{r_3^2 - r_2^2}{2r_2}\right)\left[\frac{1}{1 - T_{33}P_3 - T_{31}P_1T_{13}P_3}\right] \tag{B.21}$$

To calculate j_{+N}:

$$j_{+N}^{(0)} = S_3 p_3 \left(\frac{r_3^2 - r_2^2}{2r_2}\right)\{T_{33} + T_{33}(P_3T_{33}) + T_{33}(P_3T_{33})^2 + \ldots\} \tag{B.22}$$

$$j_{+N}^{(1)} = S_3 p_3 \left(\frac{r_3^2 - r_2^2}{2r_2}\right)\left\{\left(\frac{T_{33}}{1 - T_{33}P_3}\right)[P_3T_{31}P_1T_{13} + P_3T_{31}P_1T_{13}(P_3T_{33}) + \ldots] + [T_{31}P_1T_{13} + T_{31}P_1T_{13}(T_{33}P_3) + T_{31}P_1T_{13}(T_{33}P_3)^2 + \ldots]\right\} \tag{B.23}$$

$$j_{+N}^{(2)} = S_3 p_3 \left(\frac{r_3^2 - r_2^2}{2r_2}\right) \left\{ \left(\frac{T_{33}}{1 - T_{33}P_3}\right) \left(\frac{P_3 T_{31} P_1 T_{13}}{1 - T_{33}P_3}\right)^2 + \left(\frac{T_{31}P_1T_{13}}{1 - T_{33}P_3}\right) \left(\frac{P_3 T_{31} P_1 T_{13}}{1 - T_{33}P_3}\right) \right\} \quad \text{(B.24)}$$

$$j_{+N}^{(3)} = S_3 p_3 \left(\frac{r_3^2 - r_2^2}{2r_2}\right) \left\{ \left(\frac{T_{33}}{1 - T_{33}P_3}\right) \left(\frac{P_3 T_{31} P_1 T_{13}}{1 - T_{33}P_3}\right)^3 + \left(\frac{T_{31}P_1T_{13}}{1 - T_{33}P_3}\right) \left(\frac{P_3 T_{31} P_1 T_{13}}{1 - T_{33}P_3}\right)^2 \right\} \quad \text{(B.25)}$$

$$\therefore \; j_{+N} = S_3 p_3 \left(\frac{r_3^2 - r_2^2}{2r_2}\right) \left[\frac{T_{33} + T_{31} P_1 T_{13}}{1 - T_{33}P_3 - P_3 T_{31} P_1 T_{13}} \right] \quad \text{(B.26)}$$

(All notation is defined in Section 2.1)

Appendix C

CALCULATION OF FLUX RATIOS IN THE TWO-REGION UNIT CELL

Considerable simplification of the calculation of average flux ratios in the unit cell results when the cell is represented by two regions (i.e., the clad, as a distinct region, is neglected).

Using the same notation as in Section 2.2, we consider successive events for a neutron born in the fuel, region 1: $S_1 p_1 \frac{r_1}{2}$ neutrons per cm^2 of surface per second escape the fuel initially, $\left(S_1 p_1 \frac{r_1}{2}\right)\left(P_2 P_1\right)$ escape the fuel after returning, $\left(S_1 p_1 \frac{r_1}{2}\right)\left(P_2 P_1\right)^2$ do so after a second return to the fuel, and so on. Summing up, one finds $S_1 p_1 r_1 / 2(1 - P_1 P_2)$ is the current leaving the fuel, where the source is S_1 neutrons/cm^3 sec. Similarly, the current leaving the coolant, region 2, is $S_2 p_2 (r_2^2 - r_1^2) / 2 r_1 (1 - P_1 P_2)$.

To consider neutrons returning to each region: $S_1 p_1 \frac{r_1}{2} P_2$ neutrons escape the fuel and return, $\left(S_1 p_1 \frac{r_1}{2} P_2\right)\left(P_1 P_2\right)$ re-escape and return a second time, and so on, summing up to $S_1 p_1 \frac{r_1}{2} P_2 / (1 - P_1 P_2)$ neutrons/cm^2 sec entering the fuel due to the source S_1 within the fuel. Again, similarly, the current entering the coolant due to sources within the coolant is $S_2 p_2 (r_2^2 - r_1^2) P_1 / 2 r_1 (1 - P_1 P_2)$.

The partial current entering the fuel rod is the sum of entries due to neutrons from internal and external sources:

$$j_{\substack{+ \\ S}} = \frac{S_1 p_1 r_1 P_2}{2(1 - P_1 P_2)} + \frac{S_2 p_2 (r_2^2 - r_1^2)}{2 r_1 (1 - P_1 P_2)} , \qquad \text{(C.1)}$$

while the partial current leaving is:

$$j_{\overline{S}} = \frac{S_1 p_1 r_1}{2(1-P_1P_2)} + \frac{S_2 p_2 (r_2^2 - r_1^2) P_1}{2r_1(1-P_1P_2)} \quad . \tag{C.2}$$

One notes that the three-region formulae (Eq. (2.8) through Eq. (2.11)) reduce to these expressions in the limit of zero clad thickness, at which point the transmission probabilities associated with the clad attain the limits: $T_{33} = 0$, $T_{13} = T_{31} = 1$.

As before, the average flux within the region is given by a neutron balance. For the fuel rod, one finds:

$$\Sigma_{a1}\bar{\phi}_1 \pi r_1^2 = 2\pi r_1 J + \pi r_1^2 S_1 \quad , \tag{C.3}$$

where J is the net current into the rod: $J = j_{\underset{S}{+}} - j_{\underset{S}{-}}$. One can define the flux at the rod surface as: $\phi_S = 2(j_{\underset{S}{+}} + j_{\underset{S}{-}})$. Using Eqs. (C.1), (C.12, and (C.3), one finds the flux ratio:

$$\frac{\bar{\phi}_1}{\phi_S} = \frac{1}{\Sigma_{a1} r_1} \cdot \frac{S_2 p_2 \frac{(r_2^2 - r_1^2)}{r_1}(1-P_1) - S_1 p_1 r_1 (1-P_2) + S_1(1-P_1P_2)}{S_1 p_1 r_1 (1+P_2) + S_2 p_2 \left(\frac{r_2^2 - r_1^2}{r_1}\right)(1+P_1)} \tag{C.4}$$

Noting that the partial current entering the coolant is identical to the partial current leaving the fuel, and similarly for the partial current leaving the coolant, one may proceed with an analogous derivation of:

$$\frac{\bar{\phi}_2}{\phi_S} = \frac{r_1}{\Sigma_{a2}(r_2^2 - r_1^2)} \cdot \frac{S_1 p_1 r_1 (1-P_2) - S_2 p_2 \left(\frac{r_2^2 - r_1^2}{r_1}\right)(1-P_1) + S_2(1-P_1P_2)}{S_1 p_1 r_1 (1+P_2) + S_2 p_2 \left(\frac{r_2^2 - r_1^2}{r_1}\right)(1+P_1)}$$

(C.5)

The escape probabilities are defined as before, with the exception of the P_i probabilities which require a second order term for the linearization which will be carried out below. That is,

$$p_1 = 1 - \frac{4}{3}\Sigma_{a1} r_1 \tag{C.6}$$

$$p_2 = 1 - \frac{4}{3}\Sigma_{a2} z_2 \tag{C.7}$$

$$P_1 = 1 - 2\Sigma_{a1} r_1 + \frac{8}{3}(\Sigma_{a1} r_1)^2 \tag{C.8}$$

$$P_2 = 1 - 2\Sigma_{a2} z_2 + \frac{8}{3}(\Sigma_{a2} z_2)^2 , \tag{C.9}$$

where $z_2 = r_2^2 - r_1^2/r_1$.

After considerable algebraic manipulation, in which the second order terms of Eqs. (C.8) and (C.9) are required at intermediate points, and neglecting higher order terms in the resulting expressions, one finds linearized formulae for the flux ratios:

$$\frac{\bar{\phi}_1}{\phi_S} = 1 - \frac{1}{3}\left[\Sigma_{a1} r_1 \left(\frac{S_2}{S_1+S_2}\right) - \Sigma_{a2} z_2 \left(\frac{S_1}{S_1+S_2}\right)\right] \tag{C.10}$$

$$\frac{\bar{\phi}_2}{\phi_S} = 1 + \frac{1}{3}\left[\Sigma_{a1} r_1 \left(\frac{S_2}{S_1+S_2}\right) - \Sigma_{a2} z_2 \left(\frac{S_1}{S_1+S_2}\right)\right] \tag{C.11}$$

$$\frac{\bar{\phi}_2}{\bar{\phi}_1} = 1 + \frac{2}{3}\left[\Sigma_{a1} r_1 \left(\frac{S_2}{S_1+S_2}\right) - \Sigma_{a2} z_2 \left(\frac{S_1}{S_1+S_2}\right)\right] . \tag{C.12}$$

If the shape of the flux in each region is assumed to be parabolic, the following expression relating the center-line, fuel average, and fuel surface fluxes results:

$$(\phi_S - \bar{\phi}_1) = (\bar{\phi}_1 - \phi_{\mathbb{L}}) , \tag{C.13}$$

so that:

$$\frac{\phi_S}{\phi_{\ell}} = 1 + \frac{2}{3}\left[\Sigma_{a1} r_1 \left(\frac{S_2}{S_1+S_2}\right) - \Sigma_{a2} z_2 \left(\frac{S_1}{S_1+S_2}\right)\right] . \qquad (C.14)$$

The above results may be compared to results in the literature. For thermal neutron absorption by a non-moderating fuel rod, the slowing-down source S_1 is zero; thus:

$$\frac{\bar{\phi}_1}{\phi_S} = 1 - \frac{1}{3}\Sigma_{a1} r_1 \quad \text{and} \quad \frac{\phi_{\ell}}{\phi_S} = 1 - \frac{2}{3}\Sigma_{a1} r_1 .$$

An extensive study has been carried out on metallic fuel and absorber rods in D_2O moderator [88]. Empirical curve fits to the experimental data were reported as:

$$\frac{\bar{\phi}_1}{\phi_S} = 1 - 0.34957\,\Sigma_{a1} r_1 \quad \text{and} \quad \frac{\phi_{\ell}}{\phi_S} = 1 - 0.69713\,\Sigma_{a1} r_1 ,$$

which are in substantial agreement with the theoretical predictions.

Appendix D

CROSS-SECTION LIBRARIES

The DELKHET code for calculating heterogeneous reactivity effects requires a two-group cross-section library (see Appendix E). This appendix presents standard two-group cross-section sets for an oxide core (13.1% Pu-239) and a carbide core (11% Pu-239) plus their blankets. The cross sections were generated by collapsing the 26-group ABBN set using the ANISN code. A cylindrical geometry representation was employed: core radius = 110 cm; blanket outer radius = 152.4 cm; core + blanket height (sodium-in) = 123.6 cm; core + blanket height (sodium voided from core) = 140.8 cm. The last two parameters differ for the Na In and Na Out cases due to the change in axial reflector savings which in turn affects the axial DB^2 correction. The core geometry is typical of that for a 1000-MWe reactor, and the enrichments were chosen so that $k_{eff} = 1.0$ with sodium present. Tables D.1 through D.8 list the two-group libraries (the group 1 cut-off being 1.4 MeV) for core and blanket; the sodium voided values assume the sodium to be absent from the core only, which also changes the blanket constants due to the altered spectrum.

Both the transport cross section and the total cross section are listed since the Benoist theory (see Chapter 3) requires both. The ANISN calculations were performed in the transport approximation; thus the σ_s given in the tables is in reality $\sigma_s^{inel} + (1-\bar{\mu})\sigma_s^{el}$. The group-collapse yielded the values of σ_{tr}, from which σ_t was calculated in two steps:

$$\sigma'_s = (\sigma_{tr} - \sigma_a)/(1-\bar{\mu}) \qquad (D.1)$$

and

$$\sigma_t = \sigma'_s + \sigma_a \ . \qquad (D.2)$$

The result of Eq. (D.2) is not rigorously true since it implies: $\sigma_t = \sigma_a + \sigma_s^{el} + \frac{\sigma_s^{inel}}{1 - \bar{\mu}}$ instead of the proper definition: $\sigma_t = \sigma_a + \sigma_s^{el} + \sigma_s^{inel}$. The imprecision arises because it is not possible to separate σ_s^{el} and σ_s^{inel} out of the collapsed σ_s (i.e., $\sigma_{tr} = \sigma_a + (1-\bar{\mu})\sigma_s^{el} + \sigma_s^{inel}$). However, the error is negligible since $\sigma_s^{el} \gg \sigma_s^{inel}$ for the light elements and $(1-\bar{\mu}) \geq .94 \sim 1.0$ (for the worst case, carbon, $1 - \bar{\mu} = .94$). The ultimate quantity calculated is Σ_t whose main contribution comes from the heavy elements Pu-239 and U-238 for which $1 - \bar{\mu} \sim .997$; thus the overall effect of the error in Eq. (D.2) is insignificant.

Table D.9 lists the nuclide number densities required to calculate regionwise macroscopic cross section within DELKHET.

TABLE D.1

Two-Group* Library for Oxide Core – Na In
(barns)

		Group 1	Group 2
Oxygen	σ_a	0.010256	0.0
	σ_{tr}	1.4503	3.4850
	σ_s	1.2519	3.4850
	σ_t	1.5047	3.6365
	σ_r	0.18807	–
Sodium	σ_a	0.0018692	0.0020010
	σ_{tr}	1.9707	4.9686
	σ_s	1.5644	4.9665
	σ_t	2.0174	5.1169
	σ_r	0.40442	–
Iron	σ_a	0.0036805	0.018680
	σ_{tr}	2.4241	5.0516
	σ_s	1.7278	5.0328
	σ_t	2.4449	5.1123
	σ_r	0.69255	–
Pu-239	σ_a	2.0177	2.3232
	$\nu\sigma_f$	6.3980	5.4229
	σ_{tr}	4.7911	10.450
	σ_s	1.7070	8.1267
	σ_t	4.7959	10.473
	σ_r	1.0664	–
U-238	σ_a	0.57821	0.37268
	$\nu\sigma_f$	1.5136	0.0036785
	σ_{tr}	4.9917	10.337
	σ_s	1.8282	9.9640
	σ_t	4.9968	10.365
	σ_r	2.5852	–

*Group 1 = 10.5 MeV - 1.4 MeV ; $\chi_1 = .57$
Group 2 = 1.4 MeV - 0.0252 eV ; $\chi_2 = .43$

TABLE D.2

Two-Group Library for Blanket (Oxide Core – Na In)
(barns)

		Group 1	Group 2
Oxygen	σ_a	0.010519	0.0
	σ_{tr}	1.4460	3.4629
	σ_s	1.2424	3.4629
	σ_t	1.5000	3.6135
	σ_r	0.19306	–
Sodium	σ_a	0.0018570	0.0037377
	σ_{tr}	1.9743	6.6328
	σ_s	1.5633	6.6289
	σ_t	2.0210	6.8306
	σ_r	0.40916	–
Iron	σ_a	0.0036857	0.022911
	σ_{tr}	2.4234	5.7646
	σ_s	1.7172	5.7416
	σ_t	2.4441	5.8337
	σ_r	0.70251	–
Pu-239	σ_a	2.0176	2.5315
	$\nu\sigma_f$	6.3945	5.6439
	σ_{tr}	4.7956	11.566
	σ_s	1.7113	9.0343
	σ_t	4.8004	11.591
	σ_r	1.0667	–
U-238	σ_a	0.57699	0.45871
	$\nu\sigma_f$	1.5073	0.0015791
	σ_{tr}	5.0027	11.421
	σ_s	1.8354	10.962
	σ_t	5.0079	11.452
	σ_r	2.5901	–

TABLE D.3

Two-Group Library for Oxide Core – Na Out
(barns)

		Group 1	Group 2
Oxygen	σ_a	0.010795	0.0
	σ_{tr}	1.4465	3.4907
	σ_s	1.2506	3.4907
	σ_t	1.5009	3.6425
	σ_r	0.18507	–
Iron	σ_a	0.0037397	0.016091
	σ_{tr}	2.4193	4.7622
	σ_s	1.7248	4.7460
	σ_t	2.4401	4.8194
	σ_r	0.69076	–
Pu-239	σ_a	2.0171	2.1454
	$\nu\sigma_f$	6.4043	5.1713
	σ_{tr}	4.7822	10.003
	σ_s	1.6996	7.8575
	σ_t	4.7870	10.025
	σ_r	1.0656	–
U-238	σ_a	0.57917	0.30571
	$\nu\sigma_f$	1.5204	0.0038267
	σ_{tr}	4.9785	9.9418
	σ_s	1.8213	9.6361
	σ_t	4.9836	9.9688
	σ_r	2.5779	–

TABLE D.4

Two-Group Library for Blanket (Oxide Core – Na Out)
(barns)

		Group 1	Group 2
Oxygen	σ_a	0.010860	0.0
	σ_{tr}	1.4435	3.4630
	σ_s	1.2413	3.4630
	σ_t	1.4975	3.6135
	σ_r	0.19136	–
Sodium	σ_a	0.0019155	0.0037447
	σ_{tr}	1.9704	6.6585
	σ_s	1.5607	6.6547
	σ_t	2.0170	6.8572
	σ_r	0.40777	–
Iron	σ_a	0.0037190	0.022329
	σ_{tr}	2.4205	5.7021
	σ_s	1.7150	5.6798
	σ_t	2.4412	5.7706
	σ_r	0.70176	–
Pu-239	σ_a	2.0172	2.4782
	$\nu\sigma_f$	6.3981	5.5678
	σ_{tr}	4.7903	11.438
	σ_s	1.7069	8.9599
	σ_t	4.7951	11.463
	σ_r	1.0662	–
U-238	σ_a	0.57749	0.43981
	$\nu\sigma_f$	1.5111	0.0015614
	σ_{tr}	4.9948	11.313
	σ_s	1.8314	10.873
	σ_t	4.9999	11.344
	σ_r	2.5857	–

TABLE D.5

Two-Group Library for Carbide Core – Na In
(barns)

		Group 1	Group 2
Carbon	σ_a	4.2044E-5	0.0
	σ_{tr}	1.6046	3.7372
	σ_s	1.3309	3.7372
	σ_t	1.6829	3.9571
	σ_r	0.27364	–
Sodium	σ_a	0.0018834	0.0018349
	σ_{tr}	1.9608	4.8555
	σ_s	1.5620	4.8535
	σ_t	2.0074	5.0003
	σ_r	0.39692	–
Iron	σ_a	0.0036640	0.017381
	σ_{tr}	2.4207	4.8859
	σ_s	1.7367	4.8684
	σ_t	2.4416	4.9445
	σ_r	0.68035	–
Pu-239	σ_a	2.0165	2.2256
	$\nu\sigma_f$	6.4038	5.2947
	σ_{tr}	4.7780	10.107
	σ_s	1.6959	7.8810
	σ_t	4.7827	10.129
	σ_r	1.0656	–
U-238	σ_a	0.57951	0.33646
	$\nu\sigma_f$	1.5232	0.0040714
	σ_{tr}	4.9661	10.010
	σ_s	1.8149	9.6735
	σ_t	4.9712	10.037
	σ_r	2.5716	–

TABLE D.6

Two-Group Library for Blanket (Carbide Core – Na In)
(barns)

		Group 1	Group 2
Carbon	σ_a	3.9677E-5	0.0
	σ_{tr}	1.6014	3.9040
	σ_s	1.3255	3.9040
	σ_t	1.6794	4.1336
	σ_r	0.27580	–
Sodium	σ_a	0.0018502	0.0032557
	σ_{tr}	1.9610	6.2307
	σ_s	1.5610	6.2274
	σ_t	2.0076	6.4166
	σ_r	0.39816	–
Iron	σ_a	0.0036436	0.020810
	σ_{tr}	2.4198	5.5002
	σ_s	1.7324	5.4793
	σ_t	2.4407	5.5662
	σ_r	0.68375	–
Pu-239	σ_a	2.0160	2.3765
	$\nu\sigma_f$	6.4018	5.4403
	σ_{tr}	4.7781	11.026
	σ_s	1.6963	8.6495
	σ_t	4.7828	11.050
	σ_r	1.0657	–
U-238	σ_a	0.57879	0.40119
	$\nu\sigma_f$	1.5204	0.0019778
	σ_{tr}	4.9669	10.914
	σ_s	1.8167	10.513
	σ_t	4.9720	10.944
	σ_r	2.5715	–

TABLE D.7

Two-Group Library for Carbide Core – Na Out
(barns)

		Group 1	Group 2
Carbon	σ_a	4.4366E-5	0.0
	σ_{tr}	1.6022	3.6761
	σ_s	1.3334	3.6761
	σ_t	1.6806	3.8924
	σ_r	0.26875	–
Iron	σ_a	0.0037107	0.015027
	σ_{tr}	2.4163	4.6064
	σ_s	1.7354	4.5913
	σ_t	2.4372	4.6618
	σ_r	0.67713	–
Pu-239	σ_a	2.0158	2.0896
	$\nu\sigma_f$	6.4099	5.1264
	σ_{tr}	4.7687	9.6800
	σ_s	1.6881	7.5902
	σ_t	4.773	9.7013
	σ_r	1.0648	–
U-238	σ_a	0.58049	0.28301
	$\nu\sigma_f$	1.5303	0.0043322
	σ_{tr}	4.9514	9.6122
	σ_s	1.8072	9.3293
	σ_t	4.9565	9.6383
	σ_r	2.5636	–

TABLE D.8

Two-Group Library for Blanket (Carbide Core – Na Out)
(barns)

		Group 1	Group 2
Carbon	σ_a	4.0754E-5	0.0
	σ_{tr}	1.5999	3.8848
	σ_s	1.3266	3.8848
	σ_t	1.6779	4.1134
	σ_r	0.27317	–
Sodium	σ_a	0.0018958	0.0032049
	σ_{tr}	1.9571	6.1988
	σ_s	1.5588	6.1956
	σ_t	2.0036	6.3838
	σ_r	0.39645	–
Iron	σ_a	0.0036674	0.020137
	σ_{tr}	2.4172	5.4146
	σ_s	1.7314	5.3943
	σ_t	2.4381	5.4795
	σ_r	0.68214	–
Pu-239	σ_a	2.0156	2.3317
	$\nu\sigma_f$	6.4051	5.3814
	σ_{tr}	4.7728	10.876
	σ_s	1.6920	8.5445
	σ_t	4.7775	10.900
	σ_r	1.0653	–
U-238	σ_a	0.57929	0.38403
	$\nu\sigma_f$	1.5241	0.0019839
	σ_{tr}	4.9587	10.776
	σ_s	1.8124	10.391
	σ_t	4.9638	10.805
	σ_r	2.5668	–

TABLE D.9

Nuclide Number Densities

($10^{24}/cm^3$)

Nuclide	Metal	Oxide*	Carbide*
Pu-239	0.0494	0.0222	0.02646
U-238	0.0483	0.0218	0.0295
U-235	0.0483	0.0218	0.0295
Na**	0.0224		
Fe	0.0848		

* 90 % theoretical density

** 800 °F

Appendix E

COMPUTER CODE NOTES

In this appendix, listings of the two minor codes programmed to perform the heterogeneity calculations discussed in the text are presented, as well as comments on using the programs.

E.1 DELKHET

DELKHET is a code which calculates the spatial flux distribution and anisotropic diffusion components of the heterogeneity effect. The former is calculated using the escape/transmission probability formalism of Chapter 2, while the latter is based upon the theory of Benoist discussed in Chapter 3. The reactivity effects are calculated both from a two-group, equivalent bare core, first order perturbation theory approach and from the "direct" method of Section 4.1 (i.e., calculating the total differential Δk).

E.1.1 Input to DELKHET

Variable	Columns	Format	Description
Card 1 (To run a series of cases, repeat from this card)			
TITLE(18)	1-72	18A4	Identification
CZECH	73-80	G8.0	Normally blank field. If CZECH > 0.0, program stops; to be used as an end card following last case.
Card 2			
ITAB	1-4	I4	ITAB=0, cross-section table to be input ITAB=1, use cross-section table from previous case (not input for present case)

Variable	Columns	Format	Description
Card 2 (continued)			
IFLAG	5-8	I4	IFLAG=0, full calculation for minimum critical core (R = 0.55 H) IFLAG=1, ratio of average fluxes to be input IFLAG=2, bucklings to be input IFLAG=3, flux ratios and bucklings to be input IFLAG=4, uses bucklings from previous case (not input for present case) IFLAG=5, core L/D to be input (calculates critical core size)
R(1)	9-20	G12.0	fuel rod radius (cm)
R(2)	21-32	G12.0	clad outer radius (cm)
R(3)	33-44	G12.0	unit cell outer radius (cm)
CHI1	45-56	G12.0	fraction of fission spectrum in group 1
CHI2	57-68	G12.0	fraction of fission spectrum in group 2
BETA	69-80	G12.0	total delayed neutron fraction
Cards 3-12 (absent if ITAB=1)			
MICRO1(5,5)	1-60	5G12.0	group 1 cross sections
MICRO2(5,4)	1-48	4G12.0	group 2 cross sections

Cross-section library formed in the following order:

Card	Cross-section description
3	U-238, group 1
4	U-238, group 2
5	Pu-239 (or U-235), group 1
6	Pu-239 (or U-235), group 2
7	O (or C), group 1
8	O (or C), group 2
9	Fe, group 1
10	Fe, group 2
11	Na, group 1
12	Na, group 2

Order of cross sections on each card:

group 1: absorption, nu * fission, transport, removal, total

group 2: absorption, nu * fission, transport, total

All cards must be present, even if element is absent in core (blank card may be inserted in that case). Zeros may be entered as blank fields. Last eight columns of cross-section cards may be used for any label.

Variable	Columns	Format	Description
Card 13			
DNS(5)	1-60	5G12.0	Regionwise number densities in the order: U-238 Pu-239 or U-235 } in fuel rod O or C Fe — in clad Na — in coolant region Last eight columns may be used for label.
Card 14 (absent unless IFLAG=5)			
ELDE	1-12	G12.0	L/D for core
Card 15 (absent unless IFLAG=2 or IFLAG=3)			
B2	1-12	G12.0	total buckling (cm^{-2})
B2RAD	13-24	G12.0	radial buckling (cm^{-2})
B2AX	25-36	G12.0	axial buckling (cm^{-2})
Card 16 (absent unless IFLAG=1 or IFLAG=3)			
FUCL(1)	1-12	G12.0	average clad flux ÷ average fuel flux for group 1
FUCO(1)	13-24	G12.0	average coolant flux ÷ average fuel flux for group 1
FUCL(2)	25-36	G12.0	average clad flux ÷ average fuel flux for group 2
FUCO(2)	37-48	G12.0	average coolant flux ÷ average fuel flux for group 2

E.1.2 Output from DELKHET

The output from DELKHET consists of three pages per case. The first page provides an input check and prints out the cross-section table and number densities used. The second page presents the results of the spatial flux distribution calculation. The cell radii input are printed (R), as well as the sum of $\Sigma_a + \Sigma_r + DB^2$ for each region (SIG). Regionwise sources are printed (S). The calculated flux ratios for the first-flight and multiply-collided groups are given.

On the third page, the results of the heterogeneous reactivity calculation are presented. The homogeneous (i.e., volume-averaged) and heterogeneous (i.e., spatially flux-weighted and anisotropic diffusion corrected) cell constants are printed, the left-hand column for group 1 and the right for group 2. As an input check, the fission spectrum χ_i are printed, as are the B_j^2 which may have been internally calculated depending on the IFLAG option. The k_{eff} of the homogenized core is printed (K). The nine individual reactivity contributions calculated in two ways (perturbation theory and partial differentials of k) are printed, together with the net heterogeneous effect.

E.1.3 Typical Procedures

If the two-group cross-section set for the case of interest is not available, the tables in Appendix D (which were generated for typical FBR cases) may be used. If the consistent reflector savings procedure of Section 6.1 is to be used, DELKHET calculations for the sodium-in cases with IFLAG = 0 will yield the required critical total buckling (BSQUARED). This buckling may then be divided into radial and axial components using the procedures of Section 6.1. Whereupon, the

DELKHET calculations may be repeated with IFLAG = 2 and the axial and radial buckling values calculated input on Card 15 obtain the final results.

E.1.4 Listing of DELKHET

The following pages contain a listing of the DELKHET code.

```
C                                                                       DELK    1
C                              *** DELKHET ***                          DELK    2
C                                                                       DELK    3
C   A PROGRAM TO CALCULATE THE TWO-GROUP HETEROGENEOUS REACTIVITY EFFECTSDELK    4
C     DUE TO ANISOTROPIC DIFFUSION AND NON-UNIFORM UNIT CELL FLUXES.    DELK    5
C                                                                       DELK    6
      DIMENSION TITLE(18),R(3),SIG(3),RAT(4),XAB1(3),XTRAN1(3),XNUF1(3),DELK    7
     1 XSIG12(3),XD1(3),XD2(3),XAB2(3),XNUF2(3),XTRAN2(3),FUCL(2),      DELK    8
     2 FUCO(2),XTOT1(3),XTOT2(3),ONS(5),TAG11(5),TAG12(5),TAG21(5),     DELK    9
     3 TAG22(5)                                                         DELK   10
      REAL JAPS,JAMS,JAPN,JAMN,NUF1,NUF2,K,MICRO1(5,5),MICRO2(5,4)      DELK   11
  1   READ(5,5) TITLE,CZECH                                             DELK   12
      IF(CZECH.GT.0.0)STOP                                              DELK   13
C        READ IN OPTION CONTROL, CELL RADII, FISSION SPECTRUM, BETA     DELK   14
      READ(5,10)ITAB,IFLAG,R,CHI1,CHI2,BETA                             DELK   15
C        ITAB=0, INPUT CROSS-SECTION TABLE                              DELK   16
C        ITAB=1, USE CROSS-SECTION TABLE FROM PREVIOUS CASE             DELK   17
C        IFLAG=0, FULL CALCULATION, ASSUMES MINIMUM CORE VOLUME         DELK   18
C        IFLAG=1, INPUT FLUX RATIOS                                     DELK   19
C        IFLAG=2, INPUT BUCKLING                                        DELK   20
C        IFLAG=3, INPUT RATIOS AND BUCKLING                             DELK   21
C        IFLAG=4, USES BUCKLING FROM PREVIOUS CASE                      DELK   22
C        IFLAG=5, INPUT CORE L/D, ASSUMES K=1.                          DELK   23
  5   FORMAT(18A4,G8.0)                                                 DELK   24
  10  FORMAT(2I4,6G12.0)                                                DELK   25
      V1=3.141593*(R(1)**2)                                             DELK   26
      V2=3.141593*(R(2)**2-R(1)**2)                                     DELK   27
      V3=3.141593*(R(3)**2-R(2)**2)                                     DELK   28
      Z3 = (R(3)**2-R(2)**2)/R(2)                                       DELK   29
      IF(ITAB.EQ.1)GO TO 211                                            DELK   30
C        READ IN TWO GROUP MICRO-SIGMAS                                 DELK   31
      DO 210 I=1,5                                                      DELK   32
      READ(5,82)(MICRO1(I,KK),KK=1,5),TAG11(I),TAG12(I)                 DELK   33
  210 READ(5,83)(MICRO2(I,KK),KK=1,4),TAG21(I),TAG22(I)                 DELK   34
  82  FORMAT(5G12.0,12X,2A4)                                            DELK   35
  83  FORMAT(4G12.0,24X,2A4)                                            DELK   36
```

```
C         MICRO1=ABS,NUF,TRAN,REM,TOTAL FOR GROUP 1                          DELK  37
C         MICRO2=ABS,NUF,TRAN,TOTAL FOR GROUP 2                              DELK  38
  211 CONTINUE                                                               DELK  39
C         READ IN REGION-WISE NUMBER DENSITIES                               DELK  40
      READ(5,82)(DNS(I),I=1,5),TAGA,TAGB                                     DELK  41
C         DNS=U-238,U-235/PU-239,O,FE,NA NUMBER DENSITIES                    DELK  42
      WRITE(6,84) TITLE                                                      DELK  43
   84 FORMAT(1H1,20X18A4,///,' INPUT CHECK - CROSS SECTION LIBRARY')          DELK  44
      DO 85 I=1,5                                                            DELK  45
      WRITE(6,12)(MICRO1(I,KK),KK=1,5),TAG11(I),TAG12(I)                     DELK  46
   85 WRITE(6,13)(MICRO2(I,KK),KK=1,4),TAG21(I),TAG22(I)                     DELK  47
      WRITE(6,12)(DNS(I),I=1,5),TAGA,TAGB                                    DELK  48
   12 FORMAT(1H ,5G12.5,12X,2A4)                                             DELK  49
   13 FORMAT(1H ,4G12.5,24X,2A4)                                             DELK  50
      WRITE(6,86)                                                            DELK  51
   86 FORMAT(1H ,'NOTE--ORDER OF ELEMENTS AND GROUPS ON INPUT CARDS IS UDELK  52
     1238-1,U238-2,U235-1/PU239-1,U235-2/PU239-2,O-1,O-2,FE-1,FE-2,NA-1,DELK  53
     1NA-2',                                                                 DELK  54
     2/,7X,'ORDER OF TYPES ON EACH CARD IS ABS, NUF, TRAN, REM, TOTAL FODELK  55
     3R GROUP 1',/,38X,'ABS, NUF, TRAN, TOTAL FOR GROUP 2',/,7X,'NUMBER DELK  56
     4DENSITIES INPUT IN SAME ORDER AS CROSS-SECTIONS.')                     DELK  57
      WRITE(6,20) TITLE                                                      DELK  58
C         CALCULATE REGION-WISE MACROSCOPIC CROSS-SECTIONS                   DELK  59
      XAB1(1)=DNS(1)*MICRO1(1,1)+DNS(2)*MICRO1(2,1)+DNS(3)*MICRO1(3,1)       DELK  60
      XAB2(1)=DNS(1)*MICRO2(1,1)+DNS(2)*MICRO2(2,1)+DNS(3)*MICRO2(3,1)       DELK  61
      XAB1(2)=DNS(4)*MICRO1(4,1)                                             DELK  62
      XAB2(2)=DNS(4)*MICRO2(4,1)                                             DELK  63
      XAB1(3)=DNS(5)*MICRO1(5,1)                                             DELK  64
      XAB2(3)=DNS(5)*MICRO2(5,1)                                             DELK  65
      XNUF1(1)=DNS(1)*MICRO1(1,2)+DNS(2)*MICRO1(2,2)                         DELK  66
      XNUF2(1)=DNS(1)*MICRO2(1,2)+DNS(2)*MICRO2(2,2)                         DELK  67
      XTRAN1(1)=DNS(1)*MICRO1(1,3)+DNS(2)*MICRO1(2,3)+DNS(3)*MICRO1(3,3)DELK  68
      XTRAN2(1)=DNS(1)*MICRO2(1,3)+DNS(2)*MICRO2(2,3)+DNS(3)*MICRO2(3,3)DELK  69
      XTRAN1(2)=DNS(4)*MICRO1(4,3)                                           DELK  70
      XTRAN2(2)=DNS(4)*MICRO2(4,3)                                           DELK  71
      XTRAN1(3)=DNS(5)*MICRO1(5,3)                                           DELK  72
```

```
      XTRAN2(3)=DNS(5)*MICRO2(5,3)                                          DELK  73
      XSIG12(1)=DNS(1)*MICRO1(1,4)+DNS(2)*MICRO1(2,4)+DNS(3)*MICRO1(3,4)DELK  74
      XSIG12(2)=DNS(4)*MICRO1(4,4)                                          DELK  75
      XSIG12(3)=DNS(5)*MICRO1(5,4)                                          DELK  76
      XTOT1(1)=DNS(1)*MICRO1(1,5)+DNS(2)*MICRO1(2,5)+DNS(3)*MICRO1(3,5) DELK  77
      XTOT2(1)=DNS(1)*MICRO2(1,4)+DNS(2)*MICRO2(2,4)+DNS(3)*MICRO2(3,4) DELK  78
      XTOT1(2)=DNS(4)*MICRO1(4,5)                                           DELK  79
      XTOT2(2)=DNS(4)*MICRO2(4,4)                                           DELK  80
      XTOT1(3)=DNS(5)*MICRO1(5,5)                                           DELK  81
      XTOT2(3)=DNS(5)*MICRO2(5,4)                                           DELK  82
      DO 214 I=2,3                                                          DELK  83
      XNUF1(I)=0.0                                                          DELK  84
  214 XNUF2(I)=0.0                                                          DELK  85
      DO 216 I=1,3                                                          DELK  86
      IF(XTRAN1(I).EQ.0.0) GO TO 215                                        DELK  87
      XD1(I)=.3333333/XTRAN1(I)                                             DELK  88
  215 CONTINUE                                                              DELK  89
      IF(XTRAN2(I).EQ.0.0) GO TO 216                                        DELK  90
      XD2(I)=.3333333/XTRAN2(I)                                             DELK  91
  216 CONTINUE                                                              DELK  92
C        CALCULATE VOLUME HOMOGENIZED CELL CONSTANTS                        DELK  93
      DEN=V1+V2+V3                                                          DELK  94
      AB1=(XAB1(1)*V1+XAB1(2)*V2+XAB1(3)*V3)/DEN                            DELK  95
      AB2=(XAB2(1)*V1+XAB2(2)*V2+XAB2(3)*V3)/DEN                            DELK  96
      NUF1=(XNUF1(1)*V1+XNUF1(2)*V2+XNUF1(3)*V3)/DEN                        DELK  97
      NUF2=(XNUF2(1)*V1+XNUF2(2)*V2+XNUF2(3)*V3)/DEN                        DELK  98
      SIG12=(XSIG12(1)*V1+XSIG12(2)*V2+XSIG12(3)*V3)/DEN                    DELK  99
      TRAN1=(XTRAN1(1)*V1+XTRAN1(2)*V2+XTRAN1(3)*V3)/DEN                    DELK 100
      TRAN2=(XTRAN2(1)*V1+XTRAN2(2)*V2+XTRAN2(3)*V3)/DEN                    DELK 101
C        D1,D2 ARE HOMOGENIZED D'S, BASED ON VOL. AVE. SIGMA TRANSPORT      DELK 102
      D1=.3333333/TRAN1                                                     DELK 103
      D2=.3333333/TRAN2                                                     DELK 104
      IF(IFLAG.EQ.4)GO TO 110                                               DELK 105
      IF(IFLAG.GE.2 .AND. IFLAG.LT.5)GO TO 108                              DELK 106
C        CALCULATE BUCKLINGS ASSUMING MINIMUM CORE VOLUME                   DELK 107
C                 OR INPUT L/D                                             DELK 108
```

```
      A=D1*D2                                                                DELK 109
      B=AB2*D1+(SIG12+AB1)*D2-NUF1*CHI1*D2-NUF2*CHI2*D1                      DELK 110
      C=(SIG12+AB1)*(AB2-NUF2*CHI2)-AB2*NUF1*CHI1-NUF2*CHI1*SIG12            DELK 111
      B2=(-B+SQRT(B**2-4.*A*C))/(2.*A)                                       DELK 112
      IF(IFLAG.LT.5)GO TO 109                                                DELK 113
      READ(5,2)ELDE                                                          DELK 114
    2 FORMAT(G12.0)                                                          DELK 115
      AR2=((2.404826**2)+(1.570747/ELDE)**2)/B2                              DELK 116
      B2RAD=(2.404826**2)/AR2                                                DELK 117
      B2AX=B2-B2RAD                                                          DELK 118
      GO TO 110                                                              DELK 119
  109 B2RAD=.659556*B2                                                       DELK 120
      B2AX=B2-B2RAD                                                          DELK 121
      GO TO 110                                                              DELK 122
C        OPTIONALLY READ IN BUCKLINGS. VOIDED CELL REQUIRES IFLAG=2 OR 4     DELK 123
  108 READ(5,58)B2,B2RAD,B2AX                                                DELK 124
   58 FORMAT(3G12.0)                                                         DELK 125
  110 CONTINUE                                                               DELK 126
C        OPTIONALLY READ IN FLUX RATIOS: (CLAD/FUEL(I),COOLANT/FUEL(I)),     DELK 127
C                                                    I=GROUP1,GROUP2       DELK 128
      IF(IFLAG.EQ.1.OR.IFLAG.EQ.3) READ(5,83)FUCL(1),FUCO(1),FUCL(2),        DELK 129
     1 FUCO(2),ZILTCH                                                        DELK 130
C        CALCULATION OF D'S FROM ASYMPTOTIC BENOIST THEORY                   DELK 131
C        ZERO'TH ITERATE FOR D WITH FLAT FLUX                                DELK 132
      Z1=1.                                                                  DELK 133
      Z2=1.                                                                  DELK 134
      MMM=1                                                                  DELK 135
      IF(XTRAN1(3).EQ.0.)MMM=2                                               DELK 136
      SUR=3.141593*R(2)                                                      DELK 137
      X6=V1+V2                                                               DELK 138
      MM=1                                                                   DELK 139
      ETAM=V3/SUR*XTRAN1(3)                                                  DELK 140
      ETAMT=V3/SUR*XTOT1(3)                                                  DELK 141
C        HOMOGENIZE FUEL AND CLAD FOR THIS PURPOSE                           DELK 142
      X7=XTRAN1(1)*V1/X6+XTRAN1(2)*V2/X6                                     DELK 143
      ETAU=X6/SUR*X7                                                         DELK 144
```

```
      X8=XTOT1(1)*V1/X6+XTOT1(2)*V2/X6                                  DELK 145
      ETAUT=X6/SUR*X8                                                   DELK 146
   54 CONTINUE                                                          DELK 147
C        CALCULATE PMM,O                                               DELK 148
      C=1.+1./(3.+11./3.*ETAMT)                                         DELK 149
      TR=(1.+2.*ETAMT)/(1.+2.*ETAMT*(C+ETAMT))                          DELK 150
      TZ=2.*TR/(1.+ETAMT/(.51+ETAMT))                                   DELK 151
      BPRM=ETAM*TR                                                      DELK 152
      BPZM=ETAM*TZ                                                      DELK 153
C        CALCULATE PUU,O                                               DELK 154
      C=1.+1./(3.+11./3.*ETAUT)                                         DELK 155
      TR=(1.+2.*ETAUT)/(1.+2.*ETAUT*(C+ETAUT))                          DELK 156
      TZ=2.*TR/(1.+ETAUT/(.51+ETAUT))                                   DELK 157
      IF(XTRAN1(3).EQ.0.)GO TO 71                                       DELK 158
      BPRU=ETAU*TR                                                      DELK 159
      BPZU=ETAU*TZ                                                      DELK 160
      GMR=2.*ETAM*8./9.*(1.-BPRM)                                       DELK 161
      GMZ=2.*ETAM*4./3.*(1.-BPZM)                                       DELK 162
      GUR=2.*ETAU*8./9.*(1.-BPRU)                                       DELK 163
      GUZ=2.*ETAU*4./3.*(1.-BPZU)                                       DELK 164
C        CALCULATE PUU                                                 DELK 165
      BPR=BPRU+(1.-BPRU)*(1.-GMR)*GUR/(1.-(1.-GMR)*(1.-GUR))            DELK 166
      BPZ=BPZU+(1.-BPZU)*(1.-GMZ)*GUZ/(1.-(1.-GMZ)*(1.-GUZ))            DELK 167
      IF (MM.GT.1) GO TO 53                                             DELK 168
   57 DRAD1=XD1(3)*(1.+X6/DEN*Z1*(1.-X7/XTRAN1(3))*(1.+(XTRAN1(3)/X7*Z2-DELK 169
     1 1.)*BPR))                                                        DELK 170
      DAX1 =XD1(3)*(1.+X6/DEN*Z1*(1.-X7/XTRAN1(3))*(1.+(XTRAN1(3)/X7*Z2-DELK 171
     1 1.)*BPZ))                                                        DELK 172
      GO TO 59                                                          DELK 173
C        FOR VOIDED CELL, D CALCULATED ONLY FOR FLAT FLUXES            DELK 174
   71 RM=V3/SUR                                                         DELK 175
      IF(MM.GT.1)GO TO 70                                               DELK 176
      QR=1.-2./9.*8.+1./(ETAU*(1.-ETAU*TR))                             DELK 177
      QZ=2.-2./3.*4.+1./(ETAU*(1.-ETAU*TZ))                             DELK 178
      DRAD1=.3333333/X7*(1.+V3/DEN*(1.+RM*X7*QR))                       DELK 179
      DAX1 =.3333333/X7*(1.+V3/DEN*(1.+RM*X7*QZ))                       DELK 180
```

```
   59  CONTINUE                                                              DELK 181
C      CALCULATION OF FLUX RATIOS FROM TRANSMISSION/ESCAPE/REFLECTION        DELK 182
C                              PROBABILITY THEORY                            DELK 183
       DO 52 I=1,3                                                           DELK 184
   52  SIG(I)=XAB1(I)+XSIG12(I)+DRAD1*B2RAD+DAX1*B2AX                        DELK 185
       IMAP=1                                                                DELK 186
       IF(IFLAG.EQ.1.OR.IFLAG.EQ.3)GO TO 220                                 DELK 187
  101  CONTINUE                                                              DELK 188
C         CALCULATE REGION-WISE CELL SOURCES                                 DELK 189
       IF(IMAP.EQ.1)S1=1.                                                    DELK 190
       IF(IMAP.EQ.2)S1=XSIG12(1)+CHI2*(XNUF1(1)+XNUF2(1)*(SIG12+AB1+D1*B2DELK 191
      1 -CHI1*NUF1)/(CHI1*NUF2))                                             DELK 192
       IF(IMAP.EQ.1)S2=0.0                                                   DELK 193
       IF(IMAP.EQ.2)S2=XSIG12(2)                                             DELK 194
       IF(IMAP.EQ.1)S3=0.0                                                   DELK 195
       IF(IMAP.EQ.2)S3=XSIG12(3)                                             DELK 196
       IF(IMAP.EQ.1 .AND. MMM.EQ.2)WRITE(6,23)                               DELK 197
       IF(IMAP.EQ.2 .AND. MMM.EQ.2)WRITE(6,24)                               DELK 198
   23  FORMAT(30X,' FIRST FLIGHT GROUP',/)                                   DELK 199
   24  FORMAT(30X,' MULTIPLY-COLLIDED GROUP',/)                              DELK 200
C         CALCULATE MEAN CHORD LENGTHS AND VARIOUS PROBABILITIES             DELK 201
   65  CONTINUE                                                              DELK 202
       MARK=0                                                                DELK 203
       IF(MMM.EQ.2)WRITE(6,22)R(1),SIG(1),R(2),SIG(2),R(3),SIG(3)            DELK 204
       IF(MMM.EQ.2)WRITE(6,30)S1,S2,S3                                       DELK 205
       EL1 = SIG(1)*R(1)                                                     DELK 206
       EL2=SIG(2)*(R(2)-R(1))*2.                                             DELK 207
       EL3 = SIG(3)*Z3                                                       DELK 208
       P1 = 1.0-2.0*EL1+2.666667*(EL1**2)                                    DELK 209
       T13=1.-EL2+1.333333*(EL2**2)                                          DELK 210
       P3 = 1.0-2.0*EL3+2.666667*(EL3**2)                                    DELK 211
       PP1 = 1.0-1.333333*EL1                                                DELK 212
       PP3 = 1.0-1.333333*EL3                                                DELK 213
       T31 = (R(1)/R(2))*T13                                                 DELK 214
       T33 = T13-T31                                                         DELK 215
       DNN = 1.0-T33*P3-P1*T13*P3*T31                                        DELK 216
```

```
   60  CONTINUE                                                                  DELK 217
       SS1=S1*PP1*R(1)/2.                                                        DELK 218
       IF(MARK.EQ.2)SS1=0.0                                                      DELK 219
       SSS1=SS1*R(1)/R(2)                                                        DELK 220
       SS3=S3*PP3*Z3*R(2)/(2.*R(1))                                              DELK 221
       IF(MARK.EQ.1)SS3=0.0                                                      DELK 222
       SSS3=SS3*R(1)/R(2)                                                        DELK 223
       DUM4=1.-T33*P3                                                            DELK 224
       DUM6=SS3*T31/DNN                                                          DELK 225
C         CALCULATE THE REGION INTERFACE CURRENTS 'JA..'                        DELK 226
       JAPS=SS1*T13*P3*T31/DNN      +DUM6                                        DELK 227
       JAMS=SS1*DUM4/DNN          +P1*DUM6                                       DELK 228
       DUM7=SSS1*T13/DNN                                                         DELK 229
       JAPN=DUM7      +SSS3*(T33+T31*P1*T13)/DNN                                 DELK 230
       JAMN=P3*DUM7          +SSS3/DNN                                           DELK 231
C         CALCULATE AVERAGE REGION FLUXES                                       DELK 232
       FHI1=(2.*(JAPS-JAMS)+S1*R(1))/(SIG(1)*R(1))                               DELK 233
       IF(SIG(3).EQ.0.0)GO TO 17                                                 DELK 234
       FHI3=(2.*R(2)*(JAPN-JAMN)+S3*(R(3)**2-R(2)**2))/(SIG(3)*                  DELK 235
      1(R(3)**2-R(2)**2))                                                        DELK 236
   17  FHIS=2.*(JAPS+JAMS)                                                       DELK 237
       FHIC=2.*(JAPN+JAMN)                                                       DELK 238
       IF(SIG(3).EQ.0.0)FHI3=FHIC                                                DELK 239
       FHI2=.5*(FHIS+FHIC)                                                       DELK 240
       IF(MARK.EQ.2)GO TO 63                                                     DELK 241
       IF(MARK.EQ.1)GO TO 62                                                     DELK 242
       IF(S2.EQ.0.0)GO TO 61                                                     DELK 243
       HOLD1=FHI1                                                                DELK 244
       HOLD2=FHI2                                                                DELK 245
       HOLD3=FHI3                                                                DELK 246
       MARK=1                                                                    DELK 247
C         REPEAT FOR CASE WITH CLAD SOURCES USING RECIPROCITY THEOREM            DELK 248
       S1=S2                                                                     DELK 249
       GO TO 60                                                                  DELK 250
   62  FHI2=FHI2*V2/V1                                                           DELK 251
       HOLD1=HOLD1+FHI2                                                          DELK 252
```

```
      MARK=2                                                            DELK 253
      S3=S2                                                             DELK 254
      GO TO 60                                                          DELK 255
   63 FHI2=FHI2*V2/V3                                                   DELK 256
      HOLD3=HOLD3+FHI2                                                  DELK 257
      FHI1=HOLD1                                                        DELK 258
      FHI3=HOLD3                                                        DELK 259
      FHI2=.5*(FHI1+FHI3)                                               DELK 260
   61 CONTINUE                                                          DELK 261
      IF(MMM.EQ.2)GO TO 56                                              DELK 262
C     TO CALCULATE D, ITERATE ONCE WITH NON-FLAT FLUXES                 DELK 263
      MMM=2                                                             DELK 264
      Z1=FHI3*DEN/(V1*FHI1+V2*FHI2+V3*FHI3)                             DELK 265
      Z2=(V1*FHI1+V2*FHI2)/(FHI3*X6)                                    DELK 266
      IF(IMAP.EQ.2) GO TO 70                                            DELK 267
      GO TO 57                                                          DELK 268
   56 CONTINUE                                                          DELK 269
      RAT(1)=FHI1/FHIS                                                  DELK 270
      RAT(2)=FHI1/FHI3                                                  DELK 271
      RAT(3)=FHIS/FHIC                                                  DELK 272
      RAT(4)=FHI1/FHI2                                                  DELK 273
      IF(MARK.GT.0)RAT(1)=0.0                                           DELK 274
      IF(MARK.GT.0)RAT(3)=0.0                                           DELK 275
   20 FORMAT(1H1,20X18A4,///,15X,'CALCULATION OF FLUX RATIOS BY PROBABILDELK 276
     1ITY THEORY',///)                                                  DELK 277
   22 FORMAT('    CELL PARAMETERS:',3X,'R(1)=',G12.7,3X,'SIG(1)=',G12.7, DELK 278
     1             /,22X,'R(2)=',G12.7,3X,'SIG(2)=',G12.7,/,22X,'R(3)=',DELK 279
     2             G12.7,3X,'SIG(3)=',G12.7,//)                         DELK 280
   30 FORMAT('    SOURCE DENSITY:',3X,'S(1)=',G13.7,3X,'S(2)=',G13.7,3X, DELK 281
     1'S(3)=',G13.7,//)                                                 DELK 282
      WRITE(6,25)RAT(1),RAT(2),RAT(4),RAT(3)                            DELK 283
   25 FORMAT('       AVE FUEL FLUX / FLUX AT FUEL SURFACE=',G13.7,//,    DELK 284
     1  '       AVE FUEL FLUX / AVE COOLANT FLUX=',G13.7,//,            DELK 285
     2  '       AVE FUEL FLUX / AVE CLAD FLUX=',G13.7,//,               DELK 286
     3  '       FLUX AT FUEL SURFACE / FLUX AT CLAD SURFACE=',G13.7,//, DELK 287
     4 17X,'/ZERO RESULT FOR RECIPROCITY THEOREM CASES/',///)            DELK 288
```

```
   26  FORMAT('                FLUX RATIOS WERE INPUT AND NOT CALCULATED',/DELK 289
      1  '       AVE FUEL FLUX / AVE COOLANT FLUX=',G13.7,//,                DELK 290
      2  '       AVE FUEL FLUX / AVE CLAD FLUX=',G13.7,///)                  DELK 291
       FUCL(IMAP)=1./RAT(4)                                                  DELK 292
       FUCO(IMAP)=1./RAT(2)                                                  DELK 293
       IF(IMAP.GT.1)GO TO 103                                                DELK 294
  220  CONTINUE                                                              DELK 295
C         REPEAT FOR MULTIPLY-COLLIDED GROUP                                 DELK 296
       MMM=1                                                                 DELK 297
       IF(XTRAN1(3).EQ.0.)MMM=2                                              DELK 298
       Z1=1.                                                                 DELK 299
       Z2=1.                                                                 DELK 300
       IMAP=2                                                                DELK 301
       ETAM=V3/SUR*XTRAN2(3)                                                 DELK 302
       ETAMT=V3/SUR*XTOT2(3)                                                 DELK 303
       X7=XTRAN2(1)*V1/X6+XTRAN2(2)*V2/X6                                    DELK 304
       ETAU=X6/SUR*X7                                                        DELK 305
       X8=XTOT2(1)*V1/X6+XTOT2(2)*V2/X6                                      DELK 306
       ETAUT=X6/SUR*X8                                                       DELK 307
       MM=2                                                                  DELK 308
       GO TO 54                                                              DELK 309
   53  CONTINUE                                                              DELK 310
   70  CONTINUE                                                              DELK 311
       IF(XTRAN2(3).EQ.0.)GO TO 72                                           DELK 312
       DRAD2=XD2(3)*(1.+X6/DEN*Z1*(1.-X7/XTRAN2(3))*(1.+(XTRAN2(3)/X7*Z2-DELK 313
      1 1.)*BPR))                                                            DELK 314
       DAX2 =XD2(3)*(1.+X6/DEN*Z1*(1.-X7/XTRAN2(3))*(1.+(XTRAN2(3)/X7*Z2-DELK 315
      1 1.)*BPZ))                                                            DELK 316
       GO TO 64                                                              DELK 317
C         FOR VOIDED CELL, D CALCULATED ONLY FOR FLAT FLUXES                 DELK 318
   72  QR=1.-2./9.*8.+1./(ETAU*(1.-ETAU*TR))                                 DELK 319
       QZ=2.-2./3.*4.+1./(ETAU*(1.-ETAU*TZ))                                 DELK 320
       DRAD2=.3333333/X7*(1.+V3/DEN*(1.+RM*X7*QR))                           DELK 321
       DAX2 =.3333333/X7*(1.+V3/DEN*(1.+RM*X7*QZ))                           DELK 322
   64  CONTINUE                                                              DELK 323
       DO 47 I=1,3                                                           DELK 324
```

```
   47   SIG(I)=XAB2(I)+DRAD2*B2RAD+DAX2*B2AX                              DELK 325
        IF(IFLAG.EQ.1.OR.IFLAG.EQ.3)GO TO 48                              DELK 326
        GO TO 101                                                         DELK 327
   103  CONTINUE                                                          DELK 328
        GO TO 49                                                          DELK 329
   48   RAT(2)=1./FUCO(1)                                                 DELK 330
        RAT(4)=1./FUCL(1)                                                 DELK 331
        WRITE(6,23)                                                       DELK 332
        WRITE(6,26)RAT(2),RAT(4)                                          DELK 333
        RAT(2)=1./FUCO(2)                                                 DELK 334
        RAT(4)=1./FUCL(2)                                                 DELK 335
        WRITE(6,24)                                                       DELK 336
        WRITE(6,26)RAT(2),RAT(4)                                          DELK 337
   49   CONTINUE                                                          DELK 338
C                                                                         DELK 339
C          CALCULATED FLUX RATIOS ARE NOW USED TO DETERMINE DELTA K       DELK 340
C                                                                         DELK 341
C          CALCULATE FLUX AND VOLUME WEIGHTED CROSS-SECTIONS (HET'GENEOUS)DELK 342
        DEN=V1+V2*FUCL(1)+V3*FUCO(1)                                      DELK 343
        HAB1=(XAB1(1)*V1+XAB1(2)*V2*FUCL(1)+XAB1(3)*V3*FUCO(1))/DEN       DELK 344
        HNUF1=(XNUF1(1)*V1+XNUF1(2)*V2*FUCL(1)+XNUF1(3)*V3*FUCO(1))/DEN   DELK 345
        HSIG12=(XSIG12(1)*V1+XSIG12(2)*V2*FUCL(1)+XSIG12(3)*V3*FUCO(1))/  DELK 346
       1 DEN                                                              DELK 347
        DEN=V1+V2*FUCL(2)+V3*FUCO(2)                                      DELK 348
        HAB2=(XAB2(1)*V1+XAB2(2)*V2*FUCL(2)+XAB2(3)*V3*FUCO(2))/DEN       DELK 349
        HNUF2=(XNUF2(1)*V1+XNUF2(2)*V2*FUCL(2)+XNUF2(3)*V3*FUCO(2))/DEN   DELK 350
C          CALCULATE CROSS-SECTION PERTURBATIONS                          DELK 351
        DAB1=HAB1-AB1                                                     DELK 352
        DAB2=HAB2-AB2                                                     DELK 353
        DNUF1=HNUF1-NUF1                                                  DELK 354
        DNUF2=HNUF2-NUF2                                                  DELK 355
        DSIG12=HSIG12-SIG12                                               DELK 356
        DD1=DRAD1-D1                                                      DELK 357
        DD2=DRAD2-D2                                                      DELK 358
        DDAX1=DAX1-D1                                                     DELK 359
        DDAX2=DAX2-D2                                                     DELK 360
```

```
      RAT1=SIG12+AB1+D1*B2                                                      DELK 361
      RAT2=AB2+D2*B2                                                            DELK 362
      K=CHI1*NUF1/RAT1+CHI2*NUF2/RAT2+CHI1*SIG12*NUF2/(RAT1*RAT2)               DELK 363
      DUM=0.0                                                                   DELK 364
      WRITE(6,300) TITLE                                                        DELK 365
  300 FORMAT(1H1,20X18A4)                                                       DELK 366
      WRITE(6,51)                                                               DELK 367
   51 FORMAT(1H ,///,39X,'CALCULATION OF HETEROGENEOUS DELTA K',///)            DELK 368
      WRITE(6,45)AB1,AB2,NUF1,NUF2,D1,D2,D1,D2,DUM,SIG12                        DELK 369
      WRITE(6,46)HAB1,HAB2,HNUF1,HNUF2,DAX1,DAX2,DRAD1,DRAD2,DUM,HSIG12         DELK 370
      WRITE(6,14)CHI1,CHI2,BETA,K,B2,B2RAD,B2AX                                 DELK 371
   45 FORMAT('      HOMOGENEOUS CONSTANTS',/,10X,'ABS',5X,2G14.7,/,10X,         DELK 372
     1'NUFIS',3X,2G14.7,/,10X,'DAXL',4X,2G14.7,/,10X,'DRAD',4X,2G14.7,          DELK 373
     2 /,10X,'REM',5X,2G14.7)                                                   DELK 374
   46 FORMAT('    HETEROGENEOUS CONSTANTS',/,10X,'ABS',5X,2G14.7,/,10X,         DELK 375
     1'NUFIS',3X,2G14.7,/,10X,'DAXL',4X,2G14.7,/,10X,'DRAD',4X,2G14.7,          DELK 376
     2 /,10X,'REM',5X,2G14.7)                                                   DELK 377
   14 FORMAT('      CHI(1)=',G12.7,'     CHI(2)=',G12.7,'      BETA=',         DELK 378
     1G12.7,'      K=',G12.7,'   BSQUARED=',G13.7,/,38X,'      RADIAL B2='DELK 379
     1 ,G13.7,'      AXIAL B2=',G13.7,//)                                      DELK 380
      WRITE(6,42)                                                               DELK 381
   42 FORMAT(30X,'         METHOD:  PARTIAL DIFFERENTIALS OF K')                DELK 382
C        WEIGHT CROSS-SECTION PERTURBATIONS FOR CONTRIBUTIONS TO DELTA KDELK 383
      DKNUF1=(CHI1/RAT1)*DNUF1                                                  DELK 384
      DKAB1=(NUF1/(RAT1**2)+NUF2*SIG12/((RAT1**2)*RAT2))*CHI1*DAB1              DELK 385
      DKREM=(NUF1/(RAT1**2)-NUF2*(RAT1-SIG12)/((RAT1**2)*RAT2))*CHI1*           DELK 386
     1CSIG12                                                                    DELK 387
      DKNUF2=(CHI2/RAT2+CHI1*SIG12/(RAT1*RAT2))*DNUF2                           DELK 388
      DKAB2=(CHI2/(RAT2**2)+     CHI1*SIG12/((RAT2**2)*RAT1))*DAB2*NUF2         DELK 389
      DKD1=(NUF1/(RAT1**2)+NUF2*SIG12/((RAT1**2)*RAT2))*CHI1*                   DELK 390
     1 (DD1*B2RAD)                                                              DELK 391
      DKD3=(NUF1/(RAT1**2)+NUF2*SIG12/((RAT1**2)*RAT2))*CHI1*                   DELK 392
     1            (DDAX1*B2AX)                                                DELK 393
      DKD2=(CHI2/(RAT2**2)+CHI1*SIG12/((RAT2**2)*RAT1))*NUF2*                   DELK 394
     1 (DD2*B2RAD)                                                              DELK 395
      DKD4=(CHI2/(RAT2**2)+CHI1*SIG12/((RAT2**2)*RAT1))*NUF2*                   DELK 396
```

```
     1            (DDAX2*B2AX)                                                    DELK 397
      DELK=(DKNUF1-DKAB1-DKREM+DKNUF2-DKAB2-DKD1-DKD2-DKD3-DKD4)/K                DELK 398
      DELKS=DELK/BETA*100.                                                        DELK 399
      S1=DKNUF1/(BETA*K)*100.                                                     DELK 400
      S2=DKAB1/(BETA*K)*(-100.)                                                   DELK 401
      S3=DKREM/(BETA*K)*(-100.)                                                   DELK 402
      S4=DKNUF2/(BETA*K)*100.                                                     DELK 403
      S5=DKAB2/(BETA*K)*(-100.)                                                   DELK 404
      S6=DKD1/(BETA*K)*(-100.)                                                    DELK 405
      S8=DKD3/(BETA*K)*(-100.)                                                    DELK 406
      S7=DKD2/(BETA*K)*(-100.)                                                    DELK 407
      S9=DKD4/(BETA*K)*(-100.)                                                    DELK 408
      S16=S1+S2+S3+S6+S8                                                          DELK 409
      S47=S4+S5+S7+S9                                                             DELK 410
      SS=S16+S47                                                                  DELK 411
      WRITE(6,50)DELK,DELKS                                                       DELK 412
   50 FORMAT(' ',19X,' DELTA K/K=',G15.7,    '=',F7.1,' CENTS')                 DELK 413
      WRITE(6,55)S1,S2,S16,S3,S6,S8,S4,S5,S47,S7,S9,SS                            DELK 414
   55 FORMAT('      INDIVIDUAL CONTRIBUTIONS:',/,                                DELK 415
     18X,'   DUE TO FIRST FLIGHT FISSION          =',F7.1,' CENTS',/,            DELK 416
     28X,'   DUE TO FIRST FLIGHT ABSORPTION       =',F7.1,' CENTS',5X,           DELK 417
     3'FIRST FLIGHT CONTRIBUTION      =',F7.1,' CENTS',/,                        DELK 418
     48X,'   DUE TO FIRST FLIGHT REMOVAL          =',F7.1,' CENTS',/,            DELK 419
     58X,'   DUE TO FIRST FLIGHT LEAKAGE(RADIAL)=',F7.1,' CENTS',/,             DELK 420
     58X,'   DUE TO FIRST FLIGHT LEAKAGE(AXIAL) =',F7.1,' CENTS',/,             DELK 421
     68X,'   DUE TO MULTIPLY-COLLIDED FISSION   =',F7.1,' CENTS',/,             DELK 422
     78X,'   DUE TO MULTIPLY-COLLIDED ABSORPTION=',F7.1,' CENTS',5X,            DELK 423
     8'MULTIPLY-COLLIDED CONTRIBUTION=',F7.1,' CENTS',/,                        DELK 424
     98X,'   DUE TO MULTIPLY-COLLIDED LEAK.(RAD)=',F7.1,' CENTS',/,             DELK 425
     98X,'   DUE TO MULTIPLY-COLLIDED LEAK.(AXL)=',F7.1,' CENTS',/,             DELK 426
     1  43X,'NET=',F7.1,' CENTS',/)                                             DELK 427
C         CALCULATE REACTIVITY USING PERTURBATION THEORY FORMULAE               DELK 428
      Y=RAT1-CHI1*NUF1/K                                                        DELK 429
   41 FORMAT(30X,'         METHOD:  TWO GROUP PERTURBATION THEORY')             DELK 430
      FHI12=CHI1*NUF2/(Y*K)                                                     DELK 431
      FHST12=(SIG12+CHI2*NUF1/K)/Y                                              DELK 432
```

```
      RAT3=CHI1*NUF1*FHI12*FHST12+CHI1*NUF2*FHST12+CHI2*NUF1*FHI12+      DELK 433
     1   CHI2*NUF2                                                      DELK 434
      RAT4=RAT3/K                                                       DELK 435
      DKNUF1=DNUF1*CHI1*FHI12*FHST12/RAT3+DNUF1*CHI2*FHI12/RAT3         DELK 436
      DKAB1=DAB1*FHI12*FHST12/RAT4*(-1.0)                               DELK 437
      DKREM=DSIG12*FHI12*(1.0-FHST12)/RAT4                              DELK 438
      DKNUF2=DNUF2*(CHI1*FHST12+CHI2)/RAT3                              DELK 439
      DKAB2=DAB2*(-1.0)/RAT4                                            DELK 440
      DKD1=(DD1*B2RAD)            *FHST12*FHI12*(-1.)/RAT4              DELK 441
      DKD3=           (DDAX1*B2AX)*FHST12*FHI12*(-1.)/RAT4              DELK 442
      DKD2=(DD2*B2RAD)            *(-1.)/RAT4                           DELK 443
      DKD4=           (DDAX2*B2AX)*(-1.)/RAT4                           DELK 444
      DELK=DKNUF1+DKAB1+DKREM+DKNUF2+DKAB2+DKD1+DKD2+DKD3+DKD4          DELK 445
      DELKS=DELK/BETA*100.                                              DELK 446
      S1=    (DKNUF1/BETA)*100.                                         DELK 447
      S2=     (DKAB1/BETA)*100.                                         DELK 448
      S3=     (DKREM/BETA)*100.                                         DELK 449
      S4=     (DKNUF2/BETA)*100.                                        DELK 450
      S5=    (DKAB2/BETA)*100.                                          DELK 451
      S6=    (DKD1/BETA)*100.                                           DELK 452
      S8=    (DKD3/BETA)*100.                                           DELK 453
      S7=     (DKD2/BETA)*100.                                          DELK 454
      S9=     (DKD4/BETA)*100.                                          DELK 455
      S16=S1+S2+S3+S6+S8                                                DELK 456
      S47=S4+S5+S7+S9                                                   DELK 457
      SS=S16+S47                                                        DELK 458
      WRITE(6,41)                                                       DELK 459
      WRITE(6,50) DELK,DELKS                                            DELK 460
      WRITE(6,55)S1,S2,S16,S3,S6,S8,S4,S5,S47,S7,S9,SS                  DELK 461
      GO TO 1                                                           DELK 462
C
C      **SAMPLE INPUT DECK (WITH EXTRA "C" IN COLUMN 1 FOR "COMMENT")**
C      **FOR CASE WITH ITAB=0 AND IFLAG=2**
C      **OTHER OPTIONS MAY REQUIRE DIFFERENT INPUT. REFER TO REPORT**
C
C      **FIRST CARD:  TITLE CARD**
```

```
C  G.E. 1000 MWE OXIDE CORE - NA IN - 99% NA DENSITY
C       **SECOND CARD:  OPTION CHOICES, RADII, CHIS, BETA**
C  0    2 .2921        .3175        .6563        .57          .43          .0033
C       **THIRD THRU TWELFTH CARDS:  CROSS-SECTION TABLE**
C.57821      1.5136       4.9917       2.5852       4.9968                    U238-1
C.37268      .0036785     10.337       10.365                                 U238-2
C2.0177      6.398        4.7911       1.0664       4.7959                    PU239-1
C2.3232      5.4229       10.450       10.473                                 PU239-2
C.010256                  1.4503       .18807       1.5047                    O-1
C                         3.4850       3.6365                                 O-2
C.0036805                 2.4241       .69255       2.4449                    FE-1
C.01868                   5.0516       5.1123                                 FE-2
C.0018692                 1.9707       .40442       2.0174                    NA-1
C.C020C1                  4.9686       5.1169                                 NA-2
C       **THIRTEENTH CARD:  NUMBER DENSITIES**
C.01754      .003095      .041269      .0848        .02218
C       **FOURTEENTH CARD:  BUCKLINGS**
C.00045119   .00010925    .00034194
C       **END CARD**
C  FOLLOWS THE LAST CASE. ANY NUMBER .GT. 0.0 IN THE LAST 8 COLUMNS.          99.
C
       END                                                                  DELK 463
```

E.2 SCODE

SCODE is a minor program which calculates one-group constants using Sheaffer's correlations and then applies the one-group self-shielding correlations of Chapter 5 to obtain heterogeneously self-shielded constants (assuming a typical FBR geometry).

E.2.1 Input to SCODE

Variable	Columns	Format	Description
Card 1 (To run a series of cases, repeat from this card)			
TITLE(18)	1-72	18A4	Identification
ZOPT	73-80	G12.0	ZOPT=0.0, Pu-239/UO_2 cases ZOPT=1.5, U-235/UO_2 cases ZOPT=2.5, Pu-239/UC cases For multiple-case runs: all Pu-239 cases must be run before U-235 cases; all oxide cases must be run before carbide cases.
Card 2			
XND(5)	1-60	5G12.0	Homogenized number densities in the order: Pu/U-235, U-238, O/C, Fe, Na
S	61-72	G12.0	Initial guess for S parameter; suggested: oxide core = 0.4 carbide core = 0.5

E.2.2 Output from SCODE

For both the infinite dilution representation (Sheaffer's original correlations) and the self-shielded representation, the output prints the S and R spectral indices, as well as the one-group macroscopic cross sections: Σ_a (ABSRB), $\xi\Sigma_{tr}$ (CSGTR), $\nu\Sigma_f$ (NUFIS), Σ_r (XSREM), Σ_{tr} (XSGTR). The number of iterations required to converge the one-group spectral index S is also printed (K). Between the infinite dilution

and self-shielded results, the values of the self-shielding factors are printed: the self-shielding factor for U-238 absorption (FABS), and the self-shielding factor for U-238 scattering (FSCAT).

E.2.3 Listing of SCODE

The following pages provide a listing of the SCODE program.

```
C                                                                       SCOD    1
C                              *** SCODE ***                            SCOD    2
C                                                                       SCOD    3
C A PROGRAM TO CALCULATE ONE-GROUP CROSS-SECTIONS BY SHEAFFER'S METHOD  SCOD    4
C         AND MAKE THE U-238 SELF-SHIELDING CORRECTIONS THEREOF.        SCOD    5
C                                                                       SCOD    6
C         1=PU239,2=U238,3=C,4=FE,5=NA                                  SCOD    7
C         IF ZOPT.GT.1.0.AND..LT.2.0, THEN 1=U235                       SCOD    8
C         IF ZOPT.GT.2.0, THEN 3=C                                      SCOD    9
C         ALL PU239 CASES MUST BE RUN BEFORE U235 CASES                 SCOD   10
C         ALL OXIDE CASES MUST BE RUN BEFORE CARBIDE CASES              SCOD   11
      DIMENSION XNO(5),XNU(2),CEL(5),S1FIS(2),GFIS(2),S1TR(5),GTR(5),   SCOD   12
     1   REM(5),TITLE(18),S1AB(5),GAB(5)                                SCOD   13
      DATA XNO/2.953,2.806/,CEL/.0083,.0084,.12,.0353,.0845/,           SCOD   14
     1  S1FIS/1.713,.1972/,GFIS/-.1472,.7911/,S1TR/6.661,6.331,3.307,   SCOD   15
     1   2.829,3.273/,GTR/-.2725,-.28,.02695,-.2844,-.1585/,            SCOD   16
     1   REM/3.04,2.736,.1859,.6584,.3875/,S1AB/1.813,.2147,.002468,    SCOD   17
     1   .004905,6.421E-4/,GAB/-.3067,-.6249,.6728,-.5456,-1.073/       SCOD   18
C         READ TITLE AND CASE-TYPE IDENTIFICATION                       SCOD   19
  1   READ(5,3) TITLE,ZOPT                                              SCOD   20
C         READ HOMOGENIZED NUMBER DENSITIES IN 1,2,3,4,5 ORDER          SCOD   21
C                 AND INITIAL GUESS FOR S PARAMETER.                    SCOD   22
      READ(5,10) XNO,S                                                  SCOD   23
  3   FORMAT(18A4,G8.0)                                                 SCOD   24
  10  FORMAT(6G12.0)                                                    SCOD   25
      IF(ZOPT.LT.1. .OR. ZOPT.GT.2.) GO TO 4                            SCOD   26
C         U-235 CORRELATION CONSTANTS                                   SCOD   27
      XNU(1)=2.476                                                      SCOD   28
      CEL(1)=.0085                                                      SCOD   29
      S1FIS(1)=1.37                                                     SCOD   30
      GFIS(1)=-.4356                                                    SCOD   31
      S1TR(1)=6.189                                                     SCOD   32
      GTR(1)=-.3393                                                     SCOD   33
      REM(1)=2.86                                                       SCOD   34
      S1AB(1)=1.571                                                     SCOD   35
      GAB(1)=-.5817                                                     SCOD   36
```

```
    4   CONTINUE                                                              SCOD  37
        IF(ZOPT.LT.2.) GO TO 6                                                SCOD  38
C          CARBON CORRELATION CONSTANTS                                       SCOD  39
        CEL(3)=.158                                                           SCOD  40
        REM(3)=.2396                                                          SCOD  41
        S1AB(3)=6.879E-6                                                      SCOD  42
        GAB(3)=.7102                                                          SCOD  43
        S1TR(3)=2.753                                                         SCOD  44
        GTR(3)=-.1601                                                         SCOD  45
    6   CONTINUE                                                              SCOD  46
C          CALCUALTION OF INFINITELY DILUTE ONE-GROUP CONSTANTS               SCOD  47
        SREM=0.0                                                              SCOD  48
        DO  5 I=1,5                                                           SCOD  49
    5   SREM=SREM+XND(I)*REM(I)                                               SCOD  50
        K=1                                                                   SCOD  51
   15   HOLD=S                                                                SCOD  52
        CSIGTR=0.0                                                            SCOD  53
        DO 20 I=1,5                                                           SCOD  54
   20   CSIGTR=CSIGTR+CEL(I)*XND(I)*S1TR(I)*(S**GTR(I))                       SCOD  55
        R=S*CSIGTR/(SREM*(1.-S))                                              SCOD  56
        XNUF=XNU(1)*XND(1)*S1FIS(1)*(S**GFIS(1))+XNU(2)*XND(2)*S1FIS(2)*      SCOD  57
       1    (R**GFIS(2))                                                      SCOD  58
        S=XNUF/(XNUF+CSIGTR)                                                  SCOD  59
        K=K+1                                                                 SCOD  60
        IF(K.GT.20) GO TO 25                                                  SCOD  61
        CHECK=ABS(S-HOLD)                                                     SCOD  62
        IF(CHECK.GT..0001) GO TO 15                                           SCOD  63
   25   R=S*CSIGTR/(SREM*(1.-S))                                              SCOD  64
        WRITE(6,30) TITLE,S,R,K                                               SCOD  65
   30   FORMAT(1HO,18A4,/,10X,'INFINITE DILUTION CELL',/,                     SCOD  66
       1                   7X,'S=',G14.7,10X,'R=',G14.7,10X,'K=',I2)          SCOD  67
        CSIGTR=0.0                                                            SCOD  68
        XSIGTR=0.0                                                            SCOD  69
        XAB=0.0                                                               SCOD  70
        DO 35 I=1,5                                                           SCOD  71
        CSIGTR=CSIGTR+CEL(I)*XND(I)*S1TR(I)*(S**GTR(I))                       SCOD  72
```

```
      XSIGTR=XSIGTR+        XND(I)*S1TR(I)*(S**GTR(I))                      SCOD  73
   35 XAB=XAB+XND(I)*S1AB(I)*(S**GAB(I))                                    SCOD  74
      WRITE(6,40)  XAB,CSIGTR,XNUF,SREM,XSIGTR                              SCOD  75
   40 FORMAT(1H ,15X,'CORE ABSRB=',G14.7,/,16X,'CORE CSGTR=',G14.7,/,       SCOD  76
     1   16X,'CORE NUFIS=',G14.7,/,16X,'CORE XSREM=',G14.7,/,16X,           SCOD  77
     2   'CORE XSGTR=',G14.7,/)                                             SCOD  78
      FSA28=XND(2)*S1AB(2)*(S**GAB(2))                                      SCOD  79
      FSTR28=XND(2)*CEL(2)*S1TR(2)*(S**GTR(2))                              SCOD  80
C        CALCULATION OF SELF-SHIELDING FACTORS FROM CORRELATIONS            SCOD  81
      CORR=FSA28*(1./XAB-1.4/CSIGTR)                                        SCOD  82
      IF(CORR.GT.0.1406) GO TO 100                                          SCOD  83
      EM=-.645577                                                           SCOD  84
      BE=.939868                                                            SCOD  85
      GO TO 110                                                             SCOD  86
  100 EM=-.523232                                                           SCOD  87
      BE=.922666                                                            SCOD  88
  110 EFA=EM*CORR+BE                                                        SCOD  89
      CORR=FSA28*(1./XNUF-1.0/CSIGTR)                                       SCOD  90
      IF(CORR.GT..06063) GO TO 120                                          SCOD  91
      EM=-.149001                                                           SCOD  92
      BE=.974334                                                            SCOD  93
      GO TO 140                                                             SCOD  94
  120 IF(CORR.GT..07445) GO TO 130                                          SCOD  95
      EM=-.115774                                                           SCOD  96
      BE=.972319                                                            SCOD  97
      GO TO 140                                                             SCOD  98
  130 EM=-.126925                                                           SCOD  99
      BE=.97315                                                             SCOD 100
  140 EFS=EM*CORR+BE                                                        SCOD 101
      IF(ZOPT.LT.2.) GO TO 150                                              SCOD 102
C        MODIFY CORRELATIONS FOR CARBIDE CASES                              SCOD 103
      EFA=EFA-0.030                                                         SCOD 104
      EFS=EFS-0.004                                                         SCOD 105
  150 WRITE(6,160) EFA,EFS                                                  SCOD 106
  160 FORMAT(7X,' THE F-FACTORS ARE:  FABS=',G14.7,'     FSCAT=',G14.7)     SCOD 107
      K=1                                                                   SCOD 108
```

```
      DELS=0.0                                                          SCOD 109
      SA28=EFA*FSA28                                                    SCOD 110
      STR28=EFS*FSTR28                                                  SCOD 111
      SINF=S                                                            SCOD 112
   65 HOLD=DELS                                                         SCOD 113
C        CALCULATION OF SELF-SHIELDED ONE-GROUP CONSTANTS               SCOD 114
      A=XNUF-SA28                                                       SCOD 115
      B=A+CSIGTR                                                        SCOD 116
      RAT=(SA28+B)**2                                                   SCOD 117
      CSIGTR=0.0                                                        SCOD 118
      XAB=0.0                                                           SCOD 119
      DO 55 I=3,5                                                       SCOD 120
      CSIGTR=CSIGTR+CEL(I)*XND(I)*S1TR(I)*(S**GTR(I))                   SCOD 121
   55 XAB=XAB+XND(I)*S1AB(I)*(S**GAB(I))                                SCOD 122
      CSIGTR=CSIGTR+CEL(1)*XND(1)*S1TR(1)*(S**GTR(1))+STR28             SCOD 123
      XAB=XAB+XND(1)*S1AB(1)*(S**GAB(1))+SA28                           SCOD 124
      P=S*CSIGTR/(SREM*(1.-S))                                          SCOD 125
      XNUF=XNU(1)*XND(1)*S1FIS(1)*(S**GFIS(1))+XNJ(2)*XND(2)*S1FIS(2)*  SCOD 126
     1   (R**GFIS(2))                                                   SCOD 127
      DELSA=(B-A)*(EFA-1.)*FSA28/RAT                                    SCOD 128
      DELTR=((XNUF-XAB)*(B-A)/CEL(2)+SA28+A)*FSTR28*(EFS-1.)/RAT        SCOD 129
      DELS=DELSA-DELTR                                                  SCOD 130
      S=SINF+DELS                                                       SCOD 131
      K=K+1                                                             SCOD 132
      IF(K.GT.20) GO TO 75                                              SCOD 133
      CHECK=ABS(DELS-HOLD)                                              SCOD 134
      IF(CHECK.GT..0001) GO TO 65                                       SCOD 135
   75 CONTINUE                                                          SCOD 136
      CSIGTR=0.0                                                        SCOD 137
      XSIGTR=0.0                                                        SCOD 138
      XAB=0.0                                                           SCOD 139
      DO 85 I=3,5                                                       SCOD 140
      XSIGTR=XSIGTR+        XND(I)*S1TR(I)*(S**GTR(I))                  SCOD 141
      CSIGTR=CSIGTR+CEL(I)*XND(I)*S1TR(I)*(S**GTR(I))                   SCOD 142
   85 XAB=XAB+XND(I)*S1AB(I)*(S**GAB(I))                                SCOD 143
      XAB=XAB+XND(1)*S1AB(1)*(S**GAB(1))+SA28                           SCOD 144
```

```
      CSIGTR=CSIGTR+CEL(1)*XND(1)*S1TR(1)*(S**GTR(1))+STR28                SCOD 145
      XSIGTR=XSIGTR+        XND(1)*S1TR(1)*(S**GTR(1))+STR28/CEL(2)        SCOD 146
      R=S*CSIGTR/(SREM*(1.-S))                                             SCOD 147
      XNUF=XNU(1)*XND(1)*S1FIS(1)*(S**GFIS(1))+XNU(2)*XND(2)*S1FIS(2)*     SCOD 148
     1   (R**GFIS(2))                                                      SCOD 149
      WRITE(6,80) TITLE,S,R,K                                              SCOD 150
   80 FORMAT(1H0,18A4,/,10X,'SELF-SHIELDED CELL',/,                        SCOD 151
     1                   7X,'S=',G14.7,10X,'R=',G14.7,10X,'K=',I2)        SCOD 152
      WRITE(6,40)  XAB,CSIGTR,XNUF,SREM,XSIGTR                             SCOD 153
      WRITE(6,90)                                                          SCOD 154
   90 FORMAT(' ************************************************************SCOD 155
     1**********')                                                         SCOD 156
      GO TO 1                                                              SCOD 157
C
C      **SAMPLE INPUT DECK (WITH EXTRA "C" IN COLUMN 1 FOR "COMMENT")**
C
C      **FIRST CARD:  TITLE CARD, CASE TYPE**
C13.125% PU-239 CELL - SODIUM IN
C      **SECOND CARD:  HOMOGENIZED NUMBER DENSITIES, INITIAL S GUESS**
C.0010604   .0069428    .016006     .0094917    .011286     .40
C
      END                                                                  SCOD 158
```

Appendix F

REFERENCES

1. P. Greebler and B.A. Hutchins, "Significance of Integral Parameters in the Design and Performance of Fast Breeder Reactors," in Proceedings of National Topical Meeting on New Developments in Reactor Physics and Shielding, CONF-720901, U.S. Atomic Energy Commission, 928 (1972).

2. R.G. Palmer, J.P. Plummer, and R.B. Nicholson, "Testing of Heterogeneity Methods Used in Fast Reactor Critical Analyses by Comparison with Theoretical (GEDANKEN) Experiments," Trans. Am. Nucl. Soc., 13, 253 (1970).

3. J.B. Nims and P.F. Zweifel, "Preliminary Report on Sodium Temperature Coefficients in Large Fast Reactors," APDA-135, Atomic Power Development Associates (1959).

4. L. Link et al., "An Evaluation of Four Design Studies of a 1000-MWe Ceramic Fueled Fast Breeder Reactor," COO-279, U.S. Atomic Energy Commission (1964).

5. C.W. Monroe, "Sodium Void Coefficient of Reactivity--A Review and Study of Analytical Work," UNC-5123, United Nuclear Corporation (1965).

6. H.S. Bailey and S.L. Stewart, "G.E. Nuclear Design and Benchmark Critical Experiment Plan for the LMFBR Demonstration Plant," in Proceedings of National Topical Meeting on New Developments in Reactor Physics and Shielding, CONF-720901, U.S. Atomic Energy Commission, 724 (1972).

7. I.I. Bondarenko et al., Group Constants for Nuclear Reactor Calculations, Consultants Bureau, New York (1964).

8. P. Greebler and G.R. Pflasterer, "Doppler and Sodium Void Effects in Fast Reactors," in Reactor Physics in the Resonance and Thermal Regions, vol. II, M.I.T. Press, Cambridge, 359 (1966).

9. P. Greebler and E. Goldman, "Doppler Calculations for Large Fast Ceramic Reactors," GEAP-4092, General Electric (1962).

10. G.K. Rush and F.H. Helm, "The Influence of Heterogeneity on the Measured Sodium-Void Coefficient in a 950-Liter Pancake Fast Core," Trans. Am. Nucl. Soc., 8, 246 (1965).

11. H.H. Hummel and L.K. Volodka, "Studies of Reactivity Coefficients in Large Fast Reactors," in Reactor Physics Division Annual Report, ANL-7410, Argonne National Laboratory, 189 (1969).

12. D. Meneghetti, "Calculational Studies of Effects of Thin Slab Heterogeneities upon Spectral Reactivity Component of Na-Voiding," Trans. Am. Nucl. Soc., 8, 493 (1965).

13. D. Meneghetti, "Calculational Studies of Sodium-Void Reactivity Variations Due to Thin Slab Heterogeneities in Fast Critical Assemblies," in Proceedings of the International Conference on Fast Critical Experiments and Their Analysis, ANL-7320, Argonne National Laboratory, 377 (1966).

14. D. Meneghetti, "Calculational Studies of Sodium-Void Reactivity Variations Due to Heterogeneities in Fast Critical Assemblies," in Reactor Physics Division Annual Report, ANL-7310, Argonne National Laboratory, 212 (1968).

15. F. Storrer et al., "Physics, Kinetics, and Shielding of Fast Breeder Reactors--Survey of Recent Work Done in France, in Fast Breeder Reactors, Proceedings of the London Conference, Pergamon Press, Oxford, 685 (1966).

16. F. Storrer and A. Khairallah, "Heterogeneity Calculation for Fast Reactors by a Perturbation Method," Nuc. Sci. Eng., 24, 153 (1966).

17. A. Khairallah and F. Storrer, "Calculation of the Sodium-Void and Doppler Reactivity Coefficients in Fast Reactors and Critical Assemblies, with Heterogeneity Taken into Account," in Proceedings of the International Conference on Fast Critical Assemblies and Their Analysis, ANL-7320, Argonne National Laboratory, 394 (1966).

18. A. Khairallah, "Heterogeneite dans l'Assemblage 1-A de MASURCA," in Fast Reactor Physics, Proceedings of the Karlsruhe Symposium, vol. II, International Atomic Energy Agency, 189 (1968).

19. H. Spenke, "Reducing the Void Effect in a Large Fast Power Reactor," in Fast Reactor Physics, Proceedings of the Karlsruhe Symposium, vol. II, International Atomic Energy Agency, 365 (1968).

20. V.Z. Jankus and H.H. Hummel, "Two Dimensional Study of Voiding of Sodium from a Fast Core with Zoned Enrichment," in Reactor Physics Division Annual Report, ANL-7310, Argonne National Laboratory, 209 (1968).

21. D. Wintzer, "Heterogeneous Calculations Including Space-Dependent Resonance Self-Shielding," in Fast Reactor Physics, Proceedings of the Karlsruhe Symposium, vol. II, International Atomic Energy Agency, 237 (1968).

22. K. Dance, R.A. Karam, and J.E. Marshall, "Heterogeneity Calculations for Plate-Type Heterogeneous Reactors," in Reactor Physics Division Annual Report, ANL-7410, Argonne National Laboratory, 140 (1969).

23. R.A. Karam et al., "Heterogeneity Effects in a Large UO_2 Core, Assembly 6 of ZPR," in Reactor Physics Division Annual Report, ANL-7410, Argonne National Laboratory, 133 (1969).

24. T.A. Pitterle, E.M. Page, and M. Yamamoto, "Analysis of Sodium Reactivity Measurements," APDA-216, Atomic Power Development Associates (1968).

25. E.M. Page et al., "Comparison and Analysis of Methods for Determining Heterogeneity Effects in Fast Critical Assemblies and Reactors," APDA-269, Atomic Power Development Associates (1971).

26. G. Edison, "The Effect of Heterogeneity in a Large Carbide LMFBR," Trans. Am. Nucl. Soc., 12, 276 (1969).

27. Ward W. Engle, Jr., "A User's Manual for ANISN, A One-Dimensional Discrete Ordinates Transport Code with Anisotropic Scattering," K-1693, Union Carbide (1967).

28. D.A. Newmarch, "Errors Due to the Cylindrical Cell Approximation in Lattice Calculations," AEEW-R34, Atomic Energy Establishment Winfrith (1960).

29. H.C. Honeck, "The Calculation of Thermal Utilization and Disadvantage Factors in Uranium/Water Lattices," Nucl. Sci. Eng., 18, 49 (1964).

30. Y. Fukai, "First Flight Collision Probability in Moderator-Cylindrical Fuel Systems," J. Nucl. Energy, A/B, 17, 115 (1963).

31. T.A. Pitterle and N.C. Paik, "Summary of Analysis of Plate Vs. Pin Measurements Emphasizing Reactivity and Sodium Void Effects," in Proceedings of National Topical Meeting on New Developments in Reactor Physics and Shielding, CONF-720901, U.S. Atomic Energy Commission (1972).

32. R. Meghreblian and D. Holmes, Reactor Analysis, McGraw-Hill, New York (1960).

33. H.K. Clark, "Calculation of High Energy Events in Thermal Reactors," DP-609, Savannah River Laboratory (1961).

34. W.G. Bickley and J. Nayler, "A Short Table of the Functions $Ki_n(x)$ from n = 1 to n = 16," Phil. Mag., 20, 343 (1935).

35. G.W. Stuart, "Multiple Scattering of Neutrons," Nucl. Sci. Eng., 2, 617 (1953).

36. J.R. Lamarsh, Introduction to Nuclear Reactor Theory, Addison-Wesley, Reading, 156 (1966).

37. G.I. Marchuk and V.P. Il'in, "Neutron Resonance Capture in an Annular Lump," in Theory and Methods of Nuclear Reactor Calculations, Consultants Bureau, New York, 147 (1964).

38. W.W. Little, Jr. and R.W. Hardie, "2DB User's Manual – Revision 1," BNWL-831 Rev 1, Battelle Northwest (1969).

39. M. Michelini, "Anisotropic Diffusion Theory," Energia Nucleare, 16, 11 (1969).

40. D.S. Selengut, "Diffusion Coefficients for Heterogeneous Systems," in Nuclear Physics Research Quarterly Report, HW-60220, Hanford Atomic Product Operation, 65 (1959).

41. D.S. Selengut, "Diffusion Coefficients for Heterogeneous Systems," Trans. Am. Nucl. Soc., 3, 398 (1960).

42. D.J. Behrens, "The Effects of Holes in a Reacting Material on the Passage of Neutrons," Proc. of Phys. Soc., A62, 607 (1949).

43. N.I. Laletin, "Passage of Neutrons in a Heterogeneous Medium," in Proceedings of the Second International Conference on the Peaceful Uses of Atomic Energy, United Nations, vol. 16, 601 (1958).

44. C. Carter, "Streaming Due to Holes in a Reactor," J. Nucl. Energy, A/B, 15, 76 (1962).

45. D.C. Leslie, "The Weighting of Diffusion Coefficients in Cell Calculations," J. Nucl. Energy, A/B, 16, 1 (1962).

46. M.M.R. Williams and J. Wood, "A Transport Theory Calculation of Neutron Flux, Disadvantage Factors and Effective Diffusion Constants in Square Cells and Slabs," J. Nucl. Energy, 26, 3 (1972).

47. M.M.R. Williams, "Effective Diffusion Constants in Heterogeneous Media--II. The Cylindrical Cell," J. Nucl. Energy, 26, 4 (1972).

48. P. Benoist, "Théorie du Coefficient de Diffusion des Neutrons dans un Réseau Comportant des Cavités," University of Paris Thesis (1964). (Also CEA-R-2278, 1964).

49. P. Benoist, "Theory of the Diffusion Coefficient of Neutrons in a Lattice Containing Cavities," translation of Ref. 48 by S.R. Bull et al., Stanford University (1967).

50. P. Benoist, "Streaming Effects and Collision Probabilities in Lattices," Nucl. Sci. Eng., 34, 285 (1968).

51. R. Bonalumi, "Axial Diffusion Coefficient in a Lattice: A Direct Derivation of Benoist's Formula," Energia Nucleare, 15, 608 (1968).

52. V. Pierpaoli and L. Sartori, "PROKAI, A Code for Anisotropic Diffusion in Thermal Reactors with Hollow Tube Fuel Elements," Energia Nucleare, 11, 543 (1964).

53. M. Michelini, "An Advancement in Neutron Transport Theory, Part 2: Improvement in the Classic Diffusion Coefficient Formulation," Energia Nucleare, 15, 435 (1968).

54. M. Michelini, "Anisotropic Diffusion Coefficient in Generalized X,Y Geometry: Theory and Application to Diffusion Codes," Nucl. Sci. Eng., 47, 116 (1972).

55. A. Kavenoky, "Calcul et Utilisation des Probabilités de Premier Collision pour des Milieux Hétérogènes a Une Dimension: Les Programmes ALCOLL et CORTINA," CEA-N-1077, Centre d'Etudes Nucleaires de Saclay (1969).

56. I. Carlvik, "Collision Probabilities for Finite Cylinders and Cuboids," AE-281, Aktiebolaget Atomenergi (1967).

57. R. Bonalumi, "Neutron First Collision Probabilities in Reactor Physics," Energia Nucleare, 8, 326 (1961).

58. T. Lacapelle, Private communication (1971); based on P. Benoist, private communication to T. Lacapelle (1964).

59. E.E. Pilat, H. Guéron, and D.D. Lanning, "Measurement of the Diffusion Coefficient in a Highly Anisotropic Medium," Trans. Am. Nucl. Soc., 8, 446 (1965).

60. C.S. Penn et al., "Effect of Voids on Thermal-Neutron Diffusion Length," Trans. Am. Nucl. Soc., 15, 446 (1972).

61. D.R. Harris and J.A. Mitchell, "Measurements and Calculations of Neutron Migration and Its Anisotropy in Lattices of Fuel Rods and Liquid Coolant," Nucl. Sci. Eng., 44, 221 (1971).

62. R.A. Bonalumi, "A Unified Theory of Cell Diffusion Coefficients," Energia Nucleare, 18, 395 (1971).

63. R.A. Bonalumi, "Revision of Some Practical Formulas in 'A Unified Theory of Diffusion Coefficients'," Energia Nucleare, 19, 197 (1972).

64. M.J. Bridge and N. Howarth, "Corrections to the Benoist Diffusion Coefficients for CAGR Lattices," RD/B/N1645, Central Electric Generating Board (1970).

65. A.M. Weinberg and E.P. Wigner, The Physical Theory of Neutron Chain Reactors, University of Chicago Press, Chicago (1958).

66. V.C. Rogers, "MIDI – A Fortran Code for the Calculation of Average Cross Sections in the Resonance Energy Region," M.I.T. Internal Document, 16 July 1971.

67. T.A. Pitterle and D.M. Green, "IDIOT – A Fortran IV Code for Calculation of Resonance Averaged Effective Cross Sections and Their Temperature Derivatives," Atomic Power Development Associates (1968).

68. A. Sauer, "Approximate Escape Probabilities," Nucl. Sci. Eng., 16, 329 (1963).

69. C.N. Kelber, "An Extended Equivalence Relation," Nucl. Sci. Eng., 42, 257 (1970).

70. T.C. Leung et al., "Neutronics of an LMFBR Blanket Mock-Up," COO-3060-1, MITNE-127, Massachusetts Institute of Technology (1972).

71. M.K. Sheaffer, M.J. Driscoll, and I. Kaplan, "A One-Group Method for Fast Reactor Calculations," MIT-4105-1, MITNE-108, Massachusetts Institute of Technology (1970).

72. M.K. Sheaffer, M.J. Driscoll, and I. Kaplan, "A One-Group Method for Fast Reactor Calculations," Nucl. Sci. Eng., 48, 459 (1972).

73. G. Bitelli, M. Salvatores, and G. Cecchini, "Heterogeneity Effects on Neutron Self-Shielding Factors for Fast Reactors," Nucl. Sci. Eng., 40, 138 (1970).

74. R.M. Patterson, R.P. Christman, and E.J. Hennelly, "Resonance Self-Shielding Factors for Heavy Actinides," J. Nucl. Energy, 24, 53 (1970).

75. Draft Copy, "Evaluation Report: 1000-MWe LMFBR Follow-On Studies," Argonne National Laboratory, 1970.

76. C.P. Zaleski, "Problèmes Particuliers Liés à l'Étude des Reacteurs à Neutrons Rapides," in Génie Atomique, vol. III, Presses Universitaires de France, 713 (1965).

77. Private Communication, various sources (Oct. 1972).

78. J.W. Newton, "Relative Performance of Different LMFBR Lattice Configurations Under Natural Circulation," S.M. Thesis, M.I.T. Dept. of Nucl. Eng., August 1970.

79. J.B. Dee, P. Fortesque, and J.A. Larrimore, "Gas-Cooled Fast Breeder Reactor Studies," GA-10678, Gulf General Atomic (1971).

80. P. Fortesque and W.I. Thompson, "The GCFR Demonstration Plant Design," GA-10036, Gulf General Atomic (1970).

81. B. Pellaud, "Physics Design of the Gas-Cooled Fast Breeder Demonstration Plant," GA-10509, Gulf General Atomic (1971).

82. R.B. Kidman et al., "The Shielding Factor Method of Generating Multigroup Cross Sections for Fast Reactor Analysis," Nucl. Sci. Eng., 48, 189 (1972).

83. I.A. Forbes et al., "Design, Construction and Evaluation of a Facility for the Simulation of Fast Reactor Blankets," MIT-4105-2, MITNE-110, Massachusetts Institute of Technology (1970).

84. A.M. Thompson, "Activation Profiles in Reactor Fuel Elements," S.B. Thesis, M.I.T. Dept. of Physics (June 1972).

85. P. DeLaquil, III, "Heterogeneous Effects in LMFBR Blanket Fuel Elements," in LMFBR Blanket Physics Progress Report No. 2, COO-3060-5, MITNE-131, Massachusetts Institute of Technology, 82 (1971).

86. P. DeLaquil, III, Private Communication, "Compilation of measurements by DeLaquil, Westlake, and McFarland" (1971).

87. L.T. Kim, "Heterogeneous Effects in LMFBR Blanket Using Activation Method," M.I.T. Course 22.39 Project Report (1972).

88. F.R. Taraba and S.H. Paine, "The Radial Distribution of Thermal Neutron Flux in Cylindrical Fuel Specimens During Neutron Irradiation," ANL-5872, Argonne National Laboratory (1959).

89. H. Küsters et al., "Progress in Fast Reactor Physics in the Federal Republic of Germany," (Draft Copy), KFK-1632, EACRP-U-46, Gesellschaft für Kernforschung mbH Karlsruhe, 3.32 (1972).

90. A. Travelli and J.C. Beitel, "Analysis of Sodium-Void Experiments in the FTR Engineering Mockup Critical Assembly," in Proceedings of National Topical Meeting on New Developments in Reactor Physics and Shielding, CONF-720901, U.S. Atomic Energy Commission, 739 (1972).

91. D.M. O'Shea, B.J. Toppel, and A.L. Rago, "MC^2 – A Code to Calculate Multigroup Cross Sections," ANL-7318, Argonne National Laboratory (1967).

92. Akira Oyama and Y. Higashihara, "Current Status of the Fast Reactor Physics Program in Japan," Invited Paper, ANS Meeting (November 1972).